Multimodal Instrumentation and Methods for Neurotechnology Out of the Lab

vorgelegt von
M.Sc.
Alexander von Lühmann
geb. in Warburg

von der Fakultät IV - Elektrotechnik und Informatik
der Technischen Universität Berlin
zur Erlangung des akademischen Grades

Doktor der Ingenieurwissenschaften
- Dr.-Ing. -

genehmigte Dissertation

Promotionsausschuss:

Vorsitzender:	Prof. Dr. Thomas Wiegand
Gutachter:	Prof. Dr. Klaus-Robert Müller
Gutachter:	Prof. Dr. Benjamin Blankertz
Gutachter:	Prof. Dr. David Boas

Tag der wissenschaftlichen Aussprache: 27. August 2018

Berlin 2018

Abstract

In neuroscience and related fields, progress in instrumentation, computational power, and signal processing methods continuously provide novel and increasingly powerful tools toward the investigation of brain activity in real-time and everyday environments. Research into real-life and application-oriented, non-invasive neurotechnology bears a number of multidisciplinary challenges which need to be addressed. Neurophysiological signals have to be measured subtly and safely while reliability and robustness have to be ensured. To this end, new approaches are explored in this thesis that deal with the simultaneous acquisition and utilization of multiple brain and body signals in mobile scenarios. They aim to reduce acquisition restraints for mobile neuroimaging, and at the same time increase the amount of information that is provided by hybrid acquisition equipment. This enables the exploitation of complementary and shared information in the measured modalities toward the development of methods that enhance robustness in the analysis and classification of brain signals.

The first contribution of this work comprises the development of novel architectures and devices for the mobile measurement of brain and body signals. Here, the focus lies on functional Near-Infrared Spectroscopy (fNIRS) and Electroencephalography (EEG) instruments. The primary result is *M3BA*, an architecture for *M*obile, *M*odular, *M*ultimodal *B*iosignal *A*cquisition. While miniaturized beyond previous approaches, *M3BA* offers hybrid and high-precision measurement of fNIRS, EEG, acceleration and other signals while allowing scalability and easy customization.

The second contribution targets the generation of evoked multimodal neuroimaging data under realistic environmental but yet well-controlled movement conditions. Making use of M3BA modules in a lightweight wireless headset, a novel, bespoke n-back-based cognitive workload paradigm was designed and administered in a study with 17 freely moving subjects.

Using this unique dataset, the third contribution consists of the development of a multimodal Blind-Source-Separation framework for the analysis of fNIRS signals and its application in *BLISSA*^{2}*RD*, for the accelerometer-based rejection of movement induced artifacts. Employing it along with other state-of-the-art methods, we ultimately provide a proof of feasibility toward workload classification under challenging, realistic conditions. In this unique approach, and with strict rejection of artifacts, accuracies greater than 80% based on neurophysiological EEG-fNIRS markers is achieved.

Zusammenfassung

In den Neurowissenschaften und ihren angrenzenden Feldern ermöglichen Fortschritte in der Messtechnik, Miniaturisierung, Rechenleistung und Signalverarbeitung leistungsstarke Ansätze zur Untersuchung der Gehirnaktivität in Echtzeit und unter zunehmend alltagsähnlichen Bedingungen. Die Erforschung nicht-invasiver Neurotechnologie für anwendungsorientierte Szenarien außerhalb des Labors birgt jedoch eine Vielzahl multidisziplinärer Herausforderungen. Neuartige Ansätze müssen eine unaufdringliche und schadlose Erfassung neurophysiologischer Signale ermöglichen und gleichzeitig Zuverlässigkeit und Robustheit sicher stellen. Zu diesem Zweck werden in dieser Dissertation neue Ansätze untersucht, die sich mit der simultanen Erfassung und Nutzung von multiplen Gehirn- und Körpersignalen in mobilen Szenarien beschäftigen. Durch die Verbindung von Biomedizintechnik, Neurowissenschaften und Maschinellem Lernen sollen die Möglichkeiten bei der Signalerfassung erweitert und die Menge der erfassten Informationen erhöht werden. Diese ermöglicht die Entwicklung multimodaler Methoden zur Verbesserung von Signalqualität und Robustheit.

Der erste Teil dieser Arbeit besteht aus der Entwicklung von Grundlagen und Architekturen für den Entwurf neuer Instrumente zur mobilen, miniaturisierten und hybriden Messung von Gehirn- und peripheren Körpersignalen. Dabei liegen die Schwerpunkte auf der funktionellen Nahinfrarot-Spektroskopie (fNIRS) und Elektroenzephalographie (EEG). Das primäre Resultat ist *M3BA*, eine *M*obile, *M*odulare, *M*ultimodale *B*iosignalerfassungs-*A*rchitektur. Während *M3BA* gegenüber früherer Ansätze weiter miniaturisiert ist, bietet es hochpräzise hybride fNIRS-EEG- und Accelerometer-Messungen, Skalierbarkeit und einfache Anpassung.

Diese Architektur ermöglicht im zweiten Teil die Entwicklung und experimentelle Umsetzung eines neuartigen räumlichen n-back-Paradigmas für die Erfassung der mentalen Arbeitslast in sich frei bewegenden Teilnehmern. Der resultierende Datensatz, mit einem speziell darauf ausgelegten *M3BA*-Headgear erfasst, bietet eine Vielfalt physiologischer Signale von 17 Probanden unter kontrollierten Bewegungsbedingungen.

Unter Verwendung dieses neuen Datensatzes besteht der dritte Teil aus der Entwicklung einer Methode zur Analyse von fNIRS-Signalen und der Accelerometer-basierten Entfernung von fNIRS Bewegungsartefakten mit dem Namen *BLISSA*^{2}*RD*. In Kombination dieser Methode mit anderen state-of-the art Ansätzen und unter strikter Artefaktbereinigung wird abschließend die Klassifizierung mentaler Arbeitslast unter herausfordernden, realitätsnahen Bedingungen untersucht. Ein erster Machbarkeitsnachweis wird mit erreichten Klassifikationsgenauigkeiten von $> 80\%$ unter Ausnutzung der Multimodalität der Daten erbracht.

Acknowledgements

At the point of completing this thesis, looking back feels like looking down a mountaintop that one just ascended. It becomes clear, that stamina for the way up and rocky detours should not be underestimated – and that without the training, guidance, and support of teachers, teammates, and friends, the whole endeavor would certainly have been a hopeless one.

I am immensely grateful for being able to say without euphemism that I could not have wished for better people and their support. Above all, I would like to thank my supervisor and mentor Prof. Dr. Klaus-Robert Müller and the BIMoS graduate school of TU Berlin for giving me the opportunity to follow my dream without constrains, while receiving empathic support, professional advice, and guidance, and being introduced into the fascinating world of Machine Learning. I would like to thank Prof. Dr. Benjamin Blankertz for always having an open door to listen and to discuss, for his support, and for welcoming me into his BBCI group – with some of the most amazing people in it that I have met so far in my life. The wonderful times spent at this institute within both departments in a working environment, which is both highly professional and amicable, is something I will always remember.

I thank Prof. Dr. David Boas for the reviewing and marking of my thesis and all the fruitful exchange, Prof. Dr. Tülay Adali for the fantastic opportunity to work and learn in her lab at UMBC for some time, and Dr. Zois Boukouvalas for his friendship and collaborative support on site. Similarly, I am very grateful to Dr. Heidrun Wabnitz and Dr. Tilmann Sander-Thömmes for their experienced help with the evaluation of M3BA at the PTB in Berlin. I would further like to thank Prof. Dr. Gabriel Curio and Prof. Dr. Hasan Ayaz for valuable advice for the design and evaluation of the workload experiment, and Dr. Stefan Haufe, Dr. Shinichi Nakajima, and Dr. Andreas Ziehe for their help with tips and tricks.

A huge thank you also to Prof. Dr. Olaf Dössel and Prof. Dr. Niels Birbaumer for all their teaching and support over the previous years, and for enabling me to lead my own little research project, that ultimately became one of the major first stepping stones to this work.

Thank you, Andrea Gerdes and Dominik Kühne for your great support with administrative and IT issues. Many thanks also to Till Friebe and Felix Bohlmann for your work.

For having the most awesome friends and colleagues I am beyond grateful. Thank you, Max Alber, Steffi Brandl, Sven Dähne, Manon Grube, Christian Herff, Miriam Hägele, Johannes Höhne, Daniel Miklody, Matthias Schultze-Kraft and Markus Wenzel for all the help, collaborative action, and advice during these years. Above all, thank you, all my friends whether on this list or not, for being in my life and making it fun! Thank you, Marina, for being a truly awesome partner and for your help and patience during challenging times. It is so fantastic, that you exist. Last but not least, Regine, Erik, and Manfred, thank you for your unconditional love and support, you are the best family one can possibly wish for.

Contents

List of Abbreviations

Roman Symbols

$(m)BLL$	(modified) Beer-Lambert-Law
$(r)LDA$	(regularized) Linear Discriminance Analysis
μC	Microcontroller
AC	Alternating Current
$ACCEL$	Accelerometer
ADC	Analog-to-Digital Converter
AEP	Auditory Evoked Potential
APD	Avalanche Photodiode
BCI	Brain-Computer Interface
BSS	Blind-Source Separation
CCA	Canonical Correlation Analysis
$CMRR$	Common-Mode Rejection Ratio
CSP	Common Spatial Patterns
CW	Continuous Wave
DAC	Digital-to-Analog Converter
DC	Direct Current
DPF	Differential Path Length Factor
DRL	Driven Right Leg
ECG	ElectroCardioGram
EEG	ElectroEncephaloGram

EMG	ElectroMyoGram
EOG	ElectroOculoGram
ERP	Event-Related Potential
FD	Frequency Domain
fNIRS	functional Near-Infrared Spectroscopy
HbO	Oxy-Hemoglobin
HbR	Deoxy-Hemoglobin
HMI	Human Machine Interface
IA	Instrumentation Amplifier
ICA	Independent Component Analysis
LD	Laser Diode
LED	Light Emitting Diode
M3BA	Mobile, Modular, Multimodal Biosignal Acquisition
MUX	Multiplexer
MWL	Mental Workload
NIR	Near-Infrared
OL	Optical Loss
PaC	Principal Accelerometer Component
PCA	Principal Component Analysis
PCB	Printed Circuit Board
PD	Photo Detector
PSD	Phase Sensitive Detection
PSRR	Power Supply Rejection Ratio
SDS	Source-Detector Separation
SiPD	Silicon Photodiode
SNR	Signal-to-Noise Ratio

TD	Time Domain
TDM	Time-Division Multiplexing
WBSN	Wireless Body Sensor Network

Chapter 1

Introduction

1.1 Advancing Neurotechnology

For centuries, our understanding of the human brain has been gained through inference from the combination of observed behavior in the living and anatomical studies in the dead. In 1879, Carl Reclam, a professor of medicine at the University of Leipzig, Germany, compared the morphology of a German farmworker's brain with that of the mathematician Gauss, and concluded: "How does the brain obtain an increase in convolutions? [...] Why does it become bigger? [...] The same mechanism that supports the growth of muscles [...] also increases the mass and surface of the brain: work." (in *Der Leib des Menschen*, p73, 1879 [Rec79]).

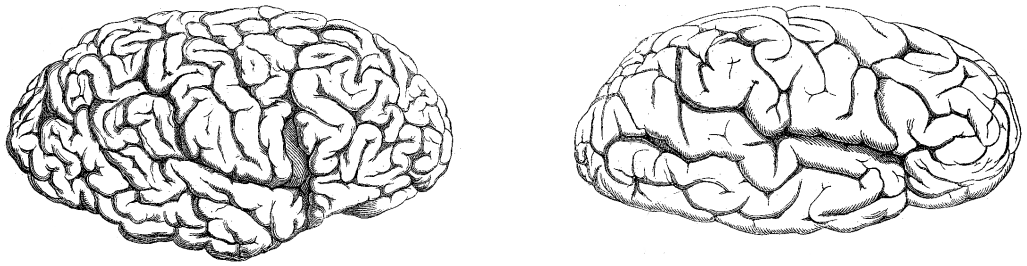

Fig. 43. Das Gehirn des Astronomen Gauß. (Geb. 1777, † 1855.)

Fig. 44. Das Gehirn eines deutschen Handarbeiters. (29 Jahre alt.)

"Wodurch erhält das Gehirn mehr Windungen? [...] Weshalb vergrößert sich das Gehirn? [...] Dasselbe Mittel, welches die Oberfläche der Muskeln ausdehnt, indem es dieselben größer und breiter macht [...] vermehrt auch Masse und Oberfläche des Gehirns: die Arbeit [...]"

Figure 1.1: Comparison of the brains of Gauss (left) and a German farmworker (right) in 1879 [Rec79]

Half a century down the line, in 1929, Berger's pioneer work established the *electroencephalogram* (EEG) as a measure of and to quantify brain activity in the living [Ber29]. Since then, EEG and other more recently developed measurement modalities enabled neuroscience and medicine to get glimpses into the immense complexity of the human brain and move forward the understanding of its physiology and the neuronal correlates of behavior and cognition [KSJ+00]. This is one illustration of the close link between the natural and engineering sciences: The generation of knowledge often relies on appropriate tools for investigation – and vice versa.

In neuroscience and related fields, progress in instrumentation, computational power,

and signal processing methods continuously provided novel and increasingly powerful tools toward the investigation of brain activity in real-time and everyday environments. As a consequence, new applications for clinical diagnostics, assistance, and rehabilitation have emerged over the last decades. Amongst them are telemedicine and pervasive healthcare [APLI+15; ZDP+14] and brain-computer interfaces (BCI). A BCI is an artificial system that bypasses the body's normal efferent pathways, which are the neuromuscular output channels [WBM+02]. These systems aim to provide an active interface for communication and control [WBM+02; BGH+99] and beyond, aiming to assess covert mental states [BTV+10; MTD+08] and to monitor the "brain at work", in so-called Neuroergonomic approaches [Par11; Par03]. BCI and more integrative human-machine interfaces (HMI) - that use both brain and body signals, have unprecedented potential to improve healthcare, work environments, efficiency, and security as well as advance the understanding of brain function and cognition in general and especially under everyday life conditions.

Research into real-life and application-oriented, non-invasive neurotechnology bears a number of multidisciplinary challenges. Experimental conditions are harder to control; environmental and physiological artifacts deteriorate signal quality; and interactions between the different brain and body signal types increase non-stationarities within the individual measures. One approach to tackle this multifaceted problem is to acquire multiple modalities, exploiting the specific strengths of each signal by the use of novel signal analysis techniques. Combining modalities from different imaging methods has been shown to robustify BCI applications [FDS+15; DBS+15; FMS+12; PAB+10] and helped improve the understanding of brain development and cognitive processing [ESM+05]. Other applications exist in the *investigation of brain dysfunction in clinical diagnostics*, for instance in epilepsy [VCR+11; DGM+07; IWS+93]. Hence, there is a clear call for high-quality multimodal methods/measures and hybrid instruments for mobile employment, such as wearable body sensors or wireless body sensor networks (WBSNs). Such instruments need to convince in terms of the minimization of size, power consumption, weight, and cost while maintaining high precision in data acquisition.

1.2 Objective and Contributions of this Thesis

This thesis contributes toward the ultimate aim to enable reliable non-invasive assessment of large-scale brain signals outside the lab by making use of multimodal measurements. The approach pursues to (1) **decrease acquisition restraints** for mobile neuroimaging and thus increase usability, and at the same time (2) **increase the amount of information** that is provided by hybrid acquisition equipment. This enables (3) the exploitation of complementary and shared information in the measured signals toward the development of methods that aid **the robustness** in the analysis and classification of brain signals (see Figure 1.2). To achieve these goals, three interdisciplinary and interdependent fields are addressed: firstly, the development of **mobile multimodal instrumentation**; consequently, the acquisition of **multimodal datasets** under real-life conditions using novel paradigms; and finally, building on those two, the development of new **multimodal signal processing** approaches making

use of the newly available large-scale amount of information in the set of data.

With an emphasis on instrumentation and application, this thesis contributes to all three fields, making use of methods from biomedical electrical engineering, computational neuroscience, as well as machine learning.

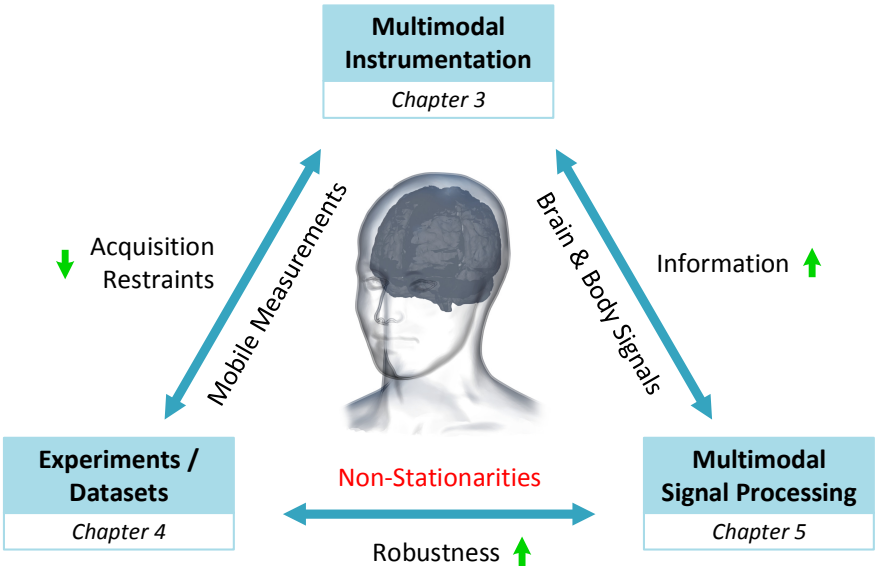

Figure 1.2: Concept and links between contributions of this thesis. The design of novel multimodal instrumentation will allow for the acquisition of not yet existing hybrid datasets, and that beyond constrained laboratory conditions. These newly available datasets then enable the development of novel multimodal signal processing methods for increased robustness against non-stationarities by exploiting shared and complementary information across modalities.

A Roadmap Through this Thesis

Chapter 2 briefly discusses the physiological background and fundamental principles of the acquisition of electroencephalography (EEG) and functional near-infrared spectroscopy (fNIRS). EEG-fNIRS is then motivated as the natural choice for multimodal neuroimaging under mobile conditions.

Chapter 3 deals with multimodal instrumentation, and begins with fundamentals and design considerations for both EEG and fNIRS technologies. On this basis, the two-stage development and evaluation of wearable hybrid EEG-fNIRS instrumentation is then introduced. The first stage, comprising a wearable miniaturized unimodal fNIRS architecture (the *openNIRS*) will be discussed briefly with focus on concepts and lessons learned for the centerpiece of this thesis: M3BA, our next-generation hybrid EEG-fNIRS architecture, that features *Multimodal, Mobile, Modular Biosignal Acquisition*.

EEG-fNIRS in motion is a fairly young, just emerging field, and there are currently no suitable datasets available that provide both evoked multimodal neuroimaging data and well-controlled movement conditions. For this purpose, making use of the M3BA modules in a lightweight wireless headset, a *novel, bespoke n-back-based cognitive workload paradigm*

was designed and administered in freely moving subjects. This is described in **Chapter 4**, which covers paradigm, protocol, channel selection and target features for classification of the signals, and a brief Section of behavioral results.

In **Chapter 5**, this unique dataset is used for method design, quantitative and qualitative evaluation, and classification: First, a novel framework and method for *multimodal blind-source separation analysis and movement artifact rejection* in fNIRS signals (*BLISSA^{2}RD*) is developed and explored. Secondly, and finally, all preceding contributions are linked with established methods in a brief feasibility study, approaching classification of cognitive operator workload under challenging moving conditions and with few channels.

Chapter 6 concludes the thesis with some final, concluding remarks and discusses remaining limitations and future directions.

Each Chapter has its own emphasis on one specific discipline within the broad fields of neurotechnology, and the respective relevant state of the art and aims are provided alongside individually for each of the novel contributions presented in this thesis.

1.2.1 Included Publications

The work in this thesis has been published in peer-reviewed journals and conferences and closely follows the publications listed in chronological order below.

Peer-Reviewed Journals

[1] von Lühmann, A., Herff, C., Heger, D., and Schultz, T. "Towards a wireless open source instrument: functional Near-Infrared Spectroscopy in mobile Neuroergonomics and BCI applications". In: *Frontiers in Human Neuroscience* 9 (2015), p. 617

[2] von Lühmann, A., Wabnitz, H., Sander, T., and Müller, K.-R. "M3BA: A Mobile, Modular, Multimodal Biosignal Acquisition Architecture for Miniaturized EEG-NIRS-Based Hybrid BCI and Monitoring". In: *IEEE Transactions on Biomedical Engineering* 64.6 (2017), pp. 1199–1210

[3] von Lühmann, A., Boukouvalas, Z., Müller, K.-R., and Adali, T. "A new blind source separation framework for signal analysis and artifact rejection in functional Near-Infrared Spectroscopy". In: *NeuroImage* (2018). (in review)

[4] von Lühmann, A., Miklody, D., Blankertz, B., and Müller, K.-R. "Multimodal cognitive workload monitoring in freely moving subjects". In: *Journal of Neural Engineering* (2018). (in preparation)

Peer-Reviewed Conferences

[1] von Lühmann, A. and Müller, K.-R. "Why build an integrated EEG-NIRS? About the advantages of hybrid bio-acquisition hardware". In: *Proceedings of the 39th Annual International Conference of the IEEE Engineering in Medicine and Biology Society (EMBS)*. 2017, pp. 4475–4478

Patents

[1] von Lühmann, A. and Müller, K.-R. "Biosignal acquisition device and system, method for acquisition of biosignals". Pat. US20170281014A1. 2018

1.2.2 Additional Publications

Additional publications in peer-reviewed journals and conferences that were (co-)authored are listed in the following.

Peer-Reviewed Journals

[1] Shin, J., von Lühmann, A., Blankertz, B., Kim, D.-W., Jeong, J., Hwang, H.-J., and Müller, K.-R. "Open access dataset for EEG + NIRS single-trial classification". In: *IEEE Transactions on Neural Systems and Rehabilitation Engineering* 25.10 (2017), pp. 1735–1745

[2] Shin, J., von Lühmann, A., Kim, D.-W., Mehnert, J., Hwang, H.-J., and Müller, K.-R. "Simultaneous acquisition of EEG and NIRS during cognitive tasks for an open access dataset". In: *Scientific Data* 5.180003 (2018)

Book Chapters

[1] Soekadar, S., Birbaumer, N., and von Lühmann, A. "Optical brain-computer interfaces: state-of-the-art, challenges, and perspectives". In: *Handbook of Clinical Neurology, Handbook Brain-Computer Interfacing: Neural Devices for paralysis in neurological practice and beyond*. Ed. by N. Ramsey and J. Millan. Vol. xx. 3. (in print). Elsevier, 2018, pp

Peer-Reviewed Conference Contributions and Abstracts

[1] von Lühmann, A., Soekadar, S., Müller, K.-R., and Blankertz, B. "Headgear for mobile neurotechnology: looking into alternatives for EEG and NIRS probes". In: *Proceedings of the 7th Graz Brain-Computer Interface Conference*. Verlag der Technischen Universität Graz, 2017, pp. 496–501

[2] von Lühmann, A., Addesa, J., Chandra, S., Das, A., Hayashibe, M., and Dutta, A. "Neural interfacing non-invasive brain stimulation with NIRS-EEG joint imaging for closed-loop control of neuroenergetics in ischemic stroke". In: *Proceedings of the 8th International IEEE EMBS Conference On Neural Engineering (NER)*. 2017, pp. 349–353

[3] von Lühmann, A. "Hybridization of bio-electrical and bio-optical acquisition technology using open fNIRS components". In: *Proceedings of the DGBMT workshop biosignal processing*. 2016

[4] von Lühmann, A. and Müller, K.-R. "M3BA: New Technology for Mobile Hybrid BCIs". In: *Proceedings of the 6th International Brain-Computer Interface Meeting*. 2016, p. 151

[5] von Lühmann, A., Wabnitz, H., Sander, T., and Müller, K.-R. "Miniaturized CW NIRS for integration and hybridization with mobile EEG / ECG / EMG and Accelerometer". In: *Proceedings of the Society for functional Near Infrared Spectroscopy Biennial Meeting*. 2016

[6] Brandl, S., von Lühmann, A., and Müller, K.-R. "Towards Brain-Computer Interfaces outside the lab: new measuring devices and machine learning challenges". In: *Proceedings of the 39th Annual International Conference of the IEEE Engineering in Medicine and Biology Society (EMBC)*. 2017

Chapter 2

Measures of Brain Activity

2.1 A Brief Overview of Methods

Methods available to acquire information about brain physiology include electrical, magnetic and hemodynamic measurements. Among them are electroencephalography (EEG) [Ber29], magnetoencephalography (MEG) [Coh68], functional near-infrared spectroscopy (fNIRS) [Jöb77], functional magnet resonance imaging (fMRI) [BKM+91], positron emission tomography (PET) [Swe53] and single photon emission computed tomography (SPECT) [KE63]. Each of these technologies has its advantages concerning temporal, spatial and anatomical resolution and specificity. Size, weight, patient positioning or radiation exposure constrain these systems in method-specific ways. Table 2.1 gives a summary.

	EEG	**MEG**	**fNIRS**	**fMRI**	**SPECT**	**PET**
Parameter	el. activity	el. activity	$[Hb]$	$[Hb]$	blood flow	blood flow
Temporal Resol.	$1\,ms$	$1\,ms$	$100\,ms$	$2-5\,s$	$1\,s$	$1\,s$
Spatial Resol.	$> cm$ (smeared)	$< cm$	$< cm$	mm^3	$10\,mm^3$	mm^3
Size/Mobility	small/yes	big/no	small/yes	big/no	big/no	big/no
Cost	med-low	high	med-low	high	high	high
Inconvenience	gel	low	low	loud, confined	injection	injection

Table 2.1: Selected methods for the measurement of brain activity. $[Hb]$: hemoglobin concentration

In contrast to most other neuroimaging modalities, EEG and fNIRS have significantly advanced toward higher miniaturization and mobility in the past years, making them well suited for bimodal applications beyond static constraints. Therefore, with mobile neurotechnology applications in mind, this work focuses on these two methods. After separate brief introductions to both, bimodal EEG-fNIRS will then be further motivated at the end of this Chapter. While EEG has been established for some time, fNIRS is a comparatively new, still progressing technology and will be discussed in considerably more detail in this thesis.

2.2 Electroencephalography (EEG)

Electrophysiological measurements of brain activity include non-invasive investigation of large neuronal assemblies with EEG [Ber29], intracellular action potentials of single neurons [HH39] and, invasively, the rather focal/localized activity of single to multiple neurons by intracranial microarrays or electrocorticography (ECoG) [WOL+84]. Here, we focus on non-invasive EEG, as introduced in neuroscience textbooks [KSJ+00].

2.2.1 Physiological Background and Acquisition Principle

The brain is a network of approximately hundred billion heavily interconnected neurons communicating via electrical and chemical processes. Information processing between neurons takes place by means of synapses, where arriving electrical action potentials either lead to excitation in the form of depolarization or inhibition in the form of hyperpolarization. The postsynaptic potential resulting from this polarization creates a small electric dipole field that spreads through the highly conductive tissue and, as a distance-dependent superposition of all fields, can be measured as local field potential (LFP) [BAK12]. Single dipoles are weak and only a large number of parallel and synchronously firing neurons sums up to an open field that can be measured as a potential difference in the form of superficial EEG. As cortical pyramid cells are spatially aligned and oriented orthogonally to the cortex and have long dendrites close to the surface, they are the main contributors to measured EEG signals (see Figure 2.1). There are significant differences between tissue conductivities, which are high in brain and cerebrospinal fluid and relatively low in cranial bones and scalp. Consequently, signals measured noninvasively at various scalp positions show almost equal contributions from different brain areas. This significantly limits the spatial sensitivity of EEG.

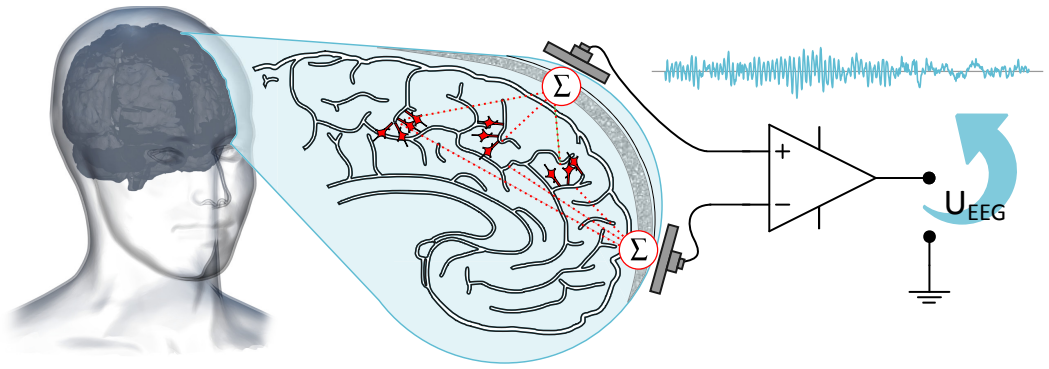

Figure 2.1: EEG acquisition principle: Volume conduction of additive single dipole fields and differential measurement of local field potential as a voltage signal U_{EEG} at the surface.

EEG signals contain four main components: (1) Oscillatory synchronous neural activity [BD04], where oscillatory power is increased with strength in synchronization [DRL+11; PS99]. (2) Synchronized transient activity following certain events or stimuli, such as event-related potentials (ERPs), whose components are attributed to various cognitive processes [Luc14; Reg89]. (3) Electrophysiological artifacts from sources other than the brain, such

as muscles (EMG) or ocular movements (EOG). (4) Non-physiological artifacts due to electromagnetic interference or instrumentation noise.

As the amplitudes of the signals of interest (1) and (2) are only in the order of microvolts (μV) on the scalp's surface and artifacts are usually of much higher magnitude, the careful design of amplification circuitry is crucial. Nowadays, it is generally based on differential amplification of the signals in instrumentation amplifiers, which aim at low noise characteristics and high suppression of common-mode signals. Reference and offset potentials as well as the state-of-the-art electrode technology must be considered in the design. These fundamentals will be briefly reviewed in Section 3.2.

2.2.2 Applications

EEG is an established tool for clinical diagnosis and psychiatric studies of neurological disorders. Among the application domains are epilepsy [Eng01], brain trauma [RMS+56] or brain death [Wij01], and surgical monitoring, e.g., during anesthesia and sedation [Ram98]. EEG is currently the primary modality used for BCI both in scenarios for communication and control [TM10; DRMH+07; WBM+02; BCM02; BGH+99] and beyond [HKK+14; ELT12; ZK11; BTV+10; MTD+08]. The former focus on oscillatory and synchronized transient features of the EEG such as sensorimotor rhythms (SMR) in imagined and performed motor actions [BTL+08], somatosensory visually evoked potentials (SSVEPs) from focused attention on flickering stimuli [MPSB+05] or ERPs in spelling devices [FD88]. The latter are adjacent to general fields of research in psychology and neuroscience and new fields such as neuromarketing and human factors. Here, EEG has successfully been used to assess mental states such as vigilance [MP83], meditation [CP06], sleep and dream states [DK57] and to assess cognitive [SJL+11] and memory performance [Kli99].

2.3 functional Near-Infrared Spectroscopy (fNIRS)

In 1977, Jöbsis pioneered the field of non-invasive optical methods by no longer considering the skull - and bones in general - to be a natural border for light. By using near-infrared light, he proved the feasibility of non-invasive local spectroscopy of cortical tissue oxygenation through the intact skull [Jöb77]. In the late 1980s and the 1990s, research enhanced the understanding of the fNIRS signal physiology, instrumentation and mathematical concepts, accompanied by a generally growing knowledge of fundamental bio-optical processes and the emergence of new optical technologies [Rol00]. In that process, several NIRS instruments were built with the aim to enhance instrumentation and finding ways to obtain absolute oxygenation values [WEB+97; WCD+90; CD88; ERC+88]. In 1993, four research groups independently demonstrated the feasibility of non-invasive brain activity investigation using fNIRS [CZU+93; HT93; KKT+93; VPH+93]. In the 2000s, many research groups focused on the design of imaging instruments for brain activity mapping from topographic information (functional near-infrared imaging, fNIRI) [VTE+04; BDF04; OV03; BBM+01; SFH+00]. Today, fNIRS has entered neuroscience as a reliable research tool [SKM+14] offering potentially complementary information to fMRI, PET, and EEG.

2.3.1 Hemodynamic Signals

2.3.1.1 Physiological Background

Optical window fNIRS is a noninvasive optical technology that makes use of at least two wavelengths in the near-infrared spectrum of light for the measurement of local oxy-hemoglobin (HbO) and deoxy-hemoglobin (HbR) concentration changes in cortical brain areas. fNIRS, fNIRI and diffuse optical tomography (DOT) are all based on the same concept [SBS02]: Near-infrared (NIR) light is emitted into the head at one position and undergoes random scattering and absorption processes in the tissue, attenuating it by several orders of magnitude. A fraction propagates on a banana-shaped path back to the surface where it is then detected by a NIR-sensitive photodetector (see Figure 2.2 **A**).

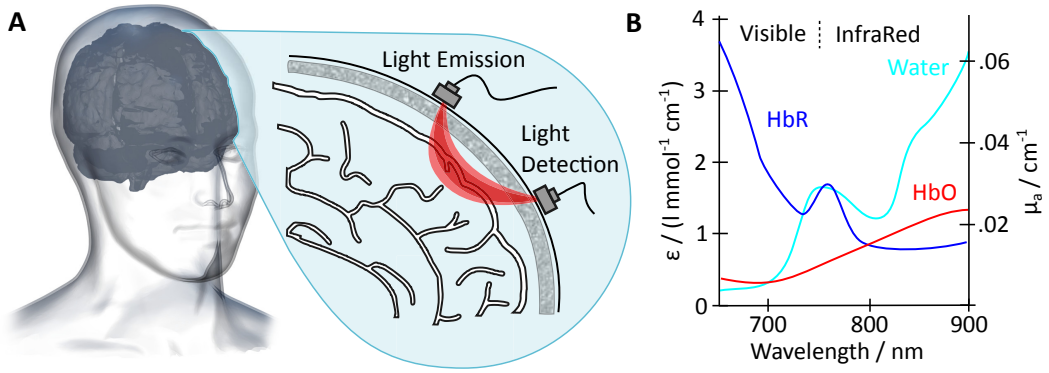

Figure 2.2: (**A**) Banana shaped path of photons between NIR light emitter and NIR light detector. (**B**) Optical window (schematic): molar extinction ε for HbO and HbR, and absorption μ_a for 100 % water.

As biological tissue, including the skull, is partially transparent to optical radiation in the NIR range, the emitted light can penetrate the cranium and reach sufficient depth [OFS+97]. This characteristic optical range of approx. $600-900\,nm$, in which tissue is relatively transparent to light, is often referred to as an *optical window*. While absorption and scattering by components of the tissue, e.g., collagen, proteins, and fat, remain relatively constant in that window, other chromophores such as HbO, HbR and cytochrome oxidase (CtOx) are strong absorbers for NIR light. HbO and HbR concentrations change with metabolism and blood flow. If two different wavelengths are chosen so that absorption by HbR and HbO are maximal, changes in concentrations of the two chromophores result in measurable attenuation changes that can be quantified, e.g., with the modified Beer-Lambert Law (see next Section). The oxygen-dependent optical absorption is also key to (pulse) oximetry. Some works also use CtOx as a chromophore for the indication of intracellular oxidative processes with CtOx being the terminal enzyme of the intracellular respiratory chain [Rol00].

The hemodynamic response During brain activation, an increase in local *Cerebral Metabolic Rate of Oxygenation* (CMRO2) is followed by a disproportional up-regulation of regional *Cerebral Blood Flow* (CBF) and *Cerebral Blood Volume* (CBV) within milliseconds to seconds, resulting in a focal hyperoxygenation [FR86]. These processes are reflected in a decrease in HbR concentration accompanied by an increase in HbO concentration of

typically 2-3-fold magnitude and thus result in an increase of total hemoglobin [OV03]. The hemodynamic signal can usually be observed with a latency of approx. 5-8 seconds after the onset of a stimulus/task and is termed *hemodynamic response* (see Figure 2.3). Neural activity can be estimated from the relative increase in oxy-Hb and t-Hb compared to a relative decrease of deoxy-Hb in the venous branch of the cerebral vascular system [WWT+02]. A focal decrease in HbO along with an increase in HbR is consequently interpreted as deactivation. The hemodynamic response results in changes in the order of about 1-2% of the optical NIRS signal's direct current (DC) amplitude [CWM07; LSL+11]. Since the change in HbO is usually larger compared to HbR, it is often preferred as a single indicator of brain activity changes. HbR, however, has been shown to have a high negative correlation with the fMRI BOLD signal [HHD+06; SCT+02; KOR+96], making it a better-validated parameter.

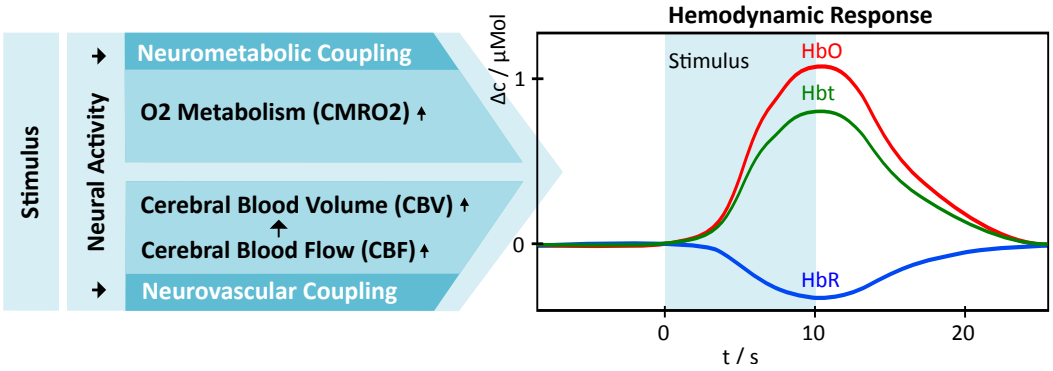

Figure 2.3: Typical hemodynamic fNIRS response after stimulus onset and contributing coupling processes. HbO: oxy-, HbR: deoxy-, HBt: total hemoglobin. Inspired by Figure from [SKM+14].

There is yet no clear mechanistic understanding of how neuronal activity regulates CBF and metabolism [DSS+12], but "metabolic" and "neurogenic" hypotheses exist [ABM11; PHR+10; RM06].
Non-stationary fNIRS signals based on HbO and HbR concentration changes are a combination of several components that include periodic artifacts, such as heartbeat ($\approx 1-2\,Hz$), respiration ($\approx 0.3-0.1\,Hz$) and Mayer waves [ESH+99] ($\approx 0.1\,Hz$). A classification of physiological and non-physiological non-stationary components in fNIRS will be done in Chapter 5, Multimodal Analysis, in Section 5.2.2.

2.3.1.2 Theoretical Background - the modified Beer-Lambert Law

For the conversion of measured raw NIR light intensities into chromophore concentrations, a modified version of the Beer-Lambert Law (BLL) is commonly used. For an in-vitro *cuvette model* as in Figure 2.4, the conventional BLL (Equation (2.1)) states that the attenuation A of an interrogating monochromatic energy with incident intensity I_0 is proportional to the product of an absorbing compound's concentration $[c]$, in mol, dissolved in a non-absorbing solvent, the compound's molar extinction coefficient ε_λ, and the optical path length d.

To determine the time-dependent concentration of i chromophores, measuring at i different wavelengths λ_i is necessary. In fNIRS, the optical path length is not straight and equal to

$$I = I_0 \cdot 10^{-\varepsilon_\lambda cd}$$
$$\Leftrightarrow A = -\log_{10}\left(\frac{I}{I_0}\right) = \varepsilon_\lambda cd. \tag{2.1}$$

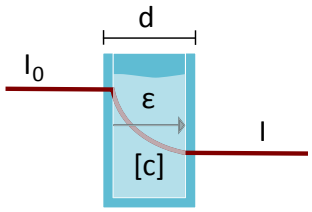

Figure 2.4: In-vitro cuvette model for BLL

the distance d between light emitter and detector, but has to be corrected by a *Differential Path length Factor* (DPF) that accounts for increased distance traveled by the light due to scattering and absorption effects in the tissue:

$$A(t,\lambda) = -\log_{10}\left(\frac{I(t,\lambda)}{I_0(t,\lambda)}\right) = \sum_{i=1}^{n} \varepsilon_{i\lambda} c_i(t) DPF(\lambda) d + G(\lambda). \tag{2.2}$$

Here, $G(\lambda)$ is an unknown geometry dependent factor that takes scattering into account and prevents the direct use of (2.2) for tissue interrogation. As a solution, Delpy et al. modified the BLL (mBLL) [SF04; DCZ+88] by calculating chromophore concentration *changes* between an initial time point t_0 and consecutive timepoints t, thereby removing effects from $G(\lambda)$, which are assumed to be constant. When attenuation changes ΔA are evaluated at two wavelengths, the resulting system of equations can easily be solved for the changes in concentrations Δc_i. For HbO and HbR these are then given by

$$\begin{bmatrix}\Delta[HbR]\\ \Delta[HbO]\end{bmatrix} = \frac{1}{d} \cdot \begin{bmatrix}\varepsilon_{HbR,\lambda_1} & \varepsilon_{HbO,\lambda_1}\\ \varepsilon_{HbR,\lambda_2} & \varepsilon_{HbO,\lambda_2}\end{bmatrix}^{-1} \begin{bmatrix}\frac{\Delta A(\Delta t,\lambda_1)}{DPF(\lambda_1)}\\ \frac{\Delta A(\Delta t,\lambda_2)}{DPF(\lambda_2)}\end{bmatrix}. \tag{2.3}$$

Using the mBLL allows only a reasonable first approximation of relative chromophore concentrations in the brain, as the underlying assumptions of a homogeneous medium and homogeneous change of parameters within the sampling volume are not valid [OV03; BBM+01]. However, it is used by a majority of approaches; and theoretical studies suggest that resulting errors can be limited to less than 10% [SBS02].

For the application of the mBLL, several parameters are crucial:

- The *chromophore extinction coefficients* at different wavelengths, which were determined in vitro using laboratory spectrophotometers, e.g., in [Cop91].
- The DPF, which cannot be directly measured using the most commonly applied continuous wave interrogation approach, was both experimentally and numerically investigated and found to be age, gender- and wavelength-dependent, and varying up to 15% between subjects with a mean value of 6.53 ± 0.99 [DMC+95; EEC+93].
- The impact of *source-detector spacing* (SDS) on the partial optical path lengths in tissue and corresponding sensitivity profiles were investigated by Okada et al. on the basis of phantom-measurements and Monte Carlo and Finite Elements predictions [OFS+97]. They concluded that for a SDS of $50\,mm$, approximately 65% of the total light path length is in scalp and skull, approximately 35% in the CSF and only

approximately 5% in the gray matter of the cortex. Nevertheless, the contribution of the gray matter layer was estimated to be at least 20-30% of the absorption change in the signal. Today, SDS of $3-4\,cm$ are commonly used with the rule of thumb that the depth of maximum brain sensitivity is approximately half the SDS distance [SBS02].

2.3.2 Instrumentation and Acquisition Principles

Currently, there are three main methodological approaches for tissue interrogation with fNIRS (see Figure 2.5):

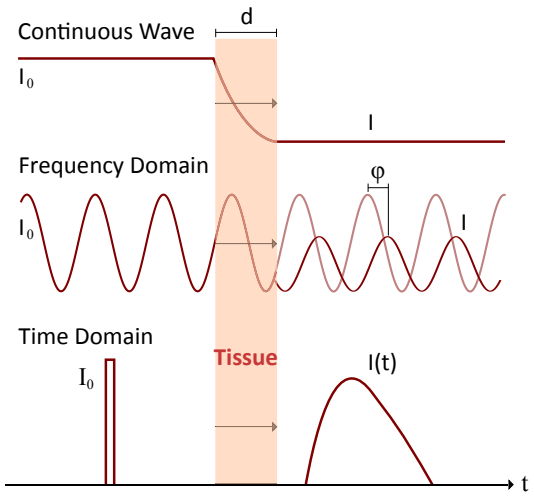

Figure 2.5: fNIRS interrogation approaches

(1) In Continuous-Wave (CW) approaches (e.g., [SMB99]), continuous, slowly (kHz) chopped or modulated light at constant amplitude I_0 trans-illuminates the tissue, and its attenuation over time is measured. While CW fNIRS achieves good SNR, it cannot determine optical path lengths/light scattering and, therefore, only relative HbO/HbR concentration changes can be obtained. The use of multiple source-detector distances, however, allows the separation of different tissue layers to some degree [GWZ+10; SB05].

(2) In Frequency-Domain (FD) techniques [PP94; GMV+90], light is modulated in the range of several $10-100\,MHz$, and amplitude changes, as well as phase shifts ϕ, are measured. The latter allows an estimation of the time of flight and optical path length; absolute chromophore concentrations can be determined. Costs, complexity, and volume of the instruments are considerably higher than in CW systems.

(3) In Time-Domain (TD) (or time-resolved) spectroscopy [BS93; CLM+88], picosecond light pulses are applied and the photon arrival times are measured directly as a temporal point spread function of arriving photons. This allows the determination of absorption and scattering information and the separation of different tissue layers [SBS02]. While TD systems yield the highest amount of information, they are expensive, require significant averaging times to improve SNR [SMB99] and are often large.

Since quantification of absolute values is often not as crucial in neuroscience as the detection of brain activity changes, most fNIRS systems in research are based on CW technology [SKM+14]. CW is comparatively low-cost, can be integrated and miniaturized, is lightweight and also works with mobile applications using wireless technology, which makes it the approach matching the requirements best for the work in this thesis.

2.3.3 Applications

Given the increased understanding of fNIRS and advances in measuring instruments, a variety of *clinical applications* were explored in recent years. These range from the long-

term monitoring of cerebral oxygenation in newborn and high-risk infants [CD88; Cop91], the study of the physiological correlates of cerebrovascular diseases, stroke [MYH+03], and epileptic disorders, to the diseased brain, e.g., in Alzheimer's or amyotrophic lateral sclerosis, brain trauma and surgical intervention monitoring [Obr14; ZSY+13; WFQ07; BII+06; BBM+01]. In the last decade, an increasing number of research groups used fNIRS technology also in *Brain-Computer Interface* tasks and proved its applicability in this field [KMM+09; MPW+08; CWM07; CWM+04]. fNIRS signals were used for BCI control in severely paralyzed patients due to stroke, spinal cord injury or ALS [Bir06; YAS+10; KMM+09] and for cognitive workload assessment [HHF+14; ASB+12; SY06; IBI+03]. Furthermore, fNIRS has been widely applied in *basic brain research*, e.g., in psychiatric research [ESD+14; IPB+07], and brain activation studies of the visual, the somatosensory, the auditory, the motor and the language system [FQ12]. Other applications are in brain dynamics monitoring during working memory training and expertise development [AOI+13] and recently also in combination with transcranial direct current stimulation [MPA15].

2.4 Summary and Motivation for Hybrid EEG-fNIRS

In consideration of the brief introduction to both modalities in this Chapter, the following box summarizes and contrasts essential characteristics of fNIRS and EEG:

fNIRS vs. EEG

- EEG provides fast signals ($0.1 - 250\,Hz$) and high temporal resolution ($> 1\,kHz$) compared to fNIRS ($0.01 - 0.2\,Hz$ at typically $> 8\,Hz$), which however offers higher temporal resolution than both fMRI and PET.
- fNIRS has a higher spatial ($< 1\,cm$) resolution compared to EEG ($> 1\,cm$).
- EEG measures neuro-electrical activity, fNIRS measures neuro-metabolic markers that are not available in other modalities, e.g., HbO or CtOx.
- EEG is a weak electrical signal (μV) easily buried in electromagnetic noise, fNIRS is a weak optical signal (μMol) easily buried in ambient light noise
- EEG is robust to ambient light changes, fNIRS is robust to electro-phyiological artifacts (EOG, EMG,...)
- Both EEG and fNIRS have a comparable complexity and set up time, are comparatively low cost and can easily be combined.
- Both EEG and fNIRS can be miniaturized and wearable, enabling brain activation studies in clinical offices and under more realistic conditions - and are usable for subjects who cannot use fMRI, e.g., are not able to stay sufficiently still.
- Both methods are non-hazardous and therefore do not limit the number of scans one can undergo, also enabling long-term monitoring.

Being noninvasive, relatively low cost, and similar in setup complexity, EEG and fNIRS together allow the investigation of interactions between neuronal electrical activity and regional microcirculation changes under various conditions, e.g., mobile or at the bedside. While constricted to near-surface brain regions, both complement each other in terms of the measured physiological signal and their spatial and temporal resolution. Both modalities also contain a variety of systemic physiological signal components. These are usually considered artifacts but can be of considerable value in hybrid holistic approaches that aim to extract as much physiological information as possible. Included in the set of non-neuronal physiological signals measured in hybrid EEG-fNIRS are EMG, EOG, ECG, pulse-wave (heart rate), (modulations by) breathing signals and Mayer-waves (Traube-Herring waves).

The combination of EEG and fNIRS enables new approaches in many domains related to neuroscience and neurotechnology. Among them are advanced diagnostic tools for medicine, e.g., toward the non-invasive real-time monitoring of the neuroenergetic status of cortical gray matter in ischemic strokes [vAC+17], and new approaches in cognitive science, psychology, Neuroergonomics [Par03; Par11] and adaptive neurotechnology research [ZK11; BTV+10; MTD+08]. In Brain-Computer Interfaces (BCI), NIRS joined the set of modalities used for either multimodal BCI or enhancement of EEG based BCI. These "hybrid BCIs" [PAB+10] demonstrate the potential to significantly increase the amount of exploitable physiological information and allow for higher robustness and classification accuracy [FDS+15; FMS+12; BPM+11; PAB+10]. A continually growing number of experiments include bimodal EEG-fNIRS data and hybrid datasets are being published for open-access in the scientific community [SvB+17; SvK+18], enabling the development of new signal analysis approaches.

These overall factors make EEG and fNIRS predestined for multimodal and hybrid integration into miniaturized and wearable non-invasive neuroimaging equipment, allowing comparably high usability. Consequently, EEG and fNIRS are the modalities of choice for the work in this thesis.

Chapter 3

Instrumentation for Novel Neurotechnology Applications

3.1 Preface

This Chapter discusses the design of novel biosignal acquisition systems that ultimately aim to enable neurotechnology applications outside the laboratory and is based on publications [vHH+15; vWS+17; vM17; vM18]. The way toward this goal is of an iterative nature, both within and between system generations (see Figure 3.1).

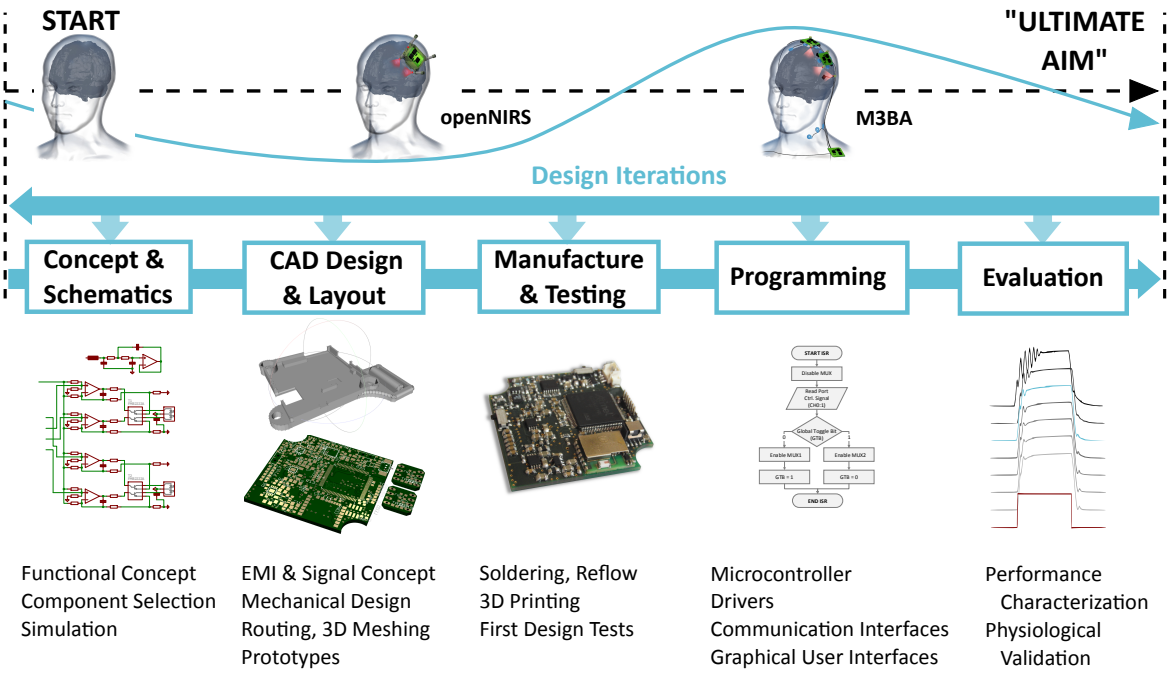

Figure 3.1: Iterative design cycle across contributing domains in the development of novel instrumentation. On the way toward the ultimate aim to enable reliable neurotechnology applications outside the lab, instrumentation generations in this thesis build upon each other: from openNIRS to M3BA.

The following work comprises two contributions which can be regarded as a first and second generation of instruments of the same family. The first generation, a unimodal mobile and modular fNIRS device (the *"openNIRS"*), serves as a testbed for a more sophisticated hybrid EEG-fNIRS approach (the *"M3BA"*) and will be presented only briefly and with focus on its concept and lessons learned. The second generation *M3BA* integrates and expands the *openNIRS* concept and will then be fully evaluated and discussed.
As a working basis for the design of both instruments, Section 3.2 will first provide comprehensive fundamentals and considerations and Sections 3.3 & 3.4 will present the current state of the art and identify aims and architectural requirements.
As details in the evolution of instrument and software generations can be valuable from an engineering perspective but are only of minor scientific interest, we then focus on the concepts, architectures and selected design aspects essential to verification and validation of the *openNIRS* (Section 3.5) and *M3BA* (Section 3.6).

High-precision and low-noise performance in the miniaturized and mixed-circuit designs are crucial, as both modalities provide small signals that easily drown in noise. In contrast to well established, widely known state of the art instrumentation principles in EEG, fNIRS is a technology still comparatively young, challenging, and rapidly progressing. For this reason, the emphasis in this Chapter lies on the design of (hybrid) fNIRS instrumentation. EEG design fundamentals are documented in many textbooks for biomedical engineering [Ged68; CB93] and will only be briefly addressed, when relevant for the overall approach and hybridization.

3.2 Fundamentals and Design Considerations

3.2.1 State of the Art Instruments

As a preparation for the system design, literature on CW fNIRS approaches, including comprehensive overviews by [SKM+14; SY06; SBS02; BGS+01]), was reviewed. State-of-the-art non-mobile fNIRS systems can comprise up to 256 channels with temporal resolutions as high as 250 Hz and lateral spatial resolutions of approximately 7-10 mm [FQ12]; commercial instruments cost between some 10,000 USD to several 100,000 USD for whole-head imaging systems. Similar in EEG, where temporal resolution can be significantly higher but spatial resolution significantly lower. While there exists a variety of wearable miniaturized EEG instruments in research and on the market, for fNIRS there are only few instruments and most are portable devices with a volume $> 500\,cm^3$, requiring an additional backpack or small bag. Tab. A.4 in Appendix A.1 summarizes and contrasts main characteristics of commercial and research fNIRS devices that support mobile use in one way or another. The vast majority of these are unimodal instruments with a moderate number of Time Division Multiplexed (TDM) channels (typically $1-32$).

Until today, in scientific studies, the majority of bimodal EEG-fNIRS research has been conducted utilizing separate and usually tabletop EEG and fNIRS instruments, as there are no commercial hybrid systems available as yet.

3.2.2 Core Components of EEG and fNIRS Instrumentation

3.2.2.1 Biopotential Measurements and Instrumentation Amplifier

High-precision instrumentation for the non-invasive acquisition of small biopotentials such as EEG has to consider key elements [BU13; KC04; CB93; Kha92; Ged68] which are displayed in Figure 3.2 and will be discussed in the following. Conventionally, electrolyte-electrodes derive biopotentials galvanically from the surface of the skin. They can be regarded as a diaphragm between electrolyte and body fluids containing the same ions. The overall skin impedance Z_s can be modeled by capacitive effects from skin layers and resistive conduction due to glands and subcutaneous tissue. At the transition between electrode metal and electrolyte, different chemical potentials lead to a charge gradient, the Helmholtz and Gouy-Chapman layer [Cha13; Hel79], modeled by Z_e including the Helmholtz capacitance and faraday impedance. Resulting polarization effects can significantly deteriorate signal quality and are dependent on applied materials; state of the art are "unpolarizable" AgCl electrodes with NaCl electrolyte. Differences between electrodes lead to a DC offset potential that has to be considered for the dynamic range of the designed instrument. Signal quality depends on the overall electrode-skin impedance $Z_s + Z_e$ that is ideally $< 10k\Omega$. Implementation of impedance measurements in the system design is therefore advisable. Due to the high source impedance, the small (μV) signals are prone to electrical interference and cross-talk before amplification (see also Section 3.6.2.2 in hybrid systems). External noise pickup has to be inherently minimized in the design by shielding and optimization of current paths.

The default solution for amplification of EEG signals is the use of Instrumentation Amplifiers (IAs) that allow precision measurements of differential voltage signals in noisy environments. IAs consist of a unity gain buffer input stage feeding into a differential amplifier. Differential amplification of biosignals enables the rejection of common mode signals on the body that are much larger than the signal of interest, e.g., electrical $50/60Hz$ mains hum. Very high Common Mode Rejection Ratios (CMRR) $> 100dB$ are advantageous. The unity gain input buffers enable extremely high input impedances $Z_i \gg Z_s + Z_e$, essential

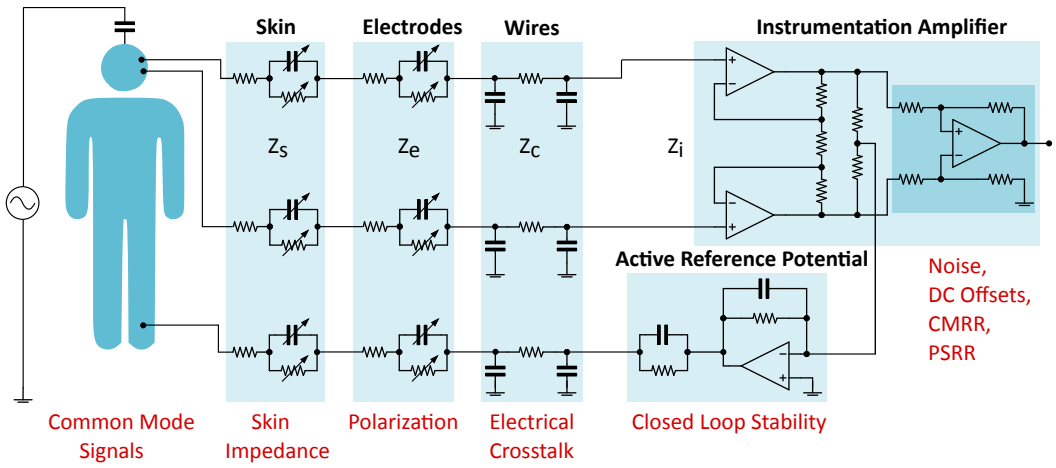

Figure 3.2: Measurement of EEG and other bio-potentials: key elements and noise factors to consider (red).

to measure signals over high impedances such as the effective electrode-skin impedance and minimize voltage divider effects. Overall, the IA has to provide low bias/offset currents and voltages, high input impedances, gains, linearity and slew rates, high CMRR and Power Supply Rejection Ratios (PSRR) all at a very low input-referred noise. Ultra low noise performance can only be achieved in a tradeoff with power consumption and dynamic range (see Section 3.2.3.1). For biopotential acquisition, instrument and body have to share a common reference. To further improve CMRR, inverted common mode signals can be fed back to the body in a closed loop providing an active reference potential (known as Driven Right Leg, DRL, from ECG [WW83]). In that case, the stability of the closed-loop control has to be ensured.

3.2.2.2 NIR Light Emitters

The ideal light source provides multiple monochromatic wavelengths in the NIR range, each at a relatively high power and with minimal radiation variance [SBS02] to yield a high number of photons penetrating deeply into tissue. Without an additional monitor, fluctuations cannot be discriminated from those caused by chromophore concentration changes. If not monochromatic, the spectrum should be as sharply peaked as possible and weighted averaging approaches can be used to correct the extinction coefficients [SKM+14], see also the finite bandwidth effect in Section 3.2.3.4. As scattering processes in the first millimeters of the tissue rapidly make the collimated interrogating beam diffuse [Cop91], collimation of light is not as important as the incident power to the detector. Three types of sources can be used for NIR light emission: (1) *Laser Diodes* (LD), (2) *Light Emitting Diodes* (LED) and 3) *White Light Sources* (e.g., Xenon flash tubes or quartz halogen light) with monochromators/interference filters. The latter are large, dissipate much heat and are not suited for mobile fNIRS instrumentation. Table 3.1 contrasts LDs and LEDs regarding their suitability for fNIRS instruments.

As LDs emit coherent light with very sharp radiation peaks and high intensities, they are usually chosen for high-precision fNIRS signal generation [AKO+07; BBM+01; CD88; Cop91]. Particularly in more recent approaches, and with progressing technology and availability, Light Emitting Diodes are often used [PKK+14; AOI+13; SGM+13; LSL+11; SMM+08; BLW+08; CWM07; CS07; BII+06; BRR+05; BO04; VTE+04]. LEDs come in smaller packaging and at lower costs and are available in a larger variety of wavelengths and multi-wavelength packages. In the application of the mBLL it is assumed that the same volume of tissue is being interrogated with different wavelengths. Consequently, emitted NIR light into scalp should optimally origin from the exact same spatial location to minimize errors. LEDs have broader emission spectra ($> 25\,nm$) than sharp peaked LDs

	heating	package sizes	sharp spectrum	emission power	safety	modulation bandwidth	available λ	multi λ packages
LD	••	••	$\approx 1\,nm$	••	•	$\leq GHz$	••	no
LED	•	•	$> 25\,nm$	•	••	$\leq MHz$	•••	yes

Table 3.1: Comparison of NIR-emitter suitability for fNIRS instrumentation: LEDs vs LDs.

($\approx 1\,nm$); their incoherent and uncollimated light decreases safety concerns in view of the maximum permissible exposure (MPE) limit for skin of about $2\,mW/mm^2$, and is safer with the human eyes, facilitating designs without additional optical elements. These characteristics make LEDs most suitable for wearable applications and allow their direct application on the head, also making optical fiber guides redundant, when small emitter-distances in a multiwavelength package are ensured.

Under these considerations, LEDs are the emitters of choice for the designs in this thesis. For a selection of appropriate NIR LEDs see table A.3 in Appendix A.1.

3.2.2.3 Wavelength Selection

An optimal choice of the wavelength pair in the optical window is crucial for signal sensitivity, separability and minimizing crosstalk of concentration changes that stems from the simplifying assumptions in the mBLL [UKBS+02; SWO+01; BGS+01; HFE+93]. Generally, one wavelength above and one below the isobestric point of $805\,nm$ in HbR and HbO absorption [CWM07; Cop91] are chosen (see also Figure 2.2) to minimize absorption artifacts due to the presence of compounds other than hemoglobin [Cop91]. As the hemoglobin absorption spectra change little in the range of $830-900\,nm$ and the sensitivity of detecting photomultiplier tubes decreases rapidly above $840\,nm$ [BDF04], $830\,nm$ was commonly chosen as one wavelength in first instrument generations. Based on this early determination, many of the later investigations used $830\,nm$ as a constant for further narrowing down the optimal wavelength pair:

Using an error propagation approach, Yamashita et al. [YMK01] concluded that $830\,nm$ together with $< 780\,nm$ is optimal. Using the Monte Carlo Method and empiric SNR tests, Yamashita, Sato, and Strangman et al. concluded that $830\,nm$ with $690\,nm$ or $760\,nm$ minimize random and systematic errors [SKK+04; SFB03; YMK01]. Funane et al. [FAS+09] concluded that SNR is maximum when both ends of the range $659-900\,nm$ are used. Using the Monte Carlo Method for minimizing crosstalk, Okui et al. [OO05] came to the conclusion that $830\,nm$ with $690-750\,nm$ are optimal. From theoretical analysis, Uludag et al., however, stated that $830\,nm$ is not the optimal wavelength and that > 730 and $< 720\,nm$ with both not $> 780\,nm$ should be used [USV+04]. Finally, based on a three-layer model analysis, Correia et al. [CGH10] concluded that $887 \pm 12\,nm$ and $704 \pm 7\,nm$ are optimal. Table A.2 in Appendix A.1 gives an extensive overview of the recommended or selected wavelength pairs in research and commercial fNIRS instruments.

3.2.2.4 NIR Light Detectors

There are three types of detectors typically employed for the measurement of near-infrared light in CW fNIRS: (1) *Photomultiplier Tubes* (PMT), (2) *Silicon Photodiodes* (SiPD) and (3) *Avalanche Photodiodes* (APD). PMTs are gold standard in terms of sensitivity and allow single photon counting based on the external photoelectric effect: Photons free electrons from a photocathode surface, which are then accelerated by a strong electric field, and knock out secondary electrons from a cascade of dynodes, leading to gains of up to 10^6 to 10^7.

SiPDs and APDs are based on the internal photoelectric effect: The semiconductor

junction absorbs incident photons, which raise electrons to higher energy, creating free charge carriers that result in a detectable photocurrent. In APDs, similar to PMTs, up to several hundred volts are applied across the semiconductor junction, accelerating free electric charge carriers. These generate more carriers through impact ionization, resulting in the so-called avalanche effect and amplification of a few hundred times. SiPDs have no internal signal amplification. Emerging photocurrents in photodiodes have to be amplified by external circuitry in one of two possible modes of operation: In *photovoltaic mode*, no bias voltage is applied and the generated photocurrent is measured over a large load resistance. The response of the signal to the optical power is logarithmic and much slower than in photoconductive mode but enables a higher dynamic range. In *photoconductive mode*, in which SiPDs and APDs are typically operated, a reverse bias voltage is applied to the semiconductor junction. Advantages are reduced capacitance, higher speed, and improved linearity, however also larger dark current.

While other photodiode types are available, silicon semiconductors are the most favorable due to their higher sensitivity and better noise characteristics in the NIR spectrum compared to, e.g., GaAs photodiodes. The detector choice largely determines the resulting sensitivity of the instrument, the maximum sampling rate and the dynamic range [SBS02] and has to include a consideration of the advantages and disadvantages in the context of mobile fNIRS application (see Table 3.2).

PMTs were mainly used in the first fNIRS generations [Rol00; SFH+00; Cop91; CD88] and more recently in Frequency Domain instruments but have mostly been replaced by Avalanche Photo Diodes [BLW+08; SMM+08; CWM07; CWM+04; BBM+01] and SiPDs [PKK+14; AOI+13; SGM+13; RSG+12; BII+06; BRR+05; VTE+04; SMB99]. Recently, also Silicon Photomultipliers [WLS+17; ZBA+13] have been exploited for fNIRS applications.

The very small packaging, high dynamic, range and speed, together with low-voltage operation make SiPDs a good choice for mobile, safe and cost-effective purposes when their main disadvantage, low sensitivity, is carefully taken into consideration. Another advantage is that they can be applied directly to the skin surface, which is the most efficient method of collecting the light [Cop91]. Although APDs are in principle suitable, the necessity of high supply voltages and cooling makes the design more complex with regard to safety aspects and direct head attachment. Table A.1 in Appendix A.1 shows a selection of available SiPDs with integrated Trans-Impedance Amplifiers, that meet the specifications requirements in the following system designs.

	sensitivity (internal gains)	speed	dynamic range	size	supply voltages (safety)	heating (cooling required)	robustness (ambient light, magn. fields)
PMT	10^7	$> 100 MHz$	$< 60 dB$	•••	1 kV	•••	•
APD	100	$> 100 MHz$	$< 60 dB$	•	100 V	••	••
SiPD	1	$< 100 MHz$	$< 100 dB$	•	1 V	•	•••

Table 3.2: Comparison of detectors for mobile fNIRS instrumentation. Photomultiplier Tubes (PMT), Avalanche Photodiodes (APD) and Silicon Photodiodes (SiPD).

3.2.2.5 Phase-Sensitive Detection

Lock-in amplification or phase-sensitive detection (PSD) [Mea83; Mea82] is a method for the recovery of weak signals masked by a strong noisy background, and is widely-used in spectroscopic applications. It is based on the modulation and demodulation of an interrogating signal using a known common reference waveform of much higher frequency than the band of interest. Being an extremely narrow-band bandpass filter, the phase-sensitive detector is only sensitive to signals coherent with the reference (same frequency and phase) and rejects others, thus significantly enhancing the signal-to-noise ratio (SNR). In fNIRS, this enables the rejection of ambient room light and other noise sources (see Section 3.2.3). Among these are dark current noise of the photodetector, amplifier offsets, and $\frac{1}{f}$ amplifier noise, given that the signal is modulated at a frequency where the amplifier noise is significantly lower than at near zero frequency. Let $s(t) = V_S(t) \cdot \cos(\omega_S t + \Phi_S)$ be the modulated signal carrying information in its amplitude $V_S(t)$ and $r(t) = V_R \cdot \cos(\omega_R t + \Phi_R)$ be the reference with constant amplitude V_R both with frequency ω and phase Φ. Furthermore, let $v(t) = s(t) \cdot r(t)$ be the demodulated signal. In case that signal and reference have the same frequency $\omega = \omega_S = \omega_R$ and a low-pass filter $A_L(\omega) = |H_L(j\omega)|$ is applied with cut-off frequency $f_c \ll \omega$, $A_L(0)$ being the magnitude of the filter response at zero frequency, the measured slow signal $v_{LP}(t)$ with frequency components $\ll f_c$ after filtering yields

$$v_{LP}^{sine}(t) \approx \frac{V_R A_L(0)}{2} V_S(t) \cdot \cos(\Phi_S - \Phi_R). \tag{3.1}$$

Here, $\cos(\Phi_S - \Phi_R)$ is an attenuation factor based on the phase between the incident and detected optical signal and is mainly determined by the propagation delays due to hardware components in the signal path. Therefore, these have to be chosen to minimize or correct the resulting total phase shift. In practice, the reference signal is often a square wave instead of a sine wave, allowing demodulation simply by a change of sign of the incoming signal. It can be shown [Mea83], that the responses of the "ideal" sinusoidal synchronous detector (Equation 3.1) and the square wave reference detector differ only in a constant scaling factor with the square wave excitation providing a 27% larger signal and also giving a phase-sensitive DC output in response to signals at frequencies $3\omega_R, 5\omega_R, \ldots$: $v_{LP}^{sqwave}(t) \approx \frac{4}{\pi} v_{LP}^{sine}(t)$.
Figure 3.3 depicts the square wave lock-in principle as it can be applied in fNIRS.

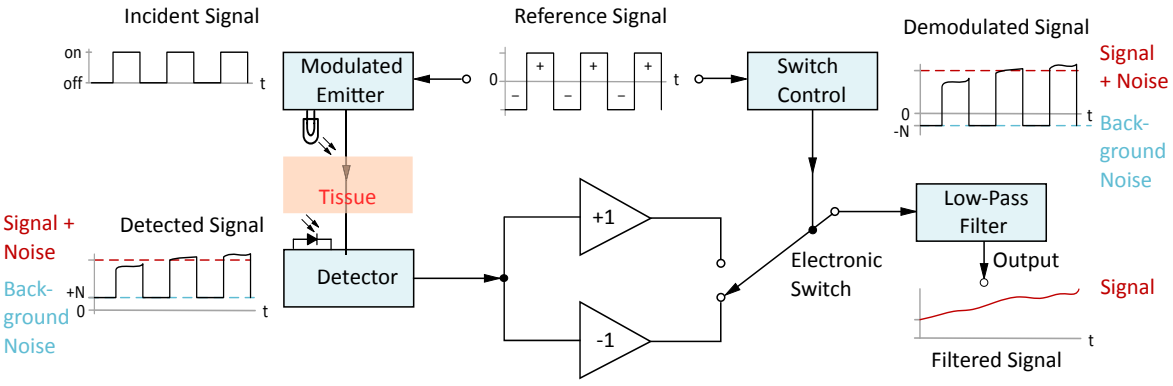

Figure 3.3: Principle of square-wave lock-in amplification.

3.2.2.6 Electrode and Optode Approaches

Optical and electrical coupling between the body and fNIRS and EEG instruments can be achieved with a variety of *optode* and *electrode* approaches (Figure 3.4). These determine signal quality, robustness, and usability, especially under moving conditions. In EEG, the default are stretch fabric head caps or nets with non-polarizable wet or dry AgCl electrodes. Wet electrodes (Figure 3.4 A) are applied with NaCl based electrolyte that also acts as a buffer, reducing shift artifacts. Application of gel requires a second person and subsequent cleaning of the hair. To improve usability, recent solutions focus on alternatives such as non-adhesive solid gel [vSM+17; TTK12] (Figure 3.4 B) and water-based electrodes (Figure 3.4 C/D) that combine sponges or rolled-up cotton soaked in a NaCl dilution [vSM+17; MGMP11; VVM+10]. Dry active electrodes do not require preparation but have higher impedances and a lower SNR [PFB+07]. Pins contact the skin through hair under relatively high contact pressure that is sometimes perceived as unpleasant. Recent approaches achieve good signal quality using dry, sticky or wet electrodes in or around the ear [DEDV+15; LKP+12].

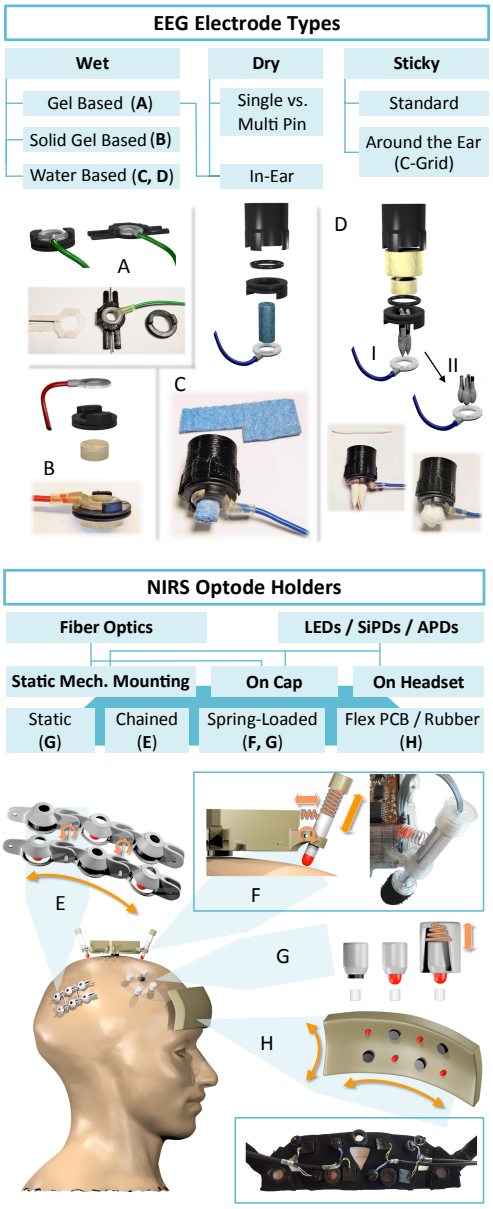

Figure 3.4: Electrode and optode types

Traditional fNIRS instruments use step-index multimode fibers and fiber optic bundles for optical conduction to and from the scalp [SKM+14]. They require attachment with holders on straps or caps and add weight and risk of optode shifts in movement. In more recent portable devices, SiPDs, APDs, LDs, and LEDs, are integrated into the optodes and placed directly on the head. This slightly constrains the geometrical probe design and potential heating, as well as electrical hazards, have to be considered. In turn, light losses are minimal and user mobility is less restricted. A conventional solution is an integration into conus- and cylinder-shaped single probes for fixation on EEG caps (Figure 3.4 G, as in [PKK+14]). Chain-link optode holders (Figure 3.4 E, as in [SGM+13]) helmets and helmet-like headsets [KAF+12; AKO+07] and fixated mechanical mounting structures to sit in [CWM07] have also been applied. Spring-loaded designs (Figure 3.4 F/G, and Section 3.5.1.1) enable easier application and minimize movement artifacts due to optode shifts, but are mechanically more sophisticated. For measurement of fNIRS signals on the forehead, optodes can be integrated into flexible PCBs or rubber mats (Figure 3.4 H, [RSG+12; BII+06; BRR+05; VTE+04; Rol00], and Section 3.7).

3.2.3 Noise, Crosstalk and Error Sources

In this Section, noise, crosstalk and other error sources are examined to extract guidelines for the design of uni- and multimodal fNIRS/EEG systems.

3.2.3.1 Noise in Biosignal Amplification

With focus on the relevance for biopotential amplification, three types of noise are of concern [DOC+14; KC04; Car01; CB93; Kha92], in the following expressed in rms noise currents:

shot noise (3.2) is caused by random fluctuations in the motion of charge carriers in any conductor. It is unavoidable, independent of temperature and has a uniform power density.

$$I_s = \sqrt{2qI_{dc}\Delta B} \quad (3.2)$$

q is the electron charge, I_{dc} the average DC current in Ampere and ΔB the Bandwidth in Hz.

thermal noise or Nyquist-noise (3.3) is white noise resulting from Brownian motion of charge carriers in resistors internal and external to a detector. It depends on the resistor value R in Ohms over which the noise is measured at temperature T in Kelvin, the Blotzmann's constant k and the measurement bandwidth. This noise contribution of larger resistors leads to an inherent trade-off between noise and power consumption, especially in battery-powered wearable precision equipment.

$$I_{th} = \sqrt{\frac{4kT\Delta B}{R}} \quad (3.3)$$

flicker noise or $\frac{1}{f}$-noise (3.4) is present in all (semi-) conductors and is not entirely understood theoretically. It increases as the frequency f decreases with the same power content in each decade and is proportional to the DC current in a device. K_i is the proportionality constant representing I_f at $1\,Hz$, f_{max} is the upper cutoff frequency or noise bandwidth and f_{min} is the lower cutoff frequency, customarily set to $0.1\,Hz$.

$$I_f = K_i\sqrt{log\frac{f_{max}}{f_{min}}} \quad (3.4)$$

3.2.3.2 Noise in Photodetector Systems

There are three types of noise in photodetector systems relevant for fNIRS [SKM+14; Kno10; Liu05; Jen87].

photon shot noise (3.5) is based on the quantum nature of the photons and, being inherent in any signal generated by the detector, cannot be avoided entirely by technical means. Being quantized and discrete, the photons arrive independently of each other, resulting in random fluctuations in photon-to-electron conversion in the detector over time. Without internal amplification, the photon shot noise power is proportional to the square root of the average intensity (the number of incident photons); the accuracy of a measurement increases with the intensity of the detected light in a constant time window. q is

$$I_{sp} = \sqrt{2qI_{ph}M^2F\Delta B} \quad (3.5)$$

the electron charge, I_{ph} is the generated DC photocurrent, M the internal gain, F the detector excess noise factor and ΔB is the electrical bandwidth of the detector amplifier combination.

detector dark noise is the noise created by current flowing in the detector in completely dark conditions (no incident photons) and is highly influenced by the temperature of the material. To minimize dark current due to thermal generation, the device can be cooled. When operated in photoconductive mode without internal amplification, the shot noise of the dark current dominates the noise of the photodiode and can be expressed by (3.6).

$$I_{sd} = \sqrt{2qI_{dark}\Delta B} \quad (3.6)$$

thermal noise in photodetector circuits is equal to (3.3). In detectors with internal gains (for instance PMTs or APDs), photonic shot noise and dark currents including their noise are amplified together with the signal. Thus, thermal noise is typically small compared to the signal and becomes negligible. In detectors without internal gains such as SiPDs, however, the preamplifier circuitry must be carefully designed to minimize thermal noise pickup.

photodetector SNR Considering the random Poisson distributed photon noise and dark shot noise, (see [Cop91]) enables a brief mathematical description of the overall SNR (3.7) of a photodetector. Here, N_p and N_d are the average photon arrival rate and the dark noise emission rate, η is the quantum efficiency of the detector and τ is the measurement interval. This illustrates that for fixed τ the dark noise should be much less than the optical signal, η near unity and the intensity used for tissue interrogation high. Furthermore, as usual, SNR increases with $\sqrt{\tau}$.

$$\mathrm{SNR}_{\mathrm{detector}} = \frac{\eta N_p \tau}{\sqrt{\eta N_p \tau + N_d \tau}} \quad (3.7)$$

A measure of photodetector sensitivity is the Noise Equivalent Power, which is the signal power that yields a signal-to-noise ratio of one in a one-hertz output bandwidth. It is measured at dark conditions and can be expressed as (3.8) for the whole input bandwidth of a detector system, where μ_d is the measured mean dark signal, σ_d its standard deviation, R_λ the detector's responsivity at wavelength λ and G_{total} the system's total gain.

$$NEP_\lambda = \frac{\mu_d + \sigma_d}{R_\lambda \cdot G_{total}} \quad (3.8)$$

3.2.3.3 Crosstalk

Optical intrinsic crosstalk Change in one chromophore may mimic a change in another and vice versa. One source of this crosstalk is a systematic error due to the *partial volume effect* that results from the estimation of the wavelength-dependent differential path length factors $DPF(\lambda)$ in (2.2), [SFB03; BGS+01]. The impact of intrinsic crosstalk between HbO and HbR is highly wavelength-pair-dependent and can be significantly reduced by the selection of an optimal wavelength pair [BDF04] (discussed in Section 3.2.2.3).

Optical crosstalk between NIR emitters occurs when several active light sources simultaneously illuminate one detector. It can be minimized by applying I-Q-/frequency modulation/demodulation or Time-Division Multiplexing (TDM) schemes.

Electrostatic/-magnetic coupling to external ac signals. Magnetic flux from external AC signals can contaminate small electric signals significantly by inducing a voltage in the measurement loop, especially when the source impedance is as high as in EEG. Examples are mains hum from power lines or intermodality crosstalk from modulated NIR light source currents into EEG channels. Electromagnetic and electrostatic noise pick-up into low-level signal conductors as in EEG can be minimized by shielding and twisting the conductors and proper grounding. In instrumentation amplifiers, common mode signals in the inputs are furthermore attenuated by a high CMRR. To robustify against power supply voltage variations, a high Power Supply Rejection Ratio (PSRR) is desirable.

Electric common-impedance coupling In circuits with more than one ground, such as signal and system grounds or split references for analog and digital circuits in mixed circuit designs, separate grounds are rarely at the same exact potential. Contacting more than one ground to the same circuit creates "ground loops" that lead to current flow along potential differences - and can introduce noise, prevent effective shielding, precise and stable referencing and good CMRR. As countermeasures, good mixed circuit design practice includes amongst others large ground planes, careful (multilayer) Printed Circuit Board (PCB) layout, optimizing current paths, power supply and -plane placement, and via stitching [Zum12; Kha92].

3.2.3.4 Other Error Sources

Finite bandwidth effect As the mBLL is only valid for monochromatic light sources, finite bandwidth effects have to be taken into account. In practice, all light sources have a finite bandwidth that is considerably more pronounced in LEDs than in LDs. The measured transmission $\tilde{T}$ within a waveband λ_1 to λ_2 can be expressed as [Cop91]

$$\tilde{T} = \frac{\int_{\lambda_1}^{\lambda_2} I(\lambda) S(\lambda) 10^{-A(\lambda)} d\lambda}{\int_{\lambda_1}^{\lambda_2} I(\lambda) S(\lambda) d\lambda}, \tag{3.9}$$

where $I(\lambda)$ is the input light intensity, $S(\lambda)$ the detector sensitivity and $A(\lambda)$ the monochromatic absorbance. The measured absorbance is then given by $\tilde{A}(\lambda) = \log_{10}(\frac{1}{\tilde{T}})$.
Where $A(\lambda)$ is not constant within the waveband, the source and detector wavelength dependencies in fNIRS instrumentation will lead to a measured attenuation smaller than the theoretically expected value for the mean of $A(\lambda)$. [Cop91].

Stray radiation and ambient light Ambient light sources, such as the sun or artificial light, also emit in the NIR range and add noise to the detected signal. This influence can be reduced by opaque covers, the aforementioned phase-sensitive detection approach, and the

subtraction of a dark current intensity baseline that is measured during inactive NIR emitter times.

System non-linearities and drifts due to heating effects, capacitive charging, variations in power supply voltages and others must be minimized by design and assessed before the instrument is used for the collection of physiological data.

Mechanical instabilities Electrode and optode shifts lead to signal artifacts that decrease SNR and can be critical. Electrode/optode and headgear concepts (see Section 3.2.2.6 and approaches in Sections 3.5.1.1 and 3.7) are crucial to minimizing mechanical instabilities, especially when applied under moving conditions.

3.2.4 Summary and Conclusions for High Precision Design

We conclude this Section by summarizing the fundamentals for directives in the subsequent system design, including a first closely related parameter selection for components:

Considerations for fNIRS instrumentation

1. Photon noise should be much lower than the optical signal. For this
   (a) the quantum efficiency / sensitivity η of the NIR detector,
   (b) the photon arrival rate N_p and thus the interrogating light intensity, and
   (c) the measurement interval τ should be as high as possible, as the photodetector $SNR \propto \sqrt{N_p},\ \sqrt{\tau},\ \sqrt{\eta}$ (3.7).
2. Ambient background shot noise should be minimized by shielding the detector from background radiation, e.g. with opaque covers or NIR bandpass filters.
3. To reduce electrical drifts, offsets and flicker noise as well as optical dark and ambient background noise, phase-sensitive detection techniques can be implemented. Propagation delays in the signal path should be kept as low as possible.
4. To stabilize emitting intensities against thermal and power supply variations, emitter currents should be controlled/regulated.
5. TDM schemes can be applied to prevent optical crosstalk between emitters.
6. To reduce optical intrinsic crosstalk, to ensure equal interrogation volume for both wavelengths and to minimize illumination of superficial tissue regions, the wavelength pair and emitter characteristics should be optimal.
   - In this work, we selected $750 + 850\,nm$ in a multi-wavelength LED with emitter-distance $< 1\,mm$, typ. total radiant power of $> 15\,mW$, half-widths $< 35\,nm$ and viewing half angles of $\pm 20\,degr.$.

7. Detectors should have maximium efficiency (proportional to its active area [Cop91]), minimal noise-pickup of the pre-amplifed signal, and a suitable bandwidth.
    - In this work, we selected monolithic SiPDs with large optical sensing surfaces of $> 5\,mm^2$ and integrated trans-impedance amplifiers (TIA) operating in photoconductive mode.

Considerations for EEG instrumentation

1. For high precision measurements of weak electric biosignals, instrumentation amplifiers with low input-referred noise ($< \mu V_{pp}$) high input impedance, low bias currents, high gains, high slew rate, high CMRR and PSRR should be employed.
2. To increase CMRR in EEG, an active reference (DRL) should be provided.
3. To ensure good SNR, low electrode-skin impedance has to be assured by performing impedance measurements and aplying non-polarizable, appropriate electrodes.

Generally, for both modalities and especially in hybrid approaches, the following considerations have furthermore to be taken into account:

General considerations for unimodal and multimodal EEG and fNIRS systems

1. Electrical crosstalk and common-impedance coupling should be minimized by good (mixed signal) PCB design practice, current path optimization, shielding and multilayer design.
2. Resistors in analog circuits should be dimensioned considering their thermal noise contribution.
3. High precision components should be used to optimize noise, drifts, and linearity.
4. User safety aspects and potential hazards have to be considered, amongst others by galvanic isolation from power lines, current limiting resistors at galvanic connections (EEG-Electrodes), limitation of emitted optical power and heating [BO04].
5. Due to dark, shot, and thermal noise, the electrical bandwidth of the system should be as close to the required bandwidth as possible.
6. For mobile employment, electrode, optodes and headgear/ fixation concepts have to consider increased mechanical requirements and robustness.

3.3 Instrumentation: State of the Art and Aims

EEG and fNIRS-based technologies for real-life-oriented research and applications in medicine, BCI and Neuroergonomics have to meet high requirements regarding signal quality, robustness, and mobility. In addition, fast application and customization are desired. While EEG is currently the primary modality used for mobile brain activity measurements, fNIRS shows a growing potential to meet these requirements and is at the center of an increasing number of research approaches.

EEG instrumentation is widely spread and open for access and thus easily customizable [DEDV+15; DME+12]. For fNIRS, on the other hand, researchers either rely on expensive and predominantly static predefined solutions or have to design their unimodal fNIRS equipment from scratch. Many attempt to overcome the restrictions of commercial instruments with undisclosed designs [WLS+17; AOI+13; SGM+13; LSL+11; AKO+07]. However, only very few of these custom devices [SGM+13] are truly miniaturized, stand-alone, unobtrusive and wearable and can be carried on the body without undue weight such as backpacks or small bags. The ideal solution allows for free movement, data transmission and processing. Oftentimes, external static instruments such as data acquisition devices, power sources, and lock-in amplifiers are required, and the latter are often sacrificed entirely for the sake of miniaturization and reduced complexity.

These limitations apply even more to combined (hybrid) EEG-fNIRS instrumentation approaches. Using complementary brain-body bio-signals toward more robust, comprehensive diagnostic and research tools and BCI, the vast majority of multimodal studies have relied on the combination of separate EEG and fNIRS tabletop systems in stationary experiments so far (e.g., [SvK+18; LAS17; SvB+17; KLN+15; FMS+12]). In mobile applications, there are currently no available commercial instruments combining fNIRS and electrophysiological signals such as EEG, electrocardiogram (ECG) or electromyogram (EMG). In research, due to the necessity of interdisciplinary expertise in hardware design and potentially high costs and development time, only few hybrid instruments have been reported. Lareau et al. presented one of the first mobile EEG-fNIRS hybrids in 2011 [LSL+11], and Sawan et al. its next generation in 2013 [SSLL+13]. Both provide high channel count and performance, but their size requires the use of a backpack ($14 \times 14 \times 5\,cm^3$). In 2014, Zhang et al. [ZIH+14] published a wearable hybrid with fNIRS, single-channel ECG and accelerometer (ACCEL) for ambulatory long-term hemodynamic and systemic monitoring, but no EEG. In 2013, Safaie et al. presented a sophisticated multichannel device for investigation of interactions between neuronal electrical and regional microcirculation activity [SGM+13]. It features high-performance fNIRS, EEG and ACCEL in a tiny volume ($3.5 \times 8 \times 1\,cm^3$).

Aims

With the ultimate aim to enable the wide-range out-of-lab use of the existing technology, it would be beneficial to integrate the following additional features into *one* wearable hybrid EEG-fNIRS device:
(1) Phase sensitive detection of optical signals, increasing robustness to changing ambient light in mobile applications.

(2) Simultaneous acquisition of different bio-electrical signals with distinct references, e.g., ECG or EMG together with EEG.
(3) Minimizing electrical intermodality crosstalk of fNIRS switching into bio-electrical input channels.
(4) Simultaneous sampling of both bio-electrical and bio-optical signals by a shared detector branch to decrease intermodality jitters.
(5) A flexible, easy to program, powerful onboard controller for software customization in stand-alone scenarios.
(6) Acceleration sensors for the acquisition of movements.
(7) Further miniaturization, decreased cost and power consumption and improved usability.

On the way to multimodal neuroimaging architectures that integrate these features, *openly documented and accessible core fNIRS technology* could also benefit other research approaches that rely on the design of custom fNIRS-based instruments.

With these aims in mind, we first identify general architectural requirements and propose a suitable concept and design toward a unimodal low-cost, customizable, miniaturized multi-channel system that provides stand-alone mobile core fNIRS functionality: The "openNIRS" [vHH+15] (Section 3.5). It is openly documented including schematics under a CC BY-NC 4.0 license. In this thesis, we will limit ourselves to its architecture and lessons learned and integrate its concept and fundamental functional units into a next-generation hybrid instrument – the "M3BA" (Section 3.6), which will be extensively evaluated and discussed.

3.4 Identification of Architectural Requirements

In the design of architectures toward flexible neurotechnology-applications out of the laboratory, the consideration of the following requirements is advisable:

- **Usability:** Miniaturization and mobility of the device, unobtrusiveness, and robustness of the electrode and optode attachment. Wearability.
- **Signal Quality:** High precision, robustness and dynamic range, low crosstalk, considerations of Section 3.2.4.
- **Safety:** Hazard-less heat & light intensities, galvanic isolation to power lines, safely designed galvanic connections to the body.
- **Configuration / Customization:** Scalability of channel number, modularity, configuration of light intensities and input gains, flexible (re-)configuration of modalities, open interface to custom hard-/software, simplicity in design.
- **Low Power Consumption:** For extended battery life and low heating.

The openNIRS and M3BA were designed with these requirements as a guideline, additionally aiming to minimize cost.

3.5 The openNIRS - Open wearable fNIRS technology

3.5.1 A Modular Architecture

The openNIRS concept is based on a scalable number of stand-alone 4-channel modules that comprise the core Continuous Wave fNIRS functionality. The modules can be controlled via a simple parallel $4\,Bit$ interface, allowing the connection to any custom or standard data acquisition (DAQ-) equipment (e.g., NI USB600x and others), given that 4 digital I/O, and a symmetric $\pm 5V$ power rail are provided. This enables full customization with respect to the number of physical channels, power consumption, sampling rate and depth and enables spatial distribution of the hardware components (and weight). By default, the modules are interfaced by a mainboard that provides power supplies, analog-to-digital conversion (ADC), channel-control and wireless communication. Localized signal generation, detection and amplification on the modules minimize noise and interferences. The stand-alone fNIRS module software sets up onboard peripheral hardware and is based on an interrupt-based architecture that is controlled via the $4\,Bit$ interface. Figure 3.5 summarizes the modular openNIRS system concept and architecture. More details, such as selected components, are provided in Figure A.2 in Appendix A.2 and in [vHH+15].

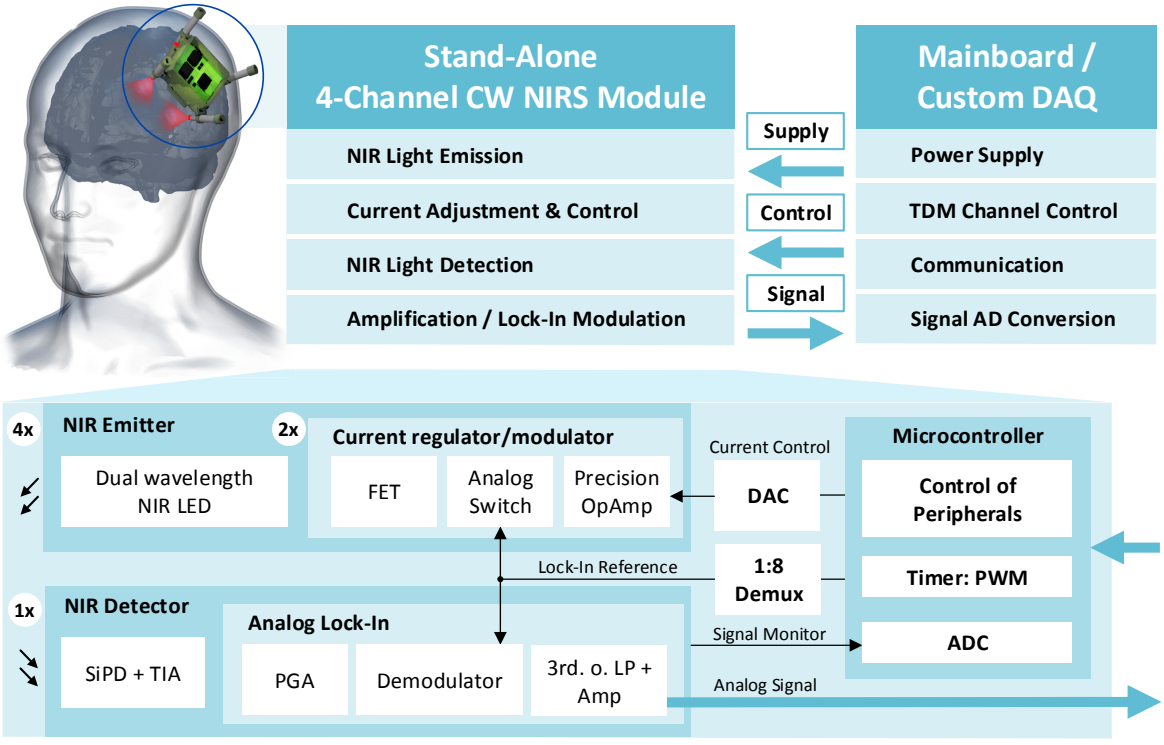

Figure 3.5: openNIRS system concept and architecture. Bottom: main units of one openNIRS module.

Each module provides four fNIRS channels using four NIR dual-wavelength LEDs (Epitex L750/850-04A) and one central detector. The LED current is regulated by custom adjustable current regulator circuits based on high precision amplifiers and field effect transistors. Channel activation and current modulation for lock-in amplification are performed

by high precision analog switches that are accessed via an analog 1:8 demultiplexer. After tissue interrogation, NIR light is detected by a central Si photodiode (Burr-Brown OPT101) with integrated trans-impedance amplifier (TIA) in photoconductive mode with a $14\,kHz$ bandwidth. The NIR light emission branch and detector characteristics will be discussed and evaluated in detail in the M3BA Section 3.6.1. The signal is then amplified and lock-in demodulated using an analog demodulator IC. An $8\,Bit$ microcontroller controls the peripheral hardware and provides a $3.125\,kHz$ PWM square wave reference for lock-in (de-) modulation using an external crystal for jitter minimization. It also processes incoming signals from the $4\,Bit$ control interface, adjusts LED currents at the current regulators via an $8\,Bit$ digital-to-analog converter (DAC) and adjusts a programmable gain amplifier that performs pre-amplification of the detected NIR signal with a variable gain from $G = 0.688$ to 88. This way, added amplifier noise components are reduced by the subsequent lock-in demodulation in an analog demodulator IC. Finally, the analog signal is filtered by a 3rd-order Butterworth low-pass and is then again amplified ($G = 5.1$) and stabilized by a set of two high precision amplifiers before being fed out of the fNIRS module for external AD conversion.

Channels are Time-Division Multiplexed (TDM) for a trade-off between minimizing inter-channel crosstalk, system complexity, heating [BO04] and battery consumption on the one hand and sacrificing SNR, due to the limited time windows applied (Equation 3.7). While demultiplexing the module's analog output signal at the acquisition unit, a variable (sample rate dependent) dwell time is inserted after channel activation onset to ensure sampling of the steady-state photodetector signal. Sample rate and dwell time are the only limiting factors when scaling the total channel/module count. Configurable PGA gain ($G = 0.6875 - 88$) and LED-intensity (256 DAC levels) in combination with a feedback "signal monitor" line allow the adaption of the dynamic range of the instrument.

For the default use of the modules in mobile applications, a microcontroller-based mainboard was developed for wireless data acquisition. Using a 4 channel $16\,Bit$ ADC and a Bluetooth wireless controller with a range of max. $20\,m$, the mainboard supports up to 4 modules (16 channels), transmits the data to a computer via Serial Port Profile (SPP) and processes incoming user controls. The symmetric $\pm 5\,V$ power rail is provided from battery DC voltage using a stabilized linear power regulator circuit. The use of low-voltage supplies from batteries also ensures user safety. The SPP and ASCII-command based software concept allows convenient platform and driver independent communication and control. Together with the graphical user interface it will be addressed in the context of M3BA in Section 3.8.

3.5.1.1 A Spring-loaded Modular Optode Design

Making use of the new modular design, a new mechanical spring-loaded optode concept was developed to optimize signal quality, sensitivity and light penetration depth together with comfortable and robust, adaptive fixation (see Figure 3.6). Based on a spherical approximation of the head with diameter $D = 20\,cm$, the central NIR light detector and the four NIR LEDs are placed perpendicular to the scalp with a source-detector separation (SDS) of $d = 35\,mm$. For perpendicular fixation of the emitters/detector and to allow alignment to the natural unevenness of the head, the LEDs are integrated into movable spring-loaded holders. These are based on two nested tubes that are spring-loaded against each other

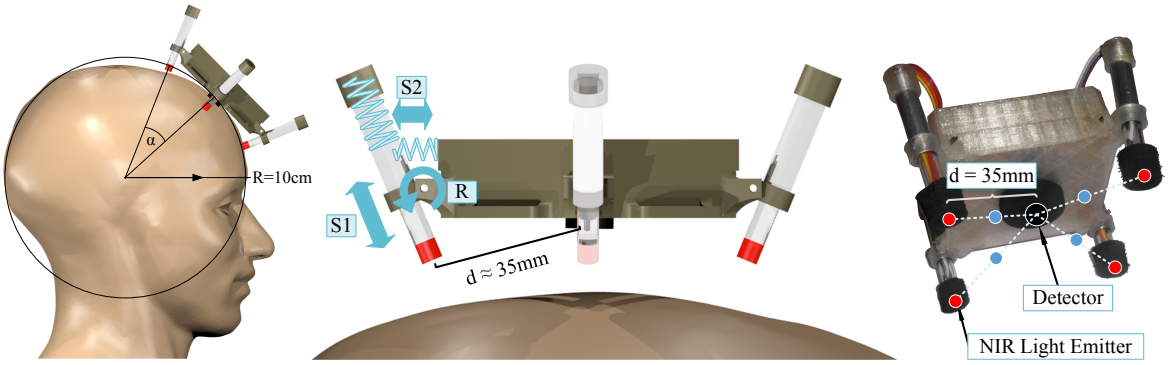

Figure 3.6: Spring-loaded optode concept of the openNIRS with a single centered detector.

(Figure 3.6 S1) and against the module housing (Figure 3.6 S2), and can rotate around an axis R (Figure 3.6 R): While S1 presses the LED toward the surface of the head, enabling alignment and buffering movements, S2 and R keep the LED perpendicular to the surface while enabling small deviations for comfort and alignment. To minimize ambient light influences and for cushioning purposes, the detector and emitters are encased by an opaque cell rubber tubing. For single-module fixation, a flexible ribbon with hook-and-loop fastener can be used that is sewed to the module housing. Without a cap or other concealing elements, the mechanical concept facilitates use on any regions of the head by easy access of the single spring-loaded optodes, allowing the application in a shuffling motion or by manually brushing aside obstructing hair from under the optodes.
The default mainboard, Bluetooth module, and batteries can be worn on the upper arm of a user in a chained multiple-unit housing, see also Figure 3.7 in the next section.

3.5.2 Brief Performance Discussion and Lessons Learned for M3BA

In the following, performance evaluation results will be briefly reviewed in light of the architectural requirements from Section 3.4. In order to avoid repetition and redundancies, we refrain from methodological details at this point: An extensive evaluation and performance characterization will be provided shortly for the hybrid M3BA architecture which builds upon the openNIRS.

Dark measurements yielded a Noise Equivalent Power of $NEP \approx 0.8\,nW_{rms}$ for the full input bandwidth. Hardware performance evaluation and physiological verification of the designed instrument indicated a *sufficient signal quality* and system performance for brain activity measurements with an approximated Signal-to-Noise Ratio (SNR) of $28\,dB$. This is a first rough approximation based on the initial ratio of $128\,dB$ between incident power into tissue at 50% LED intensity and measured NEP, reduced by an assumed typical optical loss of $-60\,dB$ within tissue, and another $-40\,dB$ by physiological fNIRS signals being typically in the order of 1% of the measured DC amplitude. By using the full range of the PGA, the dynamic range of the instrument is approximately $55\,dB$ and can be further increased by the configuration of LED intensities on the emitter side. To minimize changes in the LED

current regulation due to temperature variations, sensing resistors with a low temperature coefficient of resistance ($TCR = \pm 50 \cdot 10^{-6}/^{\circ}C$) were employed. Measurements of overall system drift due to semiconductor junction temperature changes in the LEDs, supply voltage variations and others yielded a negative drift coefficient of $C_D = -1 \cdot 10^{-6} V/s$ and a respective long-term stability coefficient of $< -0.42\%$ for both wavelengths.

For a preliminary physiological validation, qualitative investigations and a mental arithmetic study with N=12 subjects were conducted. Details on the study are provided in Appendix A.2. Single channel measurements showed pronounced physiological signals such as pulse waves (verified with conventional reference pulse measurements) and low-frequency oscillations in HbO, the raw signal, and their power spectrum. These are first indicators for sufficient signal quality, as their amplitudes are in the order of metabolic variations due to brain activity ([SKM+14; LSL+11; BDF04]). In the study, hemodynamic responses were measured in mental arithmetic vs. relaxation tasks and classified on a single-trial basis using two frontal channels placed between EEG 10-20 positions AFz (detector) and Fp1 and Fp2 (emitter) with a source-detector separation of $3.5\,cm$. Single-trial classification accuracies exceeded chance level for 9 out of 12 participants and yielded results comparable to those measured with a commercial device in a similar study [HHP+13] using 2 out of 8 channels at similar positions (65.14 % vs. 67.26 %).

In the course of the experiments, subjects appraised the *usability* of the device to be high compared to commercial reference systems with longer preparation times, added weight of optical fiber guides and non-cushioned optodes. Battery supply and wireless communication, low heating due to time multiplexing of the channels and the use of LEDs as light sources assured a *safe* usage of the device. Miniaturization of the modules and mobility through Bluetooth based wireless transmission allowed free movement. The modular concept, simple schematics, flexible parallel fNIRS module interface, and configurable emission and detection gains allow *easy customization and configuration* of the hardware.
The following Figure and Table summarize the openNIRS and its performance characteristics.

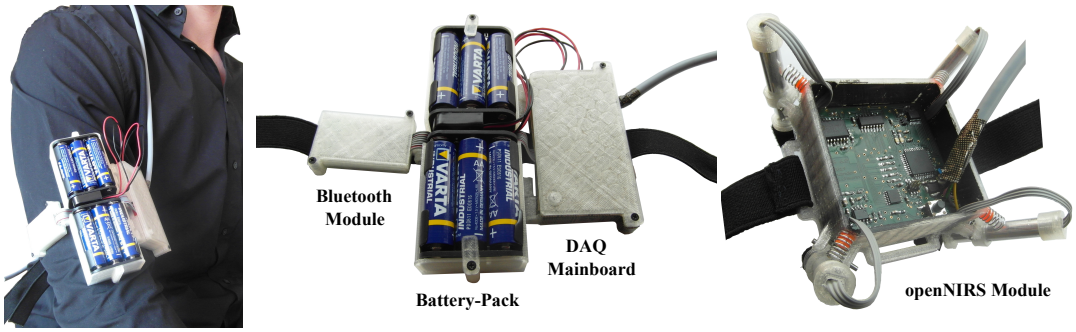

Noise Equivalent Power		**Opt. Power** $@I_{LED} = 50\%$	**Opt. Power** $@I_{LED} = 100\%$	**Estimated SNR**
$NEP_{\lambda=750}$:	$0.80 nW rms$	$P_{\lambda=750} = 5.70 mW$	$P_{\lambda=750} = 11.10 mW$	$\approx 28 dB$
$NEP_{\lambda=850}$:	$0.78 nW rms$	$P_{\lambda=850} = 5.38 mW$	$P_{\lambda=850} = 10.30 mW$	

Intensity levels	**Detection Gains**	**Drift**	**Dynamic Range**	**Sample Rate**
256	$G = 3.5 \cdots 450$	$< -1 \cdot 10^{-6} V/s$ / $< -0.5\%$	$> 55 dB$	variable

Analog Lock-In Amplification	**Spring-Loaded Optodes**	**Stand-alone Interface**

Figure 3.7 & Table 3.3: openNIRS Hardware Overview and Characteristics.

3.5.2.1 From openNIRS to M3BA

The openNIRS showed sufficient performance, comparable to other documented CW fNIRS instruments. It fulfills its purpose as an aid in the design of novel fNIRS instrumentation by providing an open and simple architecture that is easy to grasp and to modify. Using other LED wavelengths, the modules can also be used for other spectroscopy applications aside from fNIRS. However, its concept also comprises limitations to be overcome in next-generation approaches. Higher miniaturization, improved performance, and hybridization with other biosignals are desirable.

Acquisition, control, and communication have to be fused onto a single module to achieve higher miniaturization and stand-alone WBSN functionality. Shifting phase-sensitive detection from the analog to the digital domain bears further advantages: The number of hardware components, cost, and power consumption can be reduced and phase shifts due to propagation delays can be corrected for higher precision. In the openNIRS, the overall propagation delay between the detected signal for lock-in demodulation and the reference signals ($\Delta t = 25.7\,\mu s$) results in a small attenuation (see Equation 3.1) of $A = \cos(\Delta\Phi) = \cos(\frac{\Delta t}{T} \cdot 2\pi) \approx 0.875$ or $-0.6\,dB$. This can be easily alleviated in the digital domain. While the single centered detector reduces the complexity of the detection circuitry on a single module, it is not optimal regarding channel density, power consumption, and TDM. The simultaneous acquisition with multiple detectors during illumination of a single emitter is an obvious advantage. In the openNIRS, electrical crosstalk of the up to $100\,mA$ square wave $3.125\,kHz$ modulated emitter currents was observed to influence the power supply voltage stability and noise performance of the detection circuit. These effects are synchronous with the demodulation and strongly suppressed by the subsequent low-pass filter. Nonetheless, their minimization by voltage supply decoupling and layout optimization is desirable to improve performance, and vital when other sensitive sensing circuitry, such as EEG, is to be incorporated.

Figure 3.8 depicts the evolution from the openNIRS to the hybrid M3BA architecture by integrating openNIRS core funcitonality with a large number of additional features into the hybrid M3BA concept that will be the focus of the rest of this Chapter.

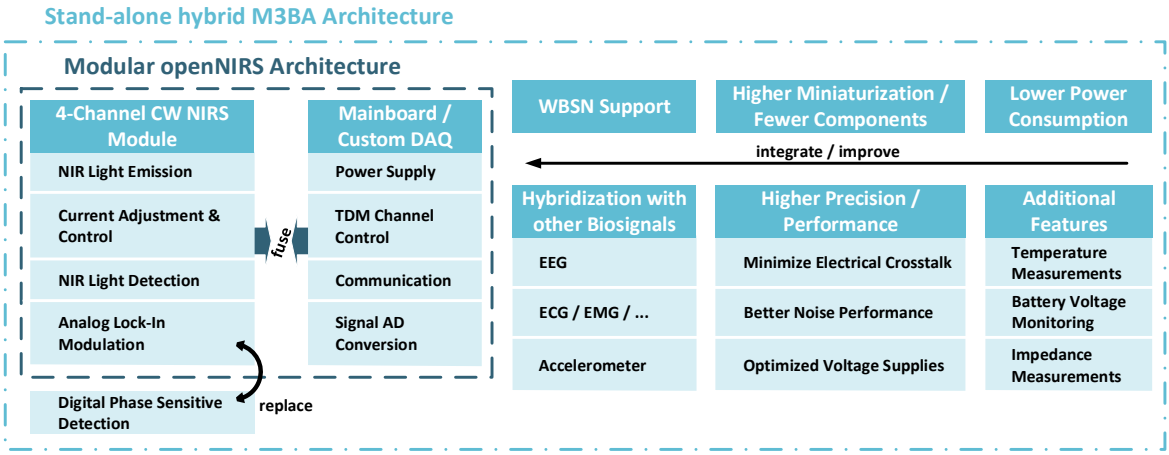

Figure 3.8: Evolution of architectures: from openNIRS to M3BA.

3.6 M3BA - Hybrid Modular EEG-fNIRS Acquisition

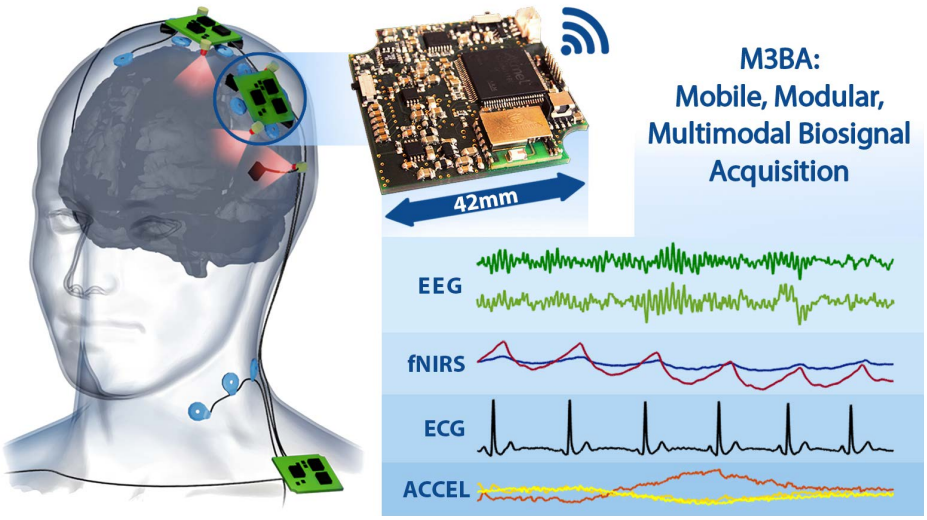

Figure 3.9: M3BA: An Architecture for Mobile, Modular, Multimodal Biosignal Acquisition

The M3BA – for Mobile, Modular Multimodal Biosignal Acquisition – is an architecture for a new generation of highly customizable mobile, hybrid bio-optical/ -electrical designs that are compatible with Wireless Body Sensor Network (WBSN) scenarios. Using a shared Analog Front-End (AFE) and a powerful microcontroller, we integrate the requirements and features outlined in Sections 3.3 and 3.4, use functional units from the openNIRS design, improve resolution ($24\,vs.\,16\,Bit$), decrease costs and at the same time further miniaturize beyond previous approaches ($4.2 \times 4.2 \times 0.6\,cm^3$). In the following Section 3.6.1 concept, architecture and selected design aspects are presented. Section 3.6.2 elaborates on performance characterization, physiological validation in in-vivo studies, and the methods and phantoms employed. Section 3.6.3 will give an overview and results will be discussed in Section 3.6.4. While the architecture works for a variety of signals and applications, the instrument is dedicated to hybrid neurotechnology solutions in this thesis, in particular BCI and Neuroergonomics. The focus lies on fNIRS and EEG signals and ACCEL, ECG, and EMG measurements are supported as additional modalities within the same device, and with a separate reference-input.

3.6.1 Architecture and Design

3.6.1.1 Concept

To illustrate the system concept and scope of applications for the M3BA architecture, Figure 3.10 shows an exemplary hybrid WBSN BCI scenario for which the modules were designed. Taking into account Section 3.4, necessary for that are, amongst others, modularity, mobility, miniaturization and multimodality, scalability and reconfigurable references. Also, the scenario implies the resulting potential for multimodal signal analysis approaches.

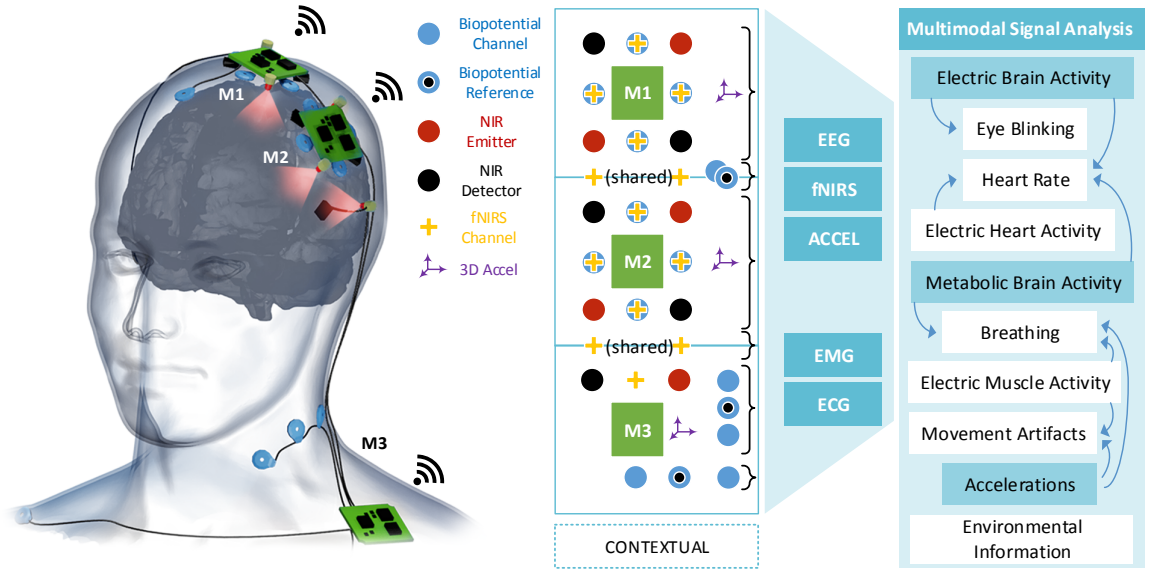

Figure 3.10: Multimodal modular concept and example scenario: Modules ($M_{x=1...3}$) can be combined to increase channel count and number of measured modalities. Each module provides 4+2 bio-electrical and 4+2 bio-optical signal acquisition channels and one 3D accelerometer. Multimodal signal analysis allows extraction of shared and complementary information in the simultaneously acquired data.

A single M3BA module provides $4+2$ channels for bio-electrical signal acquisition. These are designed for high precision acquisition of EEG signals and can also be used for ECG, EMG and EOG recordings. 4 channels derive signals against a fixed common reference. The additional 2 channels can be used for derivation against the same common electrode or (via microswitch) against another independent reference. Each module also has two optical detectors and emitters and thus provides $4+2$ fNIRS channels, where the $+2$ channels are available when neighboring M3BA modules share emitter-detector pairs in a time division multiple access manner. Additionally, each module incorporates a 3D-accelerometer for the acquisition of acceleration data. Electrodes and optodes can but do not have to be fixed to the module as in the openNIRs concept. Thus, the module can but does not have to be worn "on-site"; depending on the application, headgear or caps can be used.

In the example scenario in Figure 3.10, three modules M1-M3 are combined for simultaneous measurement of EEG, fNIRS, EMG and ECG: M1 and M2 and one (detached) optode pair of M3 measure 8 EEG and 13 fNIRS channels over the left somatosensory cortex, while M3 measures 2 EMG channels at the neck and 2 ECG channels on the chest. M1 and M2 share a reference and ground electrode and make no use of the 4 bio-electrical channels that are additionally available. M3 uses the available reference split for the independent acquisition of EMG and ECG. M1, M2, and M3 share emitter/detector resources and thus create 4 shared fNIRS channels. Optionally, the modules can share a physical (non-wireless) interface for common time-critical signals such as a shared sampling clock and fNIRS channel control signals and - as in the case of M1 and M2 - a common reference. In the standard case, this is established by flat ribbon wires with micro cable-to-PCB connectors. All modules acquire movements (speed changes) via their 3D accelerometers.

The resulting set of synchronously acquired (bio-)signals enables a variety of new approaches for multimodal signal analysis and robustifying against artifacts. We will return to this topic in Chapter 5. Since the idea of multimodality is inherent to the system concept, some potential benefits are briefly pointed out here: As opposed to single modality analysis, exploiting several modalities in the analysis procedure enables a better identification, extraction or rejection of physiological artifacts (e.g., heart rate, eye blinking frequency, ...) and movement-induced artifacts. Typical examples for shared components in the acquired signals are (1) the time-locked artifacts from heart activity as ECG in the EEG and pulse-waves in fNIRS recordings and (2) respiratory or movement-related artifacts in EEG (EMG interference or electrode shifts) and (3) in fNIRS (modulation of oxy-/deoxy hemoglobin signals and optode shifts) that are co-modulating with synchronously acquired accelerometer data. The latter will be addressed in Section 5.2. Raw multimodal data that further illustrates this is depicted in Figure 3.23, Section 3.6.2.3 and Figure 4.4, Section 4.3.3.

3.6.1.2 Architecture

The hardware architecture (see Fig. 3.11) was designed to concord with the described system concept and to provide high system performance, precision, and user safety.

In the design of new miniaturized hybrid instruments for bio-electrical and bio-optical measurements, attention has to be paid on how to implement these hybrids so that high precision can be achieved and crosstalk between the signals and crosstalk from digital components in the mixed-circuit design are minimized. Here, essential advantages of unified hybrid approaches opposed to the combination of two separate instruments are both the synchronicity of the acquisition and a common ground that allows more sophisticated consideration of current paths and fields to minimize noise and electrical cross-talk. Especially considering miniaturization and precision aspects in a mixed-circuit design, we solved this by using a common Analog Front-End (AFE) integrated circuit for both, bio-electrical and bio-optical signals:

The M3BA hardware architecture is based on the high precision circuit ADS1299 [Tex12] from Texas Instrument, which is a very low-noise ($1\mu V_{pp}(70HzBW)$) 24-Bit Delta-Sigma AFE with 8 differential inputs optimized for EEG bio-potential measurements. It provides many peripheral features such as programmable gain amplifiers (PGAs, $G = 1-24$), configurable sample rate ($250SPS - 16kSPS$), a built in bias-drive amplifier and a multifunctional input multiplexer (MUX). Furthermore, an extensive documentation of electrical and performance characteristics for bio-potential measurements is provided by the manufacturer. We embedded the AFE in a framework made up of a powerful $32Bit$ ARM Cortex M4 microcontroller, an ADXL343 Accelerometer and enhanced functional units for near-infrared (NIR) light emission and detection, that are based on those from the openNIRS:

The configurable NIR light emitter units use dual-wavelength Light Emitting Diodes (LEDs) with $750nm$ and $850nm$ (Epitex L750/850-04A) that are stabilized and modulated by further improved current regulation and modulation circuits (see following Section). The openNIRS units were improved by applying an OpAmp with better noise characteristics, higher slew rate, and lower operation voltage.

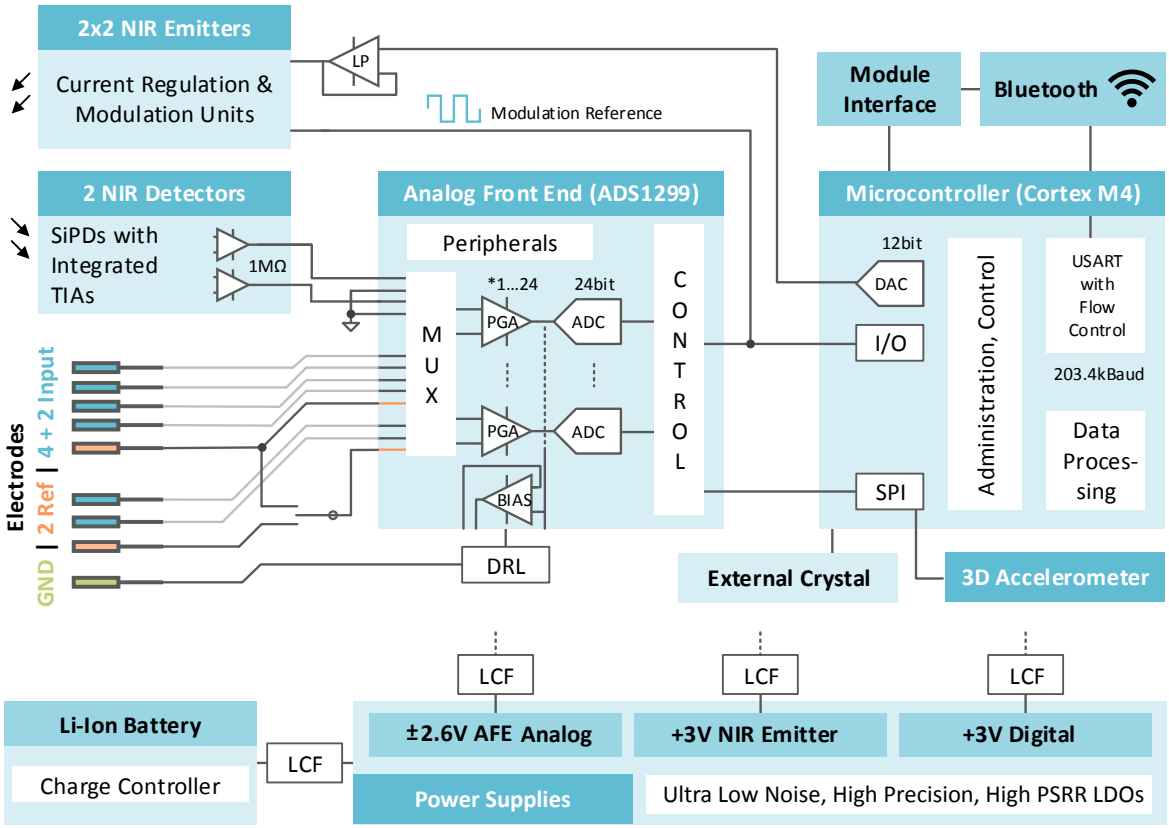

Figure 3.11: M3BA Hardware Architecture: Stand-alone high precision hybrid biosignal acquisition by utilizing an ultra low noise biosignal AFE and a powerful 32 Bit microcontroller together with improved NIR emitter and detector units from the openNIRS design. 4+2 differential bio-potential inputs (blue: meas., orange: switchable reference, green: ground (configurable Driven Right Leg)). Units are buffered and supplied individually by ultra low noise, high power supply rejection ratio (PSSR) low drop-out regulators (LDO) from a charge-controlled Li-Ion Battery. Communication and data transfer via integrated Bluetooth module.

The NIR light detector units are based on Si-photodiodes (Burr-Brown OPT101) with integrated trans-impedance amplifiers (TIA). The selection is a tradeoff between safety and minimization aspects (lower supply voltages and smaller size), responsivity ($0.45 A/W$ @$650 nm$), noise minimization and bandwidth ($14 kHz$) for phase-sensitive detection. In the openNIRS design, the analog detection was based on an analog lock-in demodulation circuit. Here, attenuation by phase shifts, size, cost and number of components are minimized by performing demodulation on the microcontroller in the digital domain.

The eight differential AFE signal inputs are split into 2 channels that measure the single-ended optical time division multiplexed fNIRS signal against analog system ground and $4+2$ differential bio-potential channels that are measured against a split or common reference (selectable via a microswitch). In this way, the AFE fuses the high precision measurements of both analog signal types. Configuration, control, processing and communication tasks are performed by the Cortex M4 microcontroller running at $120 MHz$ with an external crystal for jitter minimization. In particular, it performs:

- data processing and retrieval from AFE and Accelerometer (via Serial Peripheral Interface, SPI)
- configuration of AFE (PGA, MUX, sample rate, ...) and peripherals
- adjustment, regulation and modulation of NIR LED currents. For adjustment, a filtered internal $12\,Bit$ DAC signal is used as regulator command variable
- fNIRS channel control and timing, digital phase-sensitive demodulation
- communication with host (e.g. notebook) via flow controlled ring-buffered USART Bluetooth module, and with other modules (physical interface for timing and control)
- power management and supply control

To minimize noise and electrical crosstalk between analog signals but also between the analog and digital circuits, the architecture was carefully designed considering the best practice for mixed-signal, multi-layer and multi-power supply designs. To maximally decouple the functional analog and digital units in the instrument, the LED-emitter units, the bipolar analog detector and AFE circuits and the digital components (microcontroller, accelerometer, digital AFE side, ...) are supplied separately by ultra-low noise, high precision and high PSRR low drop out regulator based power supplies and are additionally buffered with LC- and ferrite low-pass filters (LCF). The instrument is supplied by a single Li-Ion Battery with integrated protection circuit and provides a charge controller for fast recharging via USB. As M3BA is completely wireless and running on voltages $< 3.7V$ user safety and power consumption issues are dramatically decreased: For fault conditions, current limiting resistors are placed between electrodes and ADS1299 circuitry, which itself was designed by the manufacturer to conform with the safety regulations for medical electrical equipment.

3.6.1.3 Selected Design Aspects

Emitter Branch and Current Regulation A careful design of the emitter circuit for high accuracy is crucial, as fluctuations in the radiation intensity due to variations in supply voltage or temperature cannot be discriminated from those due to changes in chromophore concentrations. To enable stabilization, control, intensity adjustment and modulation of the current through the LED semiconductor junctions, a customized current regulator circuit was designed and evaluated, originating in the openNIRS design (see Figure 3.12). Analog switches are used for square-wave modulation of the current, by pulling the inputs of the regulator circuits low when deactivated. Activation and modulation of a selected channel are thus realized simply by configuration of the channel multiplexer which feeds through the lock-in reference to the respective current regulator. To minimize transient oscillation and settling times of the regulated currents during kHz modulation, a passive negative RC feedback was added. Simulations and measurements of different feedback decoupling capacitors $C = 0 - 330\,pF$ and high precision OpAmps for different current levels yielded the best trade-off between high edge steepness and low transient oscillations for $C = 100\,pF$ in the selected OpAmps with high slew rates. Detailed NIR emission characteristics of the adapted current regulator design in conjunction with L750/850-04A AlGaAs multiwavelength LEDs will be provided shortly in the following Section on performance characterization.

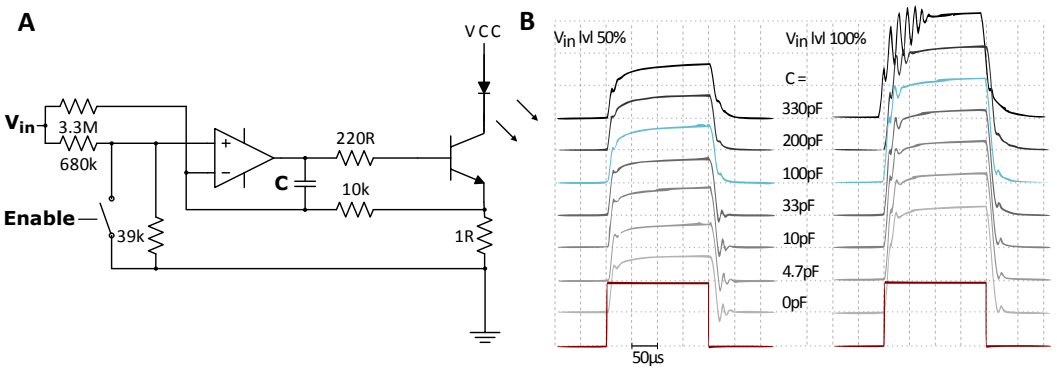

Figure 3.12: (**A**) Current regulator circuit & (**B**) decoupling capacitor evaluation, currents measured over 1R.

Hybrid Bio-Signal Acquisition and Timing To administrate and synchronize the acquisition of both signal types, EEG and fNIRS, the AFE and microcontroller (μC) build a closed loop in the M3BA architecture. Once a continuous measurement is started, the AFE acquires signals with a sample rate previously set (using an internal oscillator) and indicates complete conversions to the μC via a Data Ready (DRDY) signal. The DRDY signals trigger data retrieval and time division multiplexing of the NIR emitters by the μC. Figure 3.13 exemplifies such a typical hybrid acquisition cycle of a single M3BA module.

The AFE runs at a fixed sample rate of $1\,kSPS$ (with an input bandwidth of $BW = 262Hz$); one complete fNIRS measurement cycle takes 60 sample (DRDY) events. While the EEG data is continuously saved, exponentially averaged and down-sampled to a user-configurable sample rate of $500\,or\,250\,SPS$, the fNIRS routine is called every second DRDY iteration. In one fNIRS measurement cycle, it subsequently switches twice (I/II) through all available emitter states (here five: two LEDs $L_{y=1}$ and $L_{y=2}$ each with two wavelengths $\lambda_{x=1} = 750\,nm$ and $\lambda_{x=2} = 850\,nm$ and a dark measurement period). Signals of all photodiodes during

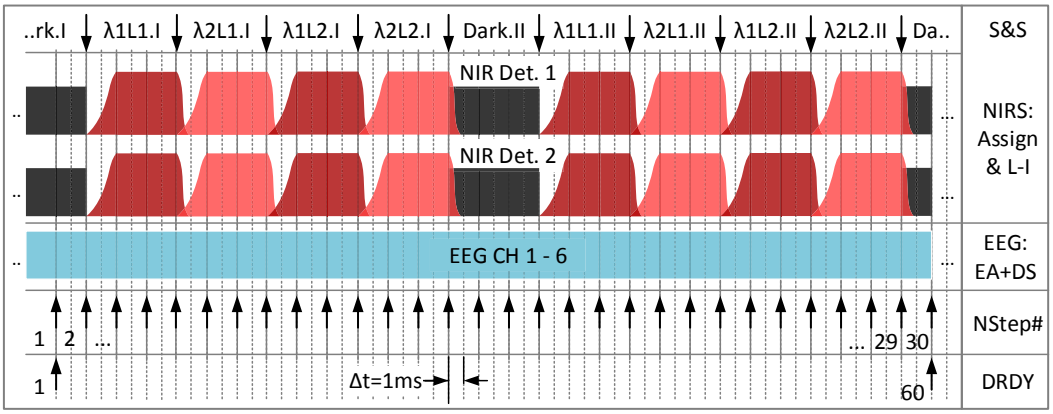

Figure 3.13: Hybrid acquisition timing scheme. *DRDY*: Data Ready signal of AFE sampling all channels with $1\,kSPS$; *NStep #*: iteration of fNIRS administration routine for one complete measurement for all active channels (here: 4); *EEG: EA+DS*: Exponential Averaging and DownSampling of EEG signal; *S&S*: Sample and Switch on/off new wavelengths (λ)/ LEDs (L); *Assign & L-I*: Assignment of emitter-detector combinations to channels and phase-sensitive demodulation.

one state are simultaneously measured. For one module, each state is sampled 6 times, where at least the first two samples are discarded during the settling of the photodiode signal ($t_{dwell} \geq 2\,ms$). The last of the acquired samples is saved, assigned, and the next emitter state is activated. Once each $60\,ms$, when a fNIRS measurement cycle is finished, all resulting four measurements of each emitter-detector pair (2 active emitter and two dark measurements) are combined in a phase-sensitive demodulation step ($\lambda_x {L_y}^I + \lambda_x {L_y}^{II} - Dark^I - Dark^{II}$) for dark current and ambient light subtraction. This results in a fNIRS sample rate of $f_s = 1/60ms = 16.66\,Hz$ with the fNIRS samples being time-locked to the EEG signal. Since each emitter state is activated two times per measurement cycle, this yields an LED current switching frequency of $f_{switch} = 33.33\,Hz$ and its multiples, potentially creating crosstalk into EEG inputs. The aforementioned PCB design minimizes this and we evaluate the quality of the approach in Section 3.6.2.2.

For the synchronization of several M3BA modules, one declared master module shares a physical 8-wire parallel interface with the slave modules. Over this interface, all AFEs are synchronized with a shared sample clock provided by one master AFE; fNIRS TDMA channel control is administrated and common references are shared. Each module communicates with a host Notebook or PC via an integrated Bluetooth module (BTM) from ST-Microelectronics (SPBT2632C2A) using Serial Port Profile (SPP). Other processing units that support Bluetooth SPP (like smartphones or tablets) can as well be used for data acquisition. Data between μC and BTM is transferred via a flow-controlled and ring buffered USART interface to minimize packet loss. The software concept will be further discussed in Section 3.8.

Layout and Functional separation The 6 layer mixed-signal printed circuit board (PCB) was lay-outed with split analog, digital and supply planes in a star ground (GND) manner with dedicated spatial and functional separation of circuits and optimized return current routing. Figure 3.14 gives a schematic overview of the M3BA layout. To minimize EEG-fNIRS

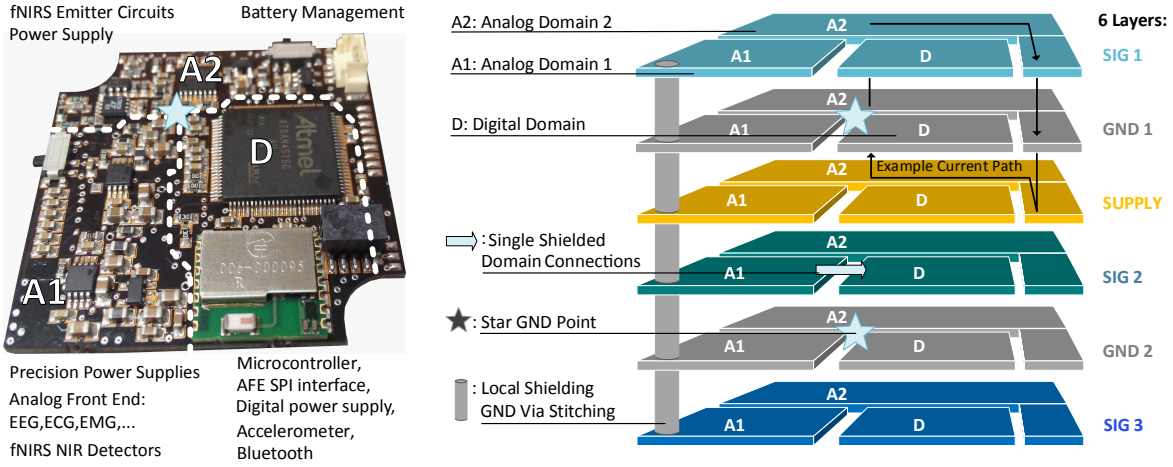

Figure 3.14: M3BA 6 layer PCB concept: Three signal layers (SIG1-3), two ground planes (GND1-2) and one supply plane (SUPPLY), separated into two analog (A1-2) and one digital (D) domain for crosstalk-minimization. Reference potentials are brought together in a star GND point close to the battery connector.

crosstalk, fNIRS emitter circuits have dedicated voltage supplies and reference potential planes and are spatially separated from the precision analog AFE bio-potential and NIR-detector branches. GND and supply planes, and via stitching were used for local shielding of conductor tracks for sensitive signals, such as fNIRS and EEG before amplification.

3.6.2 Performance Evaluation and Characteristics

3.6.2.1 Hardware Performance Characterization

In this Section, we discuss methods and phantoms used for evaluation of the hybrid architecture and the corresponding results. Since the ADS1299 is designed for EEG-acquisition and performance details are provided by the manufacturer [Tex12], we focus on the optical (fNIRS) and hybrid performances as well as crosstalk characteristics.

Evaluation of fNIRS signal quality and phantom The evaluation of the fNIRS characteristics was performed employing a solid homogeneous optical phantom with tissue-like scattering and absorption properties, to mimic (1) the total attenuation that occurs in the tissue at a source-detector separation of 30 mm, (2) the diffuse nature (in terms of its spatial and angular distribution) of light exiting the tissue. We made use of a phantom of known diffuse transmittance that was devised and characterized to assess the responsivity of the detection system of time-domain optical brain imagers [WTM+14; WTF+16].

The phantom was a cylindrical slab of thickness $20\,mm$ and diameter $105\,mm$, made of epoxy resin with TiO_2 particles added as a scattering medium and black toner as an absorbing medium, following the recipe published by Swartling et al. [SDAE03]. Its optical properties at $750\,nm$ were: reduced scattering coefficient $0.53\,mm^{-1}$, absorption coefficient $0.0126\,mm^{-1}$, refractive index 1.55. As a measure of diffuse attenuation we adopted the "optical loss" (OL) as defined in the international (IEC/ISO) standard for functional fNIRS equipment [IEC], i.e. as the ratio of the total optical power exiting a circular aperture of specified

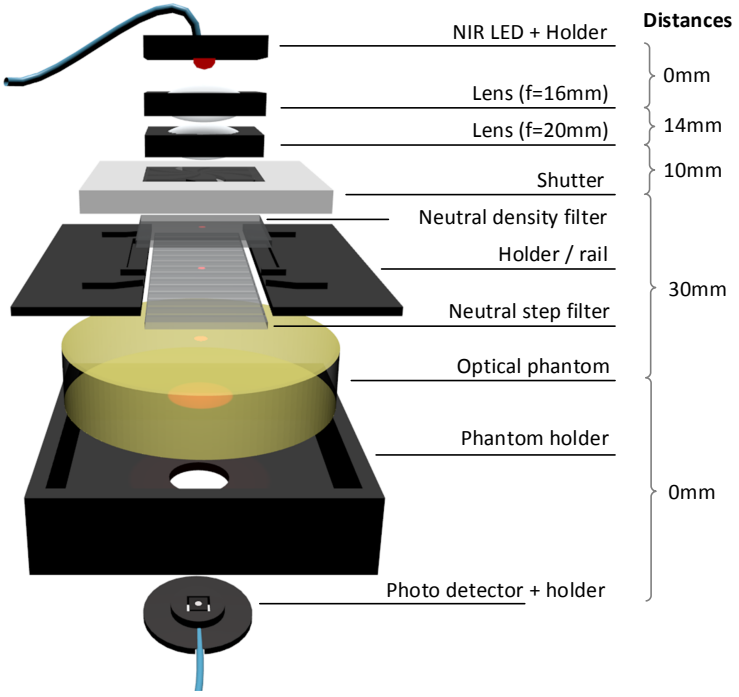

Figure 3.15: Experimental setup for fNIRS characterization using an optical phantom with neutral step filters.

diameter ($8\,mm$) on the exit side of the phantom and the power injected on the entrance side. In the following, the optical loss is either given as a ratio (OL) or in dB units, where $X\,dB$ optical loss is equivalent to $10^{-X/10}$. The optical loss of the phantom used was $24.7\,dB$ at $750\,nm$ and $23.5\,dB$ at $850\,nm$. The tests in the IEC/ISO standard refer to optical losses of $> 40\,dB$ or $> 60\,dB$, depending on the particular test, to mimic a typical attenuation for fNIRS. We achieved such values by using additional gray filters.

The tests were performed in a custom experimental setup with one NIR emitter-detector pair and the phantom in transmission geometry, as shown in Figure 3.15. The phantom was placed in a black plastic holder, with its bottom surface in direct contact with the fNIRS photodetector.

On the top side, the phantom holder case was closed with a custom black two-piece lid (3D-printed) that acted as a rail for an absorbing neutral step filter (15 steps covering an optical density range of approximately 2 orders ($20\,dB$)) and additional neutral density glass filters. These filters were used to vary the overall optical loss. Light from the NIR emitter mounted on top of the structure was imaged onto the phantom (diameter of illuminated spot: $5\,mm$) by two convex lenses and passed through a controllable optical shutter (type Melles Griot 04 IES 211, controller 04 IPS 850, actuation speed: $17\,ms$). The shutter was controlled via an M3BA hardware-trigger output; shutter (de-)activation was acquired and labeled to the acquired fNIRS data stream. The attenuation of all used neutral density filters and filter steps were determined independently via power transmission measurements using a supercontinuum laser (SC500-6, Fianium Ltd, UK) with acousto-optic tunable filter tuned to $750\,nm$ and $850\,nm$, respectively, and a Coherent Fieldmaster power meter with sensor head LM-2.

The following measurements were conducted with an input gain setting of $G = 4$ and an emission level setting of $I = 8$ ($8.94\,mW$ @$750\,nm$, $8.34\,mW$ @$850\,nm$):

Drifts / Stability At a fixed total optical loss ($OL_{750nm} = 47.3\,dB$, $OL_{850nm} = 50.2\,dB$), the optical signal was acquired continuously for $15\,min$ twice. For estimation of the continuous drift, the slope and R^2 of a linear least squares fit were calculated.

The drift measurements revealed the need for a warm-up time of max. $5\,min$ after switching on, in which the emitted $850\,nm$ power settles by 1.7%. After that, the optical signals drifted less than $27.5\,nV/s$, which in relation to the signal amplitude at $40\,dB$ optical loss is less than $1.6\,ppm/s$.

Signal to Noise Ratio (SNR) / Coefficient of Variation (CV) and Linearity (LIN) of the instrument In a continuous acquisition, after $5\,min$ free-running for warm up, 42 measurements of the fNIRS signal in a range of $OL = 4 \cdot 10^{-2} - 9 \cdot 10^{-6}$ ($26.0\,dB - 69.5\,dB$) were conducted in approx. $1.5\,dB$ steps. The last $10\,s$ of data (170 samples) were used for the evaluation of each step. During manual filter step transitions, the shutter was closed. For each measurement, the shutter was opened, thus also providing a Step Response (SR) in the acquired signal s. Standard deviation (σ_s) and mean ($\bar{m}_s$) were calculated for all steps and both acquired wavelengths. CV and SNR were calculated as $CV_s = \sigma_s/\bar{m}_s$ and $SNR_s = 20\,log(\bar{m}_s/\sigma_s)$. It should be noted that for hardware performance characterization

this SNR is related to the total optical signal, not to the hemoglobin concentration changes derived in fNIRS. For LIN evaluation, slopes and R^2 values of linear least squares regression fits on the $\bar{m}_s$ for each wavelength were calculated. Results are shown in Figure 3.16.

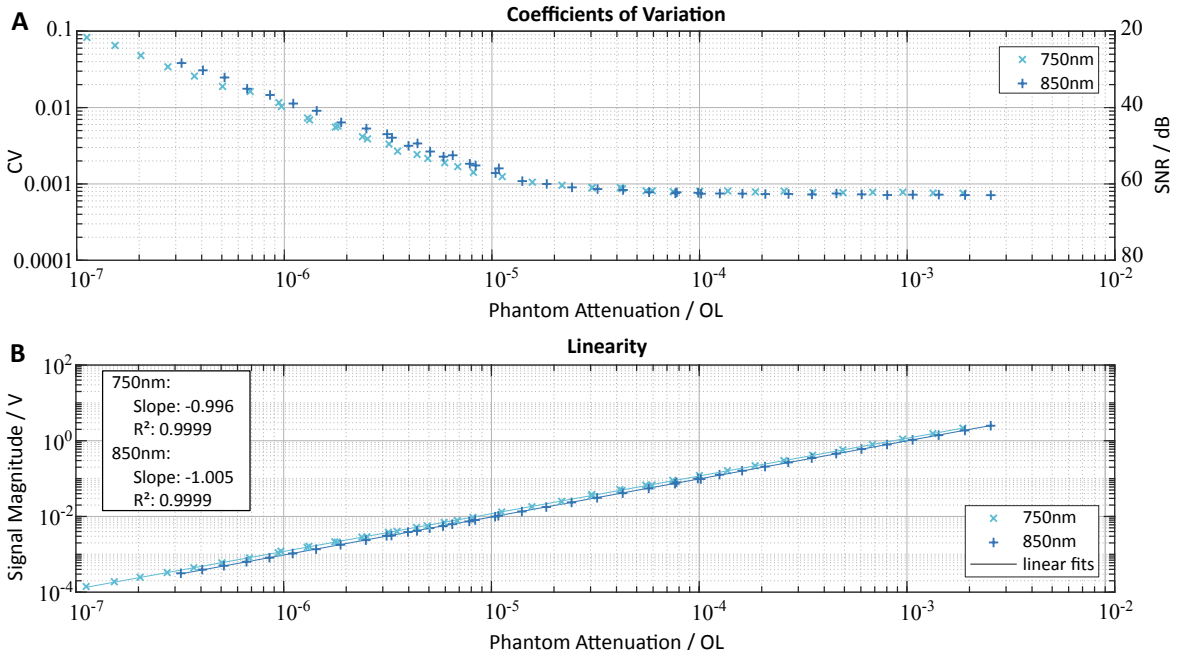

Figure 3.16: (**A**) Coefficient of Variation / SNR of fNIRS measurements. (**B**) Linearity of measured optical fNIRS signals over the whole range of optical loss (OL).

The device showed very distinct *linearity* for both wavelengths (slopes $S_{750} = 0.996, S_{850} = 1.005$, corr. coeff. $R^2_{750|850} = 0.999$) over the full tested optical range.

The evaluation of *CV* and *SNR* for both wavelengths yielded predominantly constant values ($CV < 0.001$, $SNR > 60\,dB$) for low attenuation $OL < 5 \cdot 10^{-}4$ and linearly increasing CV / decreasing SNR above $OL = 5 \cdot 10^{-4}$. Even at very high optical losses in the range of 10^{-7}, the SNR is about $20\,dB$, indicating that small changes in optical power occurring in fNIRS experiments can still be measured.

Step responses measured with the shutter for all OL-configurations showed a settling of the signal within one fNIRS sample ($60\,ms$) without further oscillations.

NIR Emitter Power and Spectrum The continuously emitted radiant power (no switching) for each wavelength was measured with a Coherent Fieldmaster power meter with sensor head LM-2. The LED was mounted in such a way, that the illuminated area was fully covered by the sensor's photosensitive area. The emitted power at 6 different current levels ($I = i \cdot 10\,mA \mid i \in \{5,6,...,10\}$) and the illuminated area on the optode surface were measured to determine the incident intensity at a user's scalp.

The spectra of the NIR emitters for both wavelengths and different current levels were measured with an Avantes AvaSpec 3648 spectrometer with an integration time of $t_I = 50\,ms$ and averaging over 200 measurements. The NIR light was attenuated by $32.4\,dB$ ($750\,nm$) and $33.3\,dB$ ($850\,nm$) using neutral density filters. The measured spectra were corrected by

the previously determined calibrated spectral sensitivity and by dark measurements. Spectral dependence on emission directions due to varying local semiconductor characteristics was evaluated by measuring the spectra at different tilts of the emitter. Peak wavelengths (PW) were calculated by a maximum search of a Gaussian fitted to the top 10% area of each spectrum. Maximum PW shifts over all intensities were determined ($\Delta PW_{\lambda,max}$). The Full Width at Half Maximum (FWHM) of the spectral power distribution was calculated as the difference of the wavelength between the two points whose corresponding power values are equal and $3\,dB$ lower than the values at each peak wavelength.

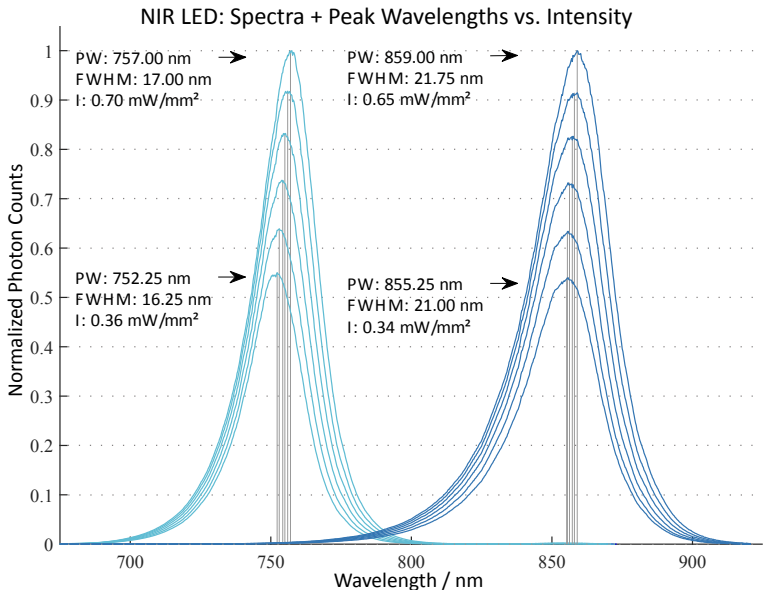

Figure 3.17: NIR emitter spectra for six intensity levels (I), peak wavelengths (PW) and Full Width at Half Maximum (FWHM) at min. and max. level of emitted intensities.

Results are shown in Figure 3.17. Tilting experiments did not show a significant dependence between spectrum and tilt of the LED relative to the measurement probe. The spectra measured for all six implemented intensity levels show a slight shift toward higher peak wavelengths with higher illumination intensities ($\Delta PW_{750,max} = 4.75\,nm$, $\Delta PW_{850,max} = 3.75\,nm$). Changes in the FWHM for both wavelengths are marginal ($\Delta FWHM_{max} = 0.75\,nm$). Due to the TDM of channels, the effectively emitted intensities during fNIRS acquisition are $\frac{1}{5}$ of the ones measured during continuous emission.

Noise Equivalent Power (NEP) For determination of the NEP of the fNIRS detector branch of the instrument, $60\,s$ (1000 samples) of the signal were acquired for each PGA input gain $G = 1...24$, while the fNIRS emitters were active but the detectors were put into an opaque box with no incident light. With OPT101 responsivities $R_{\lambda=750} = 0.55\,\frac{V}{\mu W}$ and $R_{\lambda=850} = 0.60\,\frac{V}{\mu W}$, the NEP for all PGA gain levels yielded $NEP_{min,850} = 295\,fW/\sqrt{Hz}$ to $NEP_{max,750} = 366\,fW/\sqrt{Hz}$ and for the full $262\,Hz$ input bandwidth respectively$NEP_{min,850} = 4.77\,pW$ to $NEP_{max,750} = 5.92\,pW$.

3.6.2.2 About the Advantage of Hybrid Bio-Signal Acquisition

Since the design and development of hybrid devices are labor-intensive and costly, the question arises why, and under which conditions it is worth to integrate both technologies into one hybrid device. In the following, we investigate electrical crosstalk and intermodality jitter (see Figure 3.18), comparing the M3BA EEG-fNIRS hybrid to separate commercial instruments.

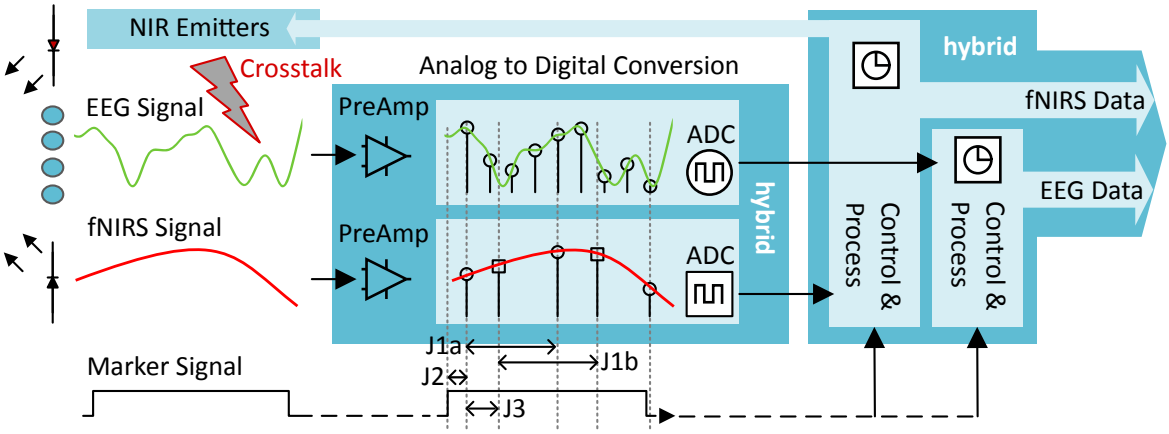

Figure 3.18: Advantages of hybrid acquisition: Separate (light blue) and hybrid (dark blue) bimodal acquisition of EEG and fNIRS. NIR emitter currents can introduce electrical crosstalk into EEG-inputs that can be minimized in hybrid designs. Non-synchronized unimodal acquisition (circles and squares) increases jitters: J1a/b) asynchronous analog to digital conversion with individual clock sources. J2) Within-modality marker-sample assignment jitters. J3) Between-modality marker imprecision due to largely differing sample rates. These can be minimized in a hybrid instrument (only circles).

NIRS LED current switching crosstalk into EEG Many miniaturized fNIRS instruments suitable for mobile and bedside monitoring use near-infrared light from Laser Diode or LED sources close to or directly placed on the head. The emitter currents are often sine- or square wave-modulated and channels are either frequency division or time division multiplexed. Switching and modulation of currents can, however, create considerable electrical crosstalk by field coupling on the PCB and between fNIRS optode and EEG electrode wires. In hybrid designs, a common ground and good mixed-circuit design practice, including shielded lines and current return path optimization, can decrease these effects.

Setup: Electrical crosstalk into EEG inputs was investigated using a resistor network made from metal film 0.1 % resistors as shown in Figure 3.19. The phantom consists of a polystyrene head covered with a resistive network with nodes ("electrodes") at 10-20 EEG-positions, which can be accessed via DIN-electrode jacks. The resistive network simulates electrode-to-skin impedance ($2.7\,k\Omega$) and between-electrode skin conduction ($200\,\Omega$). Clearly, this network does not have the same AC properties as the human scalp probed with EEG. However, it allows well defined comparative measurements which rather favor non-hybrid systems, as electrode impedances are low and equal and the network topology homogeneous: Inhomogeneities in realistic applications, e.g., varying electrode

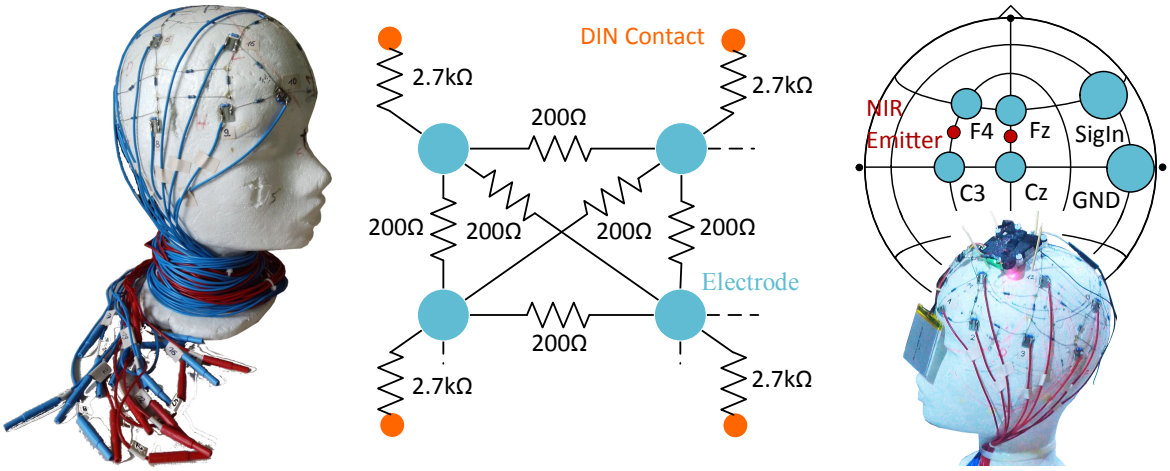

Figure 3.19: Electrical phantom for crosstalk-evaluation of fNIRS switching into EEG-inputs of M3BA and commercial device and measurement of system bandwidth.

impedances (resulting in a worse common mode rejection), are likely to have a lesser effect in optimized hybrid systems with common ground than in combined stand-alone instrumentation approaches. At position F8, voltage divided sine signals with $A = 150\mu V$ and $f_s = \{1, 10, 100\}\,Hz$ from an Agilent 3500B signal generator were fed into the network. The two NIR emitters of one M3BA module were placed between Fz&Cz and F3&C3 and either active or inactive ($a = 0, 1$). Signals were measured at positions $p = \{Cz, Fz, C3, F3, F8\}$ against a common reference (GND) at T5. Each $70\,s$ measurement $m_{f,p,a}$, was repeated with both the M3BA module ($@500\,SPS$) and with a separate commercial reference EEG amplifier for comparison (g-tec USB Amp, 2009, $@512\,SPS$). All experiments were conducted in a magnetically and electrically shielded room (two-mu meta layer Ak3b, Vakuumschmelze, Hanau).

Investigation: NIRS crosstalk in frequency bands above the EEG spectrum of interest (typically $0.1 - 40\,Hz$) can be suppressed by appropriate low-pass filters and will therefore not cause serious problems. For evaluation of the crosstalk in the band of interest, the FFT power spectra of the last $60\,s$ of the $m_{f,p,a}$ were calculated and the spectrum converted to V_{rms} amplitudes. Then, for all channels, and all conditions we extracted the signal intensities at $f_{switch} \pm 0.155\,Hz$.

To differentiate between crosstalk external and internal to the EEG amplifier circuitry, we additionally measured the input-referred noise using an internal feature of the ADS1299 AFE multiplexer. For active and non-active fNIRS ($I = 8$) and all PGA gains $G = 1 - 24$, the *input referred noise* was determined by calculation of the standard deviation of 2000 samples ($@500\,SPS$) for each condition.

Results: The comparative measurements during active and inactive fNIRS revealed an increase of the high-precision bipolar supply voltage noise from $6.6\,\mu V_{rms}$ to $21.4\,\mu V_{rms}$ ($262\,Hz - BW$). However, the input-referred noise of the hybrid system's EEG amplifier for all PGA-settings did not show any significant deviations from the manufacturer's reference

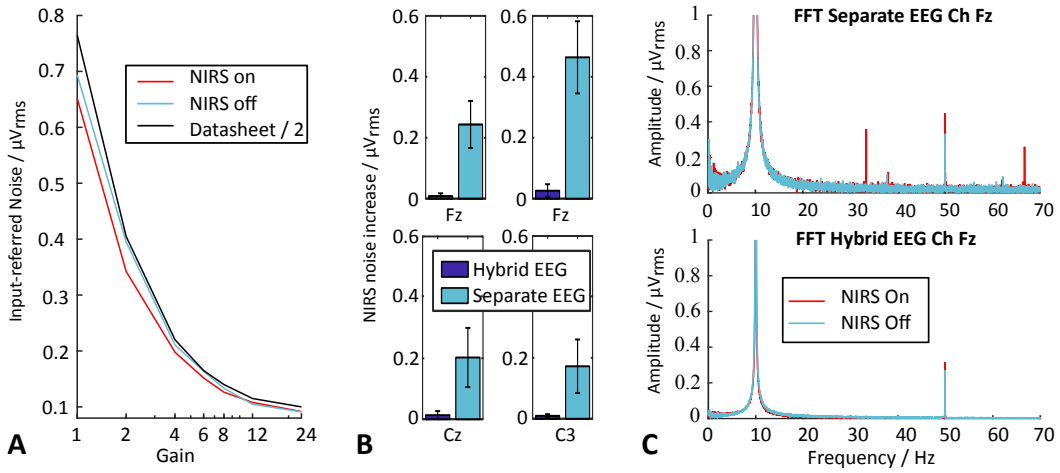

Figure 3.20: Results of fNIRS-EEG crosstalk evaluation. (**A**) Input-referred noise with in-/active fNIRS in M3BA. (**B**) average increase of 33.3Hz fNIRS switching noise in separate EEG and hybrid instrument. Error bars show standard deviation. (**C**) Typical FFT spectra of signals measured at Fz with separate and hybrid EEG.

values, regardless of active or non-active fNIRS switching ($< 0.28\,\mu V_{rms}$ at $1\,kSPS$ with $262\,Hz$ bandwidth and $G = 24$), see Figure 3.20 **A**. This indicates good decoupling by a successful PCB layout and shielding. The crosstalk by fNIRS switching on the electrical phantom lead to distinct peaks at f_{switch} and its higher harmonics in the FFT-power spectra for all test signals measured with the separate EEG device (Figure 3.20 **C**). Measured with the M3BA module, they are almost entirely indiscernible from the generally lower noise floor. While the noise around the switching frequency increased on average by less than $0.02 \pm 0.02\,\mu V_{rms}$ for each channel in the hybrid system, a spatially dependent increase of up to $0.46 \pm 0.12\,\mu V_{rms}$ noise was picked up by the separate EEG on one channel, and of $0.21 \pm 0.09\,\mu V_{rms}$ on average, across all other channels (Figure 3.20 **B**). The higher noise within the comparative device may be due to longer cable length and unavoidable ground loops as the combined setup was not optimized for low noise performance.

Marker precision and jitter in multimodal data streams Most biosignal acquisition experiments require labeling of the data with marker signals for time-precise mapping of events and conditions. These signals are usually fed into a dedicated trigger/marker input of the instrument and data streams have to be fused and matched in time subsequently. In separate instruments, different kinds of delay/jitter can affect the matching precision of modalities (see Figure 3.18): J1a/b) asynchronous analog to digital conversion with individual clock sources and jitters, J2) Marker signals may either be acquired synchronously at biosignal-inputs or at separate inputs. In the latter case, jitters in the marker-assignment to the current biosignal sample time can occur. J3) Regardless of individual internal oscillator jitters and assignment imprecisions, marker signal edges are assigned to biosignal samples acquired with significantly differing sample rates between modalities. Whilst in unimodal signals the sampling rate sets the time precision limit, alignment of multimodal data can at the maximum only be as precise as the lowest individual marker timing resolution. In hybrid instruments, such as the M3BA, signals of different modalities can be sampled and markers

assigned based on one shared clock source serving for all timing-based processes.

To investigate the difference in precision between dedicated unimodal commercial scientific instruments and the hybrid M3BA design, a recently published large open access hybrid EEG-NIRS dataset was used [SvB+17]. In this dataset, data was acquired with a BrainAmp EEG amplifier (Brain Products GmbH, Gilching, Germany) and a NIRScout device (NIRx GmbH, Berlin, Germany). The dataset comprises synchronously acquired data from 29 subjects: 3 hours in 6 acquisition blocks labeled with 19 trial markers each, summing up to a total of 3309 markers for the entire dataset. In the experiments, the marker signal was fed into both instruments' trigger inputs simultaneously via a PC's parallel port. For comparison, hybrid EEG-NIRS dummy data was acquired with M3BA on a test bench, feeding the marker signal into both the digital trigger- and an analog EEG measurement input, resulting in 4410 markers and analog transitions each, of which the first 3309 were used. For the dataset acquired with separate instruments, the marker timing jitters between modalities were calculated by building the differences between corresponding EEG and fNIRS marker times for all 3309 trials. In the M3BA data, the two modalities inherently do not show marker-timing differences due to the synchronous sampling and allocation. Instead, the time delays between the trigger edges in the sampled analog signal and the corresponding digital trigger flags allocated by the processing unit were calculated. 1^{st} and 2^{nd} order statistics were then calculated on the resulting 174 blocks of 19 marker timing differences for both the hybrid and the separate system.

Results from the marker jitter evaluation are depicted in Figure 3.21. The mean and standard deviation of the absolute jitter in marker timings amounted to $28.98 \pm 18.17\,ms$ for the separately acquired data. There was inherently zero difference in marker timing between simultaneously acquired EEG+fNIRS in the hybrid device, but an imprecision of $1.59 \pm 0.97\,ms$ due to edge-detection and sample assignment by the M3BA processing unit. Statistical analysis of the absolute jitter variance across blocks confirmed significantly higher intermodality timing precision for the hybrid device (one-sided Welch's t-test, $p \ll 0.001$).

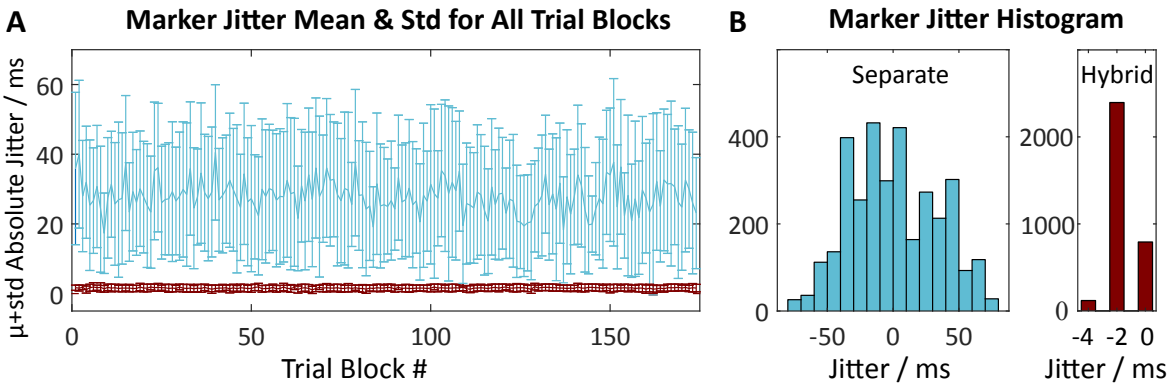

Figure 3.21: Evaluation of bimodal marker timing precision. (**A**) $\mu \pm \sigma$ of marker to signal sample assignment differences between separately (blue) acquired EEG- and fNIRS markers and hybrid (dark red). (**B**) Histograms of all measured intermodality marker jitters (blue: separate, dark red: hybrid)

EEG linearity and frequency response To verify the desired EEG input linearity and cut-off (mainly influenced by the AFE input bandwidth and implemented exponential averaging on the μC), the *input frequency response* was investigated by acquiring a linear $5s$ sweep from $0.1\,Hz - 2\,kHz$ with constant step width and $100\,mV_{pp}$ and $100\,\mu V_{pp}$ amplitudes, generated by the Agilent 3500B on the previously discussed electrical phantom setup. The frequency response was extracted by applying a polynomial curve fit with order 21 through the Hilbert envelope of the acquired raw sweep signal and confirmed flatness ($< 0.1dB$) in the pass band and the cut-offs set by the configurable exponential averaging ($f_{cEA500\,Hz} = 210\,Hz$, $f_{cEA250\,Hz} = 100\,Hz$) and AFE bandwidth ($f_{cBW} = 262\,Hz$).

3.6.2.3 Physiological Validation

Extensive evaluation using the optical phantom showed a high performance in optical sensitivity and a significant improvement over the openNIRS design. To characterize the practical capabilities of EEG amplifiers, it is often best to perform evoked potential measurements with human subjects. Pure technical parameters can be easily determined using proper test equipment, but for EEG signal generation phantoms are rarely known. Instead, human subject data are considered the "gold standard". For the EEG-functionality and multimodal acquisition, the following human subject studies were conducted according to the declaration of Helsinki and approved by institutional ethics committees. All participants were comprehensively informed and gave written consent before the experiments.

EEG: Comparative measurements of Auditory Evoked Potentials (AEPs) Auditory evoked potentials [PHK+74] were measured on five right-handed subjects (3 male, 2 female, avg. age $26 \pm 2y.$) stimulating the left ear with $1\,kHz$ sine tones of $400\,ms$ duration. Tones were delivered using an Etymotic ER-30 insert earphone and an RME HDSP 9632 sound card. Tones had $92\,dB\,SPL$ as measured with a Bruel&Kjaer type 4153 artificial ear. In total, 300 tones were delivered with a randomized inter-stimulus interval of $1.5 - 2.5\,s$. This resulted in an experiment time of roughly $12\,mins$ and after $6\,mins$ subjects were notified of half-time. Each subject was measured with the M3BA and a commercial g.USBamp EEG amplifier (www.gtec.at). The electrode plugs were moved between device inputs and the session lasted $30\,mins$ (12 + 12 + change of EEG plugs) in total for both amplifiers. The sequence of M3BA and g.USBamp was randomized between subjects. The signals were acquired over the left fronto-parietal region at the 10-20 positions C3, F3, T3, and T5 and measured against the right mastoid with GND (DRL) placed at Fpz. AgCl ring electrodes were used with gel and impedances were below $10\,k\Omega$. The recorded signals were digitally filtered with a zero delay bandpass of $0.1 - 45\,Hz$ and 4th order Butterworth characteristics. Epochs were baseline corrected in a $100\,ms$ pre-stimulus interval and then averaged for each subject and channel to obtain the AEP. The obtained AEPs were compared to literature results [PHK+74] with respect to amplitude and latency of the N1-P2 complex.

The signals of one out of five subjects were discarded due to very high mains hum in the comparative measurement using the separate commercial EEG instead of the M3BA EEG channels. Signal analysis showed distinct N1-P2 peaks typical for AEPs in the EEG signals of all the remaining four subjects. Here, the positions C3 and F3 showed strong N100

amplitudes, where less typical positions (T3 and T5) showed less distinct signals, as expected. Figure 3.22 shows the signals of both devices for each channel averaged over all subjects for comparison. The characteristics of the N1-P2 complex in the signals (timing, amplitude, and shape) indicate that the M3BA performs like a standard precision EEG recording unit.

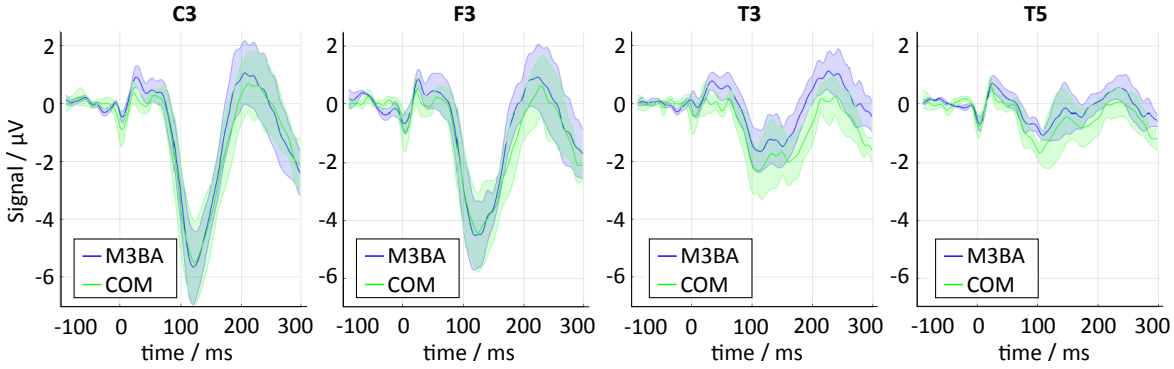

Figure 3.22: N100 comparative results between M3BA and commercial separate EEG (COM) device. Solid lines are signals averaged over all subjects, measured at indicated 10-20 electrode. Shaded error bars indicate standard error of the mean (SEM).

Qualitative Multimodal Signals The acquisition of an extensive multimodal fNIRS-EEG dataset that ultimately also provides further evidence of the device's functionality is covered in Chapter 4. For first qualitative example data and validation of the multimodal mobile acquisition capabilities of the M3BA instrument several simple 10 trial experiments on one subject were performed: One single M3BA module was fixated to a 10-20 EEG cap (EasyCap GmbH, Germany) simultaneously measuring EEG ($@500\,Hz$) with gel electrodes at positions O1, O2, Cz and Fp2, one channel of ECG (Einthoven 2 derivation), accelerometer data and 4 fNIRS channels ($@16.6\,Hz$). fNIRS emitters were placed at AF3 and AF7, detectors at F5 and Fp1, resulting in approx. $30\,mm$ emitter-detector distances. The participant was asked to stand, close eyes and take a deep breath when a first beep sound was played and to open eyes after a second beep sound after $10\,s$. Other experiments also included sitting down, standing up, walking and turning around. Example data for these longer trials can be found in a more comprehensive Figure A.4 in Appendix A.3. For a better assessment of the raw data quality, only minimal processing was performed: EEG and ECG channels were digitally filtered with a 6th order zero delay $0.1-45\,Hz$ Butterworth bandpass. For alpha-band power estimation during eyes closed, the average of the Hilbert envelopes of the bandpass filtered (Butterworth 2nd. order, $10-13\,Hz$) signals of O1 and O2 were calculated. fNIRS O_2Hb and HHb concentration changes were calculated from the raw optical signal using effective extinction coefficients [ZBG+01] of the measured LED spectra and HomER2 [HDF+09] software and were then baseline corrected by mean subtraction.

Figure 3.23 shows a typical single trial of the raw multimodal dataset acquired in the qualitative experiment with a standing subject using one M3BA module. O1, O2, and Cz show distinct alpha activity during eyes closed ($10-20\,s$), Fp2 shows typical eye blinking

artifacts. Deep breathing in and out shows in the accelerometer signal. Also, the deep breath impacts the ECG heart rate and R-wave amplitude as well as the overall fNIRS signals. The fNIRS signals show the typically stronger pulse waves in O_2Hb compared to HHb, which are also clearly correlated to the electrical activity of the heart in the ECG.

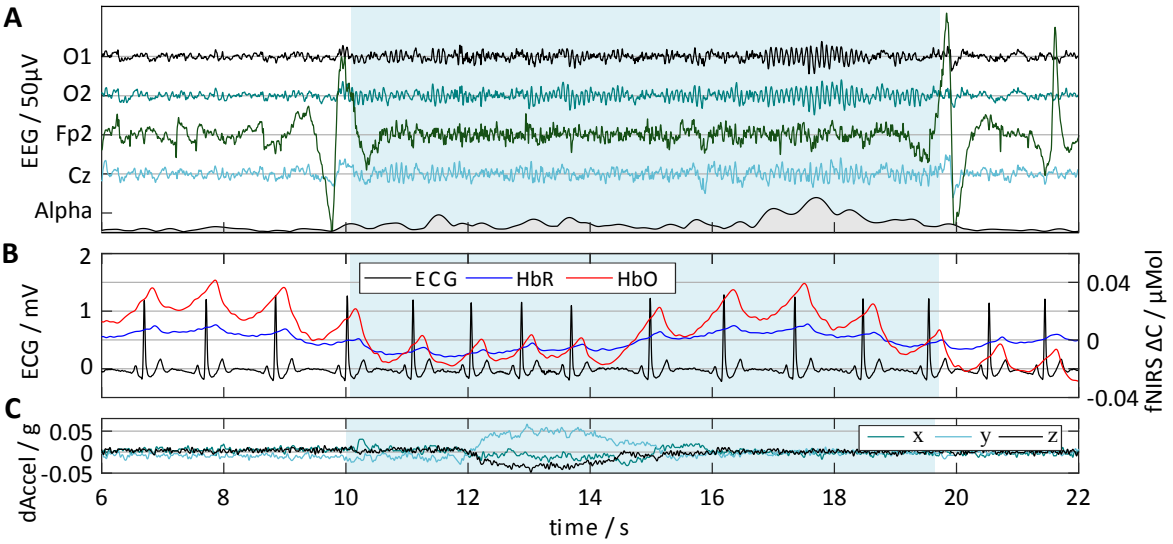

Figure 3.23: Synchronously recorded raw multimodal data from a standing subject during deep breath ($t = 12\,s$) and eyes open/closed ($t = 10\,s/20\,s$): EEG channels and alpha power (**A**), ECG and fNIRS signals (only Ch1 (AF3-F5) for better overview) (**B**) and accelerometer signal (**C**). Some typical dependencies between modalities are already observable in the raw ECG, fNIRS and accelerometer signals (R- and pulse wave correlation, ECG/fNIRS modulation by breathing (accelerometer).

3.6.3 Overview

The M3BA architecture was implemented successfully in a highly miniaturized design for precision EEG, EMG, ECG, and fNIRS acquisition, that can be used - amongst others - for WBSN based hybrid BCI scenarios. The dimensions of a stand-alone M3BA module are merely $4.2 \times 4.2 \times 0.6\,cm^3$, allowing a flexible integration into different mechanical set ups, including the openNIRS approach, and head-and-body-gears. When the optodes are directly connected to the module's edges, the fNIRS source-detector distance is $35\,mm$ and freely configurable otherwise. Different sizes and capacities of Li-Ion batteries can be connected via a standard connector: with a current consumption of $< 100mA$ (all features active), a module runs more than 3 hours on a tiny $28 \times 34 \times 2\,mm^3$ ($300\,mAh$) Li-Ion battery, and more than 18 hours on a standard mobile phone battery. The following Table and Figure give an overview of the M3BA module characteristics, and Figure A.6 in Appendix A.3 provides additional detail.

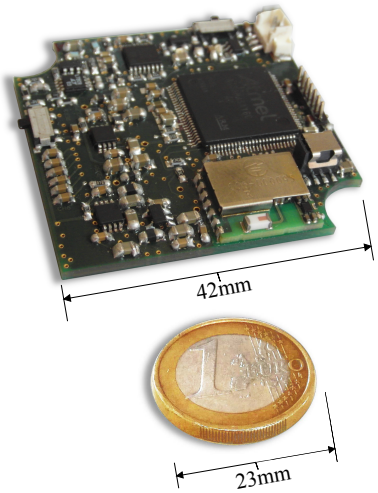

EEG/EMG/ECG/...			
# of Channels:	$4+2$	Resolution:	$24\,Bit$
Sample Rates:	$500 \mid 250\,Hz$	Common Mode RR:	$-110\,dB$
Inp. ref. Noise:	$1.39 \mid 0.98\,\mu V_{pp}$	Input PGA:	$G = 1-24$
Inp. Bandwidth:	$210 \mid 100\,Hz$	Config. Driven Right Leg (DRL)	
EEG electrode impedance measurement functionality			

fNIRS			
# of Channels:	$4+2$	Resolution:	$24\,Bit$
Sample Rate:	$16.6\,Hz$	Wavelengths:	$750 \mid 850\,nm$
Emitter lvl.:	$I = 5-10$	NEP (full BW):	$5.92 \mid 4.77\,pW$
Input PGA:	$G = 1-24$	SiPD Respons.:	$0.55 \mid 0.6\,\frac{V}{\mu W}$
Optical Drift:	$< 1.6\,\frac{ppm}{s}$	ΔPeakWavel$_{max}$:	$4.75 \mid 3.75\,nm$
Optode Dist.:	$35\,mm$ / conf.	FWHM:	$16.6 \mid 21.4\,nm$
SNR (10^4 OL):	$66\,dB$	Intensities$_{750\,nm}$:	$0.07-0.14\,\frac{mW}{mm^2}$
SNR (10^6 OL):	$40\,dB$	Intensities$_{850\,nm}$:	$0.07-0.13\,\frac{mW}{mm^2}$
Full linearity ($10^{-2}-10^{-7}\,OL$)		Digital Phase-Sensitive Detection	

Accelerometer			
# of Channels:	x,y,z	Resolution:	$10-13\,Bit$
# Sample Rate:	$0.1-1\,kHz$	Ranges:	$\pm 2,4,8,16\,g$

General	
Power consumption: $< 360\,mW$	Li-Ion Cell (replacable) + charger
Bluetooth range: Indoor $5m$	Modularity: Up to 4 modules
Hardware trigger precision: $2 \pm 1\,smpl$	

Figure 3.24 & Table 3.4: M3BA Module and Overview of Characteristics.

3.6.4 Discussion

Performance characteristics A systematic evaluation of the novel multimodal miniaturized device was performed through performance measurements using an optical and an electrical phantom, and internal features of the AFE. EEG precision was demonstrated in a N=4 AEP in-vivo study with both the new and a commercial reference instrument and showed the expected characteristic N1-P2 signal amplitudes and shapes. Multimodal acquisition was validated by a qualitative raw data experiment simultaneously acquiring fNIRS, EEG, ECG and acceleration data. The system-performance tests demonstrated excellent linearity, low optical drift, and very low noise levels amongst others. The characterization of optical noise revealed that between $20-50\,dB$ OL, the coefficient of variation (CV) remains constant with values lower than 0.1%. This noise component can be attributed to the LED light source; signal as well as noise are proportionally attenuated by the phantom, as long as photon noise can be neglected. Above $50\,dB$ OL, the CV linearly increases with an approximate slope of 1 which is indicative of the domination of a signal-independent noise component. Extrapolating the course to $80\,dB$ OL yields $CV \approx 1$ for a signal magnitude in the order of $10\,\mu V$, which coincides with the manufacturer's data for the photodiode's dark noise in the used bandwidth ($15\,\mu V - 262\,Hz\,BW$). This is also in line with the measured NEP values in the order of $10^{-12}\,W$, when considering: (1) the incident optical LED power of $10^{-3}\,W$, (2) an OL due to the phantom of 10^{-8}, (3) additional losses in the optical path, and (4) the fact that the actual detector area ($5\,mm^2$) is smaller than the area of the 8 mm diameter aperture used in the definition of the optical loss. It is therefore assumed that the signal-independent

noise component is the photodetector's thermal noise on which future attempts to improve performance should focus.

The M3BA architecture improves the openNIRS design by (1) shifting phase-sensitive detection from the analog to the digital domain and thereby removing the phase shift dependent attenuation (formerly: $A = 0.874$). This increases the SNR by approximately $1.16\,dB$ and decreases both the number of analog components and potential noise sources in the detection path, (2) stand-alone integration of all hardware into one single unit, (3) detector parallelization, and 4) better electrical decoupling and overall performance optimization / noise minimization (supplies, decoupling, amplification and conversion): The Noise Equivalent Power for optical measurements over the whole respective input bandwidths was improved by 3 orders of magnitude from nW_{pp} in the openNIRS to pW_{pp} in the M3BA.

Since the design is also based on a powerful microcontroller, the user can easily and quickly change, implement and increase the complexity of programs running on the module. Thus, new approaches such as decentralized on-line feature extraction, adaption, filtering and online impedance measurements on the modules themselves become possible. These features can be profitable in wireless tactile scenarios, where context information and the bandwidth available on the wireless infrastructure are taken into account in the provision and (pre-)processing of sensor information.

Hybridization While static hybrid fNIRS-EEG measurements can nowadays relatively easily be performed by combining two separate commercial devices, it was studied quantitatively whether dedicated hybrid systems such as the M3BA exhibit properties that are advantageous over combined setups.

To achieve the desired high-performance characteristics in all modalities, great care was taken to minimize noise and crosstalk by optimizing the mixed-circuit multilayer and multi-power-supply layout for the AFE - μC unit. The intermodality crosstalk evaluation revealed that bimodal setups combining EEG and fNIRS could indeed create switching noise crosstalk into EEG inputs in combined separate devices that can be minimized in hybrids such as the M3BA. The achieved robustness is especially important when the fNIRS current switching frequency lies within the EEG frequency band (here up to $0.66\,\mu V_{pp}$ in the β-band at $33.3\,Hz$). This can hardly be distinguished from oscillatory activity reflecting real neural processes later on. Since fNIRS and EEG instrumentation architectures differ and will exhibit different crosstalk characteristics, separate bimodal setups should be combined cautiously. This is especially important without prior knowledge about what noise characteristics may be exhibited. While crosstalk was consistently negligible in single hybrid M3BA modules, it could in some cases still be observed in setups with multiple devices, when linked by a physical cable connection for synchronization to achieve maximum time precision. In future approaches, wireless synchronization procedures could alleviate this. Not all bimodal setups will necessarily create inter-modality crosstalk. For instance, in fNIRS systems that use optical fibers for guiding light from and to the scalp.

The comparative evaluation of marker timing precision in separate vs. hybrid devices revealed a significant jitter between the separately acquired data streams. The timing imprecision increases, the more the sample rates between modalities differ. In the asynchronously acquired non-hybrid data, the fNIRS sampling rate was $12.5\,Hz$ compared to $1\,kHz$ in EEG.

Consequently, a triggering edge in the marker signal is assigned to the EEG data stream with $1\,ms$ precision, but only with $80\,ms$ precision to the fNIRS data stream. Since fNIRS signals are slow-changing signals, this precision is usually sufficient for unimodal experiments. However, when SNR is low, and high precision is required, acquisition with hybrid bimodal devices can bring advantages. This is especially noted within scenarios that need to assess fast but weak (e.g., P300-based) EEG components in conjunction with slow, yet precisely time-locked fNIRS components, and additional synchronization hardware is made redundant.

We conclude that, where high performance is of interest, a hybrid design can have some inherent advantages in terms of signal quality and timing precision.

Safety and energy consumption Using LEDs and SiPDs for the NIR light emission and detection, we were able to minimize size, power consumption, and supply voltages, thereby also decreasing safety concerns compared to laser- and avalanche photodiode (APDs) designs. The M3BA unit is supplied with a single $3.7\,V$ Li-Ion Cell that can be recharged onboard via USB. The battery cell capacity C_{batt} can be adapted to the required runtime ($t_{run} \approx \frac{C_{batt}}{100\,mAh} h$).

The time division multiplexing of fNIRS channels presents a drawback in terms of sampling rate in the simultaneous use of multiple interconnected modules. Each additional module divides it in half. Simultaneous illumination with sine-modulated light at different frequencies can alleviate this and could be implemented using the microcontroller's internal DACs. However, this comes at the cost of comparatively higher power consumption.

Wireless limitations When two or more users, wearing multiple M3BA modules in a WBSN scenario, meet at close distances, the interference from several Bluetooth-transmitters is likely to lead to a loss of data packages that cannot be buffered. There are currently no optimal solutions regarding wireless infrastructure. However, other transmission standards like ZigBee (IEEE 802.15.4) and WBAN (IEEE 802.15.6) or even entirely new (5G) standards could be taken into consideration for replacement.

Application and headset The instrument allows headgear and sensors to be tailored to application- and scenario-specific requirements in order to provide mechanical stability and high signal quality. Examples for such unobtrusive wearable sensor solutions are in-ear or around-the-ear EEG [LPK+11; DEDV+15]. The M3BA architecture provides the necessary flexibility for integration and customization and the high AFE input impedance ($1\,T\Omega$) and Common Mode Rejection Ratio ($-110\,dB$) allow the use of both wet or dry electrodes. Aside from typical procedures for applying fNIRS on haired regions (e.g., brushing aside hair under the optodes), the M3BA modules can be integrated into the openNIRS spring-loaded mechanical headgear concept. In the next Section, we will make use of the M3BA flexibility by integrating two modules into a custom-tailored headset as a prerequisite for the work in Chapter 4.

The implemented software makes use of the AFE's current source/sink peripherals and enables stand-alone AC Lead-Off detection and online electrode impedance measurements for electrode preparation and monitoring of signal quality.

The presented M3BA architecture enables a wide range of new approaches in the fields of multimodal wearable monitoring, diagnostics, BCI, and brain research.

3.7 Hybrid Headgear

3.7.1 State of the Art and Aims

In previous hybrid EEG-fNIRS studies with tabletop instruments or backpacks, electrodes and optodes are typically placed on conventional EEG caps. Cables and weight of equipment can hinder free movement and increase the risk of electrode and optode shifts.

The Aim...

...is the development of customizable, fully integrated multipurpose headgear for the application of M3BA. It should be comfortable, optimized for unconstrained movement and lightweight to minimize shifts, allow robust fixation and adaptability to individual head circumference, and 10-20 system compatibility. The primary implementation of a custom-tailored headset aims at the subsequent application in a cognitive workload experiment in Chapter 4.

3.7.2 M3BA Hybrid Headgear

Exploiting the modularity of the M3BA architecture, a multipurpose two-stage hybrid headset was developed using rapid prototyping. It integrates two modules and one rechargeable LiPo battery (up to $10\,h$ continuous acquisition), yielding 12 EEG/EMG/ECG channels, 10 fNIRS and channels and two 3D accelerometers (see Figure 3.25).

The first stage is designed for compatibility with both conventional EEG 10-20 caps and customized headset solutions. One module is placed on each side of the head above the ears, and a battery pack between the inion and upper neck. Units are connected with a flexible elastic band which is adjustable to individual head circumferences at the module cases (Figure 3.25 **A**). All electrode and optode solutions from Section 3.2.2.6 and [vSM+17] are supported. When worn on top of a cap (Figure 3.25 **B**), standardized electrode/optode positions are available, but the ease of use is decreased.

Headsets can be advantageous. However, they have to be custom-tailored to the applications/experiments, as channel selection naturally determines the availability of signals. For the application in a mobile cognitive workload scenario in Chapter 4, a second stage custom-tailored headset was designed (Figure 3.25 **C**). Its total weight of $150\,g$ is distributed across the whole head and electrode and optode cable length is minimized, reducing both shifts and noise pickup. In this layout, channels were placed to enable acquisition of frontal/parietal alpha/theta EEG power, frontal metabolism, frontal asymmetries (in both EEG spectrum and fNIRS oxygenation signals), Error Potentials and Event-Related Potentials based on a minimum count of channels. Motivation and details on the channel selection and placement are provided in Section 4.3.2. The optodes were designed for easy and robust application in a frontal patch and direct application to the skin without the need of optical fiber guides. The headset can easily be adjusted to most common head circumferences between $54-58\,cm$ by the means of a mechanical regulation screw at the back of the head and elastic band that is also adjustable at all connecting links. For EEG electrodes, standard easy-cap ring electrode holders were integrated at target 10-20 positions.

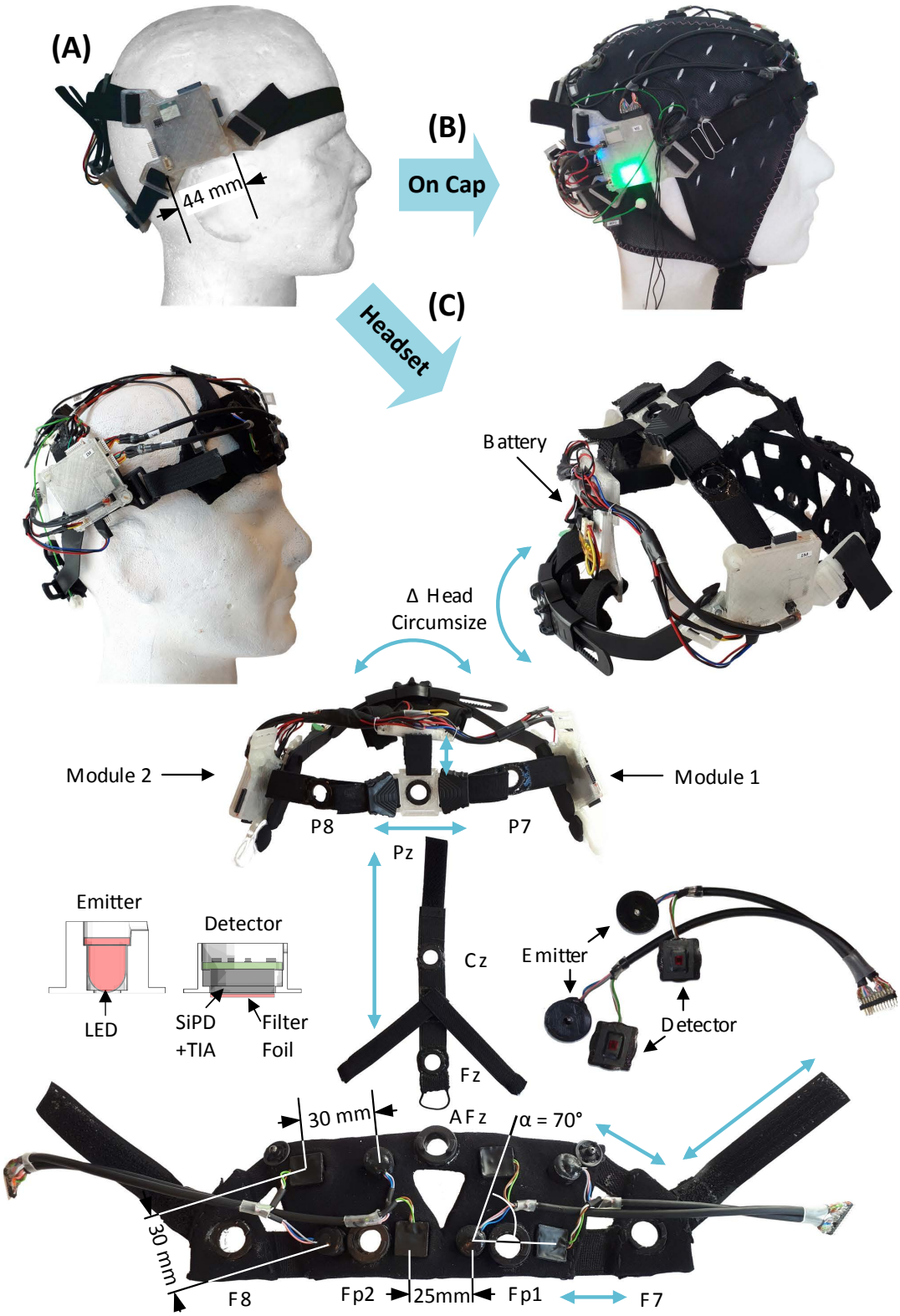

Figure 3.25: M3BA hybrid headgear. Blue arrows indicate adjustable/flexible connections. (**A**) multipurpose M3BA headgear, applied on (**B**) a standard 10-20 cap and (**C**) integrated into a custom-tailored headset for applications in Neuroergonomics.

3.8 Framework for Communication and User Interface

The software framework for communication and control of the M3BA and openNIRS instruments was designed for the support of:

1. Flexible device interfacing, independent of software, programming environment, host-unit (PC, smartphones,...) or operating system employed by the user.
2. Low-level development, customization and debugging of the instrumentation as well as efficient data transmission in normal running scenarios.
3. High stand-alone functionality of the instruments.
4. Adaptation and evolution across instrument generations.

For this purpose, Bluetooth with Serial Port Profile (SPP) was selected as the wireless interface between M3BA/openNIRS and a host for control and data logging. This way, the instruments can be installed and accessed without a driver and by any operating system that supports Bluetooth SPP via a virtual Com Port. Instruments are controlled and configured via simple ASCII commands (e.g., "*S*" for *S*tart, "*CECG6*" for *C*onfigure *E*EG *C*hannel *G*ain = 6), allowing intuitive control both manually (e.g., via a hyper terminal) or via more elaborate scripts or graphical user interfaces. Data packets from the instruments have a variable length indicated by the packet-header, identifying different modalities and allowing an adaptation to the required/limited bandwidth available on the Bluetooth-channel. Figure 3.26 depicts the implemented software framework and functional units. For use on a computer, a Graphical User Interface (GUI) was developed in LabView. Based on an event-controlled queued state machine (QSM) architecture, it supports device configuration, data logging, online visualization, filtering and mBLL-conversion, hardware and software trigger management and unit testing/debugging. Figure A.5 in Appendix A.3 shows an example.

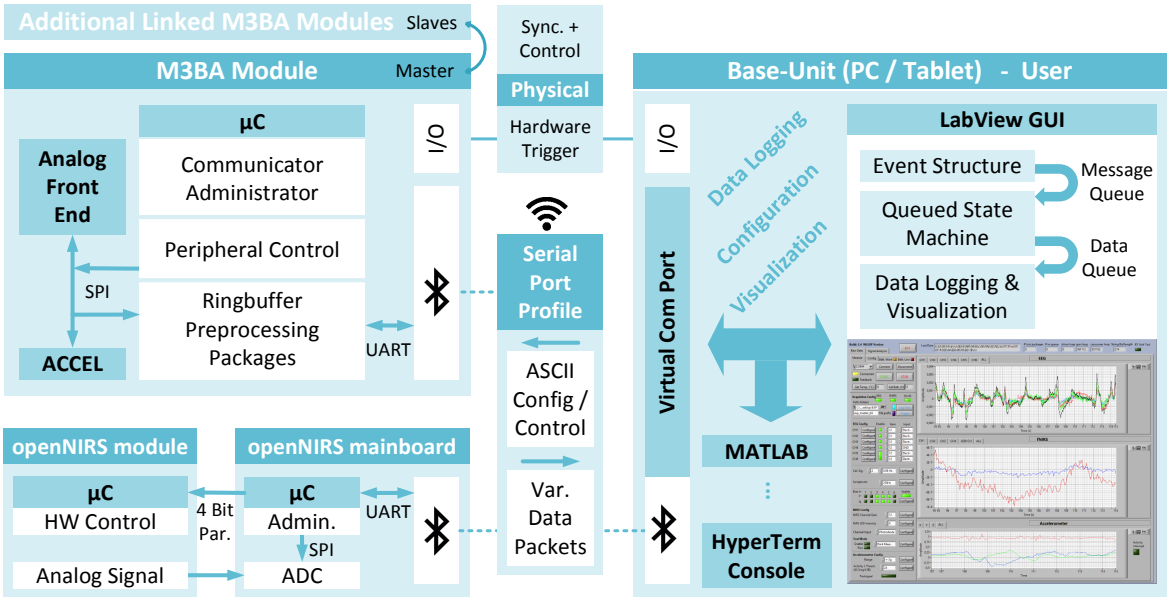

Figure 3.26: Interface and communication framework of openNIRS and M3BA utilizing Bluetooth SPP for platform- and software front-end -independent control and communication.

3.9 Summary

Advances in hybrid multimodal signal acquisition and processing technology are invaluable for real-life-oriented research and applications in the fields of neurotechnology. Currently, there are no hybrid devices commonly available that combine bio-electrical and bio-optical neurophysiological measurements such as EEG and fNIRS. We identified basic principles and requirements for the design of high precision EEG-fNIRS instrumentation for mobile application-oriented scenarios. With these as a guideline, the objective in this Section was the two-step design of such an instrument. Objectives considered were high performance, miniaturization, customization, scalability, wireless communication, usability, safety, and low power consumption.

As a first step, the openNIRS was introduced. It is an architecture for wearable modular fiberless fNIRS, providing open source core functionality to facilitate the development of novel customized fNIRS instrumentation approaches in neurotechnology research. In the second step, M3BA, a Mobile, Modular, Multimodal Biosignal Acquisition architecture, was developed and evaluated. It is based on a high-performance analog front-end optimized for bio-potential acquisition, a powerful microcontroller, and exploits functional units and concepts from the openNIRS. The designed M3BA devices are configurable high precision and low-noise modules (EEG input referred noise @ $500\,SPS$ $1.39\,\mu V_{pp}$, fNIRS noise equivalent power $NEP_{750nm} = 5.92\,pW_{pp}$, $NEP_{850nm} = 4.77\,pW_{pp}$) with full input linearity, phase sensitive detection of optical signals, Bluetooth, 3D accelerometer and low-power consumption. They support flexible, user-specified bio-potential reference setups, and Wireless Body Sensor Network (WBSN) scenarios and are further miniaturized ($10\,cm^3$) beyond previous approaches. The microcontroller enables flexible integration of additional routines. Thus, EEG impedance measurements, filtering, and new approaches such as decentralized on-line feature extraction and adaption become possible on-chip.
Performance characterization and in-vivo experiments confirmed functionality and quality of the designed architecture. It was also shown that, where high performance is of interest, a dedicated hybrid design can have some inherent advantages over separate instruments in terms of signal quality (reduced intermodality crosstalk) and timing precision (reduced jitters).

We provide both architectural details and performance characteristics of M3BA and openNIRS. This way, this work aims to significantly facilitate future designs in those fields of neurotechnology research that rely on or potentially profit from customizable mobile hybrid biosignal acquisition instruments. The design principles put forward in this Section are also applicable to other research areas than that of BCIs or Neuroergonomics, for instance to physiological monitoring approaches in telemedicine.

Chapter 4

Multimodal Neuroimaging in Moving Subjects: A Workload Experiment

4.1 State of the Art and Aims

While a multitude of new hybrid fNIRS-EEG application scenarios in more natural everyday-environments is on the horizon, experiments and datasets are still lacking. An increasing number of studies are using simultaneously acquired EEG-fNIRS signals [AJ17; CRL+17], and open access EEG-fNIRS datasets have been published that include n-back, discrimination/selection response, word generation, motor imagery and mental arithmetic tasks [SvK+18; SvB+17]. However, these studies are almost exclusively done with combined tabletop devices and focus on seated participants that move as little as possible. As fNIRS-EEG in motion is a nascent domain, there are no suitable datasets available yet that provide both evoked neuronal responses and well-controlled movement conditions, and certainly not other modalities. In particular in areas where neurotechnology is to be applied under realistic, life-like conditions, the generation of such experimental datasets is desirable and often prerequisite for the development and evaluation of novel methods. One use case is, for instance, operator workload monitoring as part of Neuroergonomics.

Aims

The aim of the work presented in this Chapter, based on publication [vMB+18], is the generation of such a dataset to infer cognitive workload from freely moving operators. To this end, a novel experimental paradigm is designed that aims to evoke working-memory related neurophysiological changes with only minimal explicit behavioral constraints under quasi-realistic circumstances, while at the same time implicitly enforcing a high control of experimental conditions. The multimodal data was acquired with the newly developed and custom-tailored M3BA headset. Its design for the acquisition of selected target signals/features in a tradeoff with low channel numbers will be motivated. The dataset thus obtained paves the way for novel analysis and artifact rejection approaches, and for a feasibility study of multimodal workload classification under challenging, realistic conditions, both discussed in Chapter 5.

4.2 Mental Workload and Neuroergonomics

Progressing beyond conventional applications for communication and control in clinical and rehabilitation contexts, more comprehensive Brain-Computer Interfaces aim to aid users in everyday-environments by adaptation and enhancement of human-machine interaction. These systems use physiological markers to assess mental or emotional states, including vigilance, attention and mental workload and aim to create supportive environments in which feedback or task demands are optimally adapted to the mental state of an operator. Mitigating the consequences of excessive workload or allowing for strategy changes [Spe78], they can increase safety, performance, effectiveness or motivation [PW08; PFS+00; SW95; Wil82].

Cognitive or mental workload (MWL), although having an intuitive appeal, is a concept in ergonomics [YBW+15] that is comparatively hard to define. One approach is to define it as the portion of a human operator's limited mental capacity to process and respond to information required to perform a particular task [BKT94]. Empirical approaches for the assessment of workload make use of (1) subjective, (2) performance-based and/or (3) physiological measures. While systemic body signals provide physiological markers such as heart rate, skin conductance, respiration and ocular and pupillary movements, more recent approaches make use of neurophysiology. Such "Neuroergonomic" approaches [Par03; PW08; Par11] use markers in brain activity to assess covert mental states, such as mental workload, independently of the reported subjective or measured overt performance of a human operator. These systems aim to predict sudden performance declines that follow sustained periods of excessive or too low task demands, for instance, to prevent catastrophic losses in safety-critical working environments such as air traffic control [ASB+12].

In experiments, task demands have to be evoked in a controlled and reproducible way. A widely used family of paradigms in cognitive neuroscience research is based on the n-back protocol [OML+05] which demands sustained attention to a train of stimuli. It provides varying task-load conditions to test associations between levels of difficulty and cortical activation due to working memory modulation. It has been validated by major neuroimaging modalities such as fMRI and PET and has been successfully applied to evoke and discriminate different workload stages in both EEG [BHVE+12] and fNIRS [HHF+14; UIS+15]

4.3 A Workload Experiment in Freely Moving Subjects

4.3.1 Study Design and Protocol: A New Spatial N-back Paradigm

To evoke task-load under well-controlled conditions but without explicit movement constraints, the following modified spatial n-back paradigm was developed. The experiment was implemented with custom multiplexing hardware for LED illumination and registration of button-presses, interfaced and controlled with a NI DAQmx USB6003 device and a LabView routine (*National Instruments*, USA) embedded into the main M3BA GUI. The overall set-up and protocol are depicted in Figure 4.1 to elucidate the following explanations.

A freely moving subject stands in front of a wall with 8 tiles equidistantly placed every 45° on a circle with an individually adjusted radius R. It is defined by the subject's height h with $R = 0.45 \times h$, which also approximates half of the span of outspread human arms. The center is located at the participant's solar plexus. Here, a screen shows instructions and visual cues. The tiles are sized $10 \times 10\,cm^2$ and are illuminated in 8 different RGB states (red, magenta, blue, light blue, green, yellow, white, OFF). Pressing a tile activates a push button.

In each of the 12 experimental blocks with a respective duration of $10\,min$, the participant performs a sequence of 7 rounds based on a modified spatial n-back task, alternating $n = 0$ with a pseudo-randomized order of $n = 1,2,3$. Each block starts with a resting period of $30\,s$. At the beginning of each round, an instruction cue is shown on the screen for $6\,s$. In this time, a pseudo-randomized *target color* (all RGB states except OFF), the constant default color OFF and the n-back instructions are displayed. 0-back rounds consist of 6 trials; 1,2,3-back rounds consist of 18 trials, each with constant duration of $6\,s$. At the beginning of each trial, the color configuration is instantaneously and pseudo-randomly reconfigured; each tile has a unique color. The participant has to decide for, and press one of the eight tiles within each

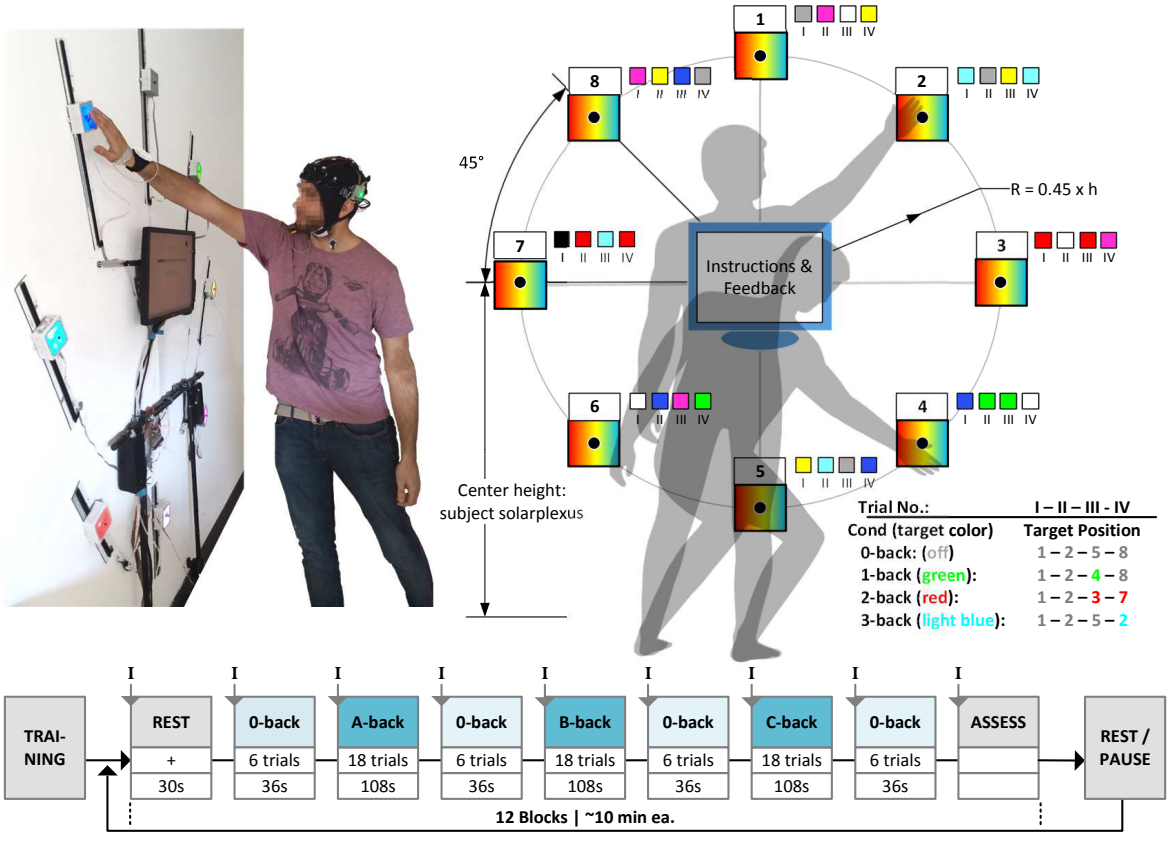

Figure 4.1: Spatial n-back based cognitive workload paradigm with freely moving subjects. A,B,C: placeholders for pseudo-randomized sequence of $1,2,3-$*back* task. Small colored squares next to tiles mark example configuration, roman letters mark number of the first four trials within an example round. "Target Position" given in the table marks the correctly selected position in each exemplary n-back task. "I" marks the display of a $6\,s$ instruction period before a new round.

trial and selection speed is not rewarded. For motivation, correct selections add points to a block-wise score, erroneous/ or no selections within the trial period lead to a small penalty. The target color and n-back level define the task to solve in each trial to follow in the same round. See also Figure 4.1 for examples:

- In 0-back, the target and default colors are both OFF. In each trial, the subject finds and selects the only tile that is not illuminated. There are $n = 0$ positions to memorize. This serves as a baseline task.

- In $n = 1,2,3-$back, a tile is to be selected whenever the target color reappears in $n+1$ subsequent trials on the same spatial location. If this condition is not met within a trial, the tile with the default color OFF has to be pressed. In each trial, the participant has to remember and mentally update the target color position of $n = 1,2,3$ preceding trials.

Only 25 % of $n = 1,2,3-$back trials within each round fulfill the target condition. Participants were instructed to use only their dominant hand for all button presses. For motivation, each correct hit adds points to a block-wise score; higher n-back conditions give more points. A wrong or no button press within a trial counts as an error, leading to a small point penalty which is constant across conditions. Speakers provide simple auditory cues for rewards, penalties and the begin and end of each trial.

At the end of each block, the participants were asked to assess their overall experienced *demand*, *concentration*, and *stress* on a 5 level Likert item using a number pad (5: strong agreement, 3: neutral, 1: strong disagreement). Afterward, there was a $3\,min$ pause, and after every 4^{th} block a break of arbitrary length chosen by the participant.

While the task difficulty is modulated by the number of positions that have to be remembered for correct selection, all other experimental conditions in each trial remain constant regardless of the task and individual performance. This includes constant trial duration, color and spatial randomization and one performed selection in each trial. The individualized tile distances lead to constant movement conditions and well defined terminating postures across all participants and enforce stepping forward/backward for full vision and access to the field. While the trial length of $6\,s$ leads to a shared frequency band between artifacts and hemodynamic responses in fNIRS, the overall block lengths also enable analysis of slower fNIRS signal changes.

During the whole experiment, EEG, fNIRS, Electrodermal Skin Activity (EDA), combined EMG - ECG at the neck, and head and hand accelerations were recorded. Furthermore, all data streams were continuously labeled with $2\,ms$ precision, including the following events: Start, end, error or time up of a trial, begin and end of a round or block, tile color configuration, target colors, n-back conditions and target positions, times of button presses and breaks. In the following, we will elaborate on the target features in the signals acquired and thus motivate the channel selection and placement in the custom-tailored headset designed for this purpose in Section 3.7.

4.3.2 Signal Acquisition, Channel Placement and Target Features

A variety of features in the acquired modalities can give insight into the cognitive state and workload of a participant. In a headset for mobile application and limited preparation time for higher usability, only a limited number of channels is available. The headset designed for this experiment (Figure 3.25 **C**) was configured for the simultaneous acquisition of 9 fNIRS, 9 EEG, 2 EMG/ECG and two 3D Accelerometer channels, employing two M3BA modules. Careful channel placement, considering the current understanding of task-related brain physiology, is crucial to allow the exploitation of valuable information in the single and combined modalities. The setup is summarized in Figure 4.2 and motivated in the following.

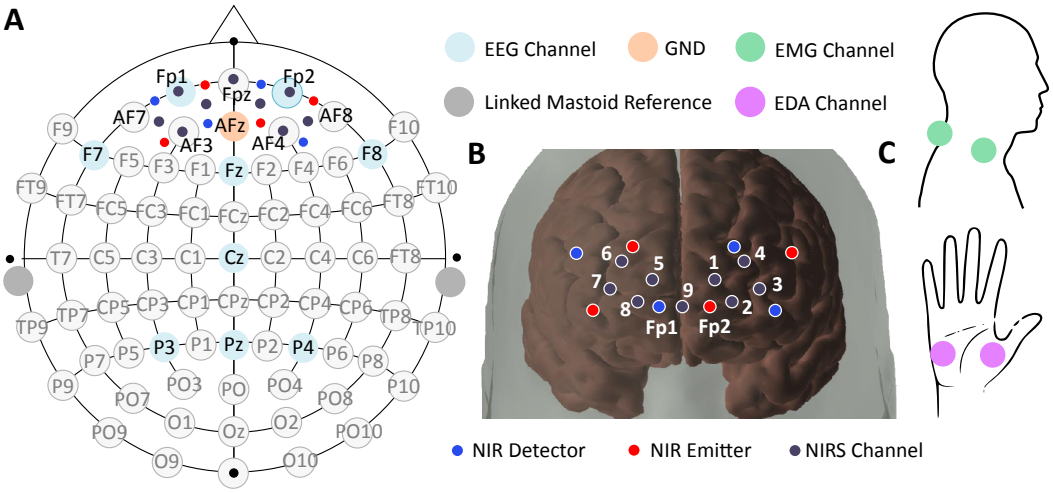

Figure 4.2: Channel Placement: (**A**) EEG and fNIRS channels and optodes, (**B**) Positions of fNIRS emitters/detectors on scalp and resulting channel positions on the cortex projected with HomER Atlas Viewer [HDF+09], (**C**) ECG/EMG and EDA channels.

In **EEG**, a variety of cognitive phenomena such as attention, memory encoding, vigilance, and fatigue, have been shown to correlate with modulations of band power in particular frequency bands [BD04; DHK+03; KÅ93; MTD+08]. Especially in the investigation of vigilance and cognitive workload, modulations of theta $(4-7\,Hz)$- and alpha $(8-13\,Hz)$-band power in frontal and parietal regions have been found to be discriminative, where frontal theta power usually is positively correlated, and parietal alpha power is negatively correlated with increasing workload [GS03; HLK+09]. Studies have also exploited information from the other frequency bands and event-related potentials (ERPs) [BHVE+12; PIFS+03; CEW+12]. ERPs and Error Related Potentials (ErrPs), measurable with few channels distributed over frontocentral-parietal regions, have furthermore successfully been used in single trial analysis and classification [MTD+08; BLT+11] also allowing for response-verification and -correction [BSD+02]. Under these considerations, wet passive AgCL electrodes (abrasive gel) were placed at frontocentral and parietal EEG-10-20 positions Fp1, Fp2, F7, F8, Fz, Cz, Pc, P3, P4 measured against linked mastoids and with an active reference potential at AFz. EEG was sampled at a rate of $250\,Hz$.

Varying task-load conditions have been shown to modulate activation in the dorsolateral (DLPFC) and ventrolateral prefrontal cortex (VLPFC) in PET and fMRI studies [OML+05;

SJK96; dAZ+98] and fNIRS [AOI+13; PBW+10; SES+08]. In **fNIRS**, frontal oxygen-dependent metabolism measured over prefrontal regions has been successfully used for the assessment of expertise development [AOI+13] and classification of cognitive workload [ASB+12; HHF+14; LAS17]. The fNIRS optodes used in this study were therefore placed on the forehead with a source-detector separation (SDS) of $30\,mm$ and with the frontmost optode pair registered to the EEG 10-20 positions $Fp1/Fp2$, resulting in 9 channels over left and right superior-, medial- and medial-orbital -frontal regions, see Figure 4.2 **B**. Signals were sampled at a rate of $8.33\,Hz$.

The frontal placement of EEG and fNIRS channels potentially also enables assessment of frontal asymmetries that have been shown to be related to affective processing, approach/withdrawal-related tendencies and motivation [PSH+05; Dav04; CA04; DLC04].

For the combined acquisition of **neck-EMG and ECG**, two sticky electrodes were placed on the left and right sternocleidomastoid muscle, with reference on vertebra C7, and sampled at $250\,Hz$. The two integrated 3D accelerometers from both M3BA modules fixated over the left and right ear, were configured for a $12\,Bit$ resolution of $\pm 2g$, sampled at $50\,Hz$. Electro Dermal Activity (EDA) provides tonic and phasic information that has been widely used as an indicator of emotional stress [Bou12]. EDA was measured with sticky electrodes placed on thenar and hypothenar muscles of the dominant hand with a mobile one-channel EDAmove device (*Movisens GmbH*, Germany), including 3D accelerometer, fixated to the wrist. EDA was sampled at $32\,Hz$, the accelerometer sampled at $50\,Hz$.

This selection of modalities and channels also allows the extraction of additional systemic body signals and their exploitation for workload assessment or artifact rejection. Among them are overall movement artifacts, especially EOG and EMG in EEG and blood pooling/indirect movement artifacts in fNIRS, that will be addressed in Section 5.2. The rate of eye blinking and movements have been successfully used as vigilance indicator, for instance in real time driver vigilance monitoring [BNS+06]. Other systemic signals are breathing and heart rate-related modulations of fNIRS and EEG components. Additionally, the dataset incorporates behavioral data from head and hand movements, EMG, reaction times, and error rates. Figure 4.3 summarizes the features available and modality interconnections in the signals.

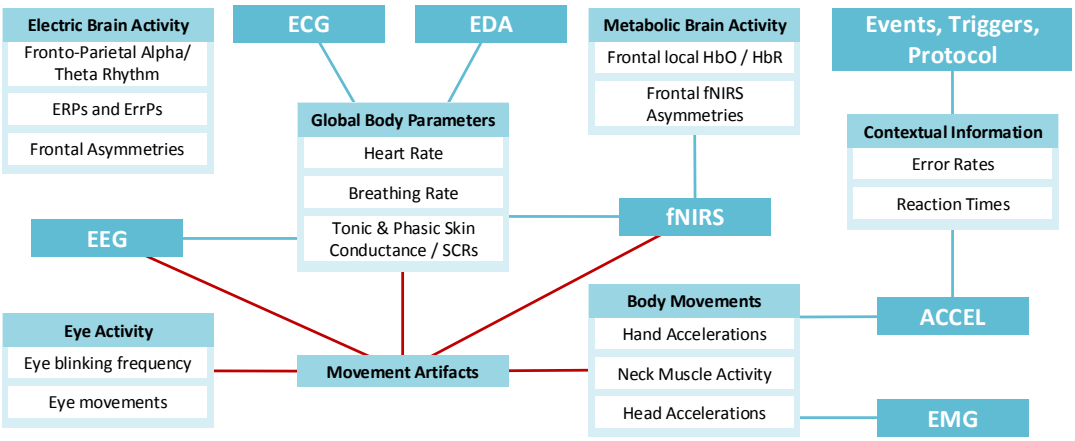

Figure 4.3: Acquired modalities and features in the dataset for analysis and workload assessment.

4.3.3 A Brief Overview of the Dataset and Behavioral Results

The experiment was performed with 17+11 participants (16 female, 27 right-handed), with age $28.1 \pm 5.8\,y$ and height $172 \pm 9.4\,cm$ (mean±std). 11 participants took part in a preliminary study with a slightly different protocol with fewer but longer blocks, but otherwise same paradigm and randomization. The experiment was conducted in accordance with the declaration of Helsinki and approved by the Ethics Committee of Berlin Institute of Technology (approval number: LUE_01_20161117). All participants had normal or corrected to normal vision, and none reported color-blindness or neurological, psychiatric, or other brain-related diseases. All participants were informed about the experimental procedure, anonymized data evaluation, and distribution, and gave written consent prior to the experiment.

The dataset of each participant in the main study contains $120\,min$ continuously recorded multimodal data, with approximately 930 movements and subsequent button-presses performed at the predefined positions. Figure 4.4 shows an excerpt of the unprocessed multimodal signals and exemplifies shared information across modalities, for instance between EMG and EEG or Acceleration and fNIRS. Figure 4.5 provides a brief overview of average behavioral data across participants.

Typical behavioral data of a single participant and experimental sequences ($n = 1,2,3-$ back rounds, target colors and button press events) is provided in Figure C.2 in Appendix C.2. Within and across subjects, no dependency was observed between specific target colors or positions and frequency of correct, wrong or no (time up) button presses.

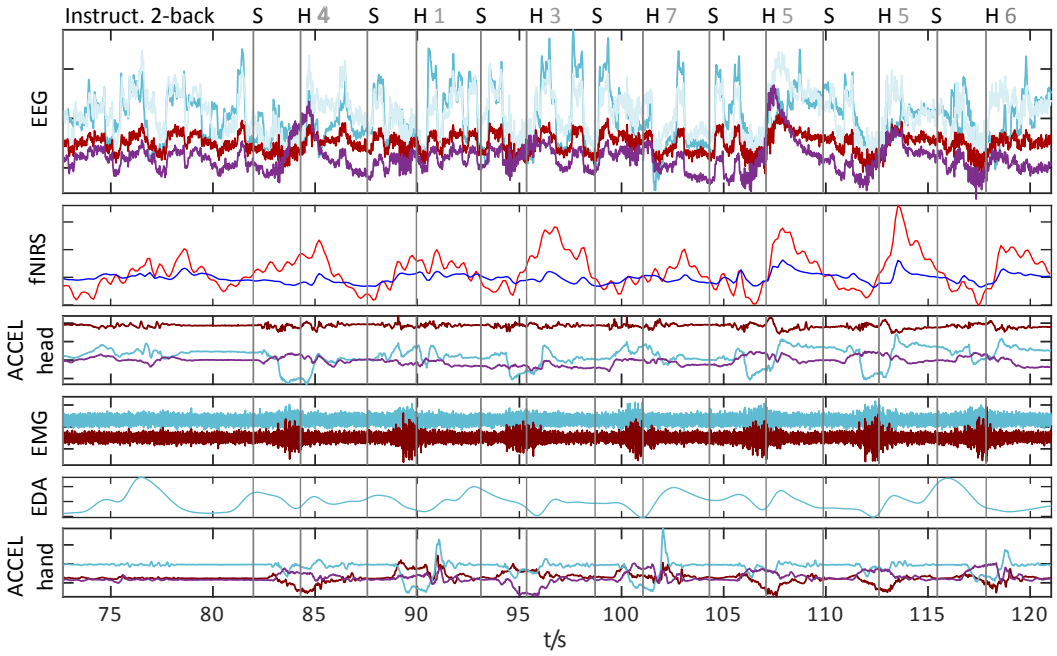

Figure 4.4: Qualitative example of raw data (excerpt of channels) from the acquired dataset. Annotated events: S - Start of a trial, H X - Hit of a button at position X, see Fiure 4.1 for position reference.

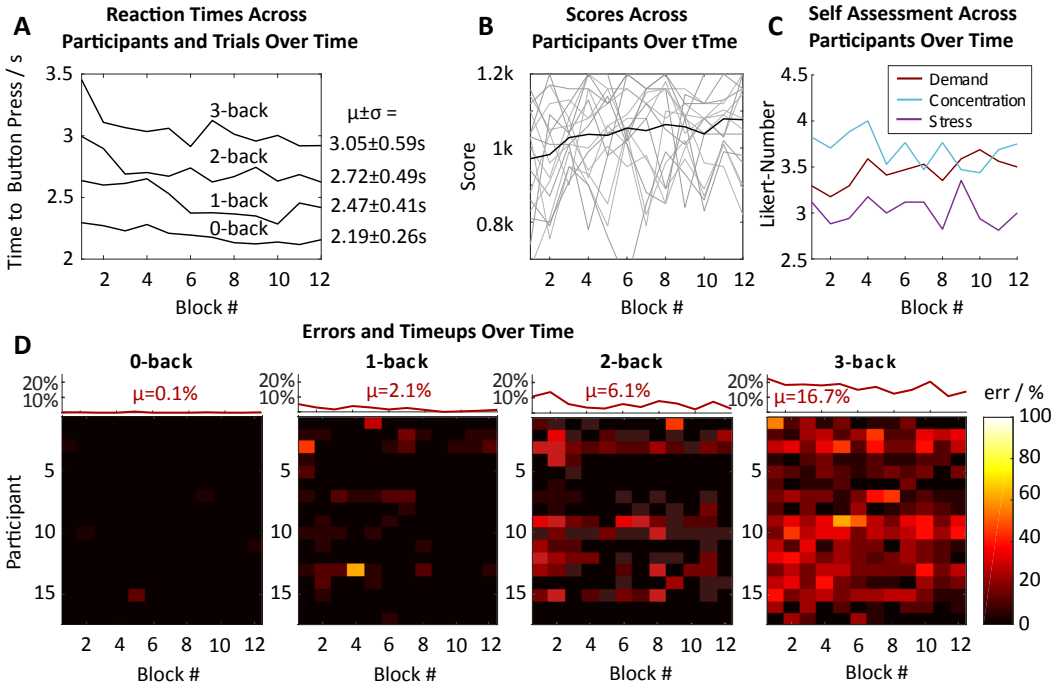

Figure 4.5: Selection of behavioral results: (**A**) reaction times from start of trial to button press. (**B**) Development of block-wise scores across participants. (**C**) average self assessment scores after each block across participants. 5: Full agreement, 1: full disagreement to statements "the experiment was demanding", "I was concentrated", and "I felt stressed". (**D**) Total number of errors in each round for each participant. μ (upper plot) is average across participants.

4.4 Observations and Discussion

The overall length of the experiment was on average 3 hours including briefing and training, and the total set up time rarely exceeded 25 minutes. As adjusting and putting on the headset is a matter of less than a minute, this was mainly due to attachment of peripherals, electrodes, and application of gel. The latter can be made redundant when water-based electrodes (Section 3.2.2.6 and [vM17]) are being used. In the main study, these electrodes were not employed to limit uncertainties due to the number of non-conventional self-designed elements in the acquisition chain. Participants welcomed the fast set-up time and comfort of the headset and the freedom to move during the experiment.

While experimental conditions remain the same across participants, the level of induced cognitive workload and performance is dependent on many subjective factors that can significantly vary between participants. Among them are motivation, wakefulness and attention and individual memory performance. It was attempted to decrease biases by (1) using colors and spatial positions instead of numbers and letters, (2) performing experiments only at 10:00 am and 03:00 pm to limit effects of postprandial somnolence, and (3) including subjective self-assessment at the end of each block to mirror trends across the 2.5 *h* experiment.

The participant's self-assessments show on average a neutral response to the statement "*I was Stressed*", a moderate bias towards agreement with the statement "*the experiment was*

Demanding" and a stronger bias towards agreement with the statement "*I was Concentrated*" (Figure 4.5 **C**), with no statistically significant changes in any of the three assessed variables over the time-course of the experiment (1-way repeated measures ANOVAs, $F_S = 0.61$, $p_S = 0.82$, $F_D = 1.44$, $p_D = 0.16$, $F_C = 1.13$, $p_C = 0.34$). A more frequent subjective assessment (e.g., after each n-back round) would be desirable but comes at the cost of an increased length of the experiment, and a decreased level of immersion due to the high number of enforced interruptions.

Investigation of the behavioral data confirmed subjective reports and observations: The average (re-)action times and the number of errors scaled with increasing task-difficulty (Figure 4.5 **A,D**), and are very similar to those in other fNIRS n-back studies [ASB+12; AGO17]. Grand average 3-back reaction times $< 3.5\,s$ indicate that errors are not due to insufficient trial length ($6\,s$). Slow decreases of average reaction times and errors and a corresponding increase in scores (Figure 4.5 **B**) reveal minor training effects over the full length of the experiment but remain highly distinguishable between different n-back conditions. Observation of movement behavior confirmed the success of the geometrical experiment design: Without exception, participants stepped back for a full field of vision before moving to execute a button press at predefined positions within each trial.

Visual inspection of the acquired raw multimodal data (as in Figure 4.4) reveals, amongst others, expected strong EOG artifacts in EEG, and slow position-dependent movement artifacts in fNIRS that comodulate with acquired head movement signals. The next Chapter on multimodal analysis will focus on the application and exploitation of this dataset.

Summary

A novel n-back based cognitive workload paradigm was developed that integrates and enforces free movements to and from individually adjusted, predefined positions. The corresponding study was conducted employing a custom-tailored M3BA headset for the multimodal acquisition of $120\,min$ continuous EEG, fNIRS, EMG/ECG, EDA and acceleration data in 17 participants. Behavioral data indicates a successful design and appropriate difficulties. We will make use of this novel multimodal dataset in the following.

Chapter 5

Multimodal Analysis

We begin this Chapter with the introduction of the General Linear Model (GLM) and a selection of GLM-based state-of-the-art analysis techniques. These form the basis for the subsequent analysis and method development based on the new experimental dataset. Section 5.2 discusses the main contribution of this chapter, a novel multi-modal, Blind-Source Separation-based Analysis and motion Artifact Rejection/Detection framework in fNIRS entitled "BLISSA^{2}RD", which is based on publication [vBM+18]. Last but not least, in Section 5.3, based on publication [vMB+18], all contributions of this thesis will be linked in an attempt to classify multimodal cognitive workload in moving participants.

5.1 State-of-the-Art Analysis Techniques

In the multimodal analysis and classification of data, the modalities can be fused at different levels for the extraction of components, features or a calculation of a classification output. In the following, we denote fusion at the signal level as *sensor fusion*, at the feature level as *early fusion* and at the decision level (after individual classification) as *late fusion*. The majority of methods introduced hereafter are unimodal methods that will be combined on a sensor fusion level in BLISSA^{2}RD and in an early fusion approach in the classification of workload. An increasing number of novel methods has been developed that relate and extract information at the *sensor fusion* level, such as group ICA methods [CLA09], temporal kernel Cross-Correlation Analysis (tkCCA) [BMG+09] and multimodal Source Power Correlation (mSPoC) [DBS+15; DBM+13]). In the following, to not exceed the scope of this thesis, we restrict ourselves to the introduction of models and methods that will be employed in the subsequent analysis and comment on the others only briefly for the sake of delimitation.

5.1.1 The General Linear Model

A commonly used abstract mathematical model for the generation of macroscopic neuroimaging data such as EEG, MEG, fMRI, and fNIRS is representing the measured data as a linear mixture of functionally distinct processes [JTF97; CAM+01; PSG+05; YTJ+09]. These *generative* or *forward models* factorize measurement data into latent factors with a

temporal signature and their corresponding spatial activation patterns.

In the following, we will denote observed data samples of modality 1 at time point t and channel n with scalars $x_n(t)$ and those of modality 2 respectively with $z_n(t)$. While x and z can be assigned to any modality, e.g., fNIRS and EEG, x is used for raw fNIRS data samples and z for acceleration data in the following to prepare for Section 5.2, where we will continue with this assignment. As the notation is congruent for all signals x and z, we will continue it exemplary on x only. We denote the observation matrix with data from all time points T_x and recorded channels N_x as $\boldsymbol{X} \in \Re^{N_x \times T_x}$, its row vectors as $\boldsymbol{x}_n \in \Re^{T_x}$ and its column vectors as $\boldsymbol{x}(t) \in \Re^{N_x}$. The former are the observed time series at constant channel n and the latter the signal at fixed time point t for all channels. In raw fNIRS intensity signals, $N_x = C_x \cdot \Lambda_x$ consists of the number of optode pairs C_x and the number of recorded wavelengths Λ_x. Usually, the modalities differ both in the number of channels and sampling rate $N_x \neq N_z$ and $T_x \neq T_z$. We assume the presence of $K_x \geq 1$ latent factors and denote these by $\mathbf{s}_n \in \Re^{T_x}$ and in analogy to above for all time points and factors by $\boldsymbol{S}_x \in \Re^{K_x \times T_x}$.

Then, the noiseless *linear forward model*, which maps latent components (sources) to observed recordings (mixtures) can be expressed by

$$\boldsymbol{X} = \boldsymbol{A}_x \boldsymbol{S}_x. \tag{5.1}$$

Here, $\boldsymbol{A}_x \in \Re^{N_x \times K_x}$ is the mapping matrix, with each column containing the spatial activation patterns for corresponding components. In general, the linear forward model can additionally contain the noise term $\boldsymbol{\epsilon}_x \in \Re^{K_x}$ capturing activity that is not explained by the K_x components. In the BLISSA^{2}RD approach, we consider the noiseless model. Here, the effect of noise can be mitigated through order selection in overdetermined cases [LAC07; FAA14] or another stage of decomposition. Usually, it is of interest to estimate the spatial activation patterns and time courses to recover the components from the data. Since estimating both $\boldsymbol{A}$ and $\boldsymbol{S}$ jointly can lead to difficult optimization problems and high computational complexity, a *backward model* approach is commonly applied. The latent sources $\hat{\boldsymbol{S}}_x$ are estimated by multiplying the observed data with a set of spatial *extraction filters* $\boldsymbol{W} \in \Re^{N_x \times K_x}$. As before, we use $\hat{\boldsymbol{s}}_n \in \Re^{T_x}$ for the n-th source estimate. The *discriminative* or *backward model* is then expressed by

$$\boldsymbol{W}_x \boldsymbol{X} = \hat{\boldsymbol{S}}_x. \tag{5.2}$$

$T_{x/z}$	Number of data points in modality x/z
$N_{x/z}$	Number of channels in modality x/z
Λ_x	Number of wavelengths per optode C_x in modality x
$K_{x/z}$	Number of latent factors (sources / components)
$\boldsymbol{x}_n / \boldsymbol{x}(t)$	T_x/N_x-dimensional row/column vector of observed data in modality x, here NIRS
$\boldsymbol{z}_n / \boldsymbol{z}(t)$	T_z/N_z-dimensional row/column vector of observed data in modality z, here Accelerometer
$\boldsymbol{X}, \boldsymbol{Z}$	$N_{x/z} \times T_{x/z}$ matrix containing the observed data in modality x/z
$s_{x/z}(t), \hat{s}_{x/z}(t)$	$K_{x/z}$-dimensional vector of (estimated) latent factors of modality x/z
$\boldsymbol{S}_{x/z}, \hat{\boldsymbol{S}}_{x/z}$	$K_{x/z} \times T_{x/z}$ matrix containing all (estimated) latent factors of modality x/z
$\boldsymbol{A}_{x/z}$	$N_{x/z} \times K_{x/z}$ matrix of sensor-space patterns in forward models
$\boldsymbol{W}_{x/z}$	$N_{x/z} \times K_{x/z}$ matrix of spatial extraction filters in backward models

Table 5.1: GLM Notation.

Table 5.1 summarizes the notation used in this Chapter. More details on the interpretation of linear models in multivariate neuroimaging are provided, e.g., in [HMG+14]. Since without additional constraints the factorization of $\boldsymbol{A}$ and $\boldsymbol{S}$ is not unique, further assumptions about spatial and temporal dynamics are required. These distinguish different approaches and their suitability for the respective application.

5.1.2 Relevant Supervised and Unsupervised Methods

Methods that attempt to factorize $\boldsymbol{A}$ and $\boldsymbol{S}$ without known labels to the data are termed *unsupervised* or Blind-Source Separation approaches and are often relevant for analysis and preprocessing. *Supervised* methods, on the other hand, make use of labeled data to increase discriminability and are therefore commonly used for classification problems. In the following, PCA, ICA, and CCA will be introduced from the former group and CSP and LDA from the latter, and other cutting edge multimodal BSS methods will be briefly pointed out.

5.1.2.1 Principal Component Analysis (PCA)

One of the most frequently used BSS methods is Principal Component Analysis (PCA) [Pea01; Jol82]. Decomposition is being performed under the assumption of mutually decorrelated / orthogonal components $\boldsymbol{w}^\top \boldsymbol{x}(t)$ so that these explain maximum variance:

$$\max_{\boldsymbol{w}} \operatorname{Var}\left(\boldsymbol{w}^\top \boldsymbol{x}(t)\right), \quad \text{subject to } \|\boldsymbol{w}\|^2 = 1. \tag{5.3}$$

If the data has been centered, (5.3) can be expressed with the covariance matrix $\boldsymbol{C} = \boldsymbol{x}\boldsymbol{x}^\top$, which yields the eigenvalue equation $\boldsymbol{C}\boldsymbol{w} = \boldsymbol{\lambda}\boldsymbol{w}$. Here, λ is the generalized eigenvalue associated with the eigenvector w. The solution can then be found by eigenvalue-decomposition of $\boldsymbol{C}$. As this decomposition is computationally efficient and explains as much variance as possible in the data, PCA is often used for dimensionality reduction.

5.1.2.2 Independent Component Analysis (ICA)

A powerful way to obtain a unique decomposition under very relaxed conditions is through the assumption of statistical independence of the source estimates $\hat{\boldsymbol{S}}$ in the linear mixture. For this, non-Gaussian distributions are commonly assumed. However, when both sample dependence and higher-order statistics are taken into account, ICA can even estimate multiple Gaussian sources [AAF14]. As preparation for the challenging application of ICA to fNIRS and the corresponding framework in Section 5.2, we include the sample dependency (SD) of the sources in the ICA formulation. For this, a natural way to estimate the extraction filters $\boldsymbol{W}$ is by the minimization of the mutual information rate which is given by [AAF14]

$$I_r(\boldsymbol{W}) = \sum_{n=1}^{N_x} H_r(\hat{\boldsymbol{s}}_n) - \log|\det(\boldsymbol{W})| - H_r(\boldsymbol{x}), \tag{5.4}$$

where H_r is the (differential) entropy rate. The cost function (5.4) takes both higher order statistics (HOS) as well as sample dependency into account. Among the widely used ICA

algorithms, Infomax [BS95] uses a fixed nonlinearity model for the underlying distribution of the sources. ICA-EBM [LA10] provides flexible density matching through the use of four measuring functions based on the maximum entropy principle and has been shown to maximize statistical independence efficiently. Most ICA algorithms take advantage of only higher-order statistics by ignoring sample dependence that exists in many signals by assuming independent and identically distributed samples. ICA-ERBM [FPA+14] (see a brief overview in Appendix B.1) builds on the flexible density model of ICA-EBM and adds the use of sample dependence in addition to HOS to achieve ICA by minimizing (5.4).

5.1.2.3 Canonical Correlation Analysis (CCA) and temporal embedding

A method for finding co-modulating components in multivariate data is Canonical Correlation Analysis (CCA) [Hot36; And58]. It estimates normalized linear filters $\boldsymbol{w}_x \in \Re^{N_x}$ and $\boldsymbol{w}_z \in \Re^{N_z}$, the canonical variates, that maximize the canonical correlation between the projections of each modality:

$$\max_{\boldsymbol{w_x},\boldsymbol{w_z}} \mathrm{Corr}\left(\boldsymbol{w}_x^\top \boldsymbol{x}(t), \boldsymbol{w}_z^\top \boldsymbol{z}(t)\right). \tag{5.5}$$

If the two modalities do not correlate instantaneously, optimal filters depend on an — usually unknown — time lag τ. One solution is to temporally embed one modality with a given set of D time lags $\{\tau_0, ..., \tau_D\}$, thus optimizing time-lag-dependent projections

$$\max_{\boldsymbol{w_x},\boldsymbol{w_z}(\tau)} \mathrm{Corr}\left(\sum_i^D \boldsymbol{w}_x^\top \boldsymbol{x}(t), \boldsymbol{w}_z(\tau_i)^\top \boldsymbol{z}(t-\tau_i)\right). \tag{5.6}$$

This method has been applied to medical imaging in various forms, for instance with temporal kernel CCA (tkCCA) for multimodal fMRI analysis [BMG+09].

5.1.2.4 Common Spatial Patterns (CSP)

Common Spatial Patterns (CSP) is a supervised method that allows the optimization of spatial filters for the discrimination of oscillatory activity within (EEG-) signals and is often used for classification [SKM14; TM10; BTL+08; Kol91]. Its spatial filters reduce the effects of volume conduction in EEG and increase the SNR of band power features by maximizing the variance of bandpass filtered signals for one class while minimizing the variance of the other. Let $\boldsymbol{C}_1$ and $\boldsymbol{C}_2$ the covariance matrices of the respective classes. Then, the CSP objective function can be expressed as

$$\max_{\boldsymbol{w}} \frac{\boldsymbol{w}^\top(\boldsymbol{C}_1 - \boldsymbol{C}_2)\boldsymbol{w}}{\boldsymbol{w}^\top(\boldsymbol{C}_1 + \boldsymbol{C}_2)\boldsymbol{w}}. \tag{5.7}$$

The optimization problem (5.7) can be solved by a generalized eigenvalue decomposition that yields the common spatial filters in the columns of $\boldsymbol{W}$. These both maximize and minimize (5.7), according to their corresponding Eigenvalues. Consequently, filters from each side of the eigenvalue spectrum are chosen, and commonly two to three per class in practice.

5.1.2.5 Linear Discriminant Analysis (LDA)

Linear Discriminant Analysis (LDA) is a method that is, due to its good performance, among those most frequently used in the classification of neuroimaging signals. LDA finds a filter $\boldsymbol{w}$ that minimizes the within-class variance and maximizes the between-class variance, here denoted with $\boldsymbol{S}_W$ and $\boldsymbol{S}_B$ respectively, by maximizing the Fisher criterion

$$\max_{\boldsymbol{w}} \frac{\boldsymbol{w}^\top \boldsymbol{S}_B \boldsymbol{w}}{\boldsymbol{w}^\top \boldsymbol{S}_W \boldsymbol{w}}. \tag{5.8}$$

In a two-class problem, the optimal extraction filter can be determined by $\boldsymbol{w} = \hat{\boldsymbol{C}}^{-1}(\hat{\boldsymbol{\mu}}_2 - \hat{\boldsymbol{\mu}}_1)$, where $\hat{\boldsymbol{C}}$ is the estimated common covariance matrix (the average of the class-wise covariance matrices), and $\hat{\boldsymbol{\mu}}_i$ are the estimated class-wise means. If data is high dimensional or when only limited observations are available for training of the classifier, the empirical estimation can be distorted by outliers. As a countermeasure, in regularized or shrinkage LDA, the empirical covariance matrix is shrunk by

$$\boldsymbol{C}^{shr}(\lambda) = (1-\lambda)\hat{\boldsymbol{C}} + \lambda \nu \boldsymbol{I} \tag{5.9}$$

where $\gamma \in [0,1]$ is the shrinking hyperparameter, and ν is the average eigenvalue of $\hat{\boldsymbol{C}}$. An optimal shrinkage parameter can be found analytically, as shown in [LW04].
For binary problems, LDA is the Bayes' optimal classifier under three assumptions: (1) features are Gaussian distributed, (2) the distributions of all classes have identical covariance matrices $\boldsymbol{C}$ and (3) the true class distributions are known [Fri89]. While the first two assumptions are largely satisfied with EEG and fNIRS data, the third assumption is usually not satisfied, but being dealt with by regularization.

5.1.2.6 Other multimodal methods

Aside from the above-mentioned (tk)CCA, a variety of BSS approaches have been proposed for multivariate analysis: joint ICA (jICA), parallel ICA (paraICA) [CLA09] and Independent Vector Analysis (IVA) [AAF14] enable the extraction of multimodal features from groups of subjects or well-aligned datasets. For the investigation of co-modulations between band power dynamics and target signals in the time domain, Dähne et al. developed the Source Power Co-modulation (SPoC) framework [DBS+15; DBM+13]. Its multimodal extension, mSPoC, allows the decomposition of multivariate data, for instance, EEG and fNIRS, such that bandpass filtered oscillatory components from one modality and time-(lagged) components from the other co-modulate maximally.

5.1.3 Challenges in Multimodal Signal Processing

Fusion of multimodal data at the sensor level has to overcome major challenges due to (1) Non-instantaneous and non-linear coupling dynamics between modalities, (2) different temporal resolutions, (3) different spatial resolutions and (4) unimodal outliers and low SNR that hinders the estimation of combined statistics. In the following Section, several of these challenges will be relevant to the multimodal BSS analysis of fNIRS signals.

5.2 A Multimodal Blind-Source-Separation Framework for fNIRS

5.2.1 State of the Art and Aims

Following the trend of EEG, new miniaturized wearable fNIRS instruments such as the presented M3BA, openNIRS, and others [MHW08; SGM+13; WLS+17] expand the spectrum of fNIRS beyond static and toward ambulatory domains. In both, static and mobile domains, the recovery of evoked brain activity from measured fNIRS signals is crucial, as neural task-related activity is masked by various physiological and non-physiological components which are often of equal or higher magnitude [SKM+14]. In fNIRS applications with moving subjects, this gains further importance, as changing environmental and behavioral conditions add significant non-stationarities [BMK+09].

Many methods in the fNIRS literature provide a remedy only for a subclass of movement artifacts (MA) which is the optical decoupling between optodes and scalp that leads to instantaneous virtual variations of chromophore concentrations in the form of fast transient changes and sudden baseline shifts (see also fig. 5.1, MA1). A second type that becomes increasingly important with the rise of new mobile applications, is challenging to identify and has been tackled only exceptionally so far: Motion-induced slow, non-instantaneous physiological processes (see also fig. 5.1, MA2), that modulate partial blood pressure, scalp- and cerebral blood flow and blood volume (CBF /CBV). We denote these as *indirect movement artifacts* (IMA). The overall impact of such modulations can be observed in our experimental dataset (see also Figure 4.4), where IMAs are repeatedly induced in a controlled way due to the designed paradigm. Once data contamination is detected, trials are often entirely rejected [SNK+17]. However, when there are few trials or many movements, this is not an option.

There is currently no gold standard for the extraction of the hemodynamic response from masking components and the rejection of movement artifacts. Univariate approaches include moving standard deviation and spline interpolation [SSM+10], wavelet filtering [MD12], Kalman filtering [ICB+10], and correlation-based approaches [CBR10]. A promising class of multivariate methods makes use of complementary signals; either by performing regression or adaptive filtering with accelerometer signals [VNK+11] or in multi-distance (MD) approaches using multiple source-detector separations [SB05; ZSG09] for the rejection of superficial components, e.g., those originating from the scalp. Scholkmann et al. 2014 gave an overview of univariate and multivariate methods [SKM+14], Brigadoi et al. 2014 compared multiple univariate motion correction techniques [BCC+14].

The majority of approaches implicitly assume the presence of latent physiological or non-physiological artefactual components, but manipulate signals in the channel domain. In contrast to other neuroimaging fields, elaborate Blind-Source Separation (BSS) -based methods are yet comparatively underrepresented in fNIRS, although they explicitly aim to identify latent processes. While Principal Component Analysis (PCA) -based approaches have successfully been applied to reduce superficial contributions from blood flow in static scenarios [ZBF+05; FJH+06], more complex methods such as Independent Component

Analysis (ICA) have mainly served as an alternative to averaging for the extraction of typical fast or slow evoked responses from a high number of time-locked epochs [MWL+04; MKB+08; AAS06] or channels (e.g., 212 channels in a DOT system [MWZ+09], 650 wavelengths in a broadband fNIRS [ST12]). When applied to remove extracerebral signals [KMS+07], Virtanen et al. concluded that (fast)ICA typically performs worse or equal than PCA [VNM09].

A variety of fNIRS signal characteristics pose serious challenges to many standard BSS approaches, depending on the assumptions and statistics in the underlying model. Among the challenges in the signals are non-instantaneous and non-constant coupling, and source dependencies [Hup16]. As a consequence, to the best of our knowledge, there exists no elaborate BSS framework for the general analysis and decomposition of single-trial fNIRS data so far. Ideally, such a framework enables extraction and analysis of functionally distinct components without affecting others — even when they share the same frequency band. Also, by taking advantage of complementary multimodal signals, it could facilitate the identification of artefactual processes that are otherwise hard to separate from the evoked hemodynamic responses, such as many indirect movement artifacts.

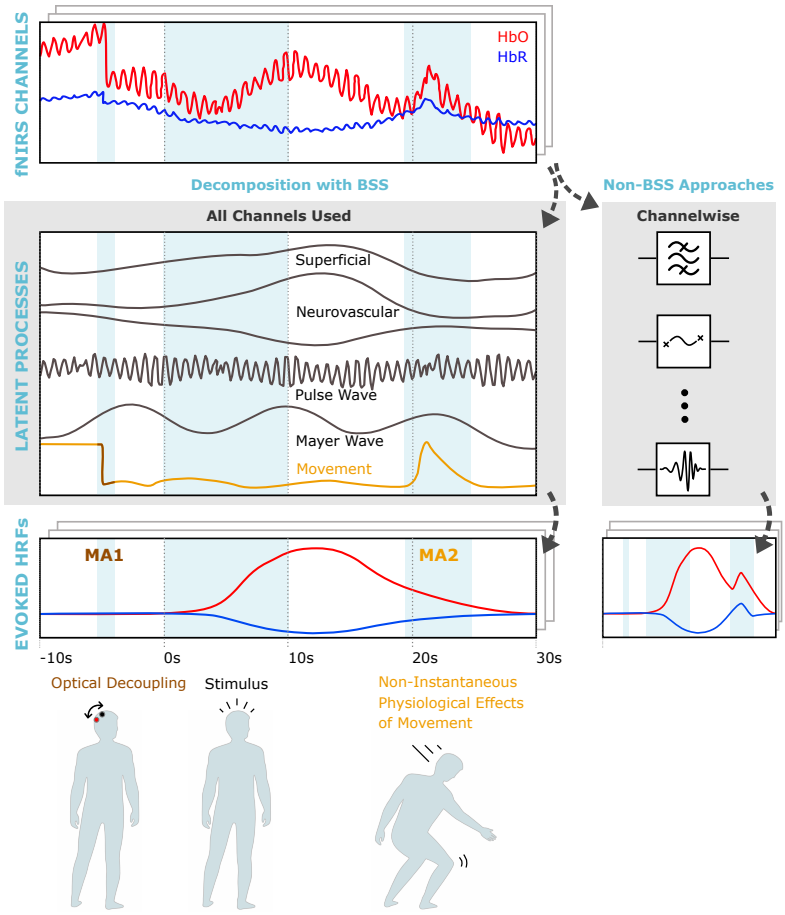

Figure 5.1: Schematic decomposition of fNIRS signal into components via BSS vs. channel-wise manipulation in other approaches. Modulation of components due to optode shifts and decoupling (**MA1**), and due to non-instantaneous motion induced physiological effects (**MA2**), compare also fNIRS signals in Figure 4.4.

Aims

In this Section an approach toward such a general BSS framework is presented for the analysis of fNIRS signals by combining

- *Independent Component Analysis* (ICA) methods that exploit both higher order statistics (HOS) and sample dependency by using mutual information rate as a unifying framework for source decomposition [AAF14; FPA+14; ALSC15],
- *multimodality* — here complementing fNIRS with accelerometer signals — assuming the presence of pairs of shared processes, and
- *Canonical-Correlation Analysis* (CCA) *with temporal embedding* to robustly extract the corresponding components.

By calculating the entropy rate of the sources using ICA-ERBM (see Section 5.1.2.2), and therefore taking advantage of multiple statistical properties, we expect to achieve a superior estimation of underlying sources in the presence of source dependence.
We apply the novel *B*lind *S*ource *S*eparation framework to *A*ccelerometer-based *A*rtifact *R*ejection and *D*etection (*BLISSA*^{2}*RD*), tackling the challenge of indirect movement artifacts in a multimodal approach and also point out common challenges and possible solutions on the way. We use the unique dataset from Chapter 4 for quantitative and qualitative evaluation of the proposed framework.

5.2.2 fNIRS Signal Components

When performing BSS to extract underlying processes from fNIRS signals, a classification of expected components can help with interpretation in the source domain (see Figure 5.2). For those of physiological origin, we adopt a classification scheme from Scholkmann et al. [SKM+14] and differentiate between six non-stationary physiological components $C1 - C6$ by categorizing them into classes as

1. *source* (intracerebral vs. extracerebral),
2. *stimulus/task relation* (evoked vs. non-evoked) and
3. *cause* (neuronal vs. systemic).

From the perspective of artifact rejection, it makes sense to extend this classification to components of non-physiological origin $NC1 - NC3$, typically introduced in the acquisition processes: *environmental influences*, *instrumentation noise* (usually stationary) and *changes in acquisition geometry* (e.g., optical decoupling).

Both types of components C_x and NC_x originate in different domains, i.e., that of physiological chromophore concentrations and that of raw signal intensities, respectively. The domains are non-linearly linked to each other by the modified Beer-Lambert Law (mBLL) [DCZ+88]. Variations in NC_x lead to virtual changes in the chromophore concentration domain. Commonly, careful instrumentation design robustifies against $NC1 - NC2$. Low-

or band-pass filtering of fNIRS signals with a typical cut-off frequency around $0.2\,Hz$ is common practice to minimize non-evoked components $C4 - C6$. Then, univariate and multivariate methods [BCC+14; SKM+14] are used to mitigate systemic cerebral & extracerebral components ($C2, C3, C5, C6$) and movement artifacts due to optode shifts ($NC3$).

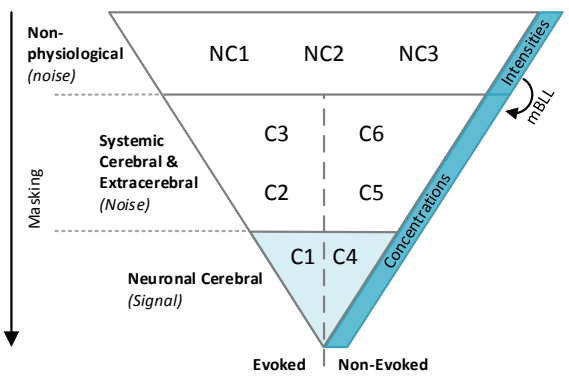

NC1:	**Environmental Influences**	*e.g., ambient light changes*
NC2:	**Instrumentation Noise**	*e.g., drifts, electr. interference, thermal /shot noise level shifts*
NC3:	**Acquisition Geom. Changes**	*e.g., optode shifts rel. to each other or the scalp*
C6:	**Systemic Activity**	e.g., *HR, RESP, MW, VLFO*
C5:	**Systemic Activity**	*e.g., HR, RESP, MW, VLFO, non-evoked hemodynamics or vasomotion*
C3:	**Systemic Activity**	*Changes in blood pressure, skin/scalp blood flow / volume*
C2:	**Systemic Activity**	*Changes in blood pressure, CBF/CBV and $PaCO_2$, hypo-/hypercapnia*
C4:	**Spontaneous Brain Activity**	*Non-evoked neurovascular coupling due to resting state activity*
C1:	**Functional Brain Activity**	*Evoked local neuronal hemodynamic response (neurovasc. coupling)*

Figure 5.2: fNIRS signal components. HR: Heart Rate, RESP: Respiratory signals, MW: Mayer Waves, VLFO: Very Low Frequency Oscillations, CBF/CBV Cerebral Blood Flow/Volume, $PaCO_2$: Partial CO_2 Pressure.

5.2.3 Challenges and Considerations

For (multimodal) BSS analysis, several challenging properties of fNIRS signals have to be taken into account, some of which can be exemplified in the observation of combined raw fNIRS intensity and accelerometer signals from the acquired dataset (see Figure 5.3):

- *Single channels include both spatially specific and global unspecific components* of neuronal or systemic, cerebral or extracerebral origin. These are subject to
- *Non-instantaneous, non-constant and non-linear coupling* of the underlying physiological processes. Global and local systemic signals are non-simultaneously mixed into channels with spatially and behaviorally dependent delays and morphology as they non-instantaneously disperse along the arteriole system and depend i.a. on relative orientation and movement speed of the head and body (e.g., the pulse wave or blood-pooling effects).
- *Non-simultaneous acquisition* of channels in time division multiplexing schemes: in BSS, samples of different channels are usually assumed to be observed simultaneously.
- *Under-determined problem:* Ideally, BSS approaches require an equal or higher number of measured signals than latent factors. As in EEG, it is often questionable whether this condition is fulfilled.
- *Dependency between fNIRS sources:* The assumption of independence in ICA collides with the fact that several underlying physiological processes in the fNIRS signals are not entirely separable and independent but form an interacting network of interlinked statistically dependent processes [Hup16; SKM+14].

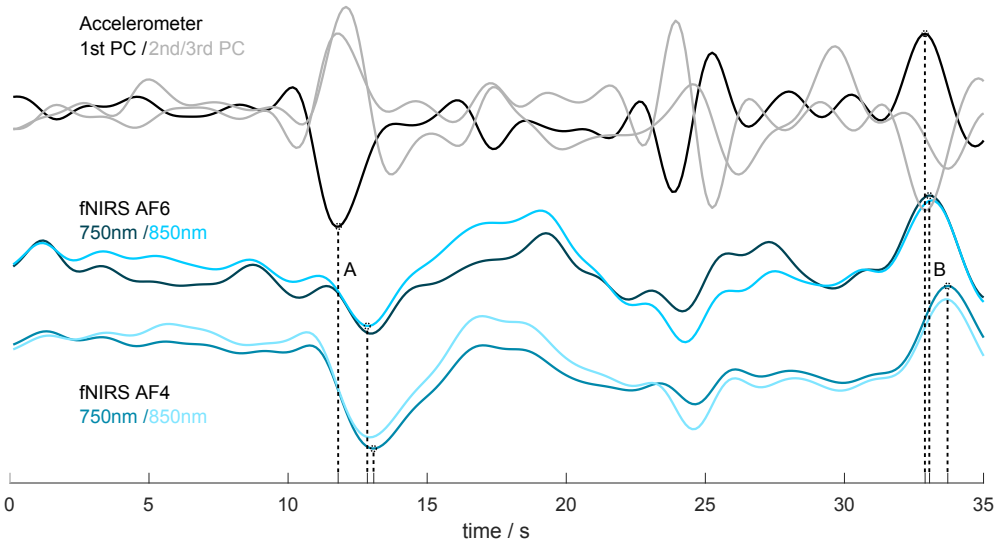

Figure 5.3: Example of spatially dependent non-instantaneous and non-constant modulation of raw fNIRS intensity signals (AF4/AF6) in motion and first three PCA components of simultaneously acquired accelerometer signals on the head. Signals normalized and low-pass filtered with $f_c = 0.5\,Hz$. Peak-to-peak delays: $A_{min|max} = 1050|1280\,ms$, $B_{min|max} = 120|780\,ms$.

Due to these properties, even the most elaborate BSS approaches might not achieve an ideal decomposition. From a Signal to Noise Ratio (SNR) perspective this is, however, not required, as separation into component subsets of the same or similar categories ($C1-6, NC1-3$) can already enable reliable artifact rejection and thus increase the overall SNR. This is the approach of BLISSA^{2}RD, which identifies and then rejects subsets of movement-induced changes within the fNIRS signals, including but not limited to those due to blood-pooling.

5.2.4 The Framework and BLISSA^{2}RD Method

In this approach, the challenge of fNIRS signal decomposition is tackled by exploiting the combined strengths of the linear methods PCA, ICA and CCA. In a first step, the fNIRS signals are decomposed into mutually independent sources with *ERBM-ICA*, taking sample dependency and HOS into account for better performance in the presence of source dependence. Performing further analysis and processing steps in the source space then allows to increase the distance between components of interest and components for manipulation and rejection. Here, using CCA, target signals from an additional modality are exploited for the identification and extraction of co-modulating components. To take care of non-instantaneous coupling dynamics, the complementary target signal is temporally embedded. In the context of direct and indirect movement artifact rejection, the application of accelerometer signals as targets is a natural choice.

In the following, BLISSA^{2}RD is described, with one possible implementation for the rejection of (indirect) movement artifacts based on the proposed framework.

BLISSA^{2}RD: Blind Source Separation and Accelerometer based Artifact Rejection and Detection *To increase the SNR of cerebral neuronal components of interest in the fNIRS signals, we make use of the ERBM backward model in conjunction with multimodality and CCA by assuming that fNIRS and accelerometer datasets are related by pairs of shared processes whose components BLISSA^{2}RD aims to extract and reject.*

Figure 5.4 gives an overview of the method, Figure 5.8 in the next Section complements this description with typical signals observed in the different stages of BLISSA^{2}RD.

In a preprocessing step, both the fNIRS data $\boldsymbol{X}$ and accelerometer data $\boldsymbol{Z}$ are channel-wise normalized to zero mean and unit variance, then linearly detrended and low-pass filtered with a cut-off frequency of $f_c = 0.5\,Hz$. We use a comparably high cutoff frequency at this stage for better separability in the following process and apply conventional processing steps, including a low-pass with a lower cutoff after cleaning. The accelerometer signals, usually acquired with sample rates higher than that of fNIRS, are then sub-sampled to a common time base.

In the fNIRS domain, all wavelengths are pooled in $\boldsymbol{X}$ and ICA unmixing of the raw fNIRS intensity signals is performed with ERBM (Figure 5.8 I). For this, a hyperparameter, the filter length p has to be selected. Its value determines the number of samples included in the whitening process of ERBM [FPA+14]. Its selection will not be further elaborated here – a brief note is provided in Appendix B.2.

On the accelerometer data, Principal Component Analysis (PCA) is performed for dimensionality reduction to $K_z = 3$ pairwise orthogonal Euclidean dimensions by selecting the three components with highest eigenvalues. This step is redundant when only one 3D accelerometer on the head was used for the acquisition of movements. By appending D time-shifted copies of the original (PCA reduced) data $\boldsymbol{S}_z(\tau_d)$, the three main movement components are then temporally embedded into a higher dimensional space (Figure 5.8 II) to take non-instantaneous coupling into account: $\tilde{\boldsymbol{S}}_{\tau,z} = \left[\boldsymbol{S}_{\tau_0}, \boldsymbol{S}_{\tau_1}, ..., \boldsymbol{S}_{\tau_D}\right]^\top \in \Re^{DK_z \times T_z}$.

For the time shifts $\tau_d = d \cdot \Delta t, \quad d \in \{0, 1, ..., D\}$ the number of copies D and step width Δt have to be set. The selection of these parameters impacts the effectivity of the method concerning the coupling between movement (accelerometer signals) and fNIRS components. We can include apriori knowledge of the physiological signal for this purpose:

- Causality. Movement induced artefactual fNIRS components cannot precede the accelerometer signals: time-embedding is necessary only in positive directions.
- The fNIRS frequency band of interest limits the size and number of time shifts that are reasonable.

Using the time-embedded main movement components $\tilde{\boldsymbol{S}}_{\tau,z}$ and the factorized independent fNIRS components $\hat{\boldsymbol{S}}_x$, Canonical Correlation Analysis is now performed (Figure 5.8 III), finding projections $\boldsymbol{U}_x$ and $\boldsymbol{V}_z$ of both modalities that correlate maximally. On the fNIRS side, we assume n projections $\mathbf{u}_{x,n} \in \Re^{T_x}$ that exceed a canonical correlation threshold to be artefactual components caused by movements. Applying of Theorem 1 in [HMG+14], these are then projected back by the means of

$$\boldsymbol{A}_x^{\mathrm{CCA}} = \mathrm{Cov}(\hat{\boldsymbol{S}}_x)\, \boldsymbol{W}_x^{\mathrm{CCA}}\, \mathrm{Cov}(\boldsymbol{U}_x)^{-1} \tag{5.10}$$

and subtracted from the independent fNIRS sources (Figure 5.8 IV). Finally, back-projection of the cleaned fNIRS sources into the original intensity signal domain and reversing the normalization yields the raw fNIRS signals that are now cleaned from (time-delayed) processes correlating with movement signals (Figure 5.8 V).

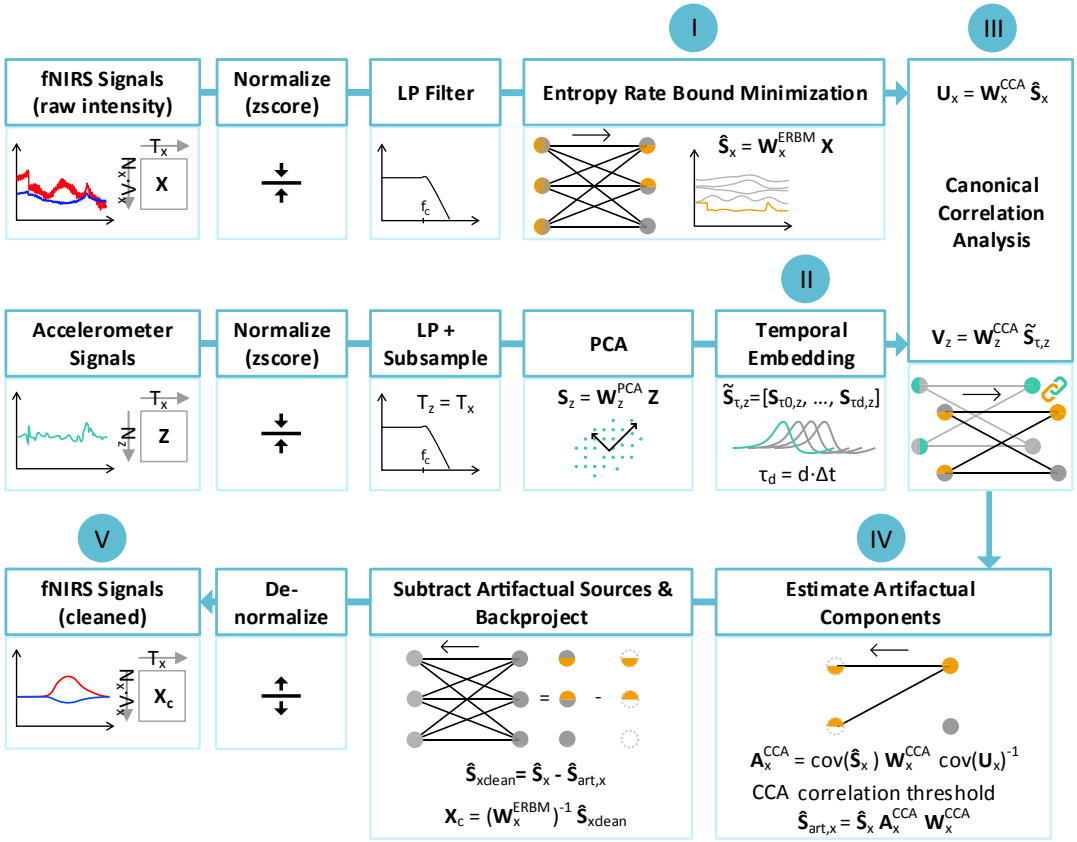

Figure 5.4: BLISSA^3RD Method Overview. (I) ICA decomposition step, (II) temporal embedding of principal accelerometer components, (III) identifying shared processes with CCA, (IV) estimating artefactual components in the ERBM source space, (V) cleaned signal.

5.2.5 Validation

A general challenge in the evaluation of motion artifact rejection techniques in fNIRS signals is that the true hemodynamic response is unknown - and thus a ground truth is lacking (compare [BCC+14]). Here, we present the methods and metrics employed for quantitative evaluation based on statistical signal properties, target signals from multimodality, physiological plausibility and simulations – and the corresponding results. The method is evaluated on the $17 \times 120 min$ dataset from the main workload study. As common preprocessing step, channels are linearly detrended to remove slow drifts. Then, a 4^{th} order zero-phase Butterworth low-pass filter with $f_{c1} = 0.5 Hz$ is applied. BLISSA^2RD artifact rejection is always performed block-wise. Signal bandwidth is further reduced ($f_{c2} \in \{0.2, 0.033 Hz\}$) as a last common step. The statistical tests employed for significance are paired t-tests.

5.2.5.1 Blind Source Separation of fNIRS signals: Real Data and Simulations

Independent Component Analysis of fNIRS The practical success of fNIRS BSS depends on the quality of decomposition achieved by the applied ICA method. Unmixing performance on the real-world and simulated data was investigated, applying ICA-ERBM, ICA-EBM, Independent Vector Analysis [AAF14] and FastICA [Hyv99]. We focus here on FastICA and ICA-ERBM. Quality in the real-world data was assessed visually with respect to separability of components, using apriori knowledge about

(1) dependencies between time logged events, movement artifacts, and complementary accelerometer signals and

(2) Morphology, smoothness, correlation and discriminability of commonly known physiological components in fNIRS (see Section 5.2.2), i.e., effects of oscillatory processes like Mayer waves, breathing and pulse waves.

Compared to all other methods, ERBM yielded superior fNIRS decomposition. Figure 5.5 depicts a typical example of 12 out of 18 sources decomposed with ERBM and fastICA from the same set of real-world data.

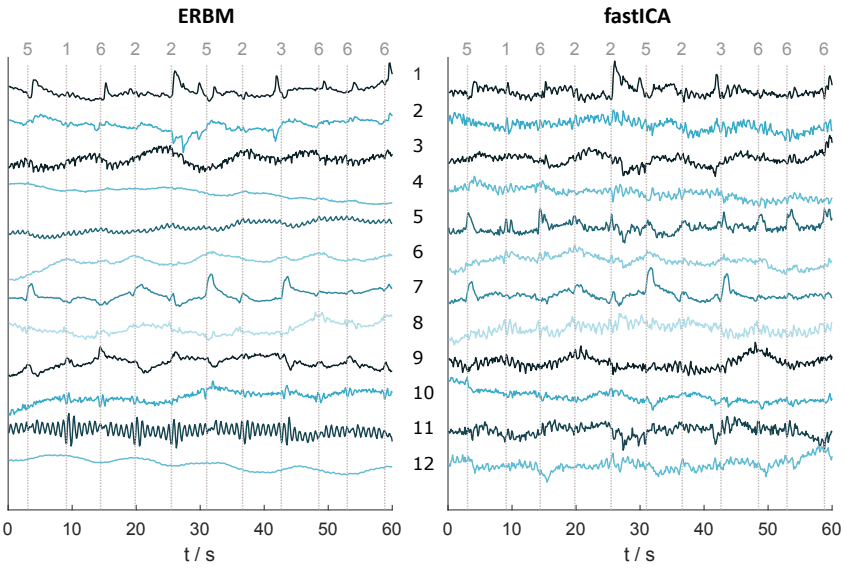

Figure 5.5: Source separation in fNIRS: 12 aligned components from Entropy Rate Bound Minimization (ERBM, **left**) and fastICA ([Hyv99], **right**). ERBM sources show a much clearer separation among e.g. artifacts from movement (1,2,7,9) pulse wave (11) and slow oscillations/Mayer waves (12). Grey dotted lines indicate button-press events and grey numbers the corresponding position (see Figure 4.1 for reference).

Sources were aligned by performing Bertsekas auction algorithm [Ber88] (one-sided, fixed epsilon) in the normalized FFT domain. ERBM consistently yielded better discriminable components, with respect to morphology, frequency content and physiological processes and artifacts that are to be expected apriori. Including but not limited to ERBM, BSS decomposition of raw intensity signals consistently outperformed decomposition of signals previously converted into physiological chromophore concentrations.

These qualitative results were quantitatively confirmed in a simplified approach to simulate fNIRS source characteristics. 7 processes were generated for $t \in 0...100\,s$, sampled at $f_s = 8\,Hz$ (see Figure 5.6), representing S_1) *Breathing*, S_2) *Heart rate*, S_3) *Mayer waves*, S_4) *Evoked responses*, S_5) *White random gaussian noise*, S_6) *Movement artifacts*, S_7) *Dependent evoked processes*). Appendix B.3 provides additional details on the signal generation.

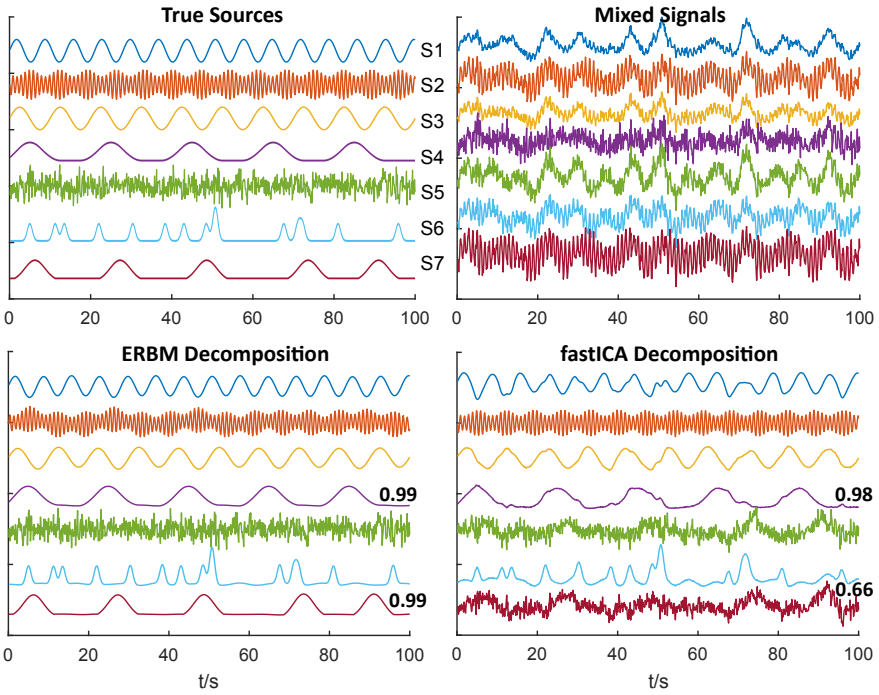

Figure 5.6: Typical example of simulated fNIRS data unmixed with ERBM and fastICA. $S1 - S7$ represent processes due to breathing (1), heart rate (2), Mayer waves (3), evoked responses (4), white noise (5), movement artifacts (6) and dependent evoked processes (7). Bold numbers: correlation between true and estimated sources.

Two pairs of sources are statistically dependent: S_1 and S_2 are weakly correlated (< 0.1) and S_4 and S_7 are moderately correlated ($\mu \pm \sigma = 0.39 \pm 0.23$, see also Figure 5.7 **B**. While sources $S_1 - S_4$ remain constant, $S_5 - S_7$ were newly generated in each iteration. Observations were generated with a constant, arbitrary mixing matrix $\boldsymbol{A}$ and performed subsequent unmixing with ERBM and fastICA. Estimated sources from each method were aligned to true sources using Bertsekas auction algorithm [Ber88] in the normalized FFT domain. In the following, the focus of interest is on the dependent target sources $S4$ and $S7$, which represent the evoked responses.

To quantify unmixing performance, two metrics were investigated: Intersymbol interference (ISI) [Mac93; EK04] as a global metric, and the correlation between aligned estimated and true sources: $\mathrm{Corr}(\hat{S}_i, S_i) \mid i \in \{4,7\}$. Simulations were repeated $N = 1000$ times. To better differentiate the ISI results, convergence / stability of the unmixing performance was assessed: Let $\boldsymbol{G} = \boldsymbol{W}\boldsymbol{A}$ with $\boldsymbol{W}$ the estimated demixing matrix and $\boldsymbol{A}$ the true mixing matrix. The unmixing is considered stable, if the locations of the largest squared elements in any two rows of $\boldsymbol{G}$ are different. Using this definition, ERBM unmixing yielded 59 and fastICA yielded 290 unstable results out of 1000, where in 87 out of 290 cases fastICA did not converge to the correct number of 7 target sources. Figure 5.6 depicts exemplary signals from the simulations, Figure 5.7 **A** shows the resulting correlation and ISI performance measures over all iterations.

For target source $S4$, ERBM yielded estimates that correlate with the true signal on average ($\mu \pm \sigma$) with 0.97 ± 0.04, fastICA yielded 0.93 ± 0.10. For the dependent target source $S7$, ERBM yielded estimates that correlate with 0.92 ± 0.17, where fastICA yielded corresponding estimates with 0.72 ± 0.19. Across all other sources, the correlation is on average 0.98 ± 0.01 and 0.96 ± 0.03 for ERBM and fastICA respectively. ISI analysis (Fig-

ure 5.7 **C**) yielded an average ($\mu \pm \sigma$) ISI of 0.042 ± 0.012 in ERBM and 0.095 ± 0.033 in fastICA for all decompositions. When only investigating unstable decompositions, ISI was found to be 0.045 ± 0.014 and 0.120 ± 0.033 respectively.

Due to the use of both HOS and sample dependence, ERBM outperforms fastICA significantly in all metrics ($p \ll 0.001$) in the presence of source-dependence and generally yields smoother results, confirming the observations from real-world fNIRS data as exemplified in Figure 5.5.

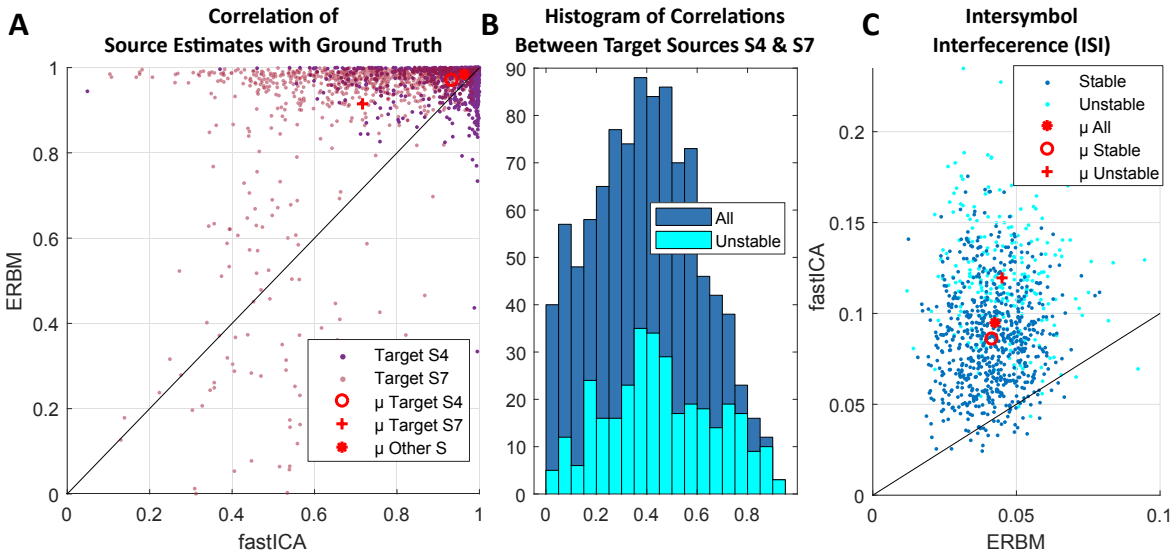

Figure 5.7: Results of fNIRS source (un-)mixing simulation in 5000 iterations. (**A**) correlation of true sources S_4 & S_7 with source estimates from ERBM/fast ICA. (**B**) histogram of correlation between true target sources S_4 & S_7 in all iterations and fraction of corresponding unstable unmixing in fastICA and ERBM. (**C**) Intersymbol interference (ISI) of ERBM and fastICA.

Exploiting Multimodality: BLISSA^{2}RD Signals Complementing the formal description of the multimodal BLISSA^{2}RD approach in Figure 5.4, Figure 5.8 exemplifies typical signals observed in the different processing steps and domains of the method, qualitatively confirming the theoretical approach.

It illustrates amongst others that

- ERBM components are modulated by movements to different degrees - displayed before and after CCA artifact rejection step (5.8 **I**).
- Temporal embedding of a principal accelerometer component (τ_D with $D \in \{0, ..., 5\}$) helps to alleviate non-instantaneous coupling (5.8 **II**).
- CCA successfully extracts shared processes from the ERBM sources and temporally embedded principal accelerometer components with high canonical correlation (5.8 **III**).
- Signals before vs. after cleaning differ significantly in both the intensity and chromophore domain (5.8 **V**).

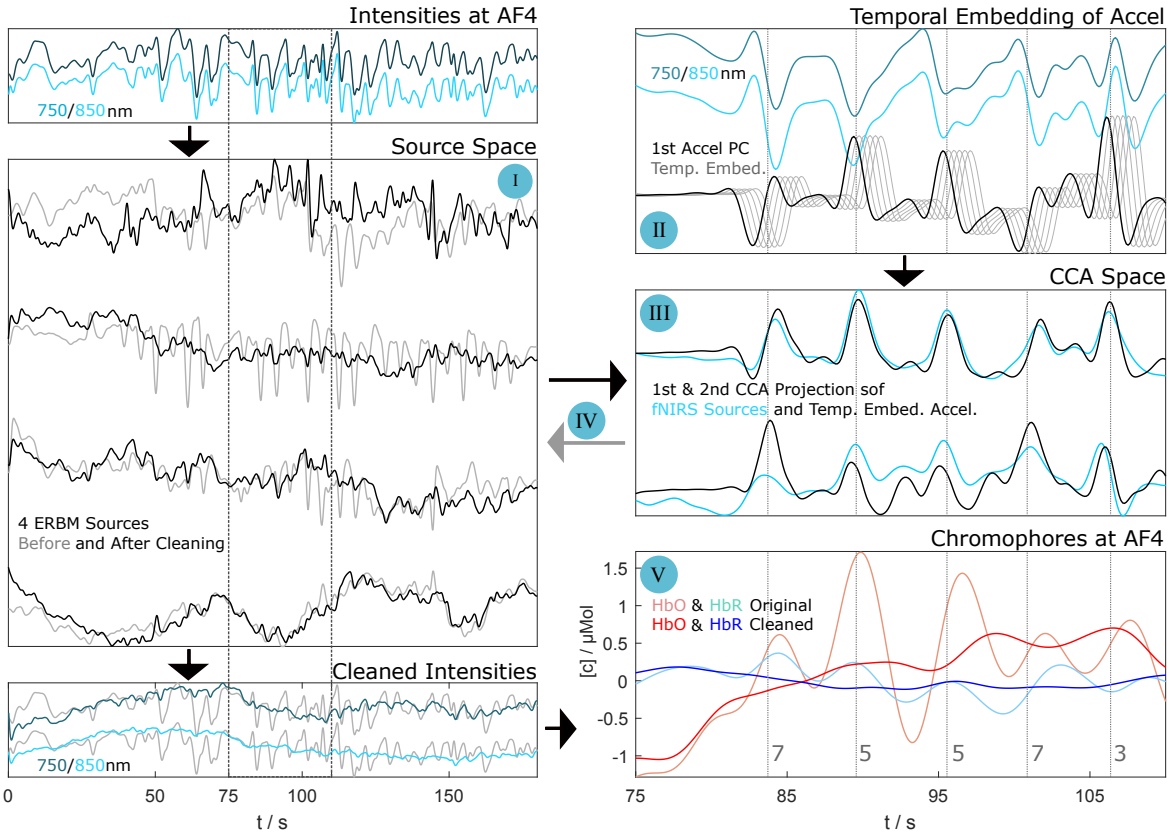

Figure 5.8: Typical BLISSA^{2}RD signals. Left side: $160\,s$ time window, right side zoomed in at $75-110\,s$. Raw intensities of channel AF4 (upper left) and 4 exemplary sources after ERBM decomposition before and after cleaning (I). Time embedded 1st principal accelerometer component with $\tau \in \{0,...1.8\,s\}$ vs. raw signal (II) and first two resulting projections from CCA (III). Raw signals (lower left) and signals converted to chromophore concentrations before and after cleaning (V). Grey dotted lines and numbers (right side) indicate button press events and positions (compare Figure 4.1).

5.2.5.2 1st and 2nd order Statistics: Hemodynamic Artifacts and SNR

Although the ground truth is unknown, essential features of hemodynamic response functions are by now well understood and typically stable. Commonly, averages are calculated, and the variability between single trials is assumed to be caused by the non-evoked processes of both systemic origin and motion artifacts. Ideally, the evoked neuronal response in a single subject should be stationary across rounds of the same cognitive task. In contrast, when averaging across many trials with constant movement conditions (here selected tile position), the induced hemodynamic motion artifacts should be stationary to a high degree. Under this assumption, 1st and 2nd order statistics are being used for investigation of average artifacts and SNR.

Average Artifacts Over the course of the experiment with 12 blocks $\times$ 7 rounds, each participant performed approximately 930 time-logged, randomly distributed button presses. This allows the calculation of average induced hemodynamic artifacts for each end-position

in all channels, both within and across subjects. For this purpose, we segment the fNIRS signals into epochs of $\pm 3\,s$ around each button-press event. On the basis of approximately 113 epochs each, the averaged hemodynamic artifacts are then calculated for HbO/HbR in each movement condition, channel, and subject, a total of $2 \times 8 \times 9 \times 17 = 2448$. This is done both for the original data and data cleaned with BLISSA^{2}RD. As the average artifact-free signal is expected to be constant and close to zero, the peak to peak amplitude A_{pp} and the standard deviation of the average signal across time $\bar{\sigma} = \mathrm{std}(\mu(t))$ in each channel are used to quantify average artifacts in each position before and after cleaning.

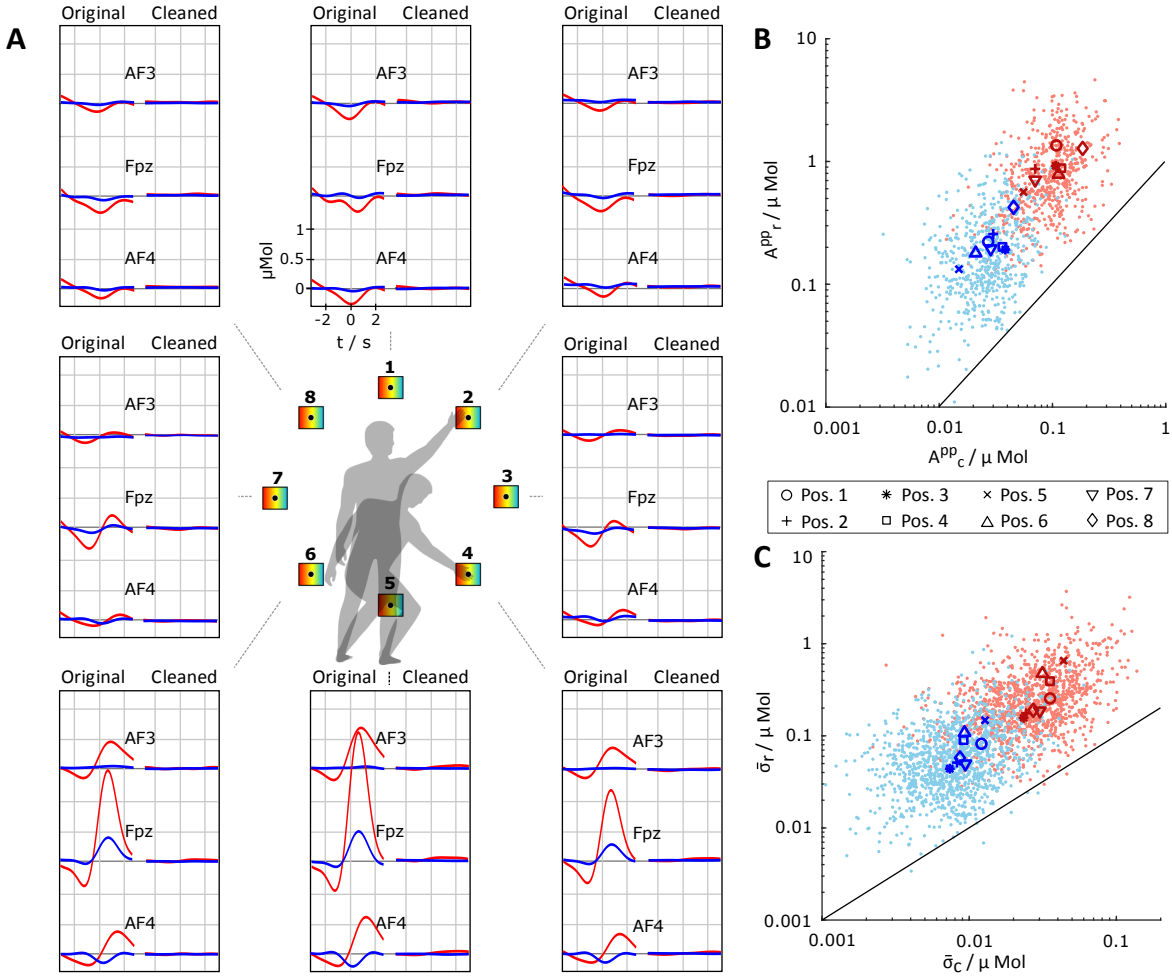

Figure 5.9: Grand average hemodynamic artifacts and statistics. (**A**) Average signals for each button position in original data and data processed with BLISSA^{2}RD of selected channels AF3, Fpz, AF4. Scatter plots of peak to peak amplitudes A^{pp} (**B**) and standard deviations σ^{μ} (**C**) of the average movement artifacts in each channel for each subject and position. subscript "o" (y-axis): original data, subscript "c" (x-axis): cleaned data. HbO: red, HbR: blue.

Figure 5.9 **A** depicts the grand average hemodynamic artifacts in three exemplary channels AF3, Fpz and AF4 for all positions of the experiment and both the original and cleaned data. Average movement artifacts were each calculated from a total number of 1920 epochs

across all subjects. In the unprocessed data, significant artifacts can be observed for all positions and channels (min. $0.2\,\mu Mol_{pp}$ in HbO). Events where the participants stooped down (pos. 4-6) go along with largest changes (up to $3\,\mu Mol_{pp}$ in HbO, up to $0.8\,\mu Mol_{pp}$ in HbR in Fpz). Artifact morphologies differ between movement conditions but also between channels and often show an undershoot followed by a more substantial overshoot in HbO, where HbR can display a similar or inverse behavior. In positions above shoulder height (1,2,8), HbO typically displays only undershoots. In contrast, the data cleaned with BLISSA^{2}RD, shows remaining average hemodynamic artifacts of max. $0.08\,\mu Mol_{pp}$ in HbO and $< 0.01\,\mu Mol_{pp}$ in HbR across all channels and positions, an attenuation of up to two orders of magnitude.

Scatter-plots in Figure 5.9 **B** & **C** depict the peak to peak amplitudes A_r^{pp} / A_c^{pp} and standard deviations σ_r^{μ} / σ_c^{μ} of the average hemodynamic artifact in single subjects, channels and movement positions for original (o) vs. cleaned (c) data. Across all subjects, channels and movement positions, application of BLISSA^{2}RD reduces A^{pp} and $\bar{\sigma}$ of averaged hemodynamic artifacts in HbO and HbR on average by more than one order of magnitude and up to two orders of magnitude in subsets.

Within-Subject Standard Deviation and Signal to Noise Ratio of the Hemodynamic Responses For each subject and experimental n-back condition ($n \in \{1,2,3\}$), the signals are segmented into $P^n = 12$ epochs using the first $90\,s$ of each round. The same metric denoted "within-subject standard deviation" in [BCC+14] is being used as a measure of noise in the evoked physiological HbO / HbR signals: $\bar{\sigma}$ is the mean of the variability of hemodynamic responses across epochs P^n of the same condition. For this, it is assumed as an approximation that the stationarity of the evoked physiological hemodynamic response prevails, while the variability between single epochs of the same condition is predominantly due to motion artifacts. The improvement of SNR achieved in each channel is furthermore quantified in terms of

$$\Delta\mathrm{SNR} = \mathrm{SNR}_{clean} - \mathrm{SNR}_{orig} = 20\log_{10}\left(\frac{\bar{\sigma}_{orig}}{\bar{\sigma}_{clean}}\right) \tag{5.11}$$

This way, noise and SNR improvement are determined in $17 \times 3 \times 9 \times 2$ (subj $\times$ conditions $\times$ ch $\times$ HbO/HbR) $= 918$ average hemodynamic responses, each from 12 experimental runs in the same n-back condition. Analysis of the within-subject standard deviation $\bar{\sigma}$ and SNR of original and processed physiological HbO / HbR responses during $n = 1,2,3$-back tasks yielded the results summarized in Figure 5.10 and Table 5.2.

	n-back	ΔSNR $/dB$ $f_c = 0.5Hz$	ΔSNR $/dB$ $f_c = 0.2Hz$	ΔSNR $/dB$ $f_c = 0.033Hz$
HbO	1	4.58 ± 1.99	4.10 ± 1.81	1.83 ± 1.13
	2	4.10 ± 1.68	3.64 ± 1.52	1.78 ± 0.99
	3	3.60 ± 1.78	3.17 ± 1.62	1.64 ± 1.14
HbR	1	3.50 ± 2.03	3.01 ± 1.76	1.80 ± 1.08
	2	3.14 ± 1.68	2.69 ± 1.42	1.64 ± 0.92
	3	2.88 ± 1.77	2.41 ± 1.47	1.40 ± 0.99

Table 5.2: $\mu \pm \sigma$ SNR improvement across all subjects and channels

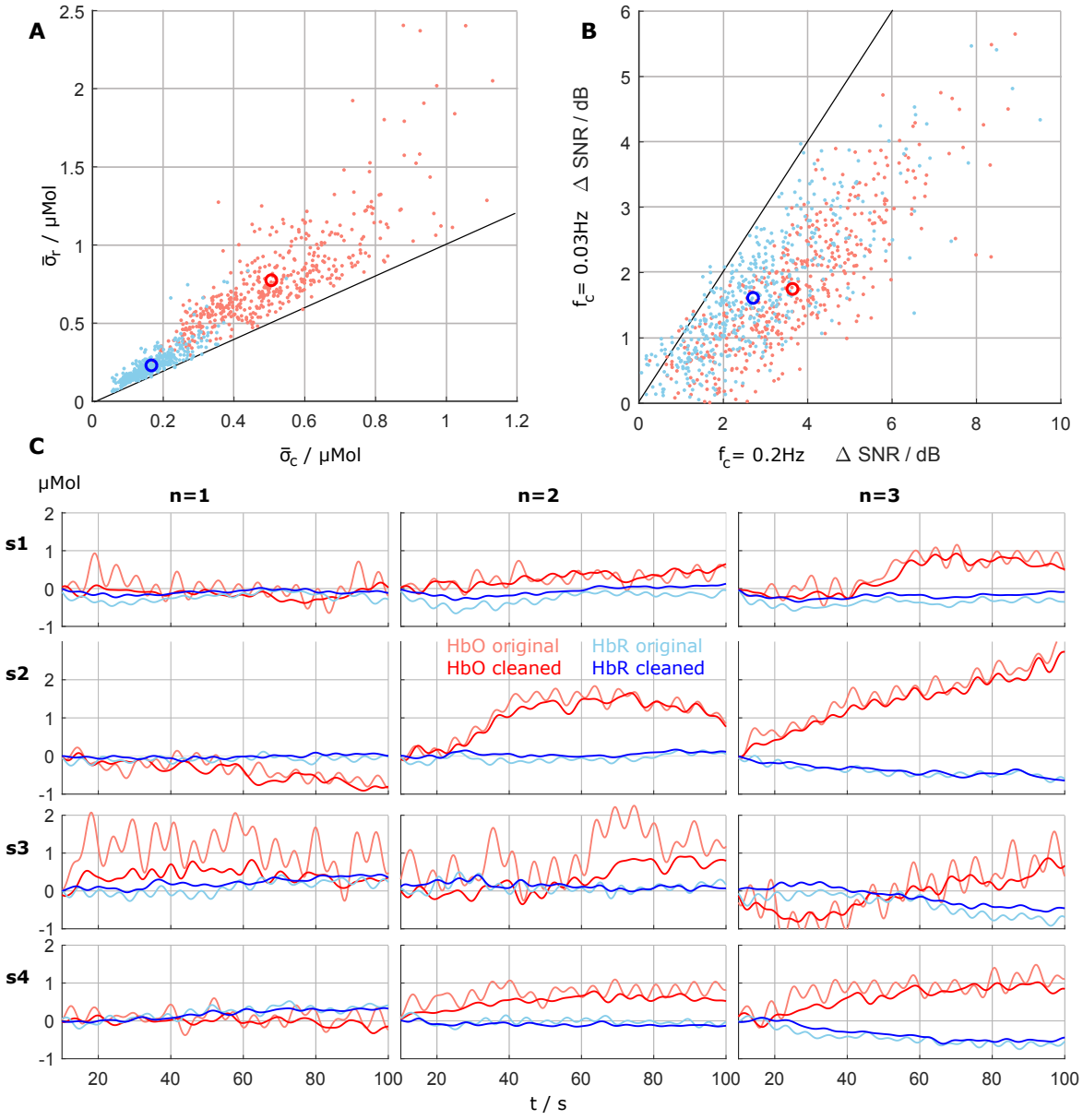

Figure 5.10: (**A**): Within-subject standard deviation of the original $\bar{\sigma}_r$ and cleaned $\bar{\sigma}_c$ signals. (**B**) Scatter plot of SNR improvement across subjects and channels for normal ($f_c = 0.2\,Hz$) and slow signals ($f_c = 0.03\,Hz$). HbO: red, HbR: blue.(**C**) Average hemodynamic responses of 4 exemplary subjects in $n = 1-3$ conditions, $f_c = 0.2\,Hz$, for both original data (HbO: salmon, HbR: sky blue) and cleaned data (HbO: red, HbR: blue) in channel AF6.

Across conditions and subjects, for low-pass filtered signals with $f_c = 0.2\,Hz$, the within-subject standard deviation $\bar{\sigma}$ of the original signal is reduced on average by a factor 1.5 for HbO and a factor 1.3 for HbR through processing with BLISSA^{2}RD. The SNR in each channel is improved on average by $3.64\,dB$ for HbO and by $2.70\,dB$ for HbR. For signals slower than $30\,s$ with $f_c = 0.033\,Hz$, the improvement is on average still $1.75\,dB$ and $1.61\,dB$ respectively. As before, in channel and subject subsets, reduction of $\bar{\sigma}$ / SNR improvement

are significantly higher up to factors around 3 / 10dB. To complement these findings, Figure 5.10 **C** shows average hemodynamic signals at position AF6 across whole 90s epochs of $n = 1-3$ conditions in 4 exemplary subjects. Figure C.3 in Appendix C.3 depicts average cleaned slow signals in all channels from three more participants. Generally, the higher n, the higher the average HbO increase / HbR decrease over the time-course of each round. Within individuals, variability in average responses of the signals across trials is distinctly higher in orginal compared to cleaned data.

5.2.5.3 Correlation Metrics in the Intensity Domain

The time embedding parameter τ and the co-modulation between raw intensity fNIRS channels/components and accelerometer target signals were investigated using the following correlation-based metrics:

1. By *Cross-correlation analysis in the channel domain*, the optimal time lag and corresponding Pearson correlation coefficient ρ between fNIRS intensity and accelerometer signals in the channel domain are investigated. We do this for all subjects, all blocks and all combinations of original/cleaned fNIRS signals and first three accelerometer components, a total of approx. $17 \times 12 \times 18 \times 3 = 11000$.

2. *Canonical correlation in BLISSA^{2}RD*: conventional (cross) correlation analysis cannot take the time-embedding, independent source decomposition, and CCA projection into account. We investigate the canonical correlation coefficients that result from the BLISSA^{2}RD CCA step, which projects decomposed fNIRS sources $\hat{\boldsymbol{S}}_x^{ERBM}$ and principal accelerometer components $\hat{\boldsymbol{S}}_z^{PCA}(\tau_d)$ into canonical space. We investigate all time embedding window lengths $\tau_d \in \{0,...,4.2\,s\}$, subjects and blocks, a total of $11 \times 17 \times 12 = 2244$ coefficients.

Figure 5.11 **A** shows scatter plots of the Pearson correlation coefficients ρ_o, ρ_c at the individual optimal lag between each fNIRS channel and first three principal accelerometer components (PaC) for original and cleaned data with $\tau \in \{0-0.96\,s\}$. For conventional fNIRS signals ($f_c = 0.2\,Hz$), the average correlation of fNIRS channels with the first PaC is 0.38 ± 0.22 vs. 0.09 ± 0.08 for original and cleaned data respectively and differs significantly ($p \ll 0.001$). For the second and third PaC, no significant statistical differences can be observed. Similarly, for slow fNIRS and movement signals with periods lower than 30s, ($f_c = 0.033Hz$) a less distinct but significant difference can be observed (0.32 ± 0.21 raw vs. 0.21 ± 0.16, $p \ll 0.001$) and none for the second and third PaC.

The histogram resulting from pooling all optimal time shifts found by cross-correlation analysis on single-channels of the original data (Figure 5.11 **B**) reveals the majority of optimal lags between $0-1.2\,s$, peaking around $0.6\,s$ with an average correlation of 0.41 ± 0.24 at the peak.

Figure 5.11 **C** shows average canonical correlation coefficients from the CCA step performed within BLISSA^{2}RD for different temporal embedding window sizes $\tau_{D=0-10} = 0-4.2\,s$ (compare Figure 5.4, and 5.8 step **III**). Coefficients correspond to identified pairs

of shared components in original fNIRS and accelerometer signals. Across all participants and blocks, the average canonical correlation coefficients increase for greater τ, and saturate toward longer time windows, where the most substantial increase can be observed for embedding windows that cover $0-1.8\,s$, coinciding with the findings from the cross-correlation analysis. On average, the first three pairs of extracted shared components show a strong and moderate- to strong canonical correlation of 0.85 ± 0.06, 0.71 ± 0.05 and 0.60 ± 0.05 for $\tau \geq 1.2\,s$.

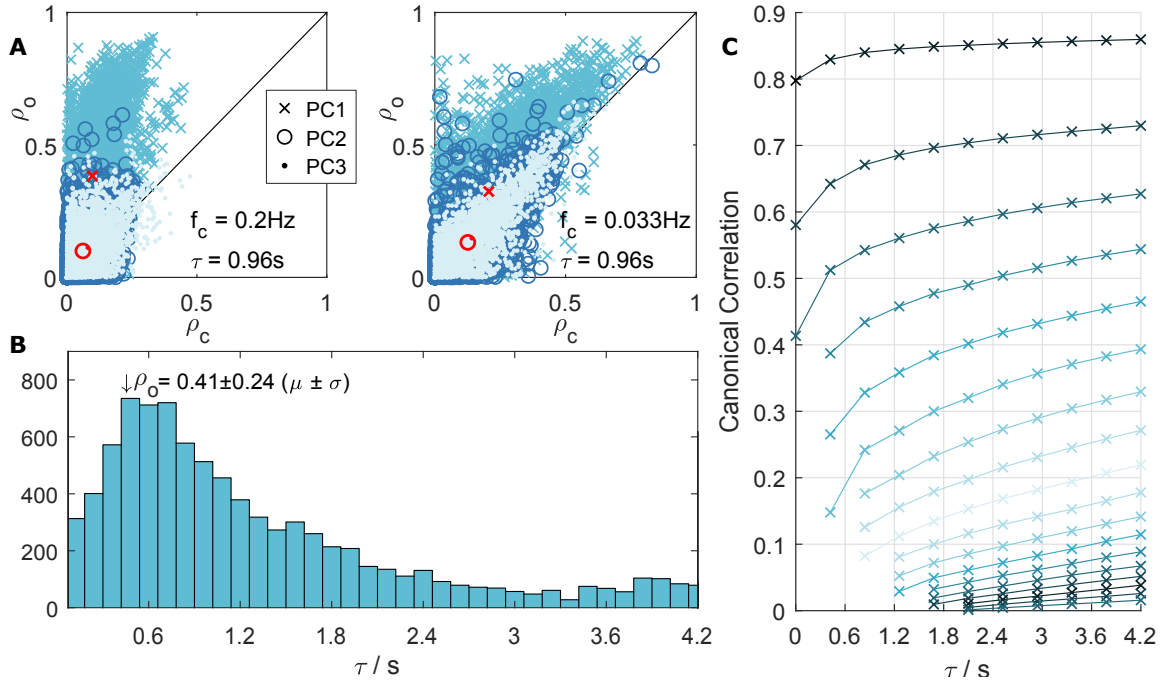

Figure 5.11: Correlation metrics. (**A**) Pearson correlation coefficients between channels of all subjects and first three principal accelerometer components for raw vs. cleaned data. (**B**) Histogram of optimal cross-correlation lags between raw fNIRS signals and accelerometer signals. (**C**) Average canonical correlation coefficients of shared components in fNIRS and accelerometer signals, extracted in BLISSA^{2}RD CCA step III), across all subjects and blocks

5.2.6 Discussion

An effective BSS framework and its implementation in the BLISSA^{2}RD method for fNIRS signal decomposition, analysis, and movement artifact rejection were proposed. In the following, key findings and their implications are discussed.

fNIRS Blind Source Separation ICA unmixing based on Entropy Rate Bound Minimization performed favorably over other tested ICA approaches that do not include both sample dependency and higher-order statistics. All methods performed better when applied to raw intensity signals compared to chromophores. Being linked by the logarithmic modified Beer-Lambert Law (mBLL) this is consistent with expectations in a linear mixing model. For a discussion of linear mixing and non-linearities, see also [DBM+13]. When decomposing

intensity signals, it is essential to note implications for the interpretation of extracted latent factors and their link to the chromophore domain.

The application of BSS is motivated with the separation of fNIRS signals into components that reflect independent physiological and non-physiological processes (e.g., Mayer Waves, respiration, pulse waves, motion and other systemic artifacts). However, the unmixing itself does not yield sources that can be interpreted physiologically without caution as such (see [HMG+14]). In contrast, they are of information-theoretical origin and should be projected back to channel space, i.e., by means of Equation 5.10 (see also Figure 5.4 E), for reliable physiological interpretation. From there, conversion from intensities to chromophores can be performed conventionally with the mBLL.

Time embedding against non-instantaneous coupling By integrating time- embedded multimodal CCA into the proposed BSS framework, non-instantaneous and non-constant coupling between shared latent processes within fNIRS and accelerometer signals was successfully tackled. Cross-correlation analysis yielded significant delays between fNIRS and movement signals of up to $1.8\,s$. The canonical correlation coefficients confirm these findings, showing the most substantial increase within time-embedding windows $\tau \leq 1.8\,s$. Overall, this emphasizes the importance of considering (co-)modulation delays in fNIRS signals.

Artifact rejection The manifestation of indirect movement artifacts varies strongly between subjects, movement conditions, and particular channels. BLISSA^{2}RD consistently performed well across all factors: On average/ in subsets, it attenuated movement artifacts by one/ up to two orders of magnitude, reduced the average within-subject standard deviation $\bar{\sigma}$ of evoked hemodynamic responses by a factor of 1.3/ up to 3, and increased its SNR by $3.64/2.70\,dB$ (HbO/HbR) up to $10\,dB$. Also for signals far slower than the semi-periodic movements ($f_c < 0.033\,Hz$) improvement could be observed ($1.75/1.61\,dB$). Behavioral changes in body posture (e.g., a tilt of the head) and movement stand to reason to be the cause and should be considered in approaches for rejection of indirect physiological movement artifacts. The impact of BLISSA^{2}RD artifact rejection on classification performance will be addressed in the next section.
Investigating the interaction between fNIRS and movement signals, cross-correlation between optimally time-lagged signals yielded only weak coefficients, noteworthy only for the first principal accelerometer component with ($\rho = 0.38$) on average. In contrast, BLISSA^{2}RD extracted shared components in fNIRS and movement signals that consistently yielded strong canonical correlations (up to 0.85) for three pairs of latent processes. As it can be assumed that at least three Euclidean degrees of freedom in movement have a considerable impact on fNIRS signals, we consider this a good indicator of success. Although powerful statistical analysis tools come at the cost of higher computational complexity, the average runtime for cleaning a block of $10\,min$ data (9×2 channels) in 2230 runs was still only $14\,s$ on an intel i7vPro notebook with Mathworks Matlab2017b.

Limitations BSS approaches require a minimum number of acquired channels to allow for stable decomposition into latent factors. For this reason, the proposed framework is not suitable in settings with very-low channel counts let alone single-channels. Single-channel

artifacts, i.e., individual optode decoupling or shifts, will not reliably be rejected. These can, however, also be minimized by lightweight instrumentation, headset and optode fixation designs and were observed only exceptionally in our M3BA-based headset. Analysis was performed on data recorded with a yet comparably low number of 9 optode pairs, which was found to be sufficient for the approach. Further investigation of the ICA decomposition performance and component stability in real-world data could take bootstrapping-based resampling approaches into account, as proposed by [MZK+02].

Due to the inherent multimodality of BLISSA^{2}RD, rigidly coupled accelerometer signals are a requirement that is currently not supported by the majority of commercial instruments. This may be a true limitation when not using M3BA or alike. Similar to trends in wearable EEG, however, it is expectable that wearable fNIRS will include accelerometers by default in the near future. Furthermore, the extension of any instrument with simple stand-alone accelerometer modules is fairly easily possible.

The endeavor to further establish the novel multimodal BLISSA^{2}RD framework will benefit from additional comparative evaluation with existing *univariate* methods [BCC+14; AH09], however, a straight-forward comparison is challenging. A way to create ground truths for method evaluation and comparison is to add prototypical evoked responses onto physiological baseline (resting state) signals. Metrics such as the area under the curve after artifact rejection can then be investigated. Transferring this approach to fNIRS in motion will require dedicated baseline measurements under realistic movement conditions. As the current experimental data only provides motionless resting periods, future work will have to incorporate such dedicated baseline measurements. For further investigation of the method's capability to identify and reject slow movement induced physiological components beyond conventional movement artifacts (e.g., optode shifts), a similar approach could aim at adding artificial channel specific movement induced fNIRS components to baseline signals, when corresponding prototypical movement signals are also provided. However, for the generation of realistic data for this purpose, there exists no model yet that describes the complex interactions between both, movement signals and induced fNIRS signal components sufficiently well.

Finally, adaptation of BLISSA^{2}RD towards real-time applications goes beyond the scope of this thesis and has not been investigated. Therefore, at this point, it remains unclear whether multimodal accelerometer-based adaptive filtering approaches would yield a better trade-off between movement artifact rejection and real-time capability.

Outlook and further applications The presented BSS framework is not limited to the analysis and rejection of artifacts and can easily be adapted to other purposes by exchanging methods and target signals, as the processing stages are modular. Possible expansions are:
(1) performing ICA decomposition with TDSEP [ZMN+00; ZM98] to exploit time structure (pronounced autocorrelation) in the signals, e.g., when targeting oscillatory components.
(2) Applying Independent Vector Analysis (IVA) [AAF14], the multivariate extension of ICA, which exploits dependencies between components as well as datasets.
It can be expected, that the performance of BLISSA^{2}RD can be further improved by expanding the degrees of freedom of provided movement target signals, e.g., by a combined accelerometer and gyroscope sensor. While accelerometer data as target signals for removal

of motion artifacts are a natural choice, other signals can be used for identification and analysis of co-modulating sources in the fNIRS time-domain. For target signals in the frequency domain, e.g., EEG band-power features, other methods such as those of the SPoC family [DBS+15; DBM+13] are predestined.

The novel BSS framework presented can serve as an introduction to a new type of multivariate methods for the BSS analysis of fNIRS signals and as a blueprint for artifact rejection in complex environments beyond the applied paradigm. In combining strengths with existing complementary methods such as multi-distance approaches, we see a promising way to achieve the robustness desired for new medical and research-oriented ambulatory neuroimaging applications.

Summary

In the analysis of functional Near-Infrared Spectroscopy (fNIRS) signals from real-world scenarios, artifact rejection is essential, but currently there exists no gold-standard. Although a plenitude of methodological approaches implicitly assume the presence of latent processes in the signal, elaborate Blind-Source-Separation methods have rarely been applied so far due to challenging fNIRS characteristics, e.g., non-instantaneous and non-constant coupling and presence of component dependencies.

In this Section, a novel suitable BSS framework was presented that tackles these issues by incorporating (1) Independent Component Analysis methods that exploit both higher order statistics and sample dependency, (2) multimodality, i.e., fNIRS with accelerometer signals, and (3) Canonical-Correlation Analysis with temporal embedding. This enables advanced analysis of signal components and rejection of motion-induced physiological hemodynamic artifacts that would otherwise be hard to identify.

A method for Blind Source Separation and Accelerometer based Artifact Rejection and Detection (BLISSA^{2}RD) was implemented and evaluated on the novel multimodal dataset with freely moving subjects. We made use of conventional metrics based on 1st and 2nd order statistics, Signal-to-Noise Ratio, and simulations. Across 17 subjects, the method rejects movement induced artifacts by up to 2 orders of magnitude and improves the SNR of hemodynamic responses in single channels by up to $10\,dB$, and on average by $3.64/2.70\,dB$ (HbO / HbR). Simulations showed improved decomposition performance in the presence of source dependence, as is the case in fNIRS, when taking both higher order statistics and sample dependence into account for ICA. The framework and methods presented can serve as an introduction to a new type of multivariate methods for the BSS analysis of fNIRS signals and as a blueprint for artifact rejection in complex environments beyond the applied paradigm. In the next Section, BLISSA^{2}RD will be put to practice for artifact rejection in multimodal workload classification and its impact on classification performance will be investigated.

5.3 Workload in Freely Moving Operators: A Feasibility Study

In this last Section, based on publication [vMB+18], all previous contributions are linked: The result is a first feasibility study on the workload classification of moving operators under comparatively challenging and realistic experimental conditions.

5.3.1 State of the Art and Aims

The assessment of mental workload (MWL) using neurophysiological markers is a central feature of research and development in fields such as Neuroergonomics, as outlined in Section 4.2. Consequently, an increasing number of studies have investigated its classification using EEG [SKDG+16], fNIRS [HHF+14; AOI+13; ASB+12], or more recently, hybrid EEG-fNIRS [AGO17; LAS17; CBE12]. While most EEG and fNIRS studies are motivated by real-life applications, only a minority is specifically designed for them [SKDG+16; AOI+13; ASB+12], and the majority requires participants to sit and move as little as possible. However, first studies prove the feasibility of non-invasive neurophysiological measurements outside of the laboratory [BAD+16; MTD+08], for instance EEG in users walking naturally outdoors [DME+12], in car driving [HKK+14; KDB+07] and fNIRS in outdoor bicycling [PKK+14].

The success of such endeavors depends both on the availability and suitability of miniaturized wearable instrumentation, and the subsequent processing approaches that have to face challenging signals. In real-world scenarios, movements are frequent and lead to high contamination with artifacts. Furthermore, the number of channels available for biosignal acquisition is usually limited. These conditions render a considerable number of approaches useless and are particularly of concern when neurophysiological signals should not be exploited together with artifacts in an undifferentiated manner. In fNIRS-based MWL studies with sitting participants, systemic physiological artifacts are typically rejected by low-pass filtering, and optode shifts - if present - are removed by application of methods as discussed in Section 5.2.1. An advantageous property is the immunity of fNIRS to electro-physiological artifacts, e.g., eye movements. In contrast, EEG studies have to take great care to minimize EOG interference [SKDG+16], as these artifacts can carry significant task-discriminative information and overlap with the alpha- and theta- bands that are typically of interest.

Aims

The aim of this Section is a first exploration of the single trial classification of mental workload based on neurophysiological markers under challenging conditions, namely a low number of channels and many movement artifacts. While the given conditions will limit classification accuracies and methodological approaches, we still try to separate neurophysiological signals from other signals by rejecting artifacts as strictly as possible. Following up on the previous Section, we will first investigate the impact of BLISSA^{2}RD artifact rejection on fNIRS classification performance and then integrate fNIRS and EEG in a hybrid classification approach.

5.3.2 Challenges

In the analysis and classification of brain states based on machine learning methods [BTL+08; BLT+11; LBD+11], a common problem is the exploitation of movement artifacts and task-related changes of non-neuronal origin by classification methods, leading to improved discriminability. This is a known pitfall, especially in BCI [BAD+16; MTD+08]. Aside from adressing the general challenges in multimodal signal processing (Section 5.1.3), the outlined endeavor has to therefore focus in particular on the extraction of neurophysiological features from noisy background and only few channels, aiming to classify task-related signals of neuronal origin while minimizing the impact of those from non-neuronal origin. The experimental paradigm aims to minimize task-related information in movement artifacts by randomization and constant movement conditions across n-back tasks. Nevertheless, behavioral changes that can be linked to task-execution and performance, have to be considered. Among them are changes in speed and frequency of eye movements and blinking, unconscious teeth-clenching or change in face- and neck-muscle tension, and changes in posture, reaction times and -speed. The following signal processing pipelines aim to minimize such influences and include steps that may sacrifice classification accuracy for better separability between neural and non-neuronal signals, wherever necessary.

5.3.3 Signal Analysis Pipelines

We compare classification performances exploiting EEG, EOG, fNIRS and ACCEL information of all 17 participants of the main study from Chapter 4 with 12 rounds per n=1,2,3-back and Resting condition and 48 for 0-back. From the corresponding rounds, we extract epochs $e_{Rest,1,2,3} \in \{1,...,12\}$ and $e_0 \in \{1,...,48\}$ of different length: Short epochs contain the first $30\,s$, long epochs the first $90\,s$ of a round after the instruction period, respectively. While the former allow classification against the resting state and 0-back baseline, both of which were limited to $30/36\,s$ periods by protocol, the latter allow only the investigation of 1,2,3-back conditions against each other but provide more realistic time spans of task involvement. No acquired trials, rounds or blocks were rejected. Filters applied are zero-phase IIR filters with butterworth characteristic (ZP-B). In addition to the focus on neurophysiological features here, the grand average results of an EDA signal analysis are provided in Figure C.1 in Appendix C.1. Including the considerations in Section 4.3.2, EEG and fNIRS feature selection and preprocessing is based on the current understanding of cognitive workload-related neurophysiology and will be described in the following. The overall signal processing pipeline is depicted in Figure 5.12. The statistical tests employed are paired t-tests.

5.3.3.1 fNIRS Preprocessing and Feature Extraction

I) we investigate the impact of BLISSA^{2}RD artifact rejection on fNIRS classification performance on short epochs: We compare unimodal conventionally filtered ($< 0.2\,Hz$) and slow ($< 0.033\,Hz$) fNIRS signals for both the original and cleaned data.

II) for the comparison to and fusion with other modalities, we perform analysis on both short and long epochs using the cleaned data and only slow signals.

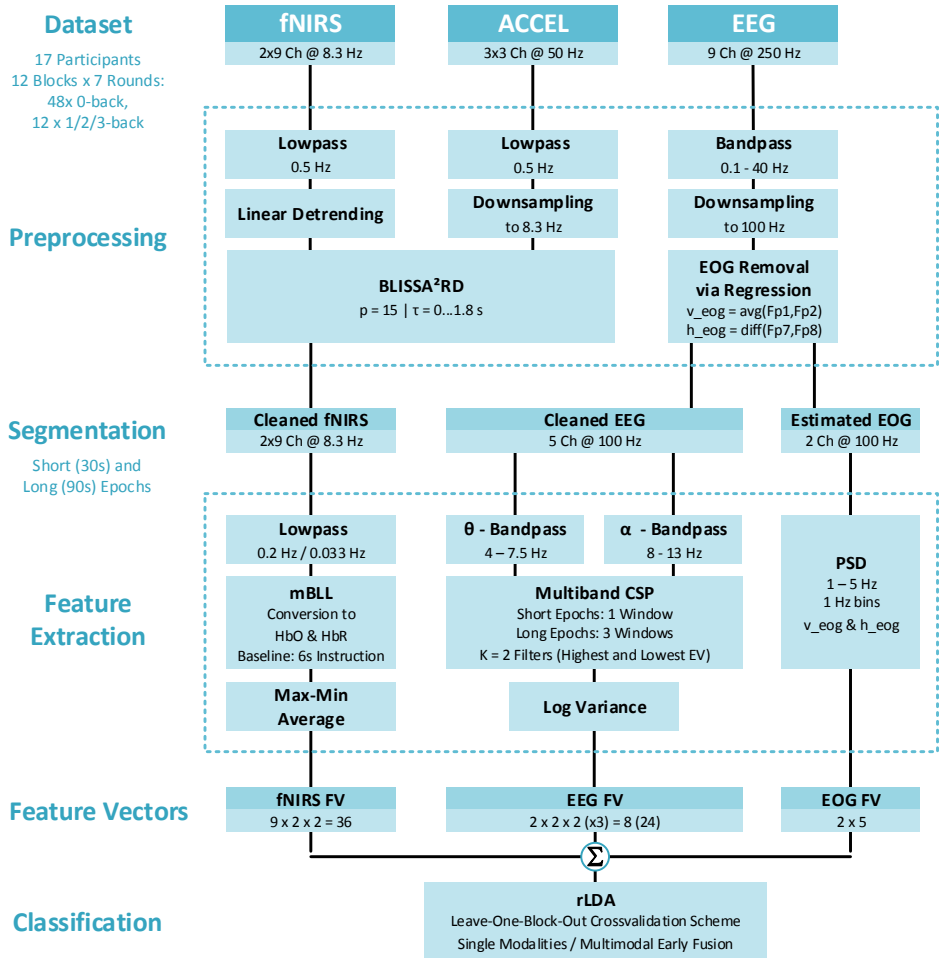

Figure 5.12: Pipeline for uni- and multimodal workload classification. Feature fusion before rLDA.

Preprocessing: Raw fNIRS Signals are linearly detrended for each experimental block and then low-pass filtered with $f_{c1} = 0.5\,Hz$ (4^{th} order ZP-B). BLISSA^{2}RD artifact rejection is performed block-wise with ERBM-ICA whitening filter parameter $p = 15$ and time embedding parameter $\tau_{D=0-5} \in \{0, 0.36, ..., 1.8\,s\}$ to yield cleaned signals. We do not perform dedicated artifact rejection of optode shifts, as these were observed extremely rarely in the signals acquired with the lightweight M3BA headset. Raw intensities are then transformed into optical densities, lowpass-filtered with $f_{c2} \in \{0.2, 0.033\,Hz\}$ (4^{th} order ZP-B) and converted to HbO/HbR concentrations by means of the modified Beer-Lambert Law implemented in the HomER toolbox [HDF+09]. We use the $6\,s$ instruction period before each epoch for baseline calculation in the mBLL. For the comparison and fusion with other modalities, we only use $f_{c2} = 0.03\,Hz$ low pass filtered signals.

Feature extraction: For each channel, we extract the difference between maximum and minimum HbO/HbR activation, and their averages. This baseline-referred average and activation amplitude has been adopted in many mental activation studies [LAS17; ASB+12; FMS+12; CWM+04] and yields a total of $9\,\text{ch} \times 2 \times 2 = 36$ features per epoch.

5.3.3.2 EEG Preprocessing and Feature Extraction

Preprocessing: EEG data is bandpass filtered to $0.1-40\,Hz$, employing a 3rd order ZP-B filter, and subsequently down-sampled to $100\,Hz$. For the suppression of motion- and eye movement artifacts, a variety of EOG rejection methods were investigated for their suitability to low-channel data, including common PCA-based approaches and the weights-adjusted variant of second order blind identification (WASOBI) [GHDCA+06]. However, all methods showed residual discriminative EOG information; BSS based methods are likely to have underperformed due to the low number of channels available. Employing the strictest remedy, we therefore remove EOG signals by means of a regression approach as described in detail in [PSG+05], sacrificing 4 out of 9 channels. Following the same procedure as employed by Schultze-Kraft et al. [SKDG+16], we use the difference between electrodes $F7$ and $F10$ and the average of electrodes $Fp1$ and $Fp2$ to estimate horizontal and vertical EOG activity respectively and excluded all four electrodes in the subsequent EEG analysis. As EMG activity is most strongly manifested above $20\,Hz$ [WPF+07], the contamination by muscle activity is minimized by selecting features from frequency bands only below $14\,Hz$.

Feature extraction: As motivated in Section 4.3.2, we focus the EEG feature extraction on spatial theta ($4-7.5\,Hz$) and alpha ($8-13\,Hz$) activity. The 5-channel EEG data is band-pass filtered (4th order ZP-B) for each band $f \in \{\theta, \alpha\}$, yielding two sets $\boldsymbol{X}_f$. For adjacent $30\,s$ windows $d \in \{1,2,3\}$ within each epoch e, we extract spatial filters $\boldsymbol{w}_f$ for each frequency band, using the Common Spatial Patterns algorithm. From the extracted CSP filters, we apply $k \in \{H_1, H_2, L_1, L_2\}$, the two with the largest and smallest absolute Eigenvalue, respectively. On the thus obtained 2×2 spatially filtered components per band, we calculate Log Variance features according to $F_{f,k}(e,d) = \log\left(\mathrm{Var}\left(\boldsymbol{w}_f^{k\top}\boldsymbol{X}_f(e,d)\right)\right)$. This yields 8 features for short epochs with only one window and 24 for long epochs with three windows.

To investigate the added value of the separated EOG, we extract power spectral density (PSD) features in the band of $1-5\,Hz$ with $1\,Hz$ bins from the two estimated horizontal and vertical EOG channels, yielding a total of 10 features per epoch.

5.3.3.3 Classification and Validation

Classification of n-back conditions is performed in a leave one block out cross-validation using regularized LDA (rLDA) with automatic shrinkage parameter selection [SS05; LW04; LBD+11]. The applied sampling in a leave one block out manner ensures independence between cross-validation blocks, which equal the 12 experimental blocks. Classifier accuracies are computed class-wise normalized. In the investigation of I) BLISS^{2}RD impact, we focus on short epochs and classification against the resting state and baseline 0-back task, and perform binary as well as multi-class classification. In II), the comparative unimodal and hybrid cases, as CSP is only defined for binary problems, we focus on binary $1\,vs\,1$ and $1\,vs$ many classification of short as well as long epochs. In hybrid cases, we perform early fusion, classifying features of different modalities jointly with rLDA. For further validation, we additionally perform the identical classification and processing pipeline, skipping only BLISSA^{2}RD and EOG-regression based artifact removal.

5.3.4 Results

5.3.4.1 I) Impacts of BLISSA^{2}RD on fNIRS Classification Performance

The impact of BLISS^{2}ARD artifact rejection on classification performance is summarized in Figure 5.13 and Table 5.3 for short epochs low-pass filtered with $f_c \in \{0.2, 0.033\,Hz\}$.

For all binary condition sets "0 vs 1/2/3" and "Rest vs 0/1/2/3", classification yielded overall average performances of $\mu^n_{raw} > 81\%$ and $\mu^n_{clean} > 76.2\%$. 3, 4 and 5 classes were discriminated with accuracies of at least $\mu^n_{raw} > 48.1\%$ and $\mu^n_{clean} > 41.9\%$ in the 5-class case. While the performance does not significantly depend on signal bandwidths reduced by f_c, removal of movement artifacts leads to a distinct and significant drop in average classification accuracy across subjects and conditions ($\Delta\mu^{7\times 2cls} = 4.9\%$, $\Delta\mu^{3cls} = 8\%$, $\Delta\mu^{4cls} = 5.2\%$, $\Delta\mu^{5cls} = 7.1\%$; $p^{2cls} \ll 0.001$, $p^{3,4,5cls} < 0.001$).

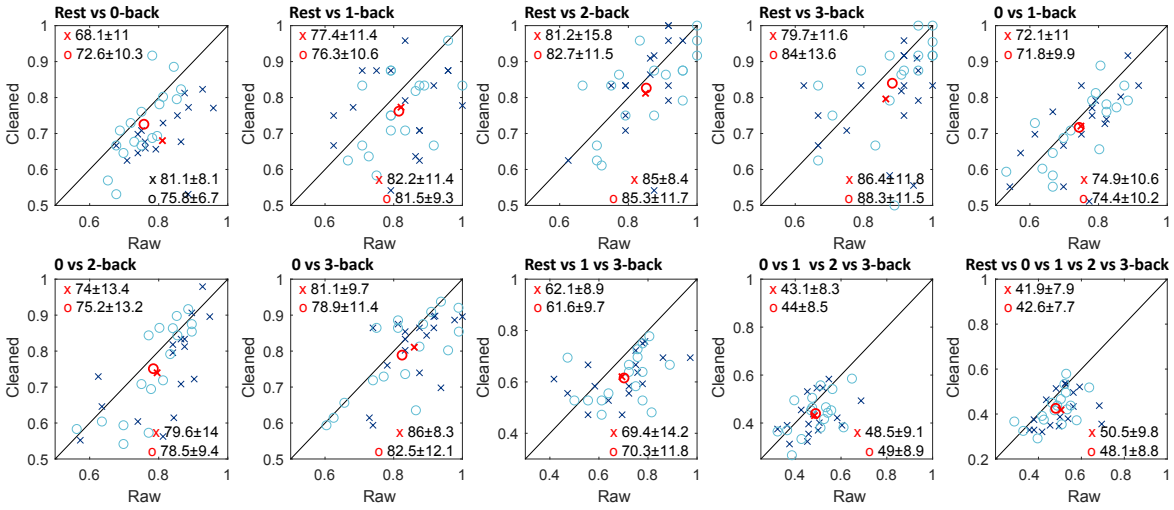

Figure 5.13: n-back workload classification in raw vs. cleaned signals. Average classification performance per subject for $f_c = 0.2\,Hz$ (dark blue crosses) / $f_c = 0.03\,Hz$ (light blue circles). Red: Average across subjects.

Classes	Accuracy Raw $\mu \pm \sigma$		Accuracy Clean $\mu \pm \sigma$		Chance level	ΔRaw-Clean	
	$f_c = 0.2$	$0.03\,Hz$	$f_c = 0.2$	$0.03\,Hz$		$f_c = 0.2$	$0.03\,Hz$
Rest vs 0	81.1 ± 08.1	75.8 ± 06.7	68.1 ± 11.0	72.6 ± 10.3	50%	13.0	03.2
Rest vs 1	83.2 ± 11.4	81.5 ± 09.3	77.4 ± 11.4	76.3 ± 10.6	50%	05.8	05.2
Rest vs 2	85.0 ± 08.4	85.3 ± 11.7	81.2 ± 15.8	82.7 ± 11.5	50%	03.8	02.6
Rest vs 3	86.4 ± 11.8	88.3 ± 11.5	79.7 ± 11.6	84.0 ± 13.6	50%	02.4	04.3
0 vs 1	74.9 ± 10.6	74.4 ± 10.2	72.1 ± 11.0	71.8 ± 09.9	50%	02.8	02.6
0 vs 2	79.6 ± 14.0	78.5 ± 09.4	74.0 ± 13.4	75.2 ± 13.2	50%	04.4	03.3
0 vs 3	86.0 ± 08.3	83.5 ± 12.1	81.1 ± 09.7	78.9 ± 11.4	50%	04.9	04.7
Rest vs 1 vs 3	69.4 ± 14.2	70.3 ± 11.8	62.1 ± 08.9	61.6 ± 09.7	33%	07.3	08.7
0 vs 1 vs 2 vs 3	48.5 ± 09.1	49.0 ± 08.9	43.1 ± 08.3	44.0 ± 08.5	25%	05.4	05.0
Rest vs 0 vs 1 vs 2 vs 3	50.5 ± 09.8	48.1 ± 08.8	41.9 ± 07.9	42.6 ± 07.7	20%	08.6	05.5

Table 5.3: Average classification performances across subjects. Highlighted column: typical L vs. H classification in literature, best performance. ΔRaw-Clean: Performance correction by artifact rejection in %.

5.3.4.2 II) Unimodal and Multimodal Workload Classification

Results of the comparative classification of operator workload in motion with EEG, fNIRS and hybrid combinations are summarized in Figure 5.14 and Table 5.4.

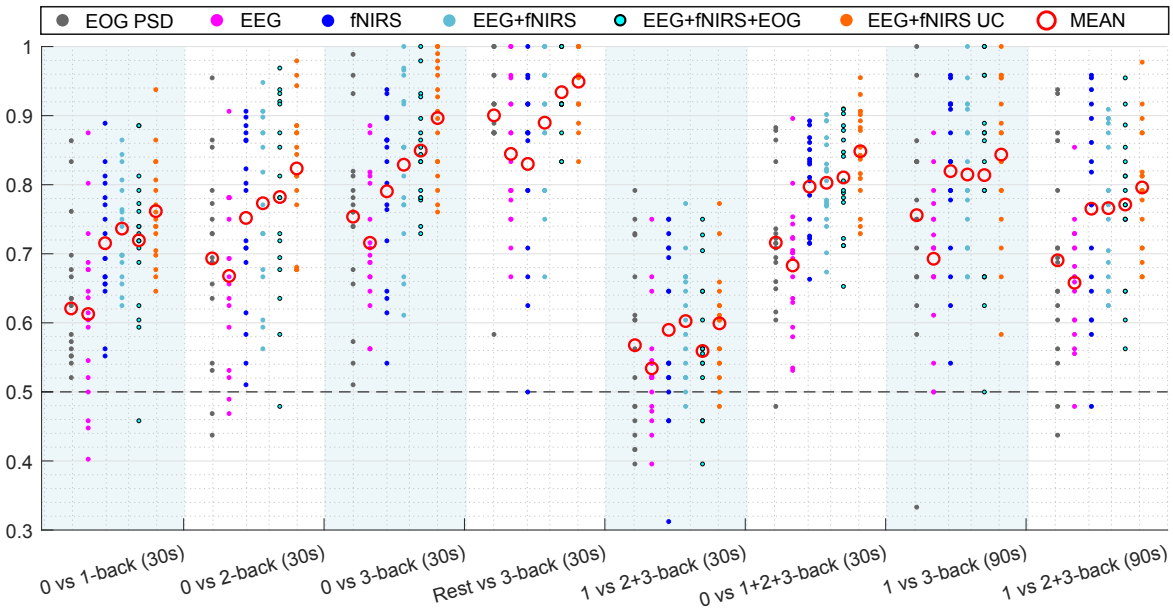

Figure 5.14: Operator Workload Classification: Accuracies of single participants (dots) and mean across participants. Unimodal classification: EOG, EEG and fNIRS. Hybrid classification: EEG+fNIRS, EEG+fNIRS+EOG and EEG+fNIRS UC (no artifact rejection with BLISSA^{2}RD and no regression-based EOG removal).

Classes	EOG	EEG	fNIRS	EEG + fNIRS	EEG + fNIRS +EOG	EEG + fNIRS Uncleaned	ΔHybrid
0 vs 1 (30s)	62.2 ± 12.8	61.3 ± 12.3	71.6 ± 09.0	73.7 ± 07.2	72.0 ± 10.4	76.2 ± 07.5	2.1%
0 vs 2 (30s)	69.4 ± 13.7	66.8 ± 11.8	75.2 ± 12.7	77.4 ± 12.0	78.3 ± 13.6	82.4 ± 09.7	2.2%
0 vs 3 (30s)	75.4 ± 13.2	71.6 ± 09.4	79.1 ± 11.7	82.9 ± 11.6	85.0± 07.7	89.7 ± 08.1	3.8%
Rest vs 3 (30s)	90.1 ± 09.2	84.5 ± 10.0	83.0 ± 13.1	89.0 ± 09.6	93.4 ± 05.6	95.0 ± 05.0	6.0%
1 vs 2+3 (30s)	56.8 ± 12.7	53.5 ± 08.5	59.0 ± 12.2	60.3 ± 08.1	56.7 ± 11.8	60.0 ± 07.5	1.3%
0 vs 1+2+3 (30s)	71.7 ± 10.3	68.4 ± 09.2	79.8 ± 06.8	80.3 ± 06.6	81.1 ± 07.7	84.9 ± 06.6	0.5%
1 vs 3 (90s)	75.6 ± 15.1	69.3 ± 10.4	82.0 ± 12.0	81.5 ± 10.2	81.4 ± 14.0	84.4 ± 11.3	-0.5%
1 vs 2+3 (90s)	69.1 ± 14.5	65.9 ± 8.7	76.6 ± 14.5	76.7 ± 10.3	77.2 ± 10.5	79.6 ± 08.9	0.1%

Table 5.4: Mean ± std classification performances across subjects in different modalities and combinations. ΔHybrid: Improvement of hybrid EEG+fNIRS classification over max(EEG,fNIRS). Highlighted rows/columns: Most relevant in application-oriented scenarios.

Overall, several trends can be observed: Unimodal fNIRS and EOG-based classification generally outperform EEG-based classification, and accuracies of all single and hybrid approaches increase with greater difference between workload levels. EEG notably improves classification of fNIRS in hybrid EEG+fNIRS approaches for short epochs ($0.5\,\% < \Delta < 6\,\%$) but not for long epochs. Short epochs enable a good discrimination between baseline 0-back and resting tasks against increasing 1,2,3-back workload levels, but do not allow a good differentiation between higher workload levels. In contrast, those can be discriminated well in longer epochs, where EEG and EOG-PSD features however do not notably improve

unimodal fNIRS classification in a hybrid approach. Toward application-oriented scenarios, the following cases are of special interest:

(1) The general detection of any shift from a baseline toward increased cognitive performance (0 vs 1+2+3-back) within short 30 s windows. For this case, average accuracies of 68.4 % (EEG) 79.8 % (fNIRS) and 80.3 % (EEG+fNIRS) were achieved.

(2) The Differentiation between moderate and high workload (1 vs 3-back) within longer 90 s windows. Here, we achieve average accuracies of 69.3 % (EEG) 82.0 % (fNIRS) and 81.5 % (EEG+fNIRS).

Across both conditions, classification was significantly better than chance level for 67.7 % (EEG), 91.2 % (fNIRS) and 94.1 % (EEG+fNIRS) of all participants (one-sided binomial, $\alpha = 0.05$). While unimodal classification of EOG outperforms EEG, including EOG features to hybrid neurophysiological fNIRS+EEG features does not always provide an added value ($-3.6\,\% < \Delta < +4.4\,\%$). Hybrid classification of features from uncleaned EEG and fNIRS data (EEG+fNIRS UC, no artifact removal) outperforms all others consistently.

5.3.4.3 Observations from Validation

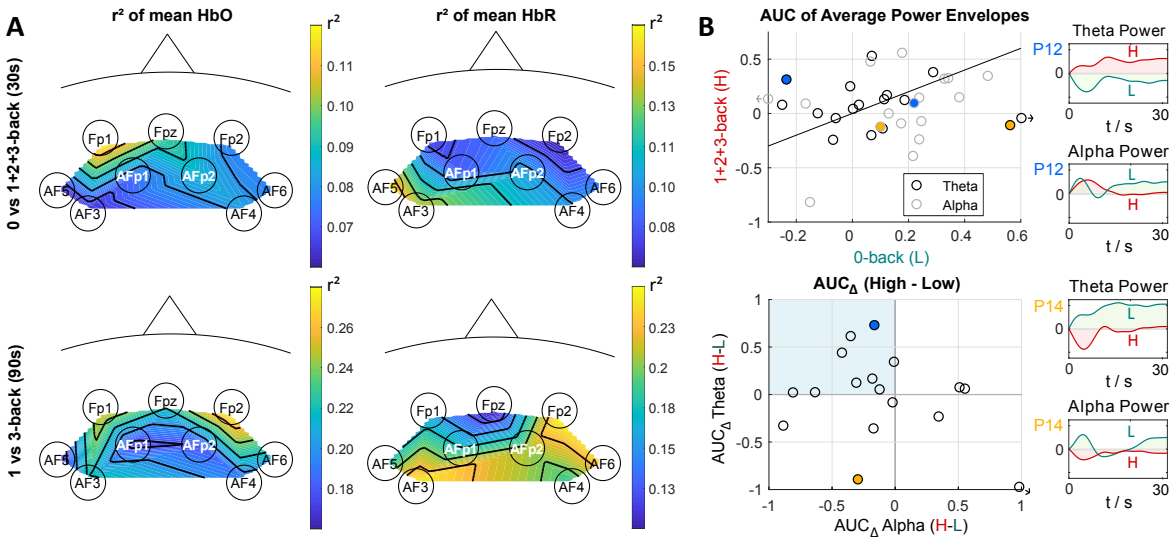

Figure 5.15: A: Grand average R² values for mean HbO/HbR features. **B**: AUC and ΔAUC of the average α and θ band power envelope time courses of the first CSP component in 0 (L) vs 1+2+3-back (H) discrimination (30 s) and corresponding time courses of two exemplary participants P12 and P14.

For further validation, the discriminative value of univariate fNIRS features in the context of their corresponding channels was investigated in terms of their point biserial correlation coefficient (r^2-value). Working memory tasks have been shown to evoke cortical activation in the dorsolateral and ventrolateral prefrontal cortex in many previous studies using PET and fMRI ([SJK96; OML+05; RLJS+00]) and fNIRS [AOI+13; PBW+10; SES+08]. The average r^2 values across participants indicate consistency with these findings, showing higher discriminability in mean activation over spatially well distinguishable fronto-lateral regions, as exemplified for both 0 vs 1+2+3-back and 1 vs 3-back classification in Figure 5.15 **A**.

In EEG, we investigated CSP components and scalp patterns calculated on the whole dataset for each band $f \in \{\alpha, \theta\}$. As patterns of only 5 centered EEG channels offer only limited explanatory power, we focus here on the respective CSP components with the highest eigenvalue, projected on the epochs e of the segmented data: $\hat{s}_{e,f} = \boldsymbol{w}_{H_1,f}^{\top} \boldsymbol{X}_{e,f}$. We investigated the corresponding power envelopes of the component's time series, averaged over all epochs of the same condition n: $\mu_{n,f}^{env} = \mathrm{E}\left(\mathrm{penv}(\hat{s}_{e,f}^{n})\right)$. Single epoch power envelope time courses were baseline-referenced to the end of each previous instruction period and low-pass filtered to $0.1\,Hz$ with a 3rd order ZP-B before averaging. We then calculated the area under the curve (AUC) of the average power envelopes for each band and condition, and the AUC of the difference between high (H) and low (L) conditions ($AUC_{\Delta,f} = AUC(\mu_{H,f}^{env} - \mu_{L,f}^{env})$. Figure 5.15 **B** depicts results for the 0 vs 1+2+3-back discrimination task:

Average power envelopes develop over time. 11 out of 17 subjects show a positive correlation of theta-band power with workload (see also 1st and 2nd quadrant of ΔAUC plot) and 13 a negative correlation of alpha-band power with workload (2nd and 3rd quadrant of ΔAUC plot). 9 out of 17 subjects show both an increase in theta and a decrease in alpha with increasing task load (2nd quadrant).

Additionally, exemplary CSP patterns and comparative classification accuracies for EEG data with and without EOG removal are provided in Figures C.4 & C.5 in Appendix C.4.

5.3.5 Discussion

Despite the challenging experimental conditions that include a multisensory scenario, a high number of movements and a low number of channels, we successfully discriminated different workload levels across freely moving operators. Within short epochs, deviations from resting and baseline tasks were discriminated best by the hybrid EEG+fNIRS approach – on average 73.7 % (0 vs 1-back) < 80.3 % (0 vs 1+2+3-back) < 89 % (Rest vs 3-back). Considering the temporal complementarity of fast EEG signals to delayed, slower hemodynamic responses in fNIRS, the average performance increase of +2.7% due to hybridization in short epochs is in line with expectations. Within longer epochs, fNIRS performed best in discriminating between moderate to high workload with an average 82% accuracy for 1 vs 3-back, and hybridization did not improve overall accuracy. However, it increased the number of participants classified significantly above chance level to 16 out of 17, an increase of 6%.

These results are comparable with those reported by other EEG-fNIRS-based n-back studies with sitting participants. In the classification of increased workload against a 0-back baseline, average classification accuracies of up to 74.0/92.0/93.8 % (fNIRS/EEG/Hybrid) using 19 fNIRS channels and 19 EEG channels [AGO17] and 65.6/79.2/83.1 % (fNIRS/EEG/Hybrid) using 28 EEG and 16 fNIRS channels [LAS17] were reported. In single fNIRS mental arithmetic-based workload studies, average accuracies of 80.5 % in 1 vs 3-back (8 fNIRS channels) [HHF+14] or 79.7 % [BSP+11], 72.6 % [PKC12] and 77.4 % [SC13] were reported, as reviewed amongst others by [NH15].

Classification methods exploit any task-related information, including that introduced by artifacts. When solely brain signals should be used, minimizing the impact of residual

artifacts is typically desired. For this purpose, strict artifact rejection, restrictive feature selection, comparative classification and physiological validation were performed. In the following, some of the resulting implications for the interpretation of the classification results are discussed.

On average, reaction times in each $6s$ trial increase with task-difficulty (see Section 4.3.3). As we employ fNIRS mean and amplitude difference features of signals filtered to periods $\geq 30s$ and use only phase-independent EEG band power features, it is assumed that these effects play a negligible role.

In addition to conventional low-pass filters for the rejection of physiological artifacts in fNIRS, multimodal BLISS^{2}RD was employed for the removal of movement induced artifacts. Artifact rejection reduces the classification performance on average by 5.05 % observable for both normal ($f_c = 0.2Hz$) and slow ($f_c = 0.033Hz$) low pass filtered signals. The latter might be indicative of the presence of slow, task-related posture changes and movements and emphasizes the importance to reject slow indirect movement artifacts that would otherwise remain untouched by simple low-pass filtering. Movement-independent, task-related changes in tissue perfusion and other systemic components (e.g., PC2-3 in Figure 5.2) have been documented [ZNH16; SKM+14]. At this time, such influences cannot be ruled out with certainty, however: (1) HbO/HbR time courses (as exemplified in Figure 5.10 in the previous Section) show comparable behavior as previously reported, for instance in [AOI+13]. (2) the spatial specificity of R^2 values and their accordance with fMRI/PET/fNIRS findings reported in literature imply that superficial global components are not of major concern in this study.

In future approaches, an optimal solution could be the combination of BLISSA^{2}RD with complementary spatially resolved multi-distance approaches [FFP+98; SKM+14].

In several hybrid studies, unimodal classification of EEG outperforms fNIRS significantly. While the low EEG performance in this study is certainly also due to the low number of channels, the strict removal of EOG is likely another reason: Surprisingly many previously mentioned hybrid studies use PSD features of the full EEG spectrum without dedicated EOG removal other than by visual inspection and discarding of strongly affected epochs. The exploitation of ocular activity in such cases is likely, and our pipeline on uncleaned data yields comparable results: See (EEG+fNIRS UC) in Figure 5.14 and a direct comparison of unimodal EEG classification with and without prior EOG removal in Figure C.4 in Appendix C.4, where artifact rejection leads to an average decrease in the classification accuracy of 8.7% across subjects and conditions.

This is also in line with observations from spatial patterns obtained by CSP analysis of EEG signals with and without previous regression-based EOG removal, as exemplified in Figure C.5 in Appendix C.4. For most participants, the patterns corresponding to the first CSP component (highest eigenvalue) from uncleaned data show typical ocular effects, for instance strong prefrontal lateralization. These disappear after EOG removal, indicating a successful rejection. The investigation of averaged power envelopes of CSP components from EEG after EOG removal show a positive correlation between theta-power and workload in 65 %, an inverse behavior in alpha-power in 76 % and both in 53 % of all participants. These trends are consistent with previously reported findings in workload literature [GS03; HLK+09] and are good further indicators that neurophysiological features and not artifacts

were classified. However, it is unclear to what extent these band-power trends should be considered as sole legitimate indicators of workload, as (1) The experimental paradigm requires engagement on a variety of levels, including spatial and visual attention, working memory, and movements and (2) Other studies have shown that, e.g., expected negative correlation of workload with alpha power, can fail to appear [SKDG+16], can be opposite [JT02] or depend on the specific task, and strategy of participants [CCD+03; Kli99]. In any case, an inverse relationship between alpha- and theta band-power further supports the absence of residual ocular activity, as electro-physiological artifacts typically lead to positive band-power correlations.

In an improved future approach, the sacrifice of frontal channels should be avoided by integrating unobtrusively, e.g., dryly, measured EOG into the headset, which is inherently already supported by the M3BA architecture.

In the presence of the strict artifact rejection and restrictive feature selection performed, and the results from the comparative classification and validation, it is plausible that the discriminative power in the classifiers is not based on artifacts. However, due to the challenging conditions in this experiment, a residual level of uncertainty remains, which is a typical and commonly known issue in the classification of biosignals in the domain of BCI [BAD+16; MTD+08].

Across condition sets, a clear trend toward improvement of classification robustness by the combined exploitation of EEG+fNIRS can be shown in short epochs. Although without statistical significance, likely due to the under-performance of the low-channel EEG, this is in line with statistically significant findings in other studies [SKM+18; SvB+17; AGO17; LAS17; HFT+15; FMS+12]. While the overall results indicate the successful reproduction of physiological and discriminatory findings of hybrid studies under static conditions, they provide further validation evidence for the employed instrumentation and paradigm and show the feasibility of studies in moving participants toward real-world conditions.

Summary

In this Section, we successfully discriminated different workload levels across freely moving operators despite the challenging experimental conditions that include a multisensory scenario, many movements and a low number of channels. We achieved (1) average hybrid accuracies of 80.3% in the detection of increased workload from a baseline task within 30 s, (2) 81.5% in the discrimination of moderate to high workload within 90 s, and (3) significantly better classification than chance level in 94.1% of cases. The results are in line with previously reported findings from hybrid working memory based studies under less challenging conditions. Experimental design, employed artifact rejection approaches, feature selection and validation results indicate that classification is based on neurophysiological signals only. Making use of hybrid EEG-fNIRS feature fusion and fNIRS-Accelerometer sensor fusion, the presented approach exploits multiple modalities toward the robust estimation of cognitive workload outside of conventional lab environments and under real-life conditions.

Chapter 6

Summary and Conclusion

It is still a long way to go to completely understand human cognition and brain functions (if ever possible within a fathomable scope). Yet, 150 years after the initially discussed manual dissection and examination of Gauss' brain, exploration of the brain is not restricted to anatomical features anymore: The emergence of advanced tools for investigating and interfacing with human brain function enables science and medicine to expand significantly the understanding of its physiology, function, and dysfunction. For this exploration to progress beyond laboratory confinement, novel tools are needed to enable reliable, unobtrusive, robust and hazard-free integration of neurotechnology into real-world scenarios. To this end, this thesis exploits new approaches that address the simultaneous acquisition and utilization of multimodal brain and body signals (see overview of contributions in Figure 6.1).

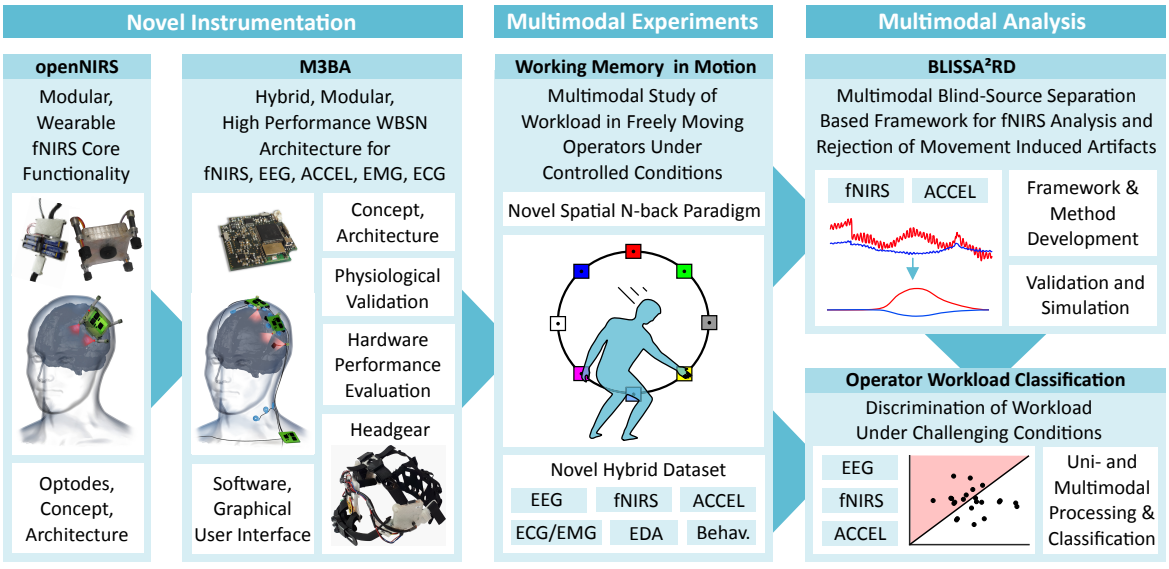

Figure 6.1: Summary of contributions of this thesis: the two-step development of miniaturized openNIRS and M3BA, hybrid multimodal EEG-fNIRS instrumentation for the mobile acquisition of brain and body signals. Employing M3BA in a customized, spatial n-back paradigm made possible a multimodal workload experiment in freely moving participants. Making use of this unique data set, BLISSA^{2}RD was developed: a multimodal framework for the analysis of fNIRS signals and the rejection of motion artifacts. Finally, linking all contributions paved the way for the successful classification of mental workload in moving operators.

Novel Instrumentation

Main Contributions This thesis presents design fundamentals and two novel instrumentation architectures that provide means for mobile fNIRS-EEG-based neurotechnology applications and optimize usability, performance, safety, and customizability.

The openNIRS is a fiberless miniaturized, modular and mobile fNIRS instrument. As a test platform for the next-generation M3BA approach, it offers core open-source fNIRS technology that simplifies the design of novel customized approaches.

The M3BA is a novel hybrid bio-signal acquisition architecture supporting Wireless Body Area Network scenarios. It integrates improved openNIRS units with high-precision bio-potential measurements, i.e., EEG, ECG, and EMG, utilizing a shared Analog Front-End and a powerful microcontroller that enables the flexible expansion of on-chip routines. Apart from being miniaturized beyond previous approaches, the presented architecture incorporates full modular stand-alone functionality, wearability, multimodality, and scalability; is fully customizable; and, yet, provides desired features such as phase sensitive detection and reconfigurable bio-potential references. Performance characterization using optical and electrical phantoms and in-vivo experiments confirmed functionality and quality of the designed instrument. It was also shown that, where high signal performance is of interest, a dedicated hybrid design can have inherent advantages over separate instruments in terms of signal quality and timing precision.

By providing design principles, architecture details and performance characteristics, this work aims to facilitate future designs in those fields of neurotechnology research that rely on or potentially profit from customizable mobile hybrid biosignal acquisition instruments.

Limitations In the openNIRS, the functional separation between modular core fNIRS technology and replaceable peripheral units naturally results in a trade-off between performance, size, wearability and cost versus a functional design that is easy to grasp, modify, and interface. Whilst providing medium precision, single modules are based on one centered detector, which simplifies the architecture but at the same time limits the scalability of simultaneously measured channels.

These trade-offs and limitations are being addressed and improved in the M3BA, which does not follow the same objective of simplicity in design. The M3BA provides high performance in all modalities and an increased total number of channels, scalable with the number of combined devices, and additionally exploiting source-detector pairs between modules. However, multi-distance measurements (MDM) are not yet supported by default. These may be crucial to making fNIRS more robust to superficial, non-cortical fNIRS signals and can be implemented to be compatible with a modular concept [WLS+17]. Incorporation of MDM in a future device generation can be achieved by further increasing the number of physical channels within a single module.

EEG-fNIRS inter-modality crosstalk minimization also seems to remain worth further investigation: While we could show that it is minimal in single hybrid modules, in some instances switching crosstalk was observed in setups with multiple, physically linked, synchronous M3BA modules. A physical cable connection is only necessary when several modules are to be used fully synchronized to achieve maximum time precision. Future

approaches could make such a connection redundant by instead relying on wireless synchronization procedures or GPS sensors to achieve a high-precision common timebase.

A final limitation results from the use of Bluetooth for wireless communication. While its SPP profile provides an easy interface, Bluetooth is not optimized for high data rates, and interference of multiple modules on close distances can lead to package loss. Depending on the application scenario, another wireless standard might be more suitable.

Multimodal Experiment

Main Contributions Within this thesis, a novel spatial n-back based cognitive workload paradigm was designed that allows for free movements to and from individually adjusted, predefined positions. The corresponding experiment was conducted employing a custom-tailored M3BA headset for the multimodal simultaneous acquisition of EEG, fNIRS, EMG/ECG, accelerations and additional EDA in 17 participants. The paradigm aimed to evoke working-memory related neurophysiological changes with minimal explicit constraints for the participants' behavior under quasi-real-life conditions. These included tasks with multi-sensory demands such as visual and spatial attention, active memorization and performing movements. At the same time, amongst others by spatial design, the paradigm implicitly ensured a high control of experimental conditions. Behavioral results demonstrate a successful approach, appropriate difficulty levels, and small training effects, comparable to previous n-back studies. Joining other existing hybrid EEG-fNIRS datasets for open access [SvB+17; SvK+18], this novel data can be exploited for the development of new multimodal methodology approaches.

Limitations The use of neurophysiological features for the objective assessment of workload is motivated by the same challenges that also apply to the design and evaluation of this experiment: Behavioral metrics, such as error rates, predefined task difficulties, and self-reported assessment do not necessarily mirror the true level of personal engagement, demand or induced cognitive workload. Furthermore, performance depends on a number of subjective factors that may significantly vary between participants: Motivation, wakefulness, attention, and individual memory performance. The experimental protocol could be further improved by a calibration phase including detailed and individual assessment. This would allow a more individualized adjustment of the n-back tasks to task-difficulty, potentially improving comparability across participants.

The acquisition of only a limited number of channels in each modality was an intended trade-off toward the use in realistic, application-oriented scenarios. In hindsight, the additional measurement of two dedicated EOG channels might have been desirable. However, at the time, the integration of EOG-channels was not incorporated in the headset design in the interest of usability and comfort. In future approaches, integration of peripheral dry or water-based EOG electrodes into the headset could be approached and is already supported by the M3BA modules. Similarly, after this first feasibility study, replacement of gel with water-based electrodes would be a next step toward yet faster and easier, less obtrusive application. Furthermore, due to the high spatial specificity of fNIRS, optimized individual

registration and placement of channels could likely increase comparability and robustness of measurements across subjects.

Multimodal Analysis

Main Contributions Making use of the present, so far unique multimodal dataset, this thesis presents the development and evaluation of a multimodal Blind-Source Separation-based framework for the analysis of fNIRS signals and its application in a method for accelerometer-based movement artifact rejection, termed BLISSA^{2}RD. This method tackles challenging fNIRS characteristics such as source dependencies, non-instantaneous and non-constant coupling across channels by combining: (1) ICA that exploits both sample dependency and higher order statistics; (2) temporal embedded CCA; and (3) multimodality in terms of additional accelerometer signals. In principle, this allows the rejection of slow, movement-induced physiological artifacts that would otherwise be hard to separate from hemodynamic responses, due to a shared frequency band. Validation based on the present dataset and simulations confirmed the success of the approach, by yielding an average attenuation of movement-induced artifacts by up to 2 orders of magnitude and an increase of SNR in single-channel hemodynamic responses by up to $10\,dB$.

The framework and methods presented serve as an introduction to a new type of multivariate methods for the BSS analysis of fNIRS signals, as well as a blueprint for artifact rejection in complex environments beyond the present paradigm.

BLISSA^{2}RD is then put to practice in a first proof-of-concept study on the classification of mental workload in freely moving operators, exploiting EEG, fNIRS and Acceleration data. This study entered the complex terrain typical of real-world scenarios, namely a low channel number, a multitude of movements, and a demanding task-environment. Employing a strict artifact rejection, the analyses presented successfully detected workload changes from a baseline task in short time windows, and discriminated between moderate and high workload in longer time windows, with an average accuracy $> 80\%$ in this hybrid approach. Overall performance is comparable to other hybrid workload studies under static laboratory conditions, and validation results are in line with the relevant literature, demonstrating a successful approach despite the challenging conditions.

Limitations Being based on Blind-Source Separation methods, BLISSA^{2}RD requires a minimum number of channels and is not guaranteed to reject single channel artifacts from optode shifts. To exploit multimodality, an accelerometer is required and has to be rigidly integrated into the headgear. Due to the novelty of the overall approach and multivariate data, the method's performance has not yet been tested against existing univariate methods or in real-time applications. These will be important steps to further establish the novel framework in the future, and for real-time application a time-windowed approach seems conceivable.

The approach of operator workload classification proved feasible despite strict artifact rejection and challenging experimental conditions. A challenge, as well as limitation of

studies under realistic conditions, is the trade-off between (1) the certainty and scientific precision in the determination of signal origin, and (2) the application-oriented classification performance achieved. The first case depends on the strict separation between artifacts and neuronal activity and is the most likely reason for the comparatively weak performance of EEG in our study. When the second case is the primary objective, e.g., in a Neuroergonomics application in a specific workplace, the differentiation between neuronal and "artefactual" signals may be less critical and joint exploitation can legitimately yield improved classification performance.

In either case, signal separation can be of advantage and is typically desired. To improve separability in an enhanced approach in the future, a multi-distance approach in fNIRS and unobtrusively measures EOG should be incorporated. Furthermore, the experimental paradigm could be improved by including rounds with reference tasks that also aim to evoke different levels of mental workload but ensure there can be no correlation with eye or body movements. However, an increased duration of the experiment would be the result.

Concluding remarks

In applied neurotechnology, i.e., BCI, a general increase in fNIRS-based approaches is observable [NH15] and the hybridization of multiple brain and body signals derived from EEG and fNIRS has been increasingly reported to improve classification performance and robustness [PAB+10; FMS+12; AJ17; CRL+17]. At the same time, the study of mental states based on neurophysiological measures has risen in popularity in both ergonomics and adaptive-BCI research [YBW+15; CRL+17]. In these fields, the importance of real-life studies is emphasized, as individuals can be expected to function differently in controlled lab environments compared to ecologically valid, every-day situations [BZVE+15]. Such developments, as well as the overwhelming increase in human-computer interactions in our everyday-lives, and the emerging field of telemedicine, are indicators of the need for advanced tools both for acquisition and processing of multiple biosignals.

This thesis identified the combination of EEG and fNIRS as one optimal bimodal pair of signals and entered the so far relatively uncharted waters of brain-activity measurements in ecologically valid conditions. It tackled a multitude of challenges by decreasing acquisition constraints, increasing the amount of available information, and its exploitation to increase robustness. Going the whole way from novel hybrid instrumentation via mobile experiments to artifact rejection and classification of workload, this work focused on the hybrid acquisition and analysis of fNIRS, EEG and accelerometer signals and provided a proof of concept study towards the successful application in a demanding, out-of-lab application. It presents a significant step towards the integration of neurotechnology into real-world applications for BCI, neuroscience-related research, and advanced clinical ambulatory tools for diagnosis and monitoring of neurological dysfunctions. The success of further steps in this direction will continue to depend on the highly interdisciplinary integration of multiple disciplines: the understanding of human brain physiology and clinical conditions, instrumentation and engineering, application design, and multimodal signal processing and machine learning.

Bibliography

[AH09] Abdelnour, A. F. and Huppert, T. "Real-time imaging of human brain function by near-infrared spectroscopy using an adaptive general linear model". In: *NeuroImage* 46.1 (2009), pp. 133–143.

[ALSC15] Adali, T., Levin-Schwartz, Y., and Calhoun, V. D. "Multimodal Data Fusion Using Source Separation: Application to Medical Imaging". In: *Proceedings of the IEEE* 103.9 (2015), pp. 1494–1506.

[AAF14] Adali, T., Anderson, M., and Fu, G.-S. "Diversity in independent component and vector analyses: Identifiability, algorithms, and applications in medical imaging". In: *Signal Processing Magazine, IEEE* 31.3 (2014), pp. 18–33.

[AGO17] Aghajani, H., Garbey, M., and Omurtag, A. "Measuring Mental Workload with EEG + fNIRS". In: *Frontiers in Human Neuroscience* 11 (2017), p. 359.

[AJ17] Ahn, S. and Jun, S. C. "Multi-modal integration of EEG-fNIRS for brain-computer interfaces–Current limitations and future directions". In: *Frontiers in Human Neuroscience* 11 (2017), p. 503.

[AAS06] Akgül, C. B., Akin, A., and Sankur, B. "Extraction of cognitive activity-related waveforms from functional near-infrared spectroscopy signals". In: *Medical and Biological Engineering and Computing* 44.11 (2006), p. 945.

[ABM11] Allaman, I., Belanger, M., and Magistretti, P. J. "Astrocyte–neuron metabolic relationships: for better and for worse". In: *Trends in Neurosciences* 34.2 (2011), pp. 76–87.

[And58] Anderson, T. W. *An introduction to multivariate statistical analysis*. Vol. 2. Wiley New York, 1958.

[APLI+15] Andreu-Perez, J., Leff, D., Ip, H., and Yang, G.-Z. "From Wearable Sensors to Smart Implants - Toward Pervasive and Personalized Healthcare". In: *Biomedical Engineering, IEEE Transactions on* 62.12 (2015), pp. 2750–2762.

[AGL+10] Ang, K. K., Guan, C., Lee, K., Lee, J. Q., Nioka, S., and Chance, B. "A brain-computer interface for mental arithmetic task from single-trial near-infrared spectroscopy brain signals". In: *Proceedings of the 20th International Conference on Pattern Recognition (ICPR)*. IEEE. 2010, pp. 3764–3767.

[AKO+07] Atsumori, H., Kiguchi, M., Obata, A., Sato, H., Katura, T., Utsugi, K., Funane, T., and Maki, A. "Development of a Multi-channel, Portable Optical Topography System". In: *Proceedings of the 29th Ann. Int. Conference of the IEEE Engineering in Medicine and Biology Society (EMBS)*. 2007, pp. 3362–3364.

[AOI+13] Ayaz, H., Onaral, B., Izzetoglu, K., Shewokis, P. A., McKendrick, R., and Parasuraman, R. "Continuous monitoring of brain dynamics with functional near infrared spectroscopy as a tool for neuroergonomic research: Empirical examples and a technological development". In: *Frontiers in Human Neuroscience* 7.871 (2013).

[ASB+12] Ayaz, H., Shewokis, P. A., Bunce, S., Izzetoglu, K., Willems, B., and Onaral, B. "Optical brain monitoring for operator training and mental workload assessment". In: *NeuroImage* 59.1 (2012), pp. 36–47.

[BLW+08] Bauernfeind, G., Leeb, R., Wriessnegger, S. C., and Pfurtscheller, G. "Development, set-up and first results for a one-channel near-infrared spectroscopy system". In: *Biomedizinische Technik* 53.1 (2008), pp. 36–43.

[BSP+11] Bauernfeind, G., Scherer, R., Pfurtscheller, G., and Neuper, C. "Single-trial classification of antagonistic oxyhemoglobin responses during mental arithmetic". In: *Medical & Biological Engineering & Computing* 49.9 (2011), p. 979.

[BSB+14] Bauernfeind, G., Steyrl, D., Brunner, C., and Muller-Putz, G. R. "Single trial classification of fNIRS-based brain-computer interface mental arithmetic data: A comparison between different classifiers". In: *Proceedings of the 36th Ann. Int. Conference of the IEEE Engineering in Medicine and Biology Society (EMBS)*. 2014, pp. 2004–2007.

[BS95] Bell, A. J. and Sejnowski, T. J. "An information-maximization approach to blind separation and blind deconvolution". In: *Neural Computation* 7.6 (1995), pp. 1129–1159.

[BKM+91] Belliveau, J., Kennedy, D., McKinstry, R., Buchbinder, B., Weisskoff, R., Cohen, M., Vevea, J., Brady, T., and Rosen, B. "Functional mapping of the human visual cortex by magnetic resonance imaging". In: *Science* 254.5032 (1991), pp. 716–719.

[BS93] Benaron, D. A. and Stevenson, D. K. "Optical time-of-flight and absorbance imaging of biologic media". In: *Science* 259.5100 (1993), pp. 1463–1466.

[BK10] Benedek, M. and Kaernbach, C. "A continuous measure of phasic electrodermal activity". In: *Journal of Neuroscience Methods* 190.1 (2010), pp. 80–91.

[BCA+95] Benni, P., Chen, B., Amory, D., and Li, J. K. J. "A novel near-infrared spectroscopy (NIRS) system for measuring regional oxygen saturation". In: *Proceedings of the IEEE 21st Ann. Northeast Bioengineering Conference*. 1995, pp. 105–107.

[BNS+06] Bergasa, L. M., Nuevo, J., Sotelo, M. A., Barea, R., and Lopez, M. E. "Real-time system for monitoring driver vigilance". In: *IEEE Transactions on Intelligent Transportation Systems* 7.1 (2006), pp. 63–77.

[Ber29] Berger, H. "Über das Elektroencephalogramm des Menschen". In: *Archiv für Psychiatrie und Nervenkrankheiten* 87.1 (1929), pp. 527–570.

[Ber88] Bertsekas, D. P. "The auction algorithm: A distributed relaxation method for the assignment problem". In: *Annals of Operations Research* 14.1 (1988), pp. 105–123.

[BPM+11] Bießmann, F., Plis, S., Meinecke, F., Eichele, T., and Müller, K. "Analysis of Multimodal Neuroimaging Data". In: *IEEE Reviews in Biomedical Engineering* 4 (2011), pp. 26–58.

[BMG+09] Bießmann, F., Meinecke, F. C., Gretton, A., Rauch, A., Rainer, G., Logothetis, N., and Müller, K.-R. "Temporal Kernel Canonical Correlation Analysis and its Application in Multimodal Neuronal Data Analysis". In: *Machine Learning* 79.1-2 (2009), pp. 5–27.

[Bir06] Birbaumer, N. "Breaking the silence: brain-computer interfaces (BCI) for communication and motor control." In: *Psychophyiology* 43.6 (2006), pp. 517–32.

[BGH+99] Birbaumer, N., Ghanayim, N., Hinterberger, T., Iversen, I., Kotchoubey, B., Kübler, A., Perelmouter, J., Taub, E., and Flor, H. "A spelling device for the paralysed". In: *Nature* 398.6725 (1999), p. 297.

[BTL+08] Blankertz, B., Tomioka, R., Lemm, S., Kawanabe, M., and Müller, K.-R. "Optimizing Spatial filters for Robust EEG Single-Trial Analysis". In: *Signal Processing Magazine, IEEE* 25.1 (2008), pp. 41–56.

[BAD+16] Blankertz, B., Acqualagna, L., Dähne, S., Haufe, S., Schultze-Kraft, M., Sturm, I., Uščumlic, M., Wenzel, M. A., Curio, G., and Müller, K.-R. "The Berlin brain-computer interface: progress beyond communication and control". In: *Frontiers in Neuroscience* 10 (2016), p. 530.

[BCM02] Blankertz, B., Curio, G., and Müller, K.-R. "Classifying single trial EEG: Towards brain computer interfacing". In: *Advances in Neural Information Processing Systems*. 2002, pp. 157–164.

[BLT+11] Blankertz, B., Lemm, S., Treder, M., Haufe, S., and Müller, K.-R. "Single-trial analysis and classification of ERP components—a tutorial". In: *NeuroImage* 56.2 (2011), pp. 814–825.

[BSD+02] Blankertz, B., Schäfer, C., Dornhege, G., and Curio, G. "Single trial detection of EEG error potentials: A tool for increasing BCI transmission rates". In: *International Conference on Artificial Neural Networks*. Springer. 2002, pp. 1137–1143.

[BTV+10] Blankertz, B., Tangermann, M., Vidaurre, C., Fazli, S., Sannelli, C., Haufe, S., Maeder, C., Ramsey, L. E., Sturm, I., Curio, G., and Müller, K.-R. "The Berlin Brain-Computer Interface: Non-Medical Uses of BCI Technology". In: *Frontiers in Neuroscience* 4 (2010), p. 198.

[BBM+01] Boas, D. A., Brooks, D., Miller, E., DiMarzio, C., Kilmer, M., Gaudette, R., and Zhang, Q. "Imaging the body with diffuse optical tomography". In: *Signal Processing Magazine, IEEE* 18.6 (2001), pp. 57–75.

[BDF04] Boas, D. A., Dale, A. M., and Franceschini, M. A. "Diffuse optical imaging of brain activation: approaches to optimizing image sensitivity, resolution, and accuracy". In: *NeuroImage* 23 (2004), pp. 275–288.

[BGS+01] Boas, D. A., Gaudette, T., Strangman, G., Cheng, X., Marota, J. J., and Mandeville, J. B. "The Accuracy of Near Infrared Spectroscopy and Imaging during Focal Changes in Cerebral Hemodynamics". In: *NeuroImage* 13.1 (2001), pp. 76–90.

[BKT94] Boff, K. R., Kaufman, L., and Thomas, J. P. *Handbook of perception and human performance*. Vol. 2. Wiley New York, 1994.

[BU13] Bolz, A. and Urbaszek, W. *Technik in der Kardiologie: eine interdisziplinäre Darstellung für Ingenieure und Mediziner*. Springer-Verlag, 2013.

[Bou12] Boucsein, W. *Electrodermal activity*. 2nd ed. Springer, 2012.

[BLSM+18] Boukouvalas, Z., Levin-Schwartz, Y., Mowakeaa, R., Fu, G.-S., and Adali, T. "Independent Component Analysis using semi-parametric density estimation via entropy maximization". In: *Proceedings of the IEEE Statistical Signal Processing Workshop, Freiburg, Germany*. 2018 (to appear).

[BO04] Bozkurt, A. and Onaral, B. "Safety assessment of near infrared light emitting diodes for diffuse optical measurements". In: *BioMedical Engineering OnLine* 3:9 (2004).

[BRR+05] Bozkurt, A., Rosen, A., Rosen, H., and Onaral, B. "A portable near infrared spectroscopy system for bedside monitoring of newborn brain". In: *BioMedical Engineering OnLine* 4.1 (2005), p. 29.

[BvM17] Brandl, S., von Lühmann, A., and Müller, K.-R. "Towards Brain-Computer Interfaces outside the lab: new measuring devices and machine learning challenges". In: *Proceedings of the 39th Annual International Conference of the IEEE Engineering in Medicine and Biology Society (EMBC)*. 2017.

[BCC+14] Brigadoi, S., Ceccherini, L., Cutini, S., Scarpa, F., Scatturin, P., Selb, J., Gagnon, L., Boas, D. A., and Cooper, R. J. "Motion artifacts in functional near-infrared spectroscopy: a comparison of motion correction techniques applied to real cognitive data". In: *NeuroImage* 85 (2014), pp. 181–191.

[BHVE+12] Brouwer, A.-M., Hogervorst, M. A., Van Erp, J. B., Heffelaar, T., Zimmerman, P. H., and Oostenveld, R. "Estimating workload using EEG spectral power and ERPs in the n-back task". In: *Journal of Neural Engineering* 9.4 (2012), p. 045008.

[BZVE+15] Brouwer, A.-M., Zander, T. O., Van Erp, J. B. F., Korteling, H., and Bronkhorst, A. W. "Using neurophysiological signals that reflect cognitive or affective state: Six recommendations to avoid common pitfalls". In: *Frontiers in Neuroscience* 9.136 (2015).

[BMK+09] Bünau, P. von, Meinecke, F. C., Király, F., and Müller, K.-R. "Finding Stationary Subspaces in Multivariate Time Series". In: *Physical Review Letters* 103 (2009), p. 214101.

[BII+06] Bunce, S., Izzetoglu, M., Izzetoglu, K., Onaral, B., and Pourrezaei, K. "Functional near-infrared spectroscopy". In: *Engineering in Medicine and Biology Magazine, IEEE* 25.4 (2006), pp. 54–62.

[BAK12] Buzsáki, G., Anastassiou, C. A., and Koch, C. "The origin of extracellular fields and currents—EEG, ECoG, LFP and spikes". In: *Nature reviews neuroscience* 13.6 (2012), p. 407.

[BD04] Buzsáki, G. and Draguhn, A. "Neuronal oscillations in cortical networks". In: *Science* 304.5679 (2004), pp. 1926–1929.

[CP06] Cahn, B. R. and Polich, J. “Meditation States and Traits: EEG, ERP, and Neuroimaging Studies”. In: *Psychological Bulletin* 132.2 (2006), pp. 180–211.

[CLA09] Calhoun, V. D., Liu, J., and Adalı, T. “A review of group ICA for fMRI data and ICA for joint inference of imaging, genetic, and ERP data”. In: *NeuroImage* 45.1 (2009), S163–S172.

[CAM+01] Calhoun, V. D., Adali, T, McGinty, V., Pekar, J. J., Watson, T., and Pearlson, G. “fMRI activation in a visual-perception task: network of areas detected using the general linear model and independent components analysis”. In: *NeuroImage* 14.5 (2001), pp. 1080–1088.

[CB93] Carr, J. J. and Brown, J. M. *Introduction to biomedical equipment technology*. Vol. 4. Prentice Hall, 1993.

[Car01] Carter, B. “Op Amp Noise Theory and Applications”. In: *Op Amps for Everyone: design reference*. Ed. by R. Mancini. 2nd ed. Texas Instruments, Newnes, 2001.

[CLM+88] Chance, B, Leigh, J., Miyake, H, Smith, D., Nioka, S, Greenfeld, R, Finander, M, Kaufmann, K, Levy, W, and Young, M. “Comparison of time-resolved and-unresolved measurements of deoxyhemoglobin in brain”. In: *Proceedings of the National Academy of Sciences* 85.14 (1988), pp. 4971–4975.

[CZU+93] Chance, B, Zhuang, Z, UnAh, C., Alter, C, and Lipton, L. “Cognition-activated low-frequency modulation of light absorption in human brain.” In: *Proceedings of the National Academy of Sciences* 90.8 (1993), pp. 3770–3774.

[CCH+11] Chang, M.-H., Cheng, C.-L., Huang, H.-M., Kuo, J.-R., and Lin, B.-S. “Wireless multi-channel near-infrared spectroscopy for monitoring middle cerebral artery occlusion”. In: *Proceedings of the IEEE/SICE International Symposium on System Integration (SII)*. 2011, pp. 1072–1077.

[Cha13] Chapman, D. L. “A contribution to the theory of electrocapillarity”. In: *The London, Edinburgh, and Dublin philosophical magazine and journal of science* 25.148 (1913), pp. 475–481.

[CS07] Chenier, F. and Sawan, M. “A New Brain Imaging Device Based on fNIRS”. In: *Biomedical Circuits and Systems Conference, 2007. BIOCAS 2007. IEEE*. 2007, pp. 1–4.

[CRL+17] Choi, I., Rhiu, I., Lee, Y., Yun, M. H., and Nam, C. S. “A systematic review of hybrid brain-computer interfaces: Taxonomy and usability perspectives”. In: *PloS one* 12.4 (2017), e0176674.

[CEW+12] Christensen, J. C., Estepp, J. R., Wilson, G. F., and Russell, C. A. “The effects of day-to-day variability of physiological data on operator functional state classification”. In: *NeuroImage* 59.1 (2012), pp. 57–63.

[CA04] Coan, J. A. and Allen, J. J. “Frontal EEG asymmetry as a moderator and mediator of emotion”. In: *Biological Psychology* 67.1 (2004), pp. 7–50.

[CBE12] Coffey, E. B., Brouwer, A.-M., and Erp, J. B. van. "Measuring workload using a combination of electroencephalography and near infrared spectroscopy". In: *Proceedings of the Human Factors and Ergonomics Society Annual Meeting*. Vol. 56. 1. 2012, pp. 1822–1826.

[Coh68] Cohen, D. "Magnetoencephalography: evidence of magnetic fields produced by alpha-rhythm currents". In: *Science* 161.3843 (1968), pp. 784–786.

[CCD+03] Cooper, N. R., Croft, R. J., Dominey, S. J., Burgess, A. P., and Gruzelier, J. H. "Paradox lost? Exploring the role of alpha oscillations during externally vs. internally directed attention and the implications for idling and inhibition hypotheses". In: *International Journal of Psychophysiology* 47.1 (2003), pp. 65–74.

[CD88] Cope, M. and Delpy, D. "System for long-term measurement of cerebral blood and tissue oxygenation on newborn infants by near infra-red transillumination". English. In: *Medical and Biological Engineering and Computing* 26.3 (1988), pp. 289–294.

[Cop91] Cope, M. "The application of near infrared spectroscopy to non invasive monitoring of cerebral oxygenation in the newborn infant". PhD thesis. Dept. of Med. Physics and Bioeng., University College London, 1991.

[CGH10] Correia, T. M., Gibson, A. P., and Hebden, J. C. "Identification of the optimal wavelengths for optical topography: a photon measurement density function analysis". In: *Journal of Biomedical Optics* 15.5 (2010), p. 056002.

[CWM07] Coyle, S., Ward, T., and Markham, C. "Brain-computer interface using a simplified functional near-infrared spectroscopy system." In: *Journal of Neural Engineering* 4.3 (2007), pp. 219–226.

[CWM+04] Coyle, S., Ward, T., Markham, C., and McDarby, G. "On the suitability of near-infrared (NIR) systems for next-generation brain–computer interfaces". In: *Physiological Measurement* 25.4 (2004), p. 815.

[CBR10] Cui, X., Bray, S., and Reiss, A. L. "Functional near infrared spectroscopy (NIRS) signal improvement based on negative correlation between oxygenated and deoxygenated hemoglobin dynamics". In: *NeuroImage* 49.4 (2010), pp. 3039–3046.

[DBS+15] Dähne, S., Bießman, F., Samek, W., Haufe, S., Goltz, D., Gundlach, C., Villringer, A., Fazli, S., and Müller, K.-R. "Multivariate Machine Learning Methods for Fusing Functional Multimodal Neuroimaging Data". In: *Proceedings of the IEEE* 103.9 (2015), pp. 1507–1530.

[DBM+13] Dähne, S., Bießman, F., Meinecke, F. C., Mehnert, J., Fazli, S., and Müller, K.-R. "Integration of Multivariate Data Streams With Bandpower Signals". In: *IEEE Transactions on Multimedia* 15.5 (2013), pp. 1001–1013.

[DGM+07] Daunizeau, J., Grova, C., Marrelec, G., Mattout, J., Jbabdi, S., Pélégrini-Issac, M., Lina, J.-M., and Benali, H. "Symmetrical event-related EEG/fMRI information fusion in a variational Bayesian framework". In: *NeuroImage* 36.1 (2007), pp. 69–87.

[Dav04] Davidson, R. J. "What does the prefrontal cortex "do" in affect: perspectives on frontal EEG asymmetry research". In: *Biological Psychology* 67.1-2 (2004), pp. 219–234.

[DEDV+15] Debener, S., Emkes, R., De Vos, M., and Bleichner, M. "Unobtrusive ambulatory EEG using a smartphone and flexible printed electrodes around the ear". In: *Scientific reports* 5 (2015), p. 16743.

[DHK+03] Debener, S., Herrmann, C. S., Kranczioch, C., Gembris, D., and Engel, A. K. "Top-down attentional processing enhances auditory evoked gamma band activity". In: *Neuroreport* 14.5 (2003), pp. 683–686.

[DME+12] Debener, S., Minow, F., Emkes, R., Gandras, K., and Vos, M. de. "How about taking a low-cost, small, and wireless EEG for a walk?" In: *Psychophysiology* 49.11 (2012), pp. 1617–1621.

[DCZ+88] Delpy, D. T., Cope, M, Zee, P van der, Arridge, S, Wray, S, and Wyatt, J. "Estimation of optical pathlength through tissue from direct time of flight measurement". In: *Physics in Medicine and Biology* 33.12 (1988), p. 1433.

[DK57] Dement, W. and Kleitman, N. "Cyclic variations in EEG during sleep and their relation to eye movements, body motility, and dreaming". In: *Electroencephalography and clinical neurophysiology* 9.4 (1957), pp. 673–690.

[DRL+11] Denker, M., Roux, S., Lindén, H., Diesmann, M., Riehle, A., and Grün, S. "The local field potential reflects surplus spike synchrony". In: *Cerebral Cortex* 21.12 (2011), pp. 2681–2695.

[dAZ+98] d'Esposito, M, Aguirre, G., Zarahn, E., Ballard, D, Shin, R., and Lease, J. "Functional MRI studies of spatial and nonspatial working memory". In: *Cognitive Brain Research* 7.1 (1998), pp. 1–13.

[DSS+12] Devor, A., Sakadžić, S., Srinivasan, V. J., Yaseen, M. A., Nizar, K., Saisan, P. A., Tian, P., Dale, A. M., Vinogradov, S. A., Franceschini, M. A., et al. "Frontiers in optical imaging of cerebral blood flow and metabolism". In: *Journal of Cerebral Blood Flow & Metabolism* 32.7 (2012), pp. 1259–1276.

[DLC04] Dolcos, F., LaBar, K. S., and Cabeza, R. "Dissociable effects of arousal and valence on prefrontal activity indexing emotional evaluation and subsequent memory: an event-related fMRI study". In: *NeuroImage* 23.1 (2004), pp. 64–74.

[DRMH+07] G. Dornhege, J. del R. Millán, T. Hinterberger, D. McFarland, and K.-R. Müller, eds. *Toward Brain-Computer Interfacing*. Cambridge, MA: MIT Press, 2007.

[DOC+14] Duke, K., Ordonez, R., Caldwell, J., Wells, C., Williams, I., and Kuehl, T. *Analog Engineer's Pocket Reference*. Ed. by A. Kay and T. Green. 4th ed. Texas Instruments, 2014.

[DMC+95] Duncan, A., Meek, J. H., Clemence, M., Elwell, C. E., Tyszczuk, L., Cope, M., and Delpy, D. T. "Optical pathlength measurements on adult head, calf and forearm and the head of the newborn infant using phase resolved optical spectroscopy". In: *Physics in Medicine and Biology* 40.2 (1995), pp. 295–304.

[ERC+88] Edwards, A., Richardson, C., Cope, M, Wyatt, J., Delpy, D., and Reynolds, E. "Cotside measurement of cerebral blood flow in ill newborn infants by near infrared spectroscopy". In: *The Lancet* 332.8614 (1988), pp. 770–771.

[ESD+14] Ehlis, A.-C., Schneider, S., Dresler, T., and Fallgatter, A. J. "Application of functional near-infrared spectroscopy in psychiatry". In: *NeuroImage* 85 (2014), pp. 478–488.

[ESM+05] Eichele, T., Specht, K., Moosmann, M., Jongsma, M. L., Quiroga, R. Q., Nordby, H., and Hugdahl, K. "Assessing the spatiotemporal evolution of neuronal activation with single-trial event-related potentials and functional MRI". In: *Proceedings of the National Academy of Sciences* 102.49 (2005), pp. 17798–17803.

[ESH+99] Elwell, C., Springett, R., Hillman, E., and Delpy, D. T. "Oscillations in cerebral haemodynamics". In: *Oxygen transport to tissue XXI*. Springer, 1999, pp. 57–65.

[Eng01] Engel, J. "A proposed diagnostic scheme for people with epileptic seizures and with epilepsy: report of the ILAE Task Force on Classification and Terminology". In: *Epilepsia* 42.6 (2001), pp. 796–803.

[EK04] Eriksson, J. and Koivunen, V. "Complex-valued ICA using second order statistics". In: *Machine Learning for Signal Processing, 2004. Proceedings of the 2004 14th IEEE Signal Processing Society Workshop*. IEEE. 2004, pp. 183–192.

[ELT12] Erp, J. van, Lotte, F., and Tangermann, M. "Brain-computer interfaces: beyond medical applications". In: *Computer* 45.4 (2012), pp. 26–34.

[EEC+93] Essenpreis, M., Elwell, C., Cope, M, Zee, P Van der, Arridge, S., and Delpy, D. "Spectral dependence of temporal point spread functions in human tissues". In: *Applied Optics* 32.4 (1993), pp. 418–425.

[FD88] Farwell, L. and Donchin, E. "Talking off the top of your head: toward a mental prosthesis utilizing event-related brain potentials". In: *Electroencephalography and Clinical Neurophysiology* 70.6 (1988), pp. 510–523.

[FDS+15] Fazli, S., Dähne, S., Samek, W., Bießmann, F., and Müller, K.-R. "Learning from more than one data source: data fusion techniques for sensorimotor rhythm-based Brain-Computer Interfaces". In: *Proceedings of the IEEE* 103.6 (2015), pp. 891–906.

[FMS+12] Fazli, S., Mehnert, J., Steinbrink, J., Curio, G., Villringer, A., Müller, K.-R., and Blankertz, B. "Enhanced performance by a hybrid NIRS-EEG brain computer interface". In: *NeuroImage* 59.1 (2012), pp. 519–529.

[FQ12] Ferrari, M. and Quaresima, V. "A brief review on the history of human functional near-infrared spectroscopy (fNIRS) development and fields of application". In: *NeuroImage* 63.2 (2012), pp. 921–935.

[FR86] Fox, P. T. and Raichle, M. E. "Focal physiological uncoupling of cerebral blood flow and oxidative metabolism during somatosensory stimulation in human subjects". In: *Proceedings of the National Academy of Sciences* 83.4 (1986), pp. 1140–1144.

[FFP+98] Franceschini, M. A., Fantini, S., Paunescu, L. A., Maier, J. S., and Gratton, E. “Influence of a superficial layer in the quantitative spectroscopic study of strongly scattering media”. In: *Applied Optics* 37.31 (1998), pp. 7447–7458.

[FJH+06] Franceschini, M. A., Joseph, D. K., Huppert, T. J., Diamond, S. G., and Boas, D. A. “Diffuse optical imaging of the whole head”. In: *Journal of Biomedical Optics* 11.5 (2006), p. 054007.

[Fri89] Friedman, J. H. “Regularized discriminant analysis”. In: *Journal of the American statistical association* 84.405 (1989), pp. 165–175.

[FAA14] Fu, G.-S., Anderson, M., and Adalı, T. “Likelihood estimators for dependent samples and their application to order detection”. In: *IEEE Transactions on Signal Processing* 62.16 (2014), pp. 4237–4244.

[FPA+14] Fu, G.-S., Phlypo, R., Anderson, M., Li, X.-L., et al. “Blind source separation by entropy rate minimization”. In: *IEEE Transactions on Signal Processing* 62.16 (2014), pp. 4245–4255.

[FAS+09] Funane, T., Atsumori, H., Sato, H., Kiguchi, M., and Maki, A. “Relationship between wavelength combination and signal-to-noise ratio in measuring hemoglobin concentrations using visible or near-infrared light”. In: *Optical Review* 16.4 (2009), pp. 442–448.

[Ged68] Geddes, L. A. *Principles of applied biomedical instrumentation*. John Wiley & Sons, 1968.

[GS03] Gevins, A. and Smith, M. E. “Neurophysiological measures of cognitive workload during human-computer interaction”. In: *Theoretical Issues in Ergonomics Science* 4.1-2 (2003), pp. 113–131.

[GHDCA+06] Gómez-Herrero, G., De Clercq, W., Anwar, H., Kara, O., Egiazarian, K., Van Huffel, S., and Van Paesschen, W. “Automatic removal of ocular artifacts in the EEG without an EOG reference channel”. In: *Proceedings of the 7th IEEE Nordic Signal Processing Symposium (NORSIG)*. 2006, pp. 130–133.

[GMV+90] Gratton, E., Mantulin, W., Van De Ven, M., Fishkin, J., Maris, M., and Chance, B. “The possibility of a near-infrared optical imaging system using frequency-domain methods.” In: *Proceedings of the 3rd International Conference on Peace through Mind/Brain Science*. 1990, pp. 183–189.

[GWZ+10] Gregg, N. M., White, B. R., Zeff, B. W., Berger, A. J., and Culver, J. P. “Brain specificity of diffuse optical imaging: improvements from superficial signal regression and tomography”. In: *Frontiers in Neuroenergetics* 2 (2010), p. 14.

[HKK+14] Haufe, S., Kim, J.-W., Kim, I.-H., Sonnleitner, A., Schrauf, M., Curio, G., and Blankertz, B. “Electrophysiology-based detection of emergency braking intention in real-world driving”. In: *Journal of Neural Engineering* 11.5 (2014), p. 056011.

[HMG+14] Haufe, S., Meinecke, F., Görgen, K., Dähne, S., Haynes, J.-D., Blankertz, B., and Bießmann, F. “On the interpretation of weight vectors of linear models in multivariate neuroimaging”. In: *NeuroImage* 87 (2014), pp. 96–110.

[Hel79] Helmholtz, H. von. “Studien über elektrische Grenzschichten”. In: *Ann. Phys.* (1879), pp. 337–382.

[HFT+15] Herff, C., Fortmann, O., Tse, C.-Y., Cheng, X., Putze, F., Heger, D., and Schultz, T. "Hybrid fNIRS-EEG based discrimination of 5 levels of memory load". In: *Neural Engineering (NER), 2015 7th International IEEE/EMBS Conference on*. IEEE. 2015, pp. 5–8.

[HHF+14] Herff, C., Heger, D., Fortmann, O., Hennrich, J., Putze, F., and Schultz, T. "Mental workload during n-back task—quantified in the prefrontal cortex using fNIRS". In: *Frontiers in Human Neuroscience* 7 (2014), p. 935.

[HHP+13] Herff, C., Heger, D., Putze, F., Hennrich, J., Fortmann, O., and Schultz, T. "Classification of mental tasks in the prefrontal cortex using fNIRS". In: *Engineering in Medicine and Biology Society (EMBC), 2013 35th Annual International Conference of the IEEE*. 2013, pp. 2160–2163.

[HFE+93] Hiraoka, M, Firbank, M, Essenpreis, M, Cope, M, Arridge, S., Van Der Zee, P, and Delpy, D. "A Monte Carlo investigation of optical pathlength in inhomogeneous tissue and its application to near-infrared spectroscopy". In: *Physics in Medicine & Biology* 38.12 (1993), p. 1859.

[HH39] Hodgkin, A. L. and Huxley, A. F. "Action potentials recorded from inside a nerve fibre". In: *Nature* 144.3651 (1939), p. 710.

[HLK+09] Holm, A., Lukander, K., Korpela, J., Sallinen, M., and Müller, K. M. "Estimating brain load from the EEG". In: *The Scientific World Journal* 9 (2009), pp. 639–651.

[HT93] Hoshi, Y. and Tamura, M. "Detection of dynamic changes in cerebral oxygenation coupled to neuronal function during mental work in man". In: *Neuroscience letters* 150.1 (1993), pp. 5–8.

[Hot36] Hotelling, H. "Relations between two sets of variates". In: *Biometrika* 28.3/4 (1936), pp. 321–377.

[Hup16] Huppert, T. J. "Commentary on the statistical properties of noise and its implication on general linear models in functional near-infrared spectroscopy". In: *Neurophotonics* 3.1 (2016), p. 010401.

[HDF+09] Huppert, T. J., Diamond, S. G., Franceschini, M. A., and Boas, D. A. "HomER: a review of time-series analysis methods for near-infrared spectroscopy of the brain". In: *Applied Optics* 48.10 (2009), pp. 280–298.

[HHD+06] Huppert, T. J., Hoge, R. D., Diamond, S. G., Franceschini, M. A., and Boas, D. A. "A temporal comparison of BOLD, ASL, and NIRS hemodynamic responses to motor stimuli in adult humans". In: *NeuroImage* 29.2 (2006), pp. 368–382.

[Hyv99] Hyvarinen, A. "Fast and robust fixed-point algorithms for independent component analysis". In: *IEEE transactions on Neural Networks* 10.3 (1999), pp. 626–634.

[IEC] IEC 80601-2-71:2015. *Medical electrical equipment - Part 2-71: Particular requirements for the basic safety and essential performance of functional near-infrared spectroscopy (NIRS) equipment*.

[IPB+07] Irani, F., Platek, S. M., Bunce, S., Ruocco, A. C., and Chute, D. "Functional near infrared spectroscopy (fNIRS): an emerging neuroimaging technology with important applications for the study of brain disorders". In: *The Clinical Neuropsychologist* 21.1 (2007), pp. 9–37.

[IWS+93] Ives, J., Warach, S, Schmitt, F, Edelman, R., and Schomer, D. "Monitoring the patient's EEG during echo planar MRI". In: *Electroencephalography and Clinical Neurophysiology* 87.6 (1993), pp. 417–420.

[IBI+03] Izzetoglu, K., Bunce, S., Izzetoglu, M., Onaral, B., and Pourrezaei, K. "fNIR spectroscopy as a measure of cognitive task load". In: *Engineering in Medicine and Biology Society, 2003. Proceedings of the 25th Annual International Conference of the IEEE*. Vol. 4. 2003, pp. 3431–34344.

[ICB+10] Izzetoglu, M., Chitrapu, P., Bunce, S., and Onaral, B. "Motion artifact cancellation in NIR spectroscopy using discrete Kalman filtering". In: *Biomedical engineering online* 9.1 (2010), p. 16.

[Jen87] Jenkins, T. E. *Optical sensing techniques and signal processing*. Prentice Hall, 1987.

[JT02] Jensen, O. and Tesche, C. D. "Frontal theta activity in humans increases with memory load in a working memory task". In: *European journal of Neuroscience* 15.8 (2002), pp. 1395–1399.

[Jöb77] Jöbsis, F. F. "Noninvasive, infrared monitoring of cerebral and myocardial oxygen sufficiency and circulatory parameters". In: *Science* 198.4323 (1977), pp. 1264–1267.

[Jol82] Jolliffe, I. T. "A note on the use of principal components in regression". In: *Applied Statistics* (1982), pp. 300–303.

[JTF97] Josephs, O., Turner, R., and Friston, K. "Event-related fMRI". In: *Human brain mapping* 5.4 (1997), pp. 243–248.

[KSJ+00] Kandel, E. R., Schwartz, J. H., Jessell, T. M., Siegelbaum, S. A., Hudspeth, A. J., et al. *Principles of neural science*. Vol. 4. McGraw-hill New York, 2000.

[KMM+09] Kanoh, S., Murayama, Y.-M., Miyamoto, K.-I., Yoshinobu, T., and Kawashima, R. "A NIRS-based brain-computer interface system during motor imagery: System development and online feedback training". In: *Proceedings of the Ann. Int. Conference of the IEEE Engineering in Medicine and Biology Society (EMBS)*. 2009, pp. 594–597.

[KKT+93] Kato, T., Kamei, A., Takashima, S., and Ozaki, T. "Human visual cortical function during photic stimulation monitoring by means of near-infrared spectroscopy". In: *Journal of Cerebral Blood Flow & Metabolism* 13.3 (1993), pp. 516–520.

[KÅ93] Kecklund, G. and Åkerstedt, T. "Sleepiness in long distance truck driving: an ambulatory EEG study of night driving". In: *Ergonomics* 36.9 (1993), pp. 1007–1017.

[Kha92] Khandpur, R. S. *Handbook of biomedical instrumentation*. Tata McGraw-Hill Education, 1992.

[KAF+12] Kiguchi, M, Atsumori, H, Fukasaku, I, Kumagai, Y, Funane, T, Maki, A, Kasai, Y, and Ninomiya, A. "Note: wearable near-infrared spectroscopy imager for haired region". In: *Review of Scientific Instruments* 83.5 (2012), p. 056101.

[KC04] Kitchin, C. and Counts, L. *A designer's guide to instrumentation amplifiers*. 2nd ed. Analog Devices, 2004.

[KOR+96] Kleinschmidt, A., Obrig, H., Requardt, M., Merboldt, K.-D., Dirnagl, U., Villringer, A., and Frahm, J. "Simultaneous recording of cerebral blood oxygenation changes during human brain activation by magnetic resonance imaging and near-infrared spectroscopy". In: *Journal of cerebral blood flow & metabolism* 16.5 (1996), pp. 817–826.

[Kli99] Klimesch, W. "EEG alpha and theta oscillations reflect cognitive and memory performance: a review and analysis". In: *Brain research reviews* 29.2-3 (1999), pp. 169–195.

[Kno10] Knoll, G. F. *Radiation detection and measurement*. John Wiley & Sons, 2010.

[KDB+07] Kohlmorgen, J., Dornhege, G., Braun, M., Blankertz, B., Müller, K.-R., Curio, G., Hagemann, K., Bruns, A., Schrauf, M., and Kincses, W. "Improving human performance in a real operating environment through real-time mental workload detection". In: *Toward Brain-Computer Interfacing*. Ed. by G. Dornhege, J. del R. Millán, T. Hinterberger, D. McFarland, and K.-R. Müller. Cambridge, MA: MIT press, 2007, pp. 409–422.

[KMS+07] Kohno, S., Miyai, I., Seiyama, A., Oda, I., Ishikawa, A., Tsuneishi, S., Amita, T., and Shimizu, K. "Removal of the skin blood flow artifact in functional near-infrared spectroscopic imaging data through independent component analysis". In: *Journal of Biomedical Optics* 12.6 (2007), p. 062111.

[Kol91] Koles, Z. J. "The quantitative extraction and topographic mapping of the abnormal components in the clinical EEG". In: *Electroencephalography and clinical Neurophysiology* 79.6 (1991), pp. 440–447.

[KLN+15] Koo, B., Lee, H.-G., Nam, Y., Kang, H., Koh, C. S., Shin, H.-C., and Choi, S. "A hybrid NIRS-EEG system for self-paced brain computer interface with online motor imagery". In: *Journal of Neuroscience Methods* 244 (2015), pp. 26–32.

[KE63] Kuhl, D. E. and Edwards, R. Q. "Image separation radioisotope scanning". In: *Radiology* 80.4 (1963), pp. 653–662.

[LSL+11] Lareau, E., Simard, G., Lesage, F., Nguyen, D., and Sawan, M. "Near infrared spectrometer combined with multichannel EEG for functional brain imaging". In: *Proceedings of the 5th International Symposium on Medical Information Communication Technology (ISMICT)*. 2011, pp. 122–126.

[LW04] Ledoit, O. and Wolf, M. "A well-conditioned estimator for large-dimensional covariance matrices". In: *Journal of Multivariate Analysis* 88.2 (2004), pp. 365–411.

[LBD+11] Lemm, S., Blankertz, B., Dickhaus, T., and Müller, K.-R. “Introduction to machine learning for brain imaging”. In: *NeuroImage* 56 (2011), pp. 387–399.

[LA10] Li, X.-L. and Adali, T. “Independent component analysis by entropy bound minimization”. In: *IEEE Transactions on Signal Processing* 58.10 (2010), pp. 5151–5164.

[LAC07] Li, Y.-O., Adalı, T., and Calhoun, V. D. “Estimating the number of independent components for functional magnetic resonance imaging data”. In: *Human Brain Mapping* 28.11 (2007), pp. 1251–1266.

[Liu05] Liu, J. *Photonic Devices*. Cambridge University Press, 2005.

[LAS17] Liu, Y., Ayaz, H., and Shewokis, P. A. “Mental workload classification with concurrent electroencephalography and functional near-infrared spectroscopy”. In: *Brain-Computer Interfaces* 4.3 (2017), pp. 175–185.

[LKP+12] Looney, D., Kidmose, P., Park, C., Ungstrup, M., Rank, M. L., Rosenkranz, K., and Mandic, D. P. “The In-the-Ear Recording Concept: User-Centered and Wearable Brain Monitoring”. In: *IEEE Pulse* 3.6 (2012), pp. 32–42.

[LPK+11] Looney, D., Park, C., Kidmose, P., Rank, M. L., Ungstrup, M., Rosenkranz, K., and Mandic, D. P. “An in-the-ear platform for recording electroencephalogram”. In: *Proceeding of the Ann. Int. Conference of the IEEE Engineering in Medicine and Biology Society (EMBS)*. 2011, pp. 6882–6885.

[Luc14] Luck, S. J. *An introduction to the event-related potential technique*. MIT press, 2014.

[Mac93] Macchi, O. “Self-adaptive source separation by direct and recursive networks”. In: *Proc. International Conference on Digital Signal Processing (DSP’93) Limasol, Cyprus*. 1993, pp. 1154–1159.

[MWZ+09] Markham, J., White, B. R., Zeff, B. W., and Culver, J. P. “Blind identification of evoked human brain activity with independent component analysis of optical data”. In: *Human Brain Mapping* 30.8 (2009), pp. 2382–2392.

[MP83] Matousek, M. and Petersén, I. “A method for assessing alertness fluctuations from EEG spectra”. In: *Electroencephalography and clinical Neurophysiology* 55.1 (1983), pp. 108–113.

[MPW+08] Matthews, F., Pearlmutter, B. A., Ward, T., Soraghan, C., and Markham, C. “Hemodynamics for Brain-Computer Interfaces”. In: *Signal Processing Magazine, IEEE* 25.1 (2008), pp. 87–94.

[MPA15] McKendrick, R., Parasuraman, R., and Ayaz, H. “Wearable functional Near Infrared Spectroscopy (fNIRS) and transcranial Direct Current Stimulation (tDCS): Expanding Vistas for Neurocognitive Augmentation”. In: *Frontiers in Systems Neuroscience* 9.27 (2015).

[Mea82] Meade, M. L. “Advances in lock-in amplifiers”. In: *Journal of Physics E: Scientific Instruments* 15.4 (1982), p. 395.

[Mea83] Meade, M. L. *Lock-in amplifiers: principles and applications*. Peter Peregrinus Ltd., London UK, 1983.

[MKB+08] Medvedev, A. V., Kainerstorfer, J., Borisov, S. V., Barbour, R. L., and VanMeter, J. "Event-related fast optical signal in a rapid object recognition task: improving detection by the independent component analysis". In: *Brain research* 1236 (2008), pp. 145–158.

[MZK+02] Meinecke, F., Ziehe, A., Kawanabe, M., and Muller, K. "A resampling approach to estimate the stability of one-dimensional or multidimensional independent components". In: *IEEE Transactions on Biomedical Engineering* 49.12 (2002), pp. 1514–1525.

[MGMP11] Mihajlovic, V., Garcia Molina, G, and Peuscher, J. "To what extent can dry and water-based EEG electrodes replace conductive gel ones?: A Steady State Visual Evoked Potential Brain-computer Interface Case Study". In: *ICBE 2011: International Conference on Biomedical Engineering, Venice, Italy, 2011*. Springer. 2011.

[MYH+03] Miyai, I., Yagura, H., Hatakenaka, M., Oda, I., Konishi, I., and Kubota, K. "Longitudinal optical imaging study for locomotor recovery after stroke". In: *Stroke* 34.12 (2003), pp. 2866–2870.

[MD12] Molavi, B. and Dumont, G. A. "Wavelet-based motion artifact removal for functional near-infrared spectroscopy". In: *Physiological measurement* 33.2 (2012), p. 259.

[MWL+04] Morren, G., Wolf, M., Lemmerling, P., Wolf, U., Choi, J., Gratton, E., De Lathauwer, L., and Van Huffel, S. "Detection of fast neuronal signals in the motor cortex from functional near infrared spectroscopy measurements using independent component analysis". In: *Medical and Biological Engineering and Computing* 42.1 (2004), pp. 92–99.

[MHW08] Muehlemann, T., Haensse, D., and Wolf, M. "Wireless miniaturized in-vivo near infrared imaging". In: *Optics express* 16.14 (2008), pp. 10323–10330.

[MTD+08] Müller, K.-R., Tangermann, M., Dornhege, G., Krauledat, M., Curio, G., and Blankertz, B. "Machine learning for real-time single-trial EEG-analysis: From brain-computer interfacing to mental state monitoring". In: *Journal of Neuroscience Methods* 167.1 (2008), pp. 82–90.

[MPSB+05] Müller-Putz, G. R., Scherer, R., Brauneis, C., and Pfurtscheller, G. "Steady-state visual evoked potential (SSVEP)-based communication: impact of harmonic frequency components". In: *Journal of Neural Engineering* 2.4 (2005), p. 123.

[NH15] Naseer, N. and Hong, K.-S. "fNIRS-based brain-computer interfaces: a review". In: *Frontiers in Human Neuroscience* 9 (2015), p. 3.

[OV03] Obrig, H. and Villringer, A. "Beyond the visible - imaging the human brain with light". In: *Journal of Cerebral Blood Flow and Metabolism* 12 (2003), pp. 1–18.

[Obr14] Obrig, H. "NIRS in clinical neurology—a 'promising'tool?" In: *NeuroImage* 85 (2014), pp. 535–546.

[OFS+97] Okada, E., Firbank, M., Schweiger, M., Arridge, S. R., Cope, M., and Delpy, D. T. "Theoretical and experimental investigation of near-infrared light propagation in a model of the adult head". In: *Applied Optics* 36.1 (1997), pp. 21–31.

[OO05] Okui, N. and Okada, E. "Wavelength dependence of crosstalk in dual-wavelength measurement of oxy-and deoxy-hemoglobin". In: *Journal of Biomedical Optics* 10.1 (2005), p. 011015.

[OML+05] Owen, A. M., McMillan, K. M., Laird, A. R., and Bullmore, E. "N-back working memory paradigm: A meta-analysis of normative functional neuroimaging studies". In: *Human Brain Mapping* 25.1 (2005), pp. 46–59.

[Par03] Parasuraman, R. "Neuroergonomics: research and practice". In: *Theoretical Issues in Ergonomics Science* 4.1-2 (2003), pp. 5–20.

[Par11] Parasuraman, R. "Neuroergonomics: brain, cognition, and performance at work". In: *Current directions in psychological science* 20.3 (2011), pp. 181–186.

[PW08] Parasuraman, R. and Wilson, G. F. "Putting the brain to work: Neuroergonomics past, present, and future". In: *Human Factors* 50.3 (2008), pp. 468–474.

[PSG+05] Parra, L. C., Spence, C. D., Gerson, A. D., and Sajda, P. "Recipes for the linear analysis of EEG". In: *NeuroImage* 28.2 (2005), pp. 326–341.

[PHR+10] Paulson, O. B., Hasselbalch, S. G., Rostrup, E., Knudsen, G. M., and Pelligrino, D. "Cerebral blood flow response to functional activation". In: *Journal of Cerebral Blood Flow & Metabolism* 30.1 (2010), pp. 2–14.

[Pea01] Pearson, K. "LIII. On lines and planes of closest fit to systems of points in space". In: *The London, Edinburgh, and Dublin Philosophical Magazine and Journal of Science* 2.11 (1901), pp. 559–572.

[PS99] Pfurtscheller, G. and Silva, F. L. da. "Event-related EEG/MEG synchronization and desynchronization: basic principles". In: *Clinical Neurophysiology* 110.11 (1999), pp. 1842–1857.

[PAB+10] Pfurtscheller, G., Allison, B. Z., Bauernfeind, G., Brunner, C., Solis Escalante, T., Scherer, R., Zander, T. O., Müller-Putz, G., Neuper, C., and Birbaumer, N. "The hybrid BCI". In: *Frontiers in Neuroscience* 4.3 (2010).

[PBW+10] Pfurtscheller, G., Bauernfeind, G., Wriessnegger, S. C., and Neuper, C. "Focal frontal (de)oxyhemoglobin responses during simple arithmetic". In: *International Journal of Psychophysiology* 76.3 (2010), pp. 186–192.

[PHK+74] Picton, T. W., Hillyard, S. A., Krausz, H. I., and Galambos, R. "Human auditory evoked potentials. I: Evaluation of components". In: *Electroencephalography and Clinical Neurophysiology* 36 (1974), pp. 179–190.

[PKK+14] Piper, S. K., Krueger, A., Koch, S. P., Mehnert, J., Habermehl, C., Steinbrink, J., Obrig, H., and Schmitz, C. H. "A wearable multi-channel fNIRS system for brain imaging in freely moving subjects". In: *NeuroImage* 85 (2014), pp. 64–71.

[PSH+05] Pizzagalli, D. A., Sherwood, R. J., Henriques, J. B., and Davidson, R. J. "Frontal brain asymmetry and reward responsiveness: a source-localization study". In: *Psychological Science* 16.10 (2005), pp. 805–813.

[PP94] Pogue, B. W. and Patterson, M. S. "Frequency-domain optical absorption spectroscopy of finite tissue volumes using diffusion theory". In: *Physics in Medicine & Biology* 39.7 (1994), p. 1157.

[PFB+07] Popescu, F., Fazli, S., Badower, Y., Blankertz, B., and Müller, K.-R. "Single trial classification of motor imagination using 6 dry EEG electrodes". In: *PloS one* 2.7 (2007), e637.

[PKC12] Power, S. D., Kushki, A., and Chau, T. "Intersession consistency of single-trial classification of the prefrontal response to mental arithmetic and the no-control state by NIRS". In: *PloS one* 7.7 (2012), e37791.

[PFS+00] Prinzel, L. J., Freeman, F. G., Scerbo, M. W., Mikulka, P. J., and Pope, A. T. "A closed-loop system for examining psychophysiological measures for adaptive task allocation". In: *The International journal of aviation psychology* 10.4 (2000), pp. 393–410.

[PIFS+03] Prinzel III, L. J., Freeman, F. G., Scerbo, M. W., Mikulka, P. J., and Pope, A. T. "Effects of a psychophysiological system for adaptive automation on performance, workload, and the event-related potential P300 component". In: *Human factors* 45.4 (2003), pp. 601–614.

[RM06] Raichle, M. E. and Mintun, M. A. "Brain work and brain imaging". In: *Annuual Reviews Neuroscience* 29 (2006), pp. 449–476.

[RSG+12] Rajkumar, E. R., Safaie, J., Gupta, R., Pattnaik, D., AbrishamiMoghaddam, H., Grebe, R., and Wallois, F. "Development of an autonomic portable single-board computer based high resolution NIRS device for microcirculation analysis". In: *Proceedings of the Ann. Int. Conference of the IEEE Engineering in Medicine and Biology Society (EMBC)*. 2012, pp. 3235–3238.

[Ram98] Rampil, I. J. "A primer for EEG signal processing in anesthesia". In: *Anesthesiology: The Journal of the American Society of Anesthesiologists* 89.4 (1998), pp. 980–1002.

[Rec79] Reclam, C. *Der Leib des Menschen. Dessen Bau und Leben*. Ed. by J. Hoffmann. 2nd ed. K. Thienemann's Verlag, Stuttgart, 1879.

[Reg89] Regan, D. *Human brain electrophysiology: evoked potentials and evoked magnetic fields in science and medicine*. Elsevier, New York, 1989.

[RLJS+00] Reuter-Lorenz, P. A., Jonides, J., Smith, E. E., Hartley, A., Miller, A., Marshuetz, C., and Koeppe, R. A. "Age differences in the frontal lateralization of verbal and spatial working memory revealed by PET". In: *Journal of Cognitive Neuroscience* 12.1 (2000), pp. 174–187.

[Rol00] Rolfe, P. "In Vivo Near Infra-Red Spectrophotometry". In: *Annual Review in Biomedical Engineering* 2 (2000), pp. 315–354.

[RMB+01] Rolfe, P., Mondo, G., Bottini, F., Repetto, D., and Ruggiero, C. "Near infra-red spectroscopy: a low cost device". In: *Proceedings of the 23rd Ann. Int. Conference of the IEEE Engineering in Medicine and Biology Society (EMBS)*. Vol. 3. 2001, pp. 3147–31493.

[RMS+56] Rosvold, H. E., Mirsky, A. F., Sarason, I., Bransome Jr, E. D., and Beck, L. H. "A continuous performance test of brain damage." In: *Journal of Consulting Psychology* 20.5 (1956), p. 343.

[SB05] Saager, R. B. and Berger, A. J. "Direct characterization and removal of interfering absorption trends in two-layer turbid media". In: *JOSA A* 22.9 (2005), pp. 1874–1882.

[SGM+13] Safaie, J, Grebe, R, Moghaddam, H. A., and Wallois, F. "Toward a fully integrated wireless wearable EEG-NIRS bimodal acquisition system". In: *Journal of Neural Engineering* 10.5 (2013), p. 056001.

[SKM14] Samek, W., Kawanabe, M., and Müller, K.-R. "Divergence-based Framework for Common Spatial Patterns Algorithms". In: *IEEE Reviews in Biomedical Engineering* 7 (2014), pp. 50–72.

[SNK+17] Samek, W., Nakajima, S., Kawanabe, M., and Müller, K.-R. "On robust parameter estimation in brain–computer interfacing". In: *Journal of Neural Engineering* 14.6 (2017), p. 061001.

[SW95] Sarter, N. B. and Woods, D. D. "How in the world did we ever get into that mode? Mode error and awareness in supervisory control". In: *Human Factors* 37.1 (1995), pp. 5–19.

[SF04] Sassaroli, A. and Fantini, S. "Comment on the modified Beer-Lambert law for scattering media". In: *Physics in Medicine and Biology* 49.14 (2004), pp. 225–257.

[SKK+04] Sato, H., Kiguchi, M., Kawaguchi, F., and Maki, A. "Practicality of wavelength selection to improve signal-to-noise ratio in near-infrared spectroscopy". In: *NeuroImage* 21.4 (2004), pp. 1554–1562.

[SSLL+13] Sawan, M., Salam, M. T., Le Lan, J., Kassab, A., Gélinas, S., Vannasing, P., Lesage, F., Lassonde, M., and Nguyen, D. K. "Wireless recording systems: from noninvasive EEG-NIRS to invasive EEG devices". In: *IEEE transactions on biomedical circuits and systems* 7.2 (2013), pp. 186–195.

[SS05] Schäfer, J. and Strimmer, K. "A shrinkage approach to large-scale covariance matrix estimation and implications for functional genomics". In: *Statistical Applications in Genetics and Molecular Biology* 4.1 (2005), pp. 1175–1189.

[ST12] Schelkanova, I. and Toronov, V. "Independent component analysis of broadband near-infrared spectroscopy data acquired on adult human head". In: *Biomedical optics express* 3.1 (2012), pp. 64–74.

[SFH+00] Schmidt, F. E., Fry, M. E., Hillman, E. M., Hebden, J. C., and Delpy, D. T. "A 32-channel time-resolved instrument for medical optical tomography". In: *Review of Scientific Instruments* 71.1 (2000), pp. 256–265.

[SKM+14] Scholkmann, F., Kleiser, S., Metz, A. J., Zimmermann, R., Pavia, J. M., Wolf, U., and Wolf, M. "A review on continuous wave functional near-infrared spectroscopy and imaging instrumentation and methodology". In: *NeuroImage* 85 (2014), pp. 6–27.

[SSM+10] Scholkmann, F., Spichtig, S., Muehlemann, T., and Wolf, M. "How to detect and reduce movement artifacts in near-infrared imaging using moving standard deviation and spline interpolation". In: *Physiological Measurement* 31.5 (2010), p. 649.

[SES+08] Schreppel, T., Egetemeir, J., Schecklmann, M., Plichta, M. M., Pauli, P., Ellgring, H., Fallgatter, A. J., and Herrmann, M. J. "Activation of the prefrontal cortex in working memory and interference resolution processes assessed with near-infrared spectroscopy". In: *Neuropsychobiology* 57.4 (2008), pp. 188–193.

[SC13] Schudlo, L. C. and Chau, T. "Dynamic topographical pattern classification of multichannel prefrontal NIRS signals: II. Online differentiation of mental arithmetic and rest". In: *Journal of Neural Engineering* 11.1 (2013), p. 016003.

[SKDG+16] Schultze-Kraft, M., Dähne, S., Gugler, M., Curio, G., and Blankertz, B. "Unsupervised classification of operator workload from brain signals". In: *Journal of Neural Engineering* 13.3 (2016), p. 036008.

[SKM+18] Shin, J., Kim, D.-W., Müller, K.-R., and Hwang, H.-J. "Improvement of Information Transfer Rates Using a Hybrid EEG-NIRS Brain-Computer Interface with a Short Trial Length: Offline and Pseudo-Online Analyses." In: *Sensors* 18.6 (2018), p. 1827.

[SvB+17] Shin, J., von Lühmann, A., Blankertz, B., Kim, D.-W., Jeong, J., Hwang, H.-J., and Müller, K.-R. "Open access dataset for EEG + NIRS single-trial classification". In: *IEEE Transactions on Neural Systems and Rehabilitation Engineering* 25.10 (2017), pp. 1735–1745.

[SvK+18] Shin, J., von Lühmann, A., Kim, D.-W., Mehnert, J., Hwang, H.-J., and Müller, K.-R. "Simultaneous acquisition of EEG and NIRS during cognitive tasks for an open access dataset". In: *Scientific Data* 5.180003 (2018).

[SMB99] Siegel, A., Marota, J., and Boas, D. A. "Design and evaluation of a continuous-wave diffuse optical tomography system". In: *Optics express* 4.8 (1999), pp. 287–298.

[SJK96] Smith, E. E., Jonides, J., and Koeppe, R. A. "Dissociating verbal and spatial working memory using PET". In: *Cerebral Cortex* 6.1 (1996), pp. 11–20.

[SBv18] Soekadar, S., Birbaumer, N., and von Lühmann, A. "Optical brain-computer interfaces: state-of-the-art, challenges, and perspectives". In: *Handbook of Clinical Neurology, Handbook Brain-Computer Interfacing: Neural Devices for paralysis in neurological practice and beyond*. Ed. by N. Ramsey and J. Millan. Vol. xx. 3. (in print). Elsevier, 2018, pp.

[SY06] Son, I.-Y. and Yazici, B. "Near Infrared Imaging and Spectroscopy for Brain Activity Monitoring". In: ed. by J. Byrnes. NATO Security through Science Series-A: Chemistry and Biology, Springer, 2006. Chap. Advances in Sensing with Security Applications, pp. 341–372.

[SMM+08] Soraghan, C., Matthews, F., Markham, C., Pearlmutter, B., O'Neill, R., and Ward, T. "A 12-Channel, real-time near-infrared spectroscopy instrument for brain-computer interface applications". In: *Engineering in Medicine and Biology Society, 2008. EMBS 2008. 30th Annual International Conference of the IEEE*. 2008, pp. 5648–5651.

[Spe78] Sperandio, J.-C. "The regulation of working methods as a function of workload among air traffic controllers". In: *Ergonomics* 21.3 (1978), pp. 195–202.

[SWO+01] Steinbrink, J, Wabnitz, H, Obrig, H, Villringer, A, and Rinneberg, H. "Determining changes in NIR absorption using a layered model of the human head". In: *Physics in Medicine & Biology* 46.3 (2001), p. 879.

[SJL+11] Stikic, M., Johnson, R. R., Levendowski, D. J., Popovic, D. P., Olmstead, R. E., and Berka, C. "EEG-derived estimators of present and future cognitive performance". In: *Frontiers in Human Neuroscience* 5 (2011), p. 70.

[SCT+02] Strangman, G., Culver, G., Thompson, J., and Boas, D. "A quantitative comparison of simultaneous BOLD fMRI and NIRS recordings during functional brain activation." In: *NeuroImage* 17 (2002), pp. 719–731.

[SBS02] Strangman, G., Boas, D. A., and Sutton, J. P. "Non-invasive neuroimaging using near-infrared light". In: *Biological Psychiatry* 52.7 (2002), pp. 679–693.

[SFB03] Strangman, G., Franceschini, M. A., and Boas, D. A. "Factors affecting the accuracy of near-infrared spectroscopy concentration calculations for focal changes in oxygenation parameters". In: *NeuroImage* 18.4 (2003), pp. 865–879.

[SDAE03] Swartling, J., Dam, J. S., and Andersson-Engels, S. "Comparison of spatially and temporally resolved diffuse-reflectance measurement systems for determination of biomedical optical properties". In: *Applied Optics* 42.22 (2003), pp. 4612–4620.

[Swe53] Sweet, W. "Localization of brain tumors with positron emitters". In: *Nucleonics* 11 (1953), pp. 40–45.

[Tex03] Texas Instruments. *Datasheet: OPT-101 Monolithic Photodiode and Single-Supply Transimpedance Amplifier*. 2003.

[Tex12] Texas Instruments. *Datasheet: ADS1299 Low-Noise, 8-Channel, 24-Bit Analog Front-End for Biopotential Measurements*. 2012.

[TM10] Tomioka, R. and Müller, K.-R. "A regularized discriminative framework for EEG analysis with application to brain–computer interface". In: *NeuroImage* 49.1 (2010), pp. 415–432.

[TTK12] Toyama, S., Takano, K., and Kansaku, K. "A non-adhesive solid-gel electrode for a non-invasive brain–machine interface". In: *Frontiers in Neurology* 3 (2012).

[UKBS+02] Uludag, K., Kohl-Bareis, M., Steinbrink, J., Obrig, H., and Villringer, A. "Crosstalk in the Lambert-Beer calculation for near-infrared wavelengths estimated by Monte simulations". In: *Journal of Biomedical Optics* 7.1 (2002), pp. 51–60.

[USV+04] Uludağ, K., Steinbrink, J., Villringer, A., and Obrig, H. "Separability and cross talk: optimizing dual wavelength combinations for near-infrared spectroscopy of the adult head". In: *NeuroImage* 22.2 (2004), pp. 583–589.

[UIS+15] Unni, A., Ihme, K., Surm, H., Weber, L., Lüdtke, A., Nicklas, D., Jipp, M., and Rieger, J. W. "Brain activity measured with fNIRS for the prediction of cognitive workload". In: *Proceedings of the 6th IEEE Int. Conference on Cognitive Infocommunications (CogInfoCom)*. 2015, pp. 349–354.

[VTE+04] Vaithianathan, T., Tullis, I. D. C., Everdell, N., Leung, T., and Gibson, A. "Design of a portable near infrared system for topographic imaging of the brain in babies". In: *Review of Scientific Instruments* 75 (2004), pp. 3276–3283.

[VPH+93] Villringer, A., Planck, J, Hock, C, Schleinkofer, L, and Dirnagl, U. "Near infrared spectroscopy (NIRS): a new tool to study hemodynamic changes during activation of brain function in human adults". In: *Neuroscience letters* 154.1-2 (1993), pp. 101–104.

[VNK+11] Virtanen, J., Noponen, T., Kotilahti, K., Virtanen, J., and Ilmoniemi, R. J. "Accelerometer-based method for correcting signal baseline changes caused by motion artifacts in medical near-infrared spectroscopy". In: *Journal of Biomedical Optics* 16.8 (2011), pp. 087005–087005.

[VNM09] Virtanen, J., Noponen, T. E., and Meriläinen, P. "Comparison of principal and independent component analysis in removing extracerebral interference from near-infrared spectroscopy signals". In: *Journal of Biomedical Optics* 14.5 (2009), p. 054032.

[VVM+10] Volosyak, I., Valbuena, D., Malechka, T., Peuscher, J., et al. "Brain-computer interface using water-based electrodes". In: *Journal of Neural Engineering* 7.6 (2010), p. 066007.

[von16] von Lühmann, A. "Hybridization of bio-electrical and bio-optical acquisition technology using open fNIRS components". In: *Proceedings of the DGBMT workshop biosignal processing*. 2016.

[vAC+17] von Lühmann, A., Addesa, J., Chandra, S., Das, A., Hayashibe, M., and Dutta, A. "Neural interfacing non-invasive brain stimulation with NIRS-EEG joint imaging for closed-loop control of neuroenergetics in ischemic stroke". In: *Proceedings of the 8th International IEEE EMBS Conference On Neural Engineering (NER)*. 2017, pp. 349–353.

[vBM+18] von Lühmann, A., Boukouvalas, Z., Müller, K.-R., and Adali, T. "A new blind source separation framework for signal analysis and artifact rejection in functional Near-Infrared Spectroscopy". In: *NeuroImage* (2018). (in review).

[vHH+15] von Lühmann, A., Herff, C., Heger, D., and Schultz, T. "Towards a wireless open source instrument: functional Near-Infrared Spectroscopy in mobile Neuroergonomics and BCI applications". In: *Frontiers in Human Neuroscience* 9 (2015), p. 617.

[vMB+18] von Lühmann, A., Miklody, D., Blankertz, B., and Müller, K.-R. "Multimodal cognitive workload monitoring in freely moving subjects". In: *Journal of Neural Engineering* (2018). (in preparation).

[vM18] von Lühmann, A. and Müller, K.-R. “Biosignal acquisition device and system, method for acquisition of biosignals”. Pat. US20170281014A1. 2018.

[vM16] von Lühmann, A. and Müller, K.-R. “M3BA: New Technology for Mobile Hybrid BCIs”. In: *Proceedings of the 6th International Brain-Computer Interface Meeting*. 2016, p. 151.

[vM17] von Lühmann, A. and Müller, K.-R. “Why build an integrated EEG-NIRS? About the advantages of hybrid bio-acquisition hardware”. In: *Proceedings of the 39th Annual International Conference of the IEEE Engineering in Medicine and Biology Society (EMBS)*. 2017, pp. 4475–4478.

[vSM+17] von Lühmann, A., Soekadar, S., Müller, K.-R., and Blankertz, B. “Head-gear for mobile neurotechnology: looking into alternatives for EEG and NIRS probes”. In: *Proceedings of the 7th Graz Brain-Computer Interface Conference*. Verlag der Technischen Universität Graz, 2017, pp. 496–501.

[vWS+16] von Lühmann, A., Wabnitz, H., Sander, T., and Müller, K.-R. “Miniaturized CW NIRS for integration and hybridization with mobile EEG / ECG / EMG and Accelerometer”. In: *Proceedings of the Society for functional Near Infrared Spectroscopy Biennial Meeting*. 2016.

[vWS+17] von Lühmann, A., Wabnitz, H., Sander, T., and Müller, K.-R. “M3BA: A Mobile, Modular, Multimodal Biosignal Acquisition Architecture for Miniaturized EEG-NIRS-Based Hybrid BCI and Monitoring”. In: *IEEE Transactions on Biomedical Engineering* 64.6 (2017), pp. 1199–1210.

[VCR+11] Vulliemoz, S., Carmichael, D. W., Rosenkranz, K., Diehl, B., Rodionov, R., Walker, M. C., McEvoy, A. W., and Lemieux, L. “Simultaneous intracranial EEG and fMRI of interictal epileptic discharges in humans”. In: *NeuroImage* 54.1 (2011), pp. 182–190.

[WTM+14] Wabnitz, H., Taubert, D. R., Mazurenka, M., Steinkellner, O., Jelzow, A., Macdonald, R., Milej, D., Sawosz, P., Kacprzak, M., Liebert, A., et al. “Performance assessment of time-domain optical brain imagers, part 1: basic instrumental performance protocol”. In: *Journal of Biomedical Optics* 19.8 (2014), p. 086010.

[WTF+16] Wabnitz, H., Taubert, D. R., Funane, T., Kiguchi, M., Eda, H., Pifferi, A., Torricelli, A., and Macdonald, R. “Characterization of homogeneous tissue phantoms for performance tests in diffuse optics”. In: *Design and Quality for Biomedical Technologies IX*. Vol. 9700. International Society for Optics and Photonics. 2016, p. 970004.

[WPF+07] Whitham, E. M., Pope, K. J., Fitzgibbon, S. P., Lewis, T., Clark, C. R., Loveless, S., Broberg, M., Wallace, A., DeLosAngeles, D., Lillie, P., et al. “Scalp electrical recording during paralysis: quantitative evidence that EEG frequencies above 20 Hz are contaminated by EMG”. In: *Clinical Neurophysiology* 118.8 (2007), pp. 1877–1888.

[Wij01] Wijdicks, E. F. “The diagnosis of brain death”. In: *New England Journal of Medicine* 344.16 (2001), pp. 1215–1221.

[Wil82] Wilde, G. J. “The theory of risk homeostasis: implications for safety and health”. In: *Risk analysis* 2.4 (1982), pp. 209–225.

[WW83] Winter, B. B. and Webster, J. G. “Driven-right-leg circuit design”. In: *IEEE Transactions on Biomedical Engineering* 1 (1983), pp. 62–66.

[WEB+97] Wolf, M, Evans, P, Bucher, H.-U., Dietz, V, Keel, M, Strebel, R, and Von Siebenthal, K. “Measurement of absolute cerebral haemoglobin concentration in adults and neonates”. In: *Oxygen Transport to Tissue XIX*. Springer, 1997, pp. 219–227.

[WFQ07] Wolf, M., Ferrari, M., and Quaresima, V. “Progress of near-infrared spectroscopy and topography for brain and muscle clinical applications”. In: *Journal of Biomedical Optics* 12.6 (2007), p. 062104.

[WWT+02] Wolf, M., Wolf, U., Toronov, V., Michalos, A., Paunescu, L. A., Choi, J. H., and Gratton, E. “Different time evolution of oxyhemoglobin and deoxyhemoglobin concentration changes in the visual and motor cortices during functional stimulation: a near-infrared spectroscopy study”. In: *NeuroImage* 16.3 (2002), pp. 704–712.

[WBM+02] Wolpaw, J. R., Birbaumer, N., McFarland, D. J., Pfurtscheller, G., and Vaughan, T. M. “Brain–computer interfaces for communication and control”. In: *Clinical Neurophysiology* 113.6 (2002), pp. 767–791.

[WCD+90] Wyatt, J., Cope, M, Delpy, D., Richardson, C., Edwards, A., Wray, S, and Reynolds, E. “Quantitation of cerebral blood volume in human infants by near-infrared spectroscopy”. In: *Journal of Applied Physiology* 68.3 (1990), pp. 1086–1091.

[WOL+84] Wyler, A. R., Ojemann, G. A., Lettich, E., and Ward Jr, A. A. “Subdural strip electrodes for localizing epileptogenic foci”. In: *Journal of Neurosurgery* 60.6 (1984), pp. 1195–1200.

[WLS+17] Wyser, D. G., Lambercy, O., Scholkmann, F., Wolf, M., and Gassert, R. “Wearable and modular functional near-infrared spectroscopy instrument with multidistance measurements at four wavelengths”. In: *Neurophotonics* 4.4 (2017), p. 041413.

[YMK01] Yamashita, Y., Maki, A., and Koizumi, H. “Wavelength dependence of the precision of noninvasive optical measurement of oxy-, deoxy-, and total-hemoglobin”. In: *Medical Physics* 28 (2001), pp. 1108–14.

[YAS+10] Yanagisawa, K., Asaka, K., Sawai, H., Tsunashima, H., Nagaoka, T., Tsujii, T., and Sakatani, K. “Brain-computer interface using near-infrared spectroscopy for rehabilitation”. In: *Proceedings of the Int. Conference on Control Automation and Systems (ICCAS)*. 2010, pp. 2248–2253.

[YTJ+09] Ye, J. C., Tak, S., Jang, K. E., Jung, J., and Jang, J. “NIRS-SPM: statistical parametric mapping for near-infrared spectroscopy”. In: *NeuroImage* 44.2 (2009), pp. 428–447.

[YBW+15] Young, M. S., Brookhuis, K. A., Wickens, C. D., and Hancock, P. A. “State of science: mental workload in ergonomics”. In: *Ergonomics* 58.1 (2015), pp. 1–17.

[ZK11] Zander, T. O. and Kothe, C. “Towards passive brain–computer interfaces: applying brain–computer interface technology to human–machine systems in general”. In: *Journal of Neural Engineering* 8.2 (2011), p. 025005.

[ZBG+01] Zhang, Q., Brukilacchio, T. J., Gaudett, T., Wang, L., Li, A., and Boas, D. A. "Experimental comparison of using continuous-wave and frequency-domain diffuse optical imaging systems to detect heterogeneities". In: *BiOS 2001 The International Symposium on Biomedical Optics*. International Society for Optics and Photonics. 2001, pp. 219–238.

[ZIH+14] Zhang, Q., Ivkovic, V., Hu, G., and Strangman, G. E. "Twenty-four-hour ambulatory recording of cerebral hemodynamics, systemic hemodynamics, electrocardiography, and actigraphy during people's daily activities". In: *Journal of Biomedical Optics* 19.4 (2014), pp. 047003–047003.

[ZSG09] Zhang, Q., Strangman, G. E., and Ganis, G. "Adaptive filtering to reduce global interference in non-invasive NIRS measures of brain activation: how well and when does it work?" In: *NeuroImage* 45.3 (2009), pp. 788–794.

[ZNH16] Zhang, X., Noah, J. A., and Hirsch, J. "Separation of the global and local components in functional near-infrared spectroscopy signals using principal component spatial filtering". In: *Neurophotonics* 3.1 (2016), p. 015004.

[ZSW+09] Zhang, Y., Sun, J., Wei, G., Scopesi, F., Serra, G., and Rolfe, P. "Design of a Portable Near Infra-Red Spectroscopy System for Tissue Oxygenation Measurement". In: *Bioinformatics and Biomedical Engineering , 2009. ICBBE 2009. 3rd International Conference on*. 2009, pp. 1–4.

[ZBF+05] Zhang, Y., Brooks, D. H., Franceschini, M. A., and Boas, D. A. "Eigenvector-based spatial filtering for reduction of physiological interference in diffuse optical imaging". In: *Journal of Biomedical Optics* 10.1 (2005), p. 011014.

[ZSY+13] Zheng, F., Sheinberg, R., Yee, M. S., Ono, M., Zheng, Y., and Hogue, C. W. "Cerebral near-infrared spectroscopy (NIRS) monitoring and neurologic outcomes in adult cardiac surgery patients and neurologic outcomes: a systematic review". In: *Anesthesia and Analgesia* 116.3 (2013).

[ZDP+14] Zheng, Y.-L., Ding, X.-R., Poon, C., Lo, B., Zhang, H., Zhou, X.-L., Yang, G.-Z., Zhao, N., and Zhang, Y.-T. "Unobtrusive Sensing and Wearable Devices for Health Informatics". In: *IEEE Transactions on Biomedical Engineering* 61.5 (2014), pp. 1538–1554.

[ZM98] Ziehe, A. and Müller, K.-R. "TDSEP – an efficient algorithm for blind separation using time structure". In: *Proc. of the 8th International Conference on Artificial Neural Networks, ICANN'98*. Ed. by L. Niklasson, M. Bodén, and T. Ziemke. Perspectives in Neural Computing. Berlin: Springer Verlag, 1998, pp. 675–680.

[ZMN+00] Ziehe, A., Müller, K.-R., Nolte, G., Mackert, B.-M., and Curio, G. "Artifact reduction in magnetoneurography based on time-delayed second-order correlations". In: *IEEE Transactions on Biomedical Engineering* 47.1 (2000), pp. 75–87.

[ZBA+13] Zimmermann, R, Braun, F, Achtnich, T, Lambercy, O, Gassert, R, and Wolf, M. "Silicon photomultipliers for improved detection of low light levels in miniature near-infrared spectroscopy instruments". In: *Biomedical Optics Express* 4.5 (2013), pp. 659–666.

[Zum12] Zumbahlen, H. "Staying Well Grounded". In: *Analog Dialogue* 46.2 (2012), p. 17.

List of Figures

List of Tables

Appendix A

Instrumentation Design: Details and Characteristics

A.1 Devices and Parameter/Component Selection

Selection of NIR Detectors

Model	Min. Supply Voltage $[V]$	TIA Gain $[\Omega]$	Typ. Sensitivity @ 850 nm $[V/\mu W]$	Max. Dark Offset $[mV]$	Typ. Dark Offs. Noise $[\mu V rms]$	Cutoff Freq. $-3dB\,[kHz]$
ODC. ODA-5W-100K	± 5	$100k$	0.056	± 1	477	800
ODC. ODA-6W-100M	± 5	$100M$	56	± 2	198	1
ODC. ODA-5W-500M	± 5	$500M$	267	± 2	500	0.315
BB OPT101	$+2.7$	$1M$	0.6	$+10$	300	14
BB OPT301	± 2.25	$1M$	0.47	± 2	160	4
API SD112-42-11-221	± 5	$100k$	0.0558	± 1	60	750
API SD112-43-11-221	± 5	$75M$	45	± 3	20	1

Table A.1: Silicon photo diodes with integrated Trans-impedance amplifier(TIA). ODC: Opto Diode Corp., BB: Burr Brown, API: Advanced Photonic Inc. Highlighted: model used in this work.

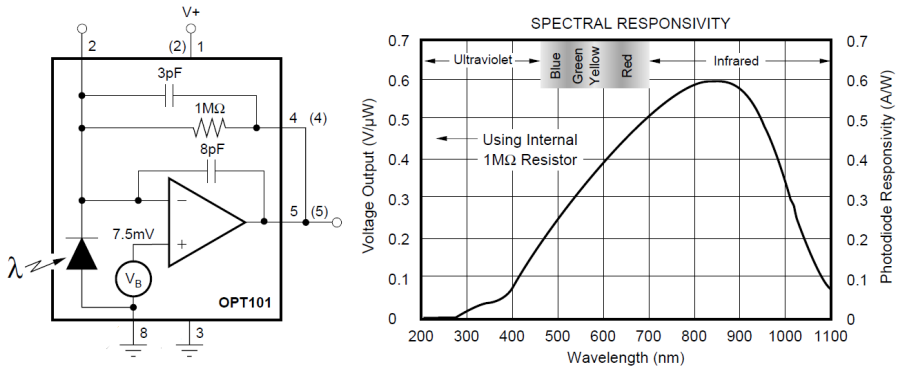

Figure A.1: OPT101 block diagram and spectral responsivity, taken from datasheet [Tex03]

Wavelength Selection

Authors / Wavelengths	≥ 650	≥ 675	≥ 700	≥ 725	≥ 750	≥ 775	≥ 800	≥ 825	≥ 850	≥ 875	≥ 900
Funane2009 [FAS+09]		659 -	- - - -	- - -	- -	-	-	- -	- - -	- - - -	- 900
Yamashita2001 [YMK01]	- - - -	- - - -	- - - -	- - - -	- - - -	- 780		830			
Uludag2004 [USV+04]	- - - -	- - - -	< 720	> 730	- - - -	- - - -	- - - -	- - - -	- - - -	- - - -	- - - -
Okui2005 [OO05]		690 -	- - - -	- - - -	- 750			830			
Strangman2003 [SFB03]					760			830			
Sato2004 [SKK+04]		692						830			
Correia2010 [CGH10]			704							887	
Piper2013 [PKK+14]					760				850		
Safaie2013 [SGM+13]					760				850		
Kiguchi2012 [KAF+12]					754			830			
Chang2011 [CCH+11]				735					850		
Lareau2011 [LSL+11]				735					850		
Kanoh2009 [KMM+09]						780		830			
Zhang2009 [ZSW+09]					760				850		
Bauernfeind2008 [BLW+08]	670									890	
Soraghan2008 [SMM+08]					760					880	
Kawaguchi2008		680						830			
Atsumori2007 [AKO+07]						790			850		
Coyle2007 [CWM07]						760				880	
Chenier2007 [CS07]				730					850		
Bunce2006 [BII+06]				730					850		
Bozkurt2005 [BRR+05]				730					850		
Vaithianathan2004 [VTE+04]						780				880	
Coyle2004 [CWM+04]			700							880	
Rolfe2001 [RMB+01]						780			850		
Boas2001 [BBM+01]						785		830			
Yamashita2001 [YMK01]	660							830			
Rolfe2000 [Rol00]					775				850		
Siegel1999 [SMB99]						780		830			
Benni1995 [BCA+95]						780		830			
Cope1991 [Cop91]						778			867		
OXYMON Mk III, Artinis					760				850		
PortaLite, Artinis					760				850		
fNIR1100, fNIR Devices				730					850		
ETG-4000, Hitachi		695							850		
ETG-7100, Hitachi		695							850		
WOT, Hitachi			705					830			
Genie, MRRA			700					830			
NIRScout(X), NIRx					760				850		
Brainsight NIRS, R. Research		685						830			
FOIRE-3000, Shimadzu						780		830			
OEG-SpO2, Spectratech					770			840			
CW6, TechEn		690						830			
UCL Optical Topography, UCL						780			850		
Imagent, ISS		690						830			
	≥ 650	**≥ 675**	**≥ 700**	**≥ 725**	**≥ 750**	**≥ 775**	**≥ 800**	**≥ 825**	**≥ 850**	**≥ 875**	**≥ 900**

Table A.2: Overview of (optimal) selection in dual-wavelength fNIRS systems. Light blue: Explicit investigations of optimal wavelength pairs. All others: selected wavelengths in implemented systems.

Selection of NIR LEDs

Model	**Wavelengths** λ_1 / nm	λ_2 / nm	**Max** I_F / nm		**Max pulse** I_P / mA		**Typ. total rad. power** / mW		**Half-width** $\Delta\lambda$ / nm		**Half -angle** / degr.	**Type** / mm
L760/850-04A	760	850	100	100			15	18	30	35	± 20	5 Mold
L760/850-38	760	850	75	75			16	18	30	35	± 40	3 Mold
L770/840-40D59	770	840	100	100	500	500	12	9	28	32	± 55	4.65 Stem
SMT735/850	735	850	75	75	300	300	10	18	20	35	± 55	2.7 SMD
L750/850-04A	750	850	100	100			15	18	30	35	± 20	5 Mold
L760/840-05A	760	840	100	100			15	18	30	35	± 40	5.4 Stem
L760/850-05A	760	850	100	100			15	18	30	35	± 40	5.4 Stem

Table A.3: Selection of multi-wavelength LEDs for NIR light emission. Highlighted: employed model.

Overview of Mobile fNIRS Instruments (Not Exhaustive)

Lock-In	**MUX**	**λ [nm]**	**# EM Type**	**# DET Type**	**Est. Volume**	**Mobility**	**Wireless**	**Probe Attachment**	**Samplerate & -depth**	**Ref.**
No	TDM	735 850	4 LED	1 APD	$600\,cm^3$	PORT	Yes	helmet	$20\,Hz$ $16\,Bit$	Lareau 2011 [LSL+11]
Yes	TDM	754 830	8 LD	8 APD	$1100\,cm^3$	PORT	Yes	$600\,g$ headset		Kiguchi 2012 [KAF+12]
No	TDM	760 850	32 LED	4 PD	$28\,cm^3$	WEAR	Yes	chain-link holder	$8\,Hz$ $16\,Bit$	Safaie 2013 [SGM+13]
No	TDM	730 850	1 LED	2 PD	$900\,cm^3$	PORT	No	Flexible PCB	$10\,Hz$ $12\,Bit$	Bozkurt 2005 [BRR+05]
No	TDM	730 805 850	1 LED	1 PD		PORT	No	Velco straps + helmet	$23\,Hz$ $18\,Bit$	Chenier 2007 [CS07]
No	TDM	N/A	8 LED	2 PD	$1500\,cm^3$	PORT	No	embedded multi-dist. silicon patch	$2\,Hz$ $16\,Bit$	Rajkumar 2012 [RSG+12]
No	TDM	760 850	1 LED	1 PD	$1200\,cm^3$	PORT	No	N/A	$40\,Hz$	Zhang 2009 [ZSW+09]
(Yes)	N/A	760 850	3 LED	1 PD	$90\,cm^3$	WEAR	Yes	N/A	$50\,Hz$	PortaLite, Artinis, Netherlands
(Yes)	TDM	730 850	4 LED	12 PD	$540\,cm^3$	(WEAR)	No	silicone forehead patch	$5\,Hz$	fNIR2000C, fNIR Devices, USA
(Yes)	TDM+ FDM	760 850	8 LED	8 PD	$710\,cm^3$	(WEAR)	Yes	cap	$62.5\,Hz$	NIRSport, NIRx, USA
(Yes)	TDM+ FDM	705 830	8 LD	8 APD	$1000\,cm^3$	PORT	Yes	forehead headset	$5\,Hz$	WOT, Hitachi, Japan
N/A	N/A	770 840	6 LED	6 PD	$2000\,cm^3$	PORT	No	forehead headset	$0.76-/6.10\,Hz$	OEG-SpO2, Spectratech, Japan

Table A.4: Overview of mobile commercial and research CW fNIRS-Systems. TDM = Time-Division Multiplex, FDM = Frequency-Division Multiplex, EM Type = Emitter Type. LED = Laser Emitting Diode, LD = Laser Diode, DET Type = Detector Type. APD = Avalanche Photodiode, PD = Silicon Photodiode, Est. Volume = Estimated volume of main acquisition device (excluding proves or headset). N/A: No information

A.2 openNIRS: Supplements

openNIRS Architecture Details

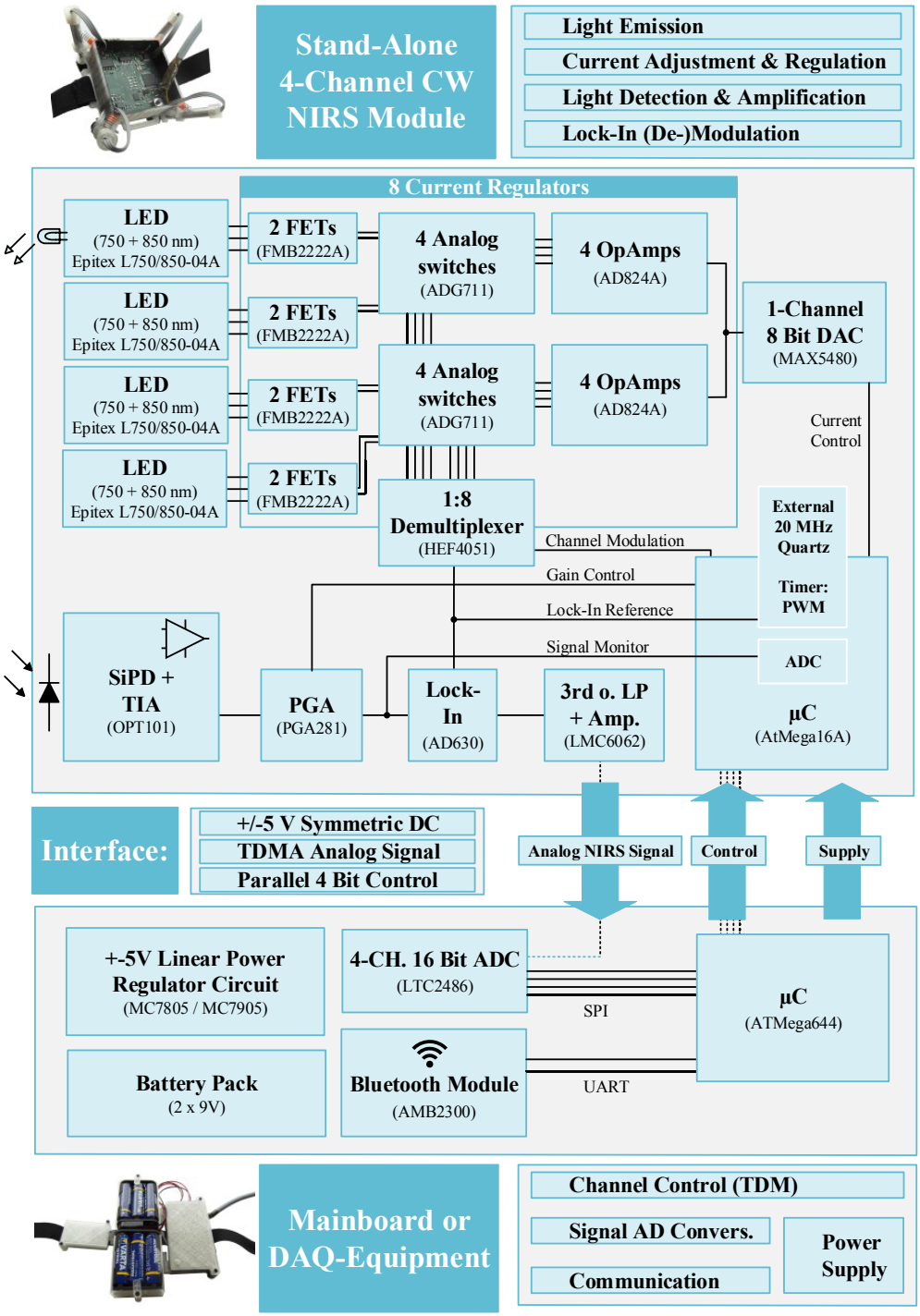

Figure A.2: openNIRS System Architecture

openNIRS Preliminary Mental Arithmetic Study

For a first verification of the openNIRS' capability to measure evoked metabolic brain activity, a BCI experiment was conducted with 12 subjects. Measured hemodynamic responses from epochs containing mental arithmetic or relaxation are classified on a single-trial basis. Mental arithmetic tasks are known to elicit strong hemodynamic reactions in frontal brain areas and have been investigated in a variate of studies with fNIRS [BSB+14; HHP+13; AGL+10].

Protocol: 30 trials of mental arithmetic data were recorded for each participant. During each $10\,s$, participants were asked to repeatedly subtract a number between 7 and 19 (excluding 10) from a randomly generated number between 501 and 999. Both numbers were presented on a screen at a distance of roughly $50\,cm$. After each trial, participants were asked to relax for $25-30\,s$. A fixation cross indicated these pause intervals cross on the screen. A break was included after 15 trials to allow participants to rest and drink.

Channel placement: One openNIRS module was placed on the forehead. Two active emitters were placed on the locations Fp1 & Fp2 of the international 10-20-system. The detector was placed on AFz, resulting in a $3.5\,cm$ emitter-detector distance.

Preprocessing: Aiming only for a first validation, the signal processing of the recorded data was performed in a straight-forward manner. The raw optical densities were converted to HbO/HbR concentration with the mBLL using the HomER2 toolbox [HDF+09]. Signals were then linearly detrended in windows of 300 seconds. Low-frequency noise was attenuated by subtracting a moving average of the mean of 30 seconds prior and after every sample. Data was then low-pass filtered using a 6^{th} order zero-phase Butterworth filter with a cut-off frequency of $0.5\,Hz$ to reduce systemic noise, like pulse artifacts.

Feature extraction and classification: Data was segmented into epochs with relaxation and arithmetic. For relaxation, the last $10\,s$ of the $25-30\,s$ pause intervals were extracted to ensure that hemoglobin levels have returned to baseline. For mental arithmetics, $10\,s$ of data were extracted with a $5\,s$ offset after stimulus presentation to ensure that the hemodynamic response has already developed. For each trial, the slopes of linear least-squares fits to the HbO and HbR data of each channel were used as a feature. Evaluation was performed using Linear Discriminant Analysis in a 10-fold cross-validation.

Results: Discrimination between pause and mental arithmetics yielded an average 65.14% accuracy (see Figure A.3). Of the 12 recorded participants, 9 yielded accuracies significantly higher than chance level (one-sided t-test, $p < 0.05$). In a similar study by [HHP+13], mental arithmetics could be discriminated from pause with 71.17 % using 8 channels and 67.26 % when using only two channels at similar positions as in this study.

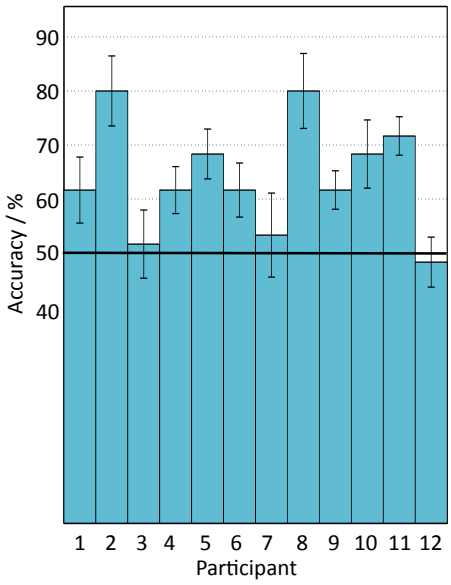

Figure A.3: Results of mental arithmetic classification using the slopes of HbO/HbR in 2 frontal openNIRS channels.

A.3 M3BA: Supplements

Preliminary Tests: Multimodal Raw Data

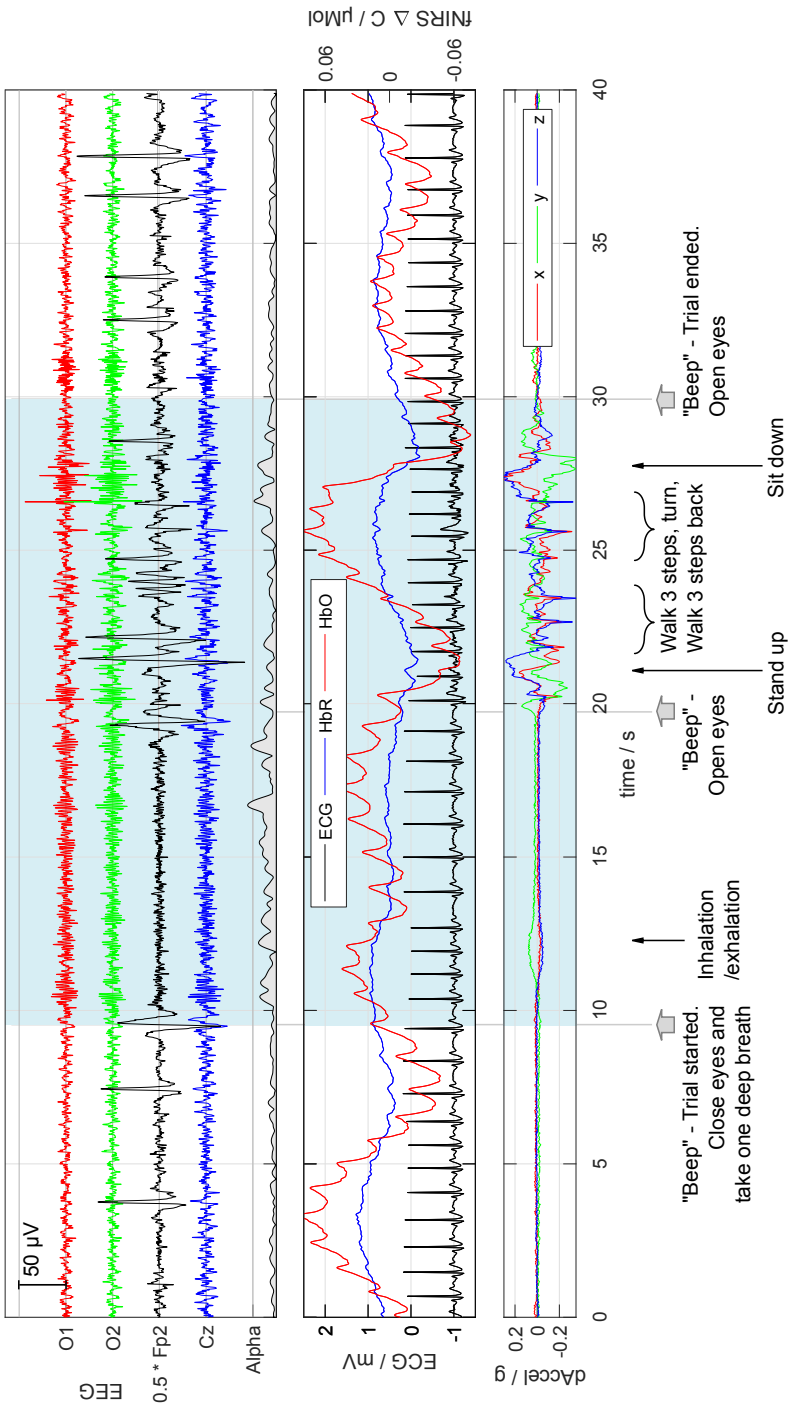

Figure A.4: M3BA raw multimodal data in 40s trial with movement. Channel placement as described in Section 3.6.2.3

Graphical User Interface

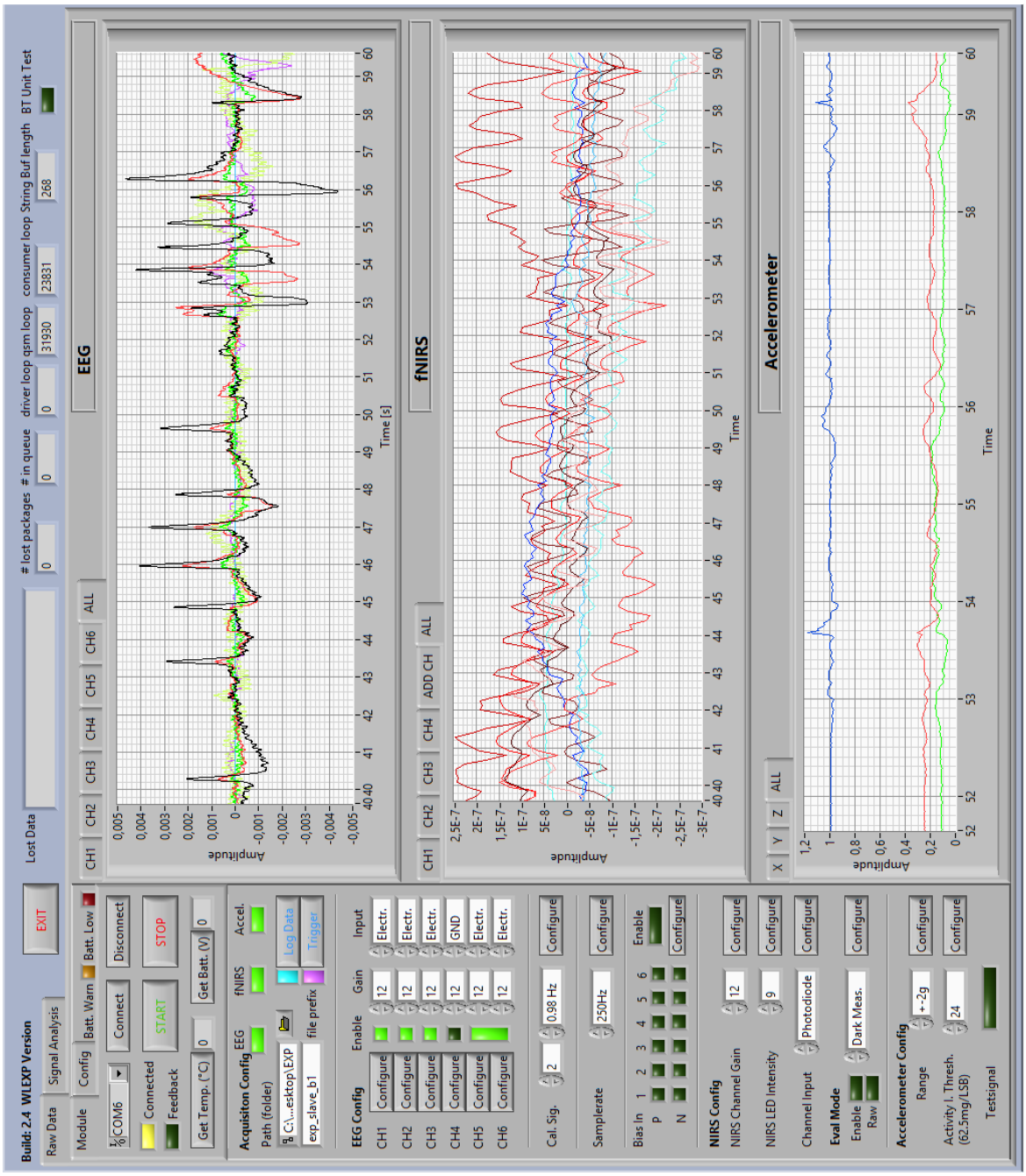

Figure A.5: LabView Graphical User Interface for openNIRS and M3BA. Comprises: Configuration and control, data visualization and logging, online filtering and mBLL conversion, trigger event management, electrode impedance measurement.

M3BA Barebone Module: Details

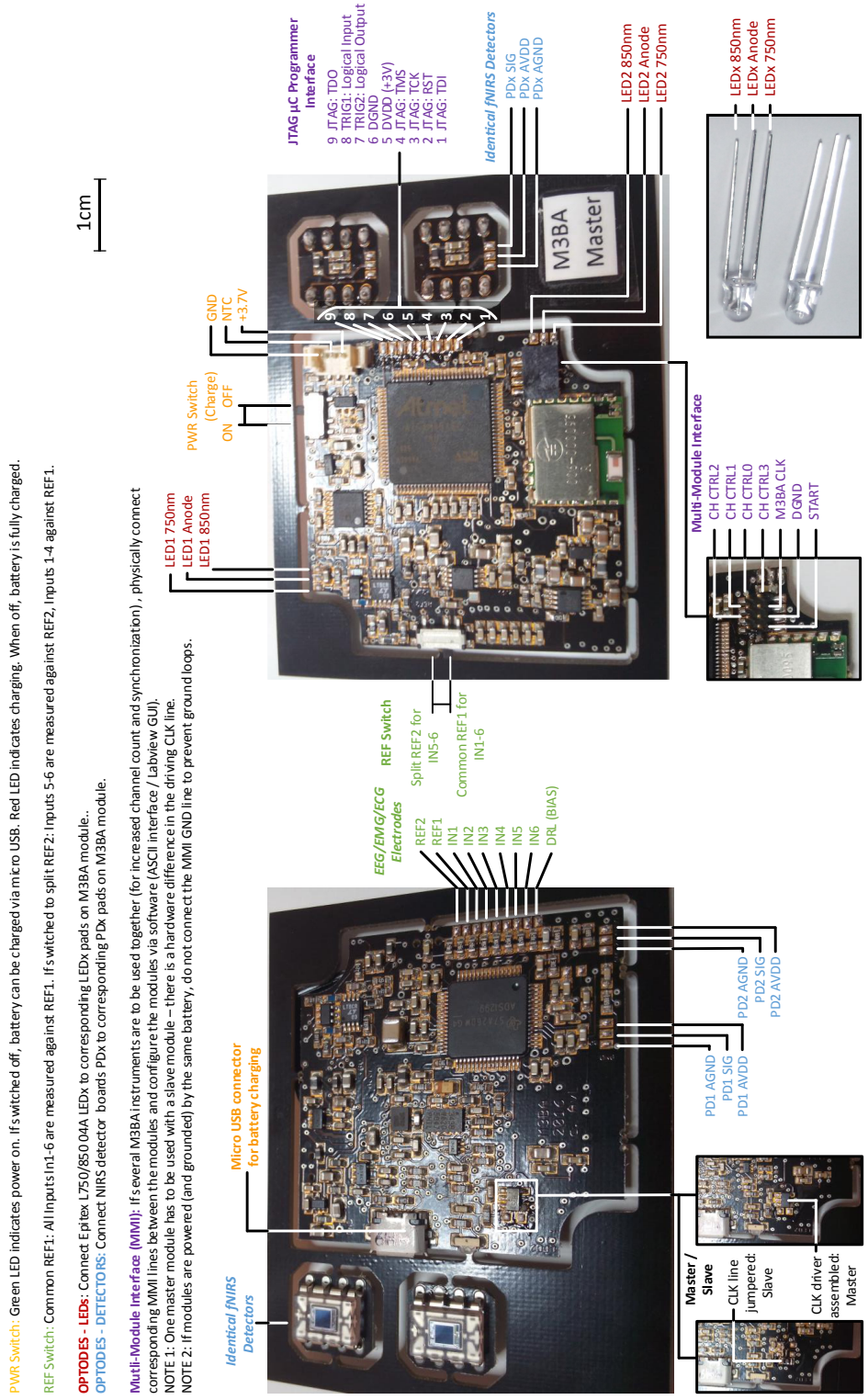

Figure A.6: M3BA barebone module details: Connectors and configuration

Appendix B

Mathematical / Methodological Notes

B.1 Entropy Rate Bound Minimization (ERBM)

This section provides algorithmic details of ICA-ERBM, which was presented in Section 5.1.2.2. For ICA-ERBM, minimization of mutual information rate given in Equation (5.4) provides the umbrella under which non-Gaussianity, and sample-to-sample dependence are jointly exploited.

ICA-ERBM estimates the entropy rate by modeling each source s_n as the output of an invertible linear filter driven by an independent and identically distributed process v_n with unknown distribution. Therefore, there exists a whitening filter that generates each v_n from $\hat{s}_n$. By scaling the whitening filter such that the entropy rate of each $\hat{s}_n$ is approximately equal to the entropy of v_n, the cost function (5.4) becomes

$$J_{ICA}(\mathbf{W}) = \sum_{n=1}^{N_x} H(v_n) - \log|\det(\mathbf{W})| - C, \tag{B.1}$$

where $H(\cdot)$ denotes the differential entropy. It is clear that minimizing (B.1) is not a straightforward task due to the difficulty of estimating the entropy of each v_n. As the model deviates from the true probability density function (PDF), a bias is introduced in the estimate of the demixing matrix that can be quantified using the Kullback-Leibler divergence between the true and the estimated PDF [AAF14; BLSM+18]. This can be avoided by integrating a flexible entropy estimation technique into the ICA framework in order to minimize the bias of the demixing matrix. Therefore, ICA-ERBM uses the same entropy estimation technique as ICA-EBM, which is based on the maximum entropy principle. The estimate of each $H(v_n)$ is given by

$$\hat{H}(v_n) = \log(\sigma_n) + \min_{1\leq m\leq M} H_m(\bar{v}_n), \tag{B.2}$$

where $\sigma_n^2 = E(v_n^2), \bar{v}_n = \frac{v_n}{\sigma}$, and $H_m(\bar{v}_n) = 0.5\log(2\pi e) - V_k\{E(G_m(\bar{v}_n))\}$ is the smallest entropy that corresponds to the mth measuring function $G_m(\cdot)$. ICA-ERBM uses four measuring functions and are based on bimodal, symmetric, or skewed distributions [LA10] resulting in successful estimates of a wide range of distributions.

In addition to the flexible model on the density of the driving process, ICA-ERBM uses a flexible model on the whitening filter in order to effectively exploit sample-to-sample dependence of the underlying sources. Since each s_i has been assumed to be the output of an invertible linear filter driven by v_i, there exists a whitening filter $Q_n(z) = \sum_{k=0}^{K} q_{nk} z^{-k}$ of length K such that

$$v_n(t) = \sum_{k=0}^{K} q_{nk} \hat{s}_n(t-k). \tag{B.3}$$

The optimum filter coefficients can be estimated by solving the following optimization problem

$$\min H(v_n), \text{ s.t. } \frac{1}{2\pi} \int_{\pi}^{\pi} \log |Q(\omega)| \, d\omega = 0, \tag{B.4}$$

where $Q(\omega) \equiv Q(z)|_{z=\exp(\sqrt{-1}\omega)}$. The constraint in Equation (B.4) ensures that $H_r(\hat{s}_n) = H(v_n)$ and each $H(v_n)$ has been estimated according to Equation (B.2).
Thus, it is clear that ICA-ERBM inherits all the advantages of ICA-EBM, namely its flexibility, though with enhanced performance due to the exploitation of sample-to-sample dependence.

B.2 ERBM Whitening Filter Parameter

For the application of the ERBM algorithm to fNIRS data the selection of the whitening-filter length parameter $p_{fl} \in \{1, ...30\}$ was evaluated. Of all u subjects with complete datasets in the preliminary study from Chapter 4, the first $10\,min$ of continuous raw data were used from all 6 experimental blocks b_i, to perform a total number of $30 \times 6 \times 6$ ($p_{fl} \times u \times b$) = 1080 ERBM decompositions. For each subject and filter length p_{fl}, consistency of ERBM unmixing across blocks (time) was evaluated on all 15 possible combinations of two blocks b_{ij} $\{(i,j) \in \{1,...,6\} \,|i < j\}$, calculating intersymbol interference (ISI) [Mac93; EK04] between each pair $(\boldsymbol{W}_{b_i}, \boldsymbol{W}_{b_j}^{-1})$. Overall, this yielded $7 \times 15 = 90$ scores per filter value p and thus a total number of 2700 scores for evaluation of the optimal parameter selection across subjects and time. After a rapid drop for small values p (normalized by the sample frequency f_s), the ISI saturates to values around 0.1 for $\frac{p_{fl}}{f_s} \geq 1\,s$ (see Figure B.1), which is thus the threshold of p-values used for decompositions in this thesis.

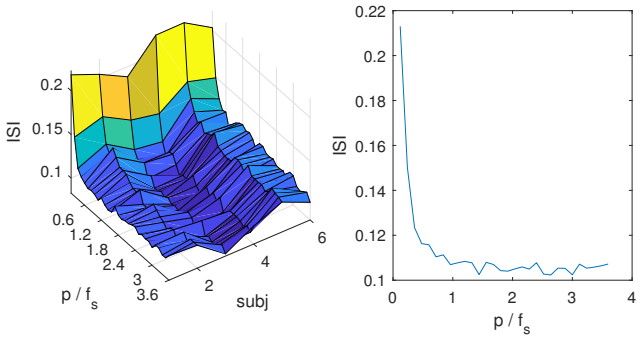

Figure B.1: ERBM p value evaluation. Median ISI per subject and whitening filter length p_{fl} (normalized by sample rate f_s). Right: overall median ISI across subjects.

B.3 fNIRS BSS: Simulations

Here we provide details for the simulations performed in Section 5.2.5.1. In a simplified approach to simulate fNIRS source characteristics, focusing on source dependencies, processes were generated for $t \in 0...100\,s$, sampled at $f_s = 8\,Hz$ (see Figure B.2), representing

1. *Breathing* ($0.14\,Hz \mid \omega_1 = \frac{2\pi}{7\,s}$): $S_1(t) = \sin(\omega_1 t)$)
2. *Heart rate* ($1\,Hz \mid \omega_2 = \frac{2\pi}{s}$), amplitude modulated by S_1:
   $S_2(t) = |(1 - 0.3\,S_1(t)|\sin(\omega_2 t)$
3. *Mayer waves* ($0.1\,Hz \mid \omega_3 = \frac{2\pi}{10\,s}$): $S_3(t) = \sin(\omega_3 t)$)
4. *Evoked responses* using $\omega_4 = \frac{2\pi}{20\,s}$ and $e(t) = \begin{cases} \sin(\omega_4 t), & \sin(\omega_4 t) \geq 0 \\ 0, & else \end{cases}$ for $S_4(t) = \text{sgolayfilt}\,(e(t))$ with Savitzky-Golay filter order 1 and frame length $5\,s$
5. *White random gaussian noise* in $S_5(t)$
6. $S_6(t)$ *Movement artifacts*: initialize $m(t) = 0$ and draw a random numbers $randn(t)$ from $\mathcal{N}(0,1)$ for all t. At each timepoint t_{idx} where $randn(t) > 2$ holds, add a gaussian curve ($\mathcal{N}(0, \frac{5}{f_s})$, cut at halfwidth $2.5\,s$) to $m(t)$, centered at t_{idx}
7. $S_7(t)$ *Dependent evoked processes*: initialize $S(t) = 0$, find time indices for local maxima t_{max} of evoked responses S_4, add a gaussian curve ($\mathcal{N}(0, \frac{20}{f_s})$, cut at halfwidth $5\,s$) centered at $t_{max} + t_d$ with a random ($\mathcal{N}\frac{8}{f_s}, \frac{1}{f_s}$)) time delay $t_d = randn \times 4\,s$.

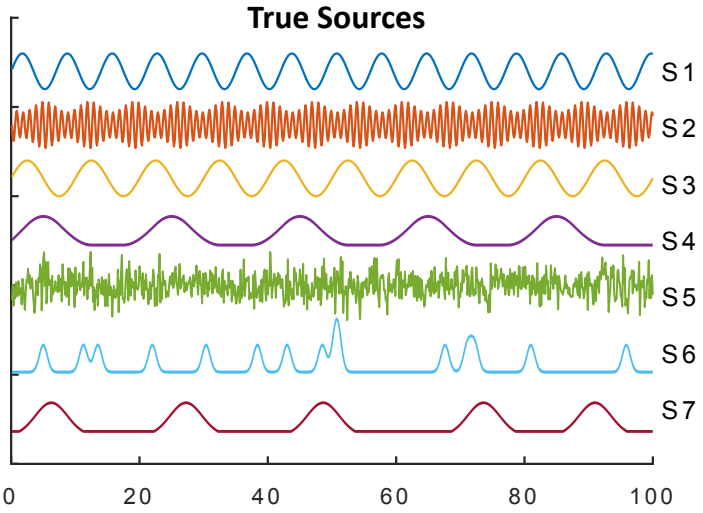

Figure B.2: Typical example of simulated fNIRS components. $S1 - S7$ represent processes due to breathing (1), heart rate (2), Mayer waves (3), evoked responses (4), white noise (5), movement artifacts (6) and dependent evoked processes (7)

Appendix C

Multimodal Study: Supplements

C.1 EDA Grand Averages

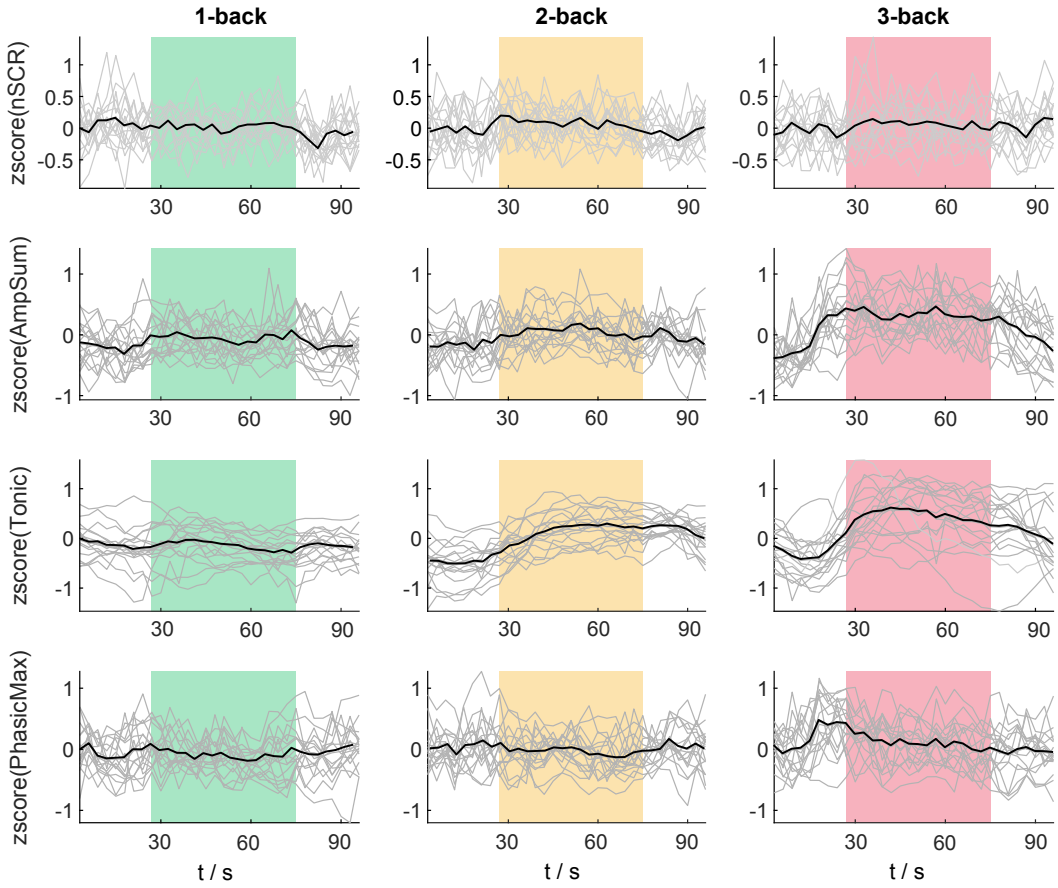

Figure C.1: Workload experiment: grand average EDA signals (black) and participant averages (grey) across n=1,2,3-back rounds. Features calculated on sliding 30 *s* windows (5 *s* step size) with Ledalab [BK10]. nSCR: Number of above-threshold Skin Conductance Responses, AmpSum: Amplitude Sum, Tonic: mean Tonic activity, PhasicMax: Maximum value of Phasic activity.

C.2 Metadata: Example

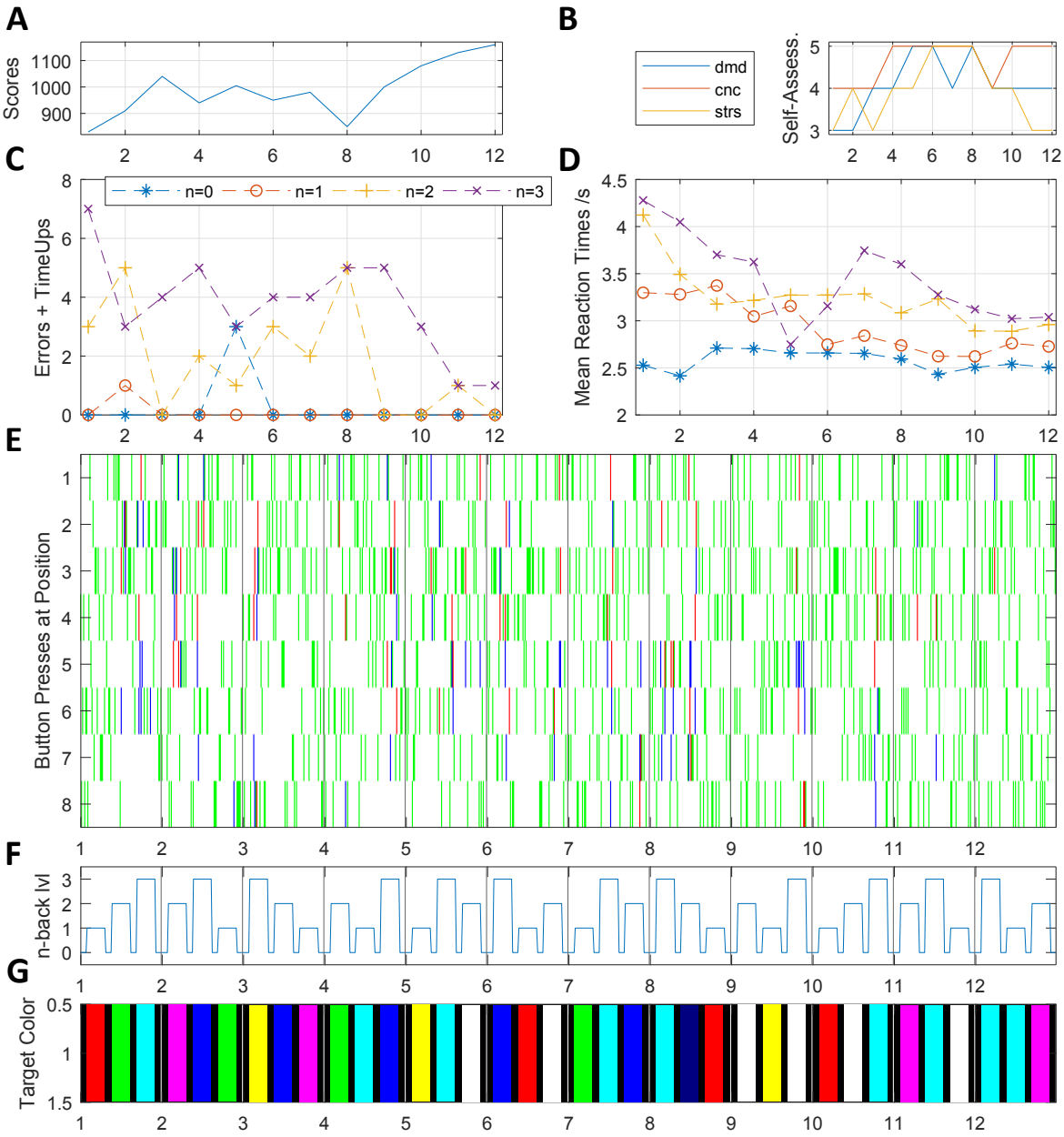

Figure C.2: Workload experiment metadata example for one participant. (**A**) Personal (game-)scores across all blocks. (**B**) Self-assessed demand (dmd), concentration (cnc) and stress (strs) on a 1-5 Likert-Scale. (**C**) Total number of errors and time-ups in n=0,1,2,3-back round in each block. (**D**) Average reaction times (time to button press-event) in n=0,1,2,3-back rounds in each block. (**E**) Spatial distribution of button press events at button positions 1-8 (compare Figure 4.1) across the whole time of the experiment = blocks 1...12. Green: Correct selection. Red: Selection error. Blue: Time up (no selection). Indicator for target position distribution without spatial bias. (**F**) n=0,1,2,3-back sequence over all blocks of the experiment. (**G**) Target color in each round over all blocks of the experiment. x-axes are time (blocks). **F** and **G** are identical for all subjects. **E** is identical for all subjects except erroneous selections and time-ups.

C.3 Average fNIRS Signals: Examples

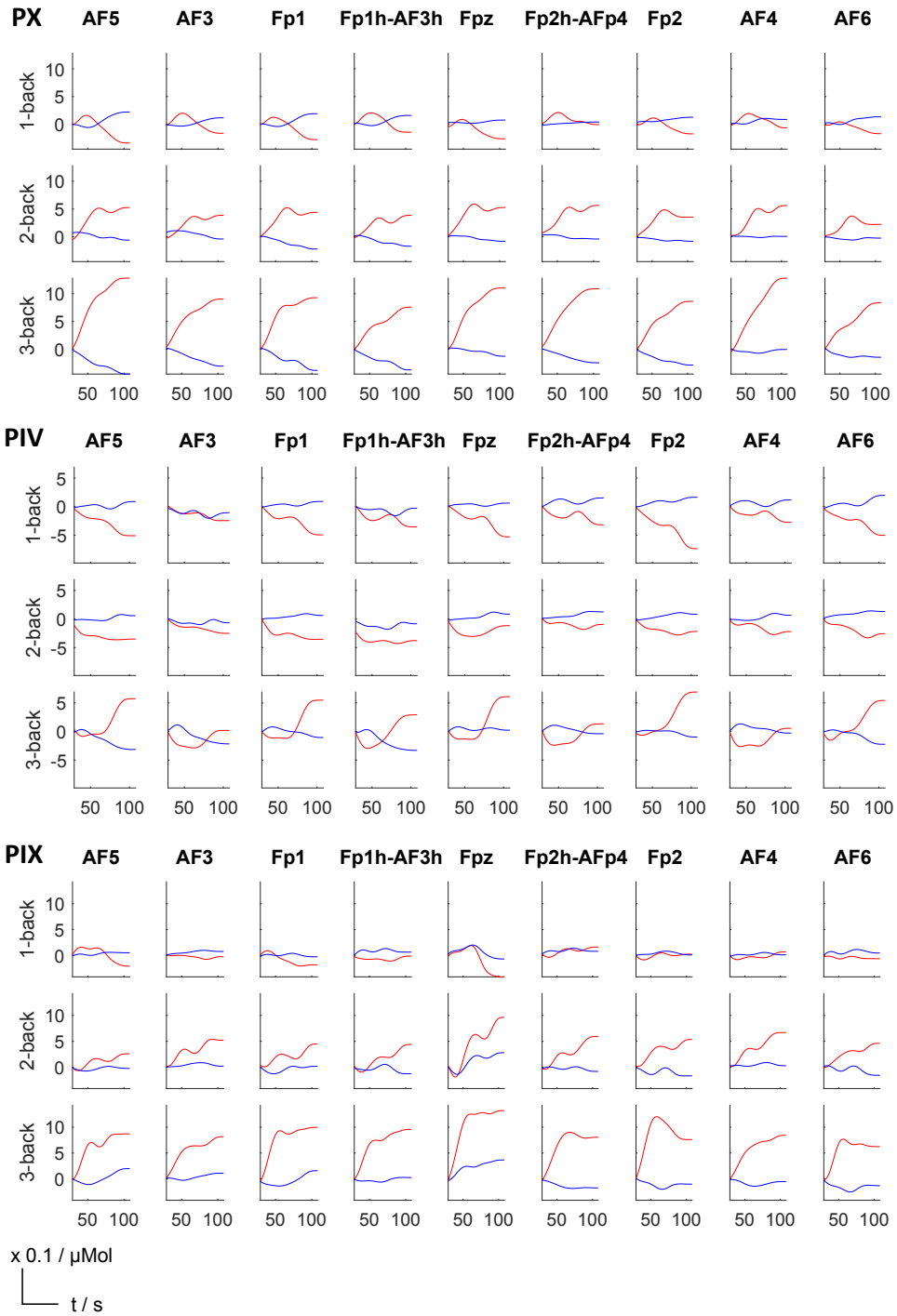

Figure C.3: Average fNIRS HbR (blue) and HbO (red) signals of 3 exemplary participants across n=1,2,3-back rounds. Signals are cleaned with BLISSA[2]RD and low-pass filtered with $f_c = 0.033\,Hz$. Positions given are 10-05 EEG positions closest to the actual fNIRS channel of each signal.

C.4 EOG in EEG Classification: Accuracies and Patterns

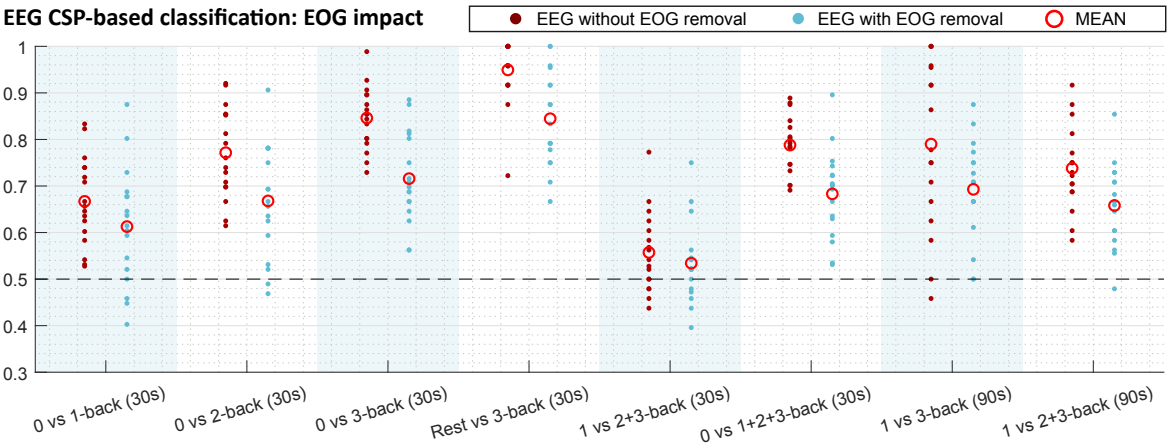

Figure C.4: Comparative classification results from identical analysis pipeline as described in Section 5.3.3 for EEG data with and without regression-based EOG removal. Average performance drop: 8.7%.

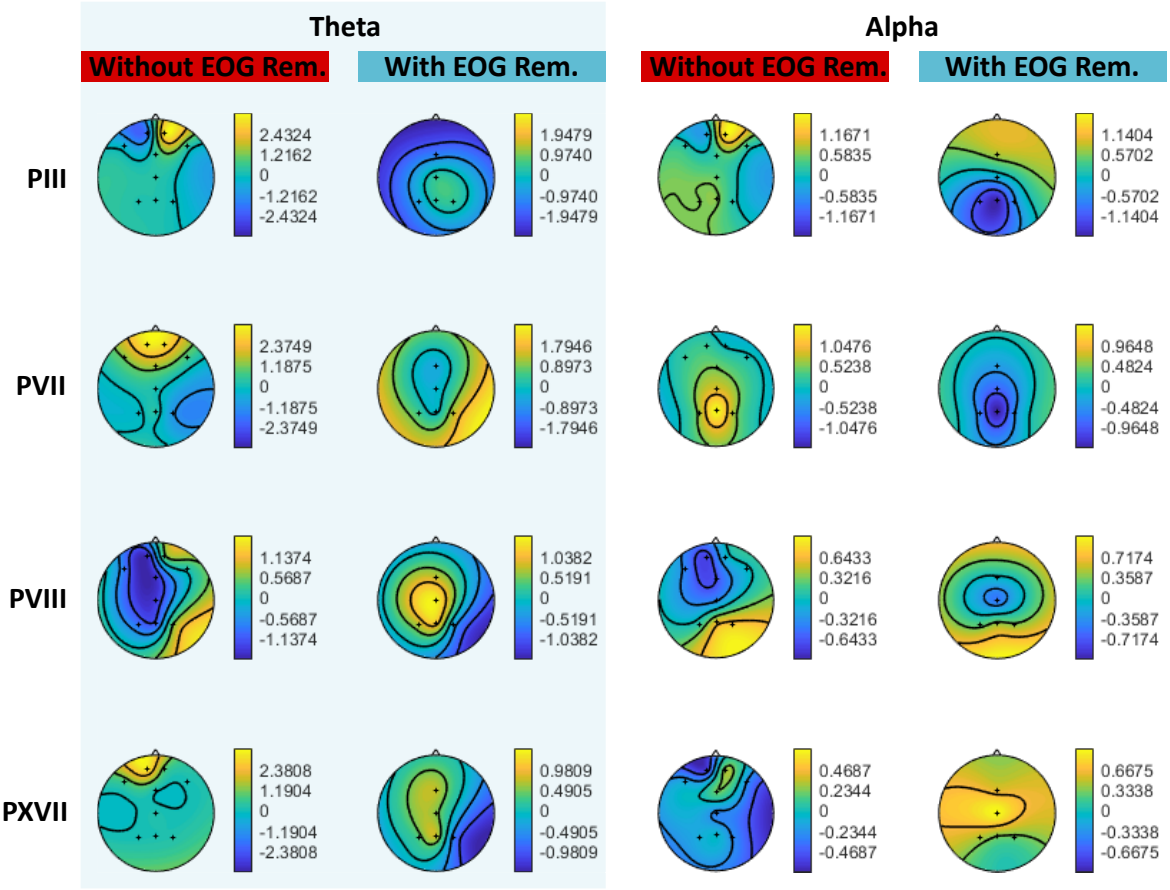

Figure C.5: Scalp plots of spatial patterns corresponding to CSP components with highest eigenvalue in four exemplary participants for both target frequency bands using EEG data with and without regression-based EOG removal. Note that the latter reduces the number of available (frontal) channels. CSP analysis was performed on the whole data set of each subject.